Récolteuses d'énergie cinétique électrostatique (e-REC) à basse fréquence pour applications de communication RFID et électronique portable

Yingxian Lu

To cite this version:

Yingxian Lu. Récolteuses d'énergie cinétique électrostatique (e-REC) à basse fréquence pour applications de communication RFID et électronique portable. Traitement du signal et de l'image [eess.SP]. Université Paris-Est, 2018. Français. NNT : 2018PESC1077 . tel-01936057

HAL Id: tel-01936057
https://theses.hal.science/tel-01936057

Submitted on 27 Nov 2018

UNIVERSITÉ
PARIS-EST

Ecole Doctorale MSTIC
Mathématiques, Sciences et Technologies de l'Information et de la Communication

Thèse
Pour obtenir le grade de
Docteur de l'Université Paris-Est

Specialité: Électronique, Optronique et Systèmes (CNU 63)

Présentée et soutenue publiquement par
Yingxian LU

Récupérateurs d'énergie cinétique électrostatique (e-REC) à basse fréquence pour applications de communication RFID et électronique portable

Low-frequency electrostatic kinetic energy harvesters (e-KEH) for RFID communication applications and wearable electronics

July 1, 2018

Thèse dirigèe par:
Prof. Philippe BASSET
Prof. Jean-Marc LAHEURTE

Jury

Prof. Elie LEFEUVRE	Université Paris-Sud	Rapporteur
Prof. Isabelle DUFOUR	Université de Bordeaux	Rapporteur
Prof. Philippe BASSET	ESIEE Paris	Directeur
Prof. Jean-Marc LAHEURTE	Université Paris-Est Marne-la-Valée	Directeur
Prof. Michaël PEIGNEY	Ecole des Ponts et Chaussées ParisTech	Examinateur
Prof. Jérôme JUILLARD	CentraleSupélec	Examinateur
Dr. Sébastien BOISSEAU	CEA	Examinateur
Dr. Arnaud VENA	Université de Montpellier	Examinateur
Dr. Dimitri GALAYKO	Université Sorbonne	Invité

Acknowledgment

I would like to give my a lot of thanks to Professor Philippe Basset and Professor Jean-Marc Laheurte, the advisors of my work, for their great help and thoughtful advices throughout the entire period of my thesis project. They are not only helpful advisors for my thesis research project, but also good collaborators and colleagues at the same time. When I am encountered with difficulties in the project, they can always find time to organize discussions with me, and they usually propose helpful and inspiring during the discussions. I have also learnt from them that we must be rigorous and even meticulous regarding the details in research, and that keeping the knowledge up with the state of the art and getting inspired are also of great importance.

I would like to thank all the collaborators during my stay in Université Paris-Est for their helpful discussions, assistance with my experiments, and suggestions on the publications. I would like to thank Professor Dimitri Galayko for his help for me to have a better understanding of the electrical model of our prototypes, and the principles of their conditioning circuits. Thank Dr. Francesco Cottone, who has set a solid basis for my thesis before my arrival at Université Paris-Est, without which I could not have got the opportunity to work on the topic of low frequency of vibration energy harvester. Dr. Frédéric Marty made the major contribution in the fabrication of all my kinetic energy harvester designs and the helpful suggestions about the mask designs. I appreciate the help of Dr. Sébastien Boisseau and his research group with the initial corona charging experiments and data transmission experiments. Thank Dr. Hatem Samaali and Med Aymen Ben Ouanes for their collaboration on the Bennet-doulber mechanical switch. Thanks to Ali Ghaffarinejad, Ronan Hinchet, and Hemin Zhang for their collaboration on the study of triboelectric kinetic energy harvesters. Thanks to Professor Jérôme Juillard helped me a lot in the discussion about the air damping model for the gap-closing KEH. Thanks to Professor Yamin Leprince-Wang for her help and guidance on my work in the fabrication of electrospun nanofibrous films. Thanks to Linda Serairi, Yamina-Ghozlane Habba, and Martine Capo-Chichi for their help with the electrospinning fabrication and the observation of the material under SEM.

Thanks to all the technicians and engineers of the clean room and the RF characterization lab of ESYCOM for their help in the fabrication, observation, and characterization of my designs. Among them, Dr. Lionel Rousseau helped a lot in the LPCVD deposition of the electret material on the harvesters, and trained me for doing the deposition; thanks to Julien Pagazani for helping me with the fabrication of the RFID module.

Thanks for the doctoral school MSTIC, Université Paris-Est for supporting my travelling expenses to present my thesis work to international conferences such as IEEE MEMS and Power-MEMS. And many thanks to the Chinese Scholarship Council for their recognition of my research achievements during thesis. And thank the SATT project for providing financial support to my research.

I would like to give my special thanks to Professor Xiaohong Wang for her kind and helpful discussions about the possibilities of future researches and collaborations; to Professor Tarik Bourouina and Professor Tianhong Cui for their helpful suggestions about the target journals of my publications; and to Professor Haixia Zhang for the inspiring seminar and discussions about triboelectric nanogenerators and for the joyful collaboration in the organization of ICAN competition, and the friendship.

In addition, I would like to thank all my officemates, labmates, and fellow PhD candidates in the doctoral school MSTIC, including David Abi-Saab, William Cesar, Stéphane Protat, Siqi Wang, Pedro Gonzalez Losada, Ferdous Jahan Shaun, Imadeddine Azzouz, Viet-Duc Pham, Mazen Sayed Ahmed, Sreyash Sarkar, and Lan Gao, etc., for their cooperation, accompany, and of course friendship. Nevertheless, I am also grateful to all my good friends for their accompany, care and support for me, among them I would like to specially thank Minxue Zhang, Lu Lu, Jie Wei, Jia Kang, Jinjin Zhao, Haidi Gao, and Jian Zhuo for their long-term friendship with me. I would like to thank all my friends for accepting nothing less than excellence from me.

Last but not the least, I would like to thank my parents for supporting me spiritually throughout writing this thesis. And special thanks to Dr. Sixin Zhang for his helpful inspirations and discussions.

Résumé

Chapitre 1. Introduction aux récupérateurs d'énergie cinétique (REC) miniatures à basses fréquences - état de l'art

Les réseaux sans fil sont avantageux en raison de leur grande flexibilité et de leur installation facile, et leurs applications généralisées pour les nœuds de capteurs sans fil nécessitent des modules d'alimentation électrique localisés et durables. Actuellement, les capteurs sans fil sont généralement alimentés par des batteries. Leur inconvénient est qu'ils ont besoin d'une maintenance régulière (remplacement ou recharge). Une solution alternative consiste à tirer parti d'une source d'énergie ambiante comme l'énergie cinétique qui est souvent abondante, grâce à un "récupérateur d'énergie cinétique" (REC). Compte tenu des caractéristiques de l'énergie cinétique ambiante et de la demande des utilisateurs, les RECs doivent pouvoir s'adapter aux fréquences dans une large bande passante, en particulier aux basses fréquences, et doivent si possible fournir une puissance de sortie élevée grâce à une efficacité de conversion énergétique élevée. La basse fréquence, ainsi que la petite taille et le faible poids, limité la puissance de sortie d'un REC, en fonction de la puissance maximale théorique donnée dans [1]. Ainsi, la conception d'un REC doit prendre en compte la maximisation de l'efficacité de conversion d'énergie. Diverses approches comme l'expansion de la bande passante du dispositif, un mécanisme de conversion vers les hautes fréquences mécaniques ou des structures rotatives peuvent être introduites dans les systèmes pour améliorer l'efficacité de la transduction d'énergie. D'autres techniques pour booster les performances d'un REC soit liées à son mécanisme de transduction d'énergie spécifique, soit à son interface électrique (circuit de conditionnement).

Principles généraux des récupérateurs d'énergie cinétique

Un REC est un système électromécanique typique composé de parties fixes et mobiles, qui sont reliées par des ressort et des modules de transduction électromécaniques. Le REC est généralement soit excité par une force directe externe ou une déformation, soit excité par une force d'inertie. Un modèle mécanique pratique à paramètres localisés est généralement utilisé pour analyser le comportement du REC. Il considère la partie mobile du prototype comme une masse discrète, qui est en relation avec des ressorts et des amortisseurs localisés. L'excitation externe est généralement décrite comme une force (ou une force d'inertie) agissant sur la masse mobile. Le modèle le plus simple considère un résonateur linéaire avec un ressort linéaire et un amortisseur linéaire, qui atteint la performance optimale à sa fréquence de résonance. Le rendement maximum de conversion d'énergie avec cette configuration est déterminé par l'amortissement parasite, et n'est atteint que si l'amortissement électrique est identique à l'amortissement liè aux pertes. Les coefficients d'amortissement de la transduction des REC électromagnétiques et électrostatiques avec charges résistives sont donnés, en soulignant les principes de base pour améliorer la puissance de sortie des prototypes. Pour les RECs avec une conception plus complexe, les résonateurs sont parfois non linéaires, soit avec une structure élastique non linéaire, soit avec un mécanisme d'amortissement non linéaire. Sous ces configurations, les forces élastiques ou d'amortissement sont exprimées soit sous la forme de polynômes, soit sous la forme de fonctions de déplacement de la masse par morceaux. Ainsi, les équations du mouvement de la masse sont parfois très compliquées pour une solution analytique, de sorte que la méthode de résolution couramment utilisée est numérique.

Etat de l'art : composants mécaniques pour applications basses fréquences

La petite taille et la basse fréquence d'un REC sont les facteurs de base qui limitent la puissance de sortie du prototype. Premièrement, la fréquence de résonance d'un système ressort-masse est augmentée par une masse réduite, il n'est donc pas facile de réduire la fréquence de résonance. Deuxièmement, la puissance disponible dans une vibration est linéairement liée à sa fréquence, ainsi la basse fréquence est désavantageuse pour l'alimentation électrique. Pour surmonter ces inconvénients, divers composants mécaniques sont mis en œuvre dans la littérature, comprenant un mécanisme de conversion de fréquence mécanique vers le haut (up-conversion), des structures spatiales répétitives, et des structures de rotation. Les structures de "up-conversion" de fréquence mécanique peuvent être basées sur des mouvements d'impact, de plissement ou de bouclage, ou sur des structures bistables. Grâce à ces structures, la masse mobile est capable de parcourir plusieurs courses au sein de chaque période d'excitation externe, réalisant plusieurs oscillations de transduction d'énergie, et multipliant ainsi l'apport d'énergie. De même, un dispositif à structure spatiale répétitive réalise également plusieurs cycles de transduction d'énergie et multiplie la puissance, même avec une seule oscillation de la structure mobile. Par ailleurs, les structures non résonantes telles que les structures rotatives sont utiles car elles peuvent fournir au système une large bande passante, et elles sont généralement combinées avec des structures résonnantes qui fournissent une amplification mécanique au système.

Etat de l'art : principes de transduction des RECs

Les principes de transduction les plus couramment utilisés dans les RECs comprennent les transductions piézoélectrique, électromagnétique, électrostatique et magnétostrictive. Parmi eux, le REC piézoélectrique comprend une structure piézoélectrique déformable, qui convertit la déformation en signaux électriques. Des aimants sont parfois utilisés dans certains prototypes piézoélectriques à l'échelle de mm pour réaliser des forces sans contact et pour réduire l'amortissement, mais ils ne peuvent pas être miniaturisés facilement en raison des limitations de la fabrication. Les RECs électromagnétiques sont basés sur la loi de Faraday d'induction électromagnétique, générant des signaux électriques dans les bobines d'un flux magnétique changeant. Les RECs électrostatiques sont basés sur l'induction électrostatique dans un condensateur variable polarisé. Il est le plus adapté à la miniaturisation et est capable de fournir une grande efficacité, grâce à sa structure simple (seulement deux électrodes) et la préparation facile du matériau fonctionnel (comme l'électret). La variation de capacité et la tension de polarisation sont les facteurs clés influençant la puissance des RECs électrostatiques, qui sont aussi les sujets principaux de cette thèse. Les RECs magnétostrictifs fusionnent des prototypes qui convertissent la déformation du matériau magnétostrictif suite à un champ magnétique changeant, qui est ensuite converti en signaux électriques par piezoélectricité. Les structures des RECs magnétostrictifs sont normalement plus compliquées que les prototypes basés sur d'autres principes de transduction, et sont donc difficiles à miniaturiser. Des RECs hybrides sont également proposés pour atteindre une puissance supérieure, mais leurs structures sont normalement plus compliquées.

Travaux antérieurs de l'équipe

Considérant les avantages de la transduction électrostatique pour la miniaturisation, notre groupe a choisi ce principe comme module d'alimentation pour les nœuds de capteurs sans fil.

En 2006, nous avons proposé un e-REC basé sur une structure de plaques à chevauchement dans le plan, où l'électrode mobile est placée en parallèle avec l'électrode fixe et se déplaçe dans le plan. Dans ce prototype, la force électrostatique d'attraction entre les électrodes augmente rapidement avec l'augmentation de la tension de polarisation et perturbe le mouvement de l'électrode mobile. En raison de l'absence de stoppeurs hors-plan efficaces confinant l'espace entre les électrodes, la tension maximale de polarisation est de 12 V, alors que la variation de capacité est également limitée ($\frac{C_{\max}}{C_{\min}} = 2$). Ainsi, l'efficacité de la conversion d'énergie du premier prototype est faible (1,4nJ par cycle mécanique avec l'accélération de 0,25 g_{rms} et 250 Hz).

Ensuite, un second prototype a été proposé, qui est basé sur une structure de silicium monocouche comprenant une électrode mobile avec des ressorts linéaires, des stoppeurs élastiques et une bille. Le transducteur capacitif du prototype a la géométrie des doigts interdigités avec fermeture de l'entrefer dans le plan. Grâce à l'impact de la bille miniature sur l'électrode mobile, le dispositif est efficace sur une large plage de fréquences, particulièrement sensible aux basses fréquences. Ce prototype a été fabriqué à partir d'une plaquette de silicium d'une épaisseur de 380-μm et est polarisé par une tension continue externe pour son fonctionnement. C'est le point de départ de cette thèse.

Contenu de la thèse

Cette thèse considère l'amélioration des récupérateurs d'énergie cinétique électrostatique à basses fréquences à partir des aspects de la conception, de la modélisation et de la fabrication. Il propose également un noeud de capteur de communication RFID autonome en énergie dans lequel la puissance est fournie par un e-REC basse fréquence. Le premier chapitre donne une introduction sur les récupérateurs d'énergie cinétique basse fréquence, l'état de l'art, et les travaux antérieurs du groupe. Dans le chapitre 2, nous présentons un modèle numérique avec amortisseur linéaire décrivant le prototype proposé dans [2], et un prototype entièrement actif en ajoutant une couche d'électret chargée verticalement. Une caractérisation complète du prototype réalisé est présentée. Dans le chapitre 3, un modèle plus sophistiqué et prédictif est introduit, en tenant compte de la non-linéarité apportée par les impacts et l'amortissement de l'air. Le chapitre 4 décrit un prototype avec des structures de peignes hiérarchiques, ce qui réduit l'effet d'amortissement de l'air. Le cinquième chapitre traite de deux approches alternatives pour améliorer les performances des RECs basses fréquences. La première approche est un prototype entièrement flexible dédié à l'électronique portable. L'autre approche est capable de répondre aux vibrations provenant de plusieurs directions. Dans le dernier chapitre, nous montrons la conception d'une étiquette RFID semi-passive pour la communication sans fil, dans laquelle la puissance est fournie par le REC à basses fréquences proposé dans cette thèse. Le module de communication est soigneusement conçu, caractérisé et évalué, suivi d'un test intégral du système complet.

Chapitre 2. Modélisation et caractérisation du REC couplé à l'impact

Nous avons introduit une couche verticale d'électret au REC basses fréquences décrit au chapitre 1, pour fournir au dispositif une tension de polarisation interne. Un modèle numérique simple du prototype est proposé, qui considère un amortissement linéaire de l'air et la non-linéarité introduite par les stoppeurs élastiques.

Modélisation du REC couplé aux impacts avec amortissement linéaire de l'air

Un modèle simplifié du REC est proposé. L'équation de Newton du mouvement de l'électrode contient une force de ressort linéaire, une force d'arrêt par morceaux, une force d'amortissement linéaire de l'air et une force électrostatique provenant des électrodes fixes. Parmi celles-ci, la force d'amortissement de l'air est linéairement liée à la vitesse de la masse mobile; les forces du ressort et du stoppeur dépendent du déplacement de la masse; tandis que la force électrostatique est également liée à la fois au déplacement de masse et à sa vitesse. Pour résoudre l'équation, nous utilisons une méthode simple de récurrence temporelle avec des pas de temps constants et des correcteurs trapézoïdaux. Les impacts et les séparations entre l'électrode mobile et les stoppeurs sont détectés à chaque pas de temps. Considérant l'influence de la force d'arrêt par morceaux, nous estimons l'occurrence d'impact / séparation et procédons à deux calculs concernant les intervalles de temps avant et après l'instance en utilisant des fonctions par morceaux. Plusieurs paramètres utilisés dans le modèle doivent être ajustés par des résultats expérimentaux.

Expériences et validation du modèle (sans bille)

Mesure de la variation de capacité : Une technique de mesure dynamique rapportée dans [3] est appliquée pour obtenir la variation de la capacité du prototype avec le temps. Le rapport de capacité du prototype ($\frac{C_{\max}}{C_{\min}}$) est d'environ 2,4 (une capacité parasite de 28 pF est incluse).

Mesure de la tension électret : Un REC électrostatique à électret est modélisé comme un condensateur variable avec une polarisation continue sur l'une de ses électrodes. Une méthode simple pour mesurer la tension fournie par l'électret est proposée. Le circuit de mesure comprend un redresseur à demi-onde, à travers lequel un condensateur de réservoir est chargé jusqu'à saturation. Le calcul de la tension électret se réfère à la plage de variation de capacité et à la tension de saturation du redresseur demi-onde. La tension de polarisation fournie par l'électret dans le prototype proposé (sans bille) se stabilise autour de 21 V.

Paramètres empirique du modèle : Dans le modèle proposé, il y a que deux paramètres qui doivent être ajustés en fonction des amplitudes d'accélération : le facteur de qualité du résonateur et la position des stoppeurs. Ces deux facteurs sont liés à la force d'amortissement non linéaire de l'air, qui augmente considérablement avec la réduction de la distance inter électrodes. Pour s'adapter à ce phénomène, nous devont diminuer le facteur de qualité inférieur et augmenter la taille des stoppeurs pour une accélération plus importante.

Energie convertie par cycle en fonction de la résistance de charge : La puissance de sortie du dispositif (sans bille) est testée, afin de déterminer la résistance de charge optimale. La mesure montre que la charge optimale est comprise entre 6 et 10 MΩ.

Puissance et energie par cycle en fonction de la fréquence : La puissance de sortie du prototype avec une charge optimale de 6.65 MΩ est ensuite mesurée un balayage en fréquences et des accélérations variées. L'énergie par cycle est calculée en divisant la puissance de sortie par la fréquence.

Performances avec le bruit gaussien à large bande : Pour tester la performance du prototype avec des excitations aléatoires, nous avons mesuré sa densité de puissance spectrale (PSD) avec un bruit gaussien.

Performance du dispositif complet (avec la bille)

Puissance en fonction de la fréquence : La puissance du prototype avec la balle est mesurée avec une charge optimale de 6.65 MΩ et avec un balayage en fréquences des vibrations. Par rapport à la puissance de sortie sans la bille, la puissance avec la bille est augmentée sur toute la gamme de fréquences, tandis qu'une augmentation de puissance plus importante est observée à basse fréquence. Dans le même temps, l'hystérésis est éliminé par l'insertion de la bille.

Signal de sortie transitoire à ultra-basse fréquence : Pour atteindre des fréquences en dessous de 10 Hz, en deçà de la bande passante du vibrateur, nous secouons le prototype à la main et enregistrons sa sortie transitoire avec une charge optimale (6,65 MΩ). Le taux de conversion d'énergie maximum du dispositif est de 30,6 nJ par cycle (143,9 nW avec une accélération de 4,7 Hz 2 g_{rms}).

Expérience de transmission de données (sans / avec la bille)

Une expérience de transmission de données d'un nœud de capteur de communication sans fil alimenté par REC est démontrée. Le REC est actionné sans ou avec la bille miniature. Le signal de sortie est redressé par un redresseur à double alternance qui est chargé par un condensateur réservoir de 47 μF. Un commutateur automatique s'allume lorsque la tension aux bornes du condensateur est supérieure à 3,5 V et s'éteint lorsque la tension est inférieure à 2,5 V. Le temps de charge pour alimenter un module de communication est de 2 min avec le dispositif sans la bille juste après la charge corona (opéré à 2 g_{rms} 300 Hz); tandis qu'avec le dispositif polarisé par l'électret stabilisé (avec la bille), le temps de charge est de 4,3 min (opéré à 3 g_{rms} 100 Hz).

Chapitre 3. Modèle d'e-REC couplé aux impacts prenant en compte l'amortissement non linéaire de l'air

Ce chapitre présente un modèle plus sophistiqué qu'au chapitre 2.

Modélisation du REC considérant l'amortissement non linéaire de l'air et la bille

Un e-REC de fermeture de gap basée sur les principes décrits au chapitre 2 est modélisée et fabriquée à partir d'une plaquette SOI comme décrit au chapitre 4. Le dispositif comprend un résonateur à ressort élastique, des stoppeurs, une masse sphérique libre impactant avec la masse du résonateur et des peignes interdigités à fermeture de gap dans le plan. Le modèle considère l'équation du mouvement à la fois de l'électrode mobile et de la bille, l'impact entre les deux masses, et l'amortissement de l'air entre les peignes.

Amortissement de l'air : Le modèle d'amortissement de l'air est développé à partir de l'équation non linéaire de Reynolds pour les films d'air compressibles. L'équation est simplifiée et résolue en supposant une petite variation de pression, une constante de temps pour atteindre l'équilibre beaucoup plus petite que celle du mouvement des électrodes, et une différence de pression négligeable entre les doigts. La solution est donnée sous la forme d'une série de Taylor, en fonction du déplacement de l'électrode mobile.

Variation de capacité : La variation de capacité du prototype en fonction du déplacement de l'électrode mobile est calculée en tenant compte des pentes de sur-gravure sur les bords des peignes.Le rapport de capacité ($\frac{C_{\max}}{C_{\min}}$) est d'environ 15 avec un déplacement maximum de 69 μm.

Détection d'impact avec la bille : Les positions initiales de la bille et de l'électrode mobile sont définies au centre de leur plage de déplacement (définie comme l'origine). Les impacts entre la bille et l'électrode mobile sont détectés en fonction des positions prédites des deux masses. Les impacts ont lieu si et seulement si la différence entre les déplacements des deux masses est plus grande que l'écart initial entre la cavité et la bille.

Changement de statut avec des impacts : Nous supposons qu'une quantité fixe d'énergie cinétique est perdue dans le prototype, et que la vitesse de l'électrode change avec un coefficient fixe au moment d'impact entre l'électrode mobile et le stoppeur élastique. En ce qui concerne les impacts entre l'électrode mobile et la bille, nous appliquons la loi de conservation de l'énergie et considérons qu'une certaine quantité d'énergie cinétique est perdue.

Validation expérimentale du modèle

Pour valider le modèle, nous avons comparé les prédictions du modèle et les mesures expérimentales du dispositif. Le dispositif est excité avec des oscillations de fréquences de balayage et des accélérations variées.

Montage expérimental : Le REC est monté sur un vibrateur, dont l'accélération est contrôlée par un système en boucle fermée, tandis qu'un signal sinusoïdal d'amplitude et de fréquence constantes est appliqué comme signal de contrôle. Le prototype est polarisé avec une tension fixe et chargé avec une résistance de charge optimale de 6.6 MΩ.

Paramètres de modélisation : La plupart des paramètres sont des constantes physiques connues. Certains paramètres sont déterminés par la conception du masque et sont facile à contrôler et à déterminer. Les paramètres restants sont liés à la fabrication ou à la configuration expérimentale, et doivent être déterminés. Des paramètres tels que la rigidité des structures élastiques sont co-influencés par le masque et la fabrication. Nous avons estimé leurs valeurs, y compris l'angle d'inclinaison des parois latérales, la rigidité des ressorts linéaires et des stoppeurs élastiques, et la position des stoppeurs, en fonction des résultats expérimentaux pour réduire la complexité de la méthodologie.

Prédictions du modèle : Les prédictions du modèle et les mesures expérimentales, que le dispositif fonctionne avec ou sans bille, avec des accélérations de fréquence de balayage et des amplitudes variées, sont comparées. Les deux résultats sont cohérents entre eux, montrant une bonne précision du modèle. A basse fréquence inférieure à 50 Hz, la puissance de sortie du prototype avec la bille est surestimée, la cause possible étant la sous-estimation de la perte d'énergie lors des impacts, ou la sous-estimation de l'écart initial des stoppeurs.

Etude paramétrique

Longueur de la cavité : En augmentant la longueur de la cavité, la fréquence de résonance de l'oscillateur est augmentée. En même temps, la bande inférieure correspondant à la fréquence de conversion vers le haut est décalée vers le bas. En conséquence, la zone chaotique est agrandie par l'augmentation de la taille de la cavité.

Position des stoppeurs: Avec un grand écart initial des stoppeurs, le dispositif nécessitera une tension de polarisation réduite, ce qui n'est pas préférable. Cependant, un plus grand écart des stoppeurs est avantageux, si le pull-in est empêché.

Rigidité des structures élastiques : Une raideur réduite des ressorts linéaires entraîne une tension d'activation inférieure (non souhaitable). Une rigidité plus faible conduit à une fréquence de résonance inférieure et à une plus grande bande passante de la réponse basse fréquence, tant qu'il n'y a pas de pull-in. Les stoppeurs élastiques sont destinés d'éviter le pull-in, donc ils doivent avoir de grandes rigidités.

Espace initial au repos : Un plus petit espace entre les électrodes au repos permet plus de doigts pour une surface donnée, et est donc avantageux pour atteindre une plus grands variation de capacité. De plus, l'effet d'adoucissement du ressort électrostatique sera plus fort, élargissant la bande passante du pic de résonance. Par contre, plus de doigts conduisent à une force d'amortissement de l'air plus forte et une grande force électrostatique, limitant le déplacement de l'électrode mobile et augmentant le risque de traction.

Tension de polarisation : Fondamentalement, une tension de polarisation plus élevée entre les électrodes entraîne une augmentation de la puissance sur l'ensemble du domaine fréquentiel, et conduit à un effet de ramollissement du ressort électrostatique plus important. Lorsque la tension est supérieure à un certain seuil, l'attraction électrostatique entre les électrodes devient trop grande et améne au pull-in.

Discussions

Nous observons plusieurs problèmes qui doivent être pris en compte dans les futurs modèles.

Pull-in : Le pull-in est l'interruption de l'oscillation de l'électrode mobile en raison de son collage électrostatique sur l'électrode fixe. La tension de polarisation et tous les facteurs liés à la variation de capacité doivent être ajustés avec soin pour l'éviter.

Pertes d'énergie des impacts : Le modèle suppose un mouvement glissant de la bille, ce qui rend l'estimation de la puissance pendant les impacts moins précise, surtout aux basses fréquences (inférieures à 50 Hz). Pour atteindre une plus grande précision, nous avons besoin d'un modèle plus sophistiqué du mouvement de la bille qui prenne en compte sa révolution.

Paramètres liés : L'effet des différents paramètres de conception se combinent dans la réponse en fréquence du prototype nous observons aussi que certains paramètres influencent la réponse fréquentielle du dispositif sous plusieurs aspects. Ainsi, nous devrons co-ajuster simultanément l'ensemble des paramètre lors de la conception.

Chapitre 4. l'E-REC avec structure capacitive hiérarchique réduisant l'effet d'amortissement de l'air

Compte tenu de l'effet négatif de l'amortissement de l'air des peignes à fermeture de gap dans le prototype du chapitre 2, ce chapitre présente un e-REC avec des peignes hiérarchiques qui fournissent une force d'amortissement de l'air plus faible. Le dispositif partage une configuration similaire au REC précédemment proposé. Grâce à la réduction de la force d'amortissement de l'air, le prototype a une puissance de sortie plus élevée que la structure classique, en particulier à basse fréquence dans la plage de 10∼40 Hz. Un nouveau procédé de fabrication basé sur des plaquettes SOI est utilisé.

Description du dispositif et fabrication

Les nouveaux prototypes comprennent chacun un résonateur linéaire, des stoppeurs et une masse sphérique mobile libre impactant la masse du résonateur. Il se compose d'une électrode mobile et de deux contre-électrodes fixes entre lesquelles se trouve un module capacitif. Pour le module capacitif, nous proposons trois modèles différents avec des structures hiérarchiques, c'est-à-dire des doigts interdigités avec des dents hexaédriques le long des doigts. Parmi les prototypes proposés, le modèle T a des rangées de dents des deux côtés des doigts; tandis que les modèles R et M ont des rangées de dents seulement sur un seul côté des doigts, ayant respectivement une symétrie de rotation et de mirroir. Une tension de polarisation continue est appliquée sur l'électrode mobile.

Le dispositif est fabriqué à partir d'un wafer SOI gravé des deux côtés. La structure est ensuite collée à un substrat de verre pré-gravé. Chaque dispositif est recouvert avec une couche de Parylène C, et préchargé avec un système corona.

Optimisation de la conception du module capacitif

Le paramètre clé de la conception des peignes hiérarchiques est l'angle (θ) entre les facettes des dents et l'axe du déplacement de l'électrode mobile. Cet angle influence à la fois la largeur de chaque dent et l'écart minimum entre les électrodes pendant l'oscillation. Les capacités maximum et minimum du dispositif ($C_{\max}$ et $C_{\min}$) en relation avec l'angle θ sont simulées par éléments finis. Avec θ croissant de $0°$ à $90°$, la variation de $C_{\min}$ est négligeable, alors que $C_{\max}$ augmente d'abord rapidement, puis diminue progressivement après avoir atteint un pic à $25,5°$. Nous choisissons $\theta = 30°$ pour les dispositifs.

Résultats expérimentaux

Variation de capacité : Les variations de capacités des trois prototypes proposés (modèles T, R et M) et du prototype avec peignes à fermeture de gap (modèle G) sont mesurées dans l'air et dans le vide puis comparées. La performance optimale (le plus grand $\frac{C_{\max}}{C_{\min}}$) dans le vide est atteinte par le modèle G comme attendu. Dans l'air, le modèle R est la configuration optimale, atteignant un ratio de $\frac{C_{\text{max}}}{C_{\text{min}}} = 10,8$. Il surpasse tous les autres dispositifs car il réduit efficacement l'amortissement de l'air.

Conversion d'énergie en fonction de la fréquence : Les puissances de sortie des prototypes (polarisées à 20 V) avec une charge optimale sont d'abord mesurées avec des balayages en fréquence dans l'air et le vide, sans insérer la bille miniature. Les résultats sont cohérents avec ceux de la mesure de capacité. Sans la bille, le modèle G produit la plus grande puissance de sortie dans le vide; tandis que le modèle R surpasse les trois autres dispositifs dans l'air. Ensuite, nous augmentons la tension de polarisation du modèle R (la configuration optimale dans l'air) à la valeur maximale possible en évitant le pull-in (45 V), atteignant la puissance maximale de 13,2 μW à 50 Hz, 3 g_{peak}, et l'efficacité la plus élevée de la conversion d'énergie de 54% à 10 Hz, 2 g_{peak}. Le dispositif est également testé avec des oscillations manuelles pour atteindre des fréquences ultra-basses (<10 Hz).

Transduction AC/DC : La puissance convertie du modèle R après redressement AC/DC d'un pont de diodes demi-onde est calculée à partir de la courbe de charge d'un condensateur réservoir. Le prototype est excité à 10 Hz, 2 g_{peak} et polarisé avec des tensions de polarisation variant de 10 V à 60 V. L'énergie maximale convertie dans un cycle mécanique est 64,4 nJ, ce qui est atteint avec la tension de polarisation de 50 V et la tension aux bornes du condensateur de 12 V.

Discussions

Mesure dynamique de la capacité : Pour la mesure dynamique de capacité, la précision de la mesure est liée à la résistance de charge, qui correspond à une capacité “cible”. Lorsque la différence entre la capacité cible et la capacité mesurée augmente, l'erreur de mesure augmente. La précision est faible également lorsque la vitesse de variation de capacité est rapide (c'est-à-dire lorsque la variation de capacité dans un cycle du signal de porteuse n'est pas négligeable). Ainsi, la mesure est imprécise lorsque la variation de capacité est importante et rapide (par exemple pour le modèle G sous vide).

Conversion de fréquence : Pour optimiser le mécanisme de conversion en fréquence, il y a deux paramètres possibles à régler: la longueur de la cavité et le rapport entre les masses de la bille et du résonateur.

Effet d'amortissement de l'air : La structure hiérarchique réduit considérablement l'effet d'amortissement de l'air par rapport à la structure à fermeture de gap, grâce aux formes triangulaires qui reduisent la force de pression sur l'air.

Circuit de conditionnement : Pour le redressement AC/DC du signal, nous choisissons un pont de diodes demi-onde qui offre la meilleure efficacité avec le ratio de capacité et la tension de polarisation [4]. La condition optimale pour le modèle R est avec une tension de polarisation de 50 V et 12 V aux bornes du condensateur réservoir.

Chapitre 5. E-RECs basses fréquences alternatifs

Ce chapitre présente deux approches pour améliorer les e-RECs basses fréquences dans des aspects alternatifs. La première approche présente un e-REC entièrement flexible pour une application à l'électronique portable. La deuxième approche est un e-REC à base de silicium qui est capable de répondre à des vibrations dans toutes les directions du plan du substrat.

l'E-REC flexible basé sur des matériaux nanofibreux électrofilées

Description du dispositif : Le prototype possède une structure simple à couches multiples obtenues par électrospinning, où plusieurs couches d'électret sont insérées entre deux électrodes. L'empilement d'électrets en forme de mousse est la source du champ électrostatique, générant une charge induite sur les deux électrodes. Sans compression, les films d'électret sont répartis de manière lâche et asymétrique, de sorte que la quantité de charges induites sur les deux électrodes est inégale. Lorsque le dispositif est comprimé, les films d'électret sont proches les uns des autres, et le champ électrostatique est symétrique, générant une quantité égale de charge sur les deux électrodes. Ainsi, le dispositif est capable de générer périodiquement un signal électrique lorsqu'il est compressé et libéré de façon répétitive. Il y a une configuration optimale du prototype (avec un nombre optimal de films électret, N_{opt})offrant la puissance de sortie maximale.

Préparation du matériel : Pour préparer les films d'électret, nous fabriquons d'abord un échafaudage nanofibreux en utilisant la technique d'électrofilage. Des poudres de PVDF et de PTFE sont dissoutes dans un solvant mixte d'acétone et de diméthylformamide. La solution est électrofilée en nanofibres à haute tension, qui sont recouverts de façon conforme avec du Parylène C par un procédé de dépôt chimique en phase vapeur. Les films sont ensuite chargés par décharge corona.

Performance du dispositif : La variation de capacité du prototype en fonctionnement est testée avec la technique de mesure dynamique, où le nombre de couches d'électret insérées entre les électrodes varie de 1 à 4. Les prototypes sont excités à 10 Hz par un pot vibrant. Avec la configuration optimale de 3 couches d'électret chargées par une résistance de 16 MΩ, l'énergie moyenne convertie est de 53 nJ/cycle. La puissance redressée du prototype avec la configuration optimale atteint 9,9 nJ/cycle.

l'E-REC 2D basé sur la structure de rotation

Un e-REC basses fréquences bidimensionnel basé sur une structure rotationnelle est proposé. L'électrode mobile a une géométrie circulaire, avec des peignes à fermeture d'espace tout le long de sa circonférence. Il est relié à des extrémités fixes à travers des ressorts linéaires serpentins à quatre nœuds. Au centre de la masse mobile, il y a une ouverture pour supporter une bille libre. La simulation modale montre que les trois premiers modes de résonance du prototype correspondent à des vibrations parallèles au plan de la plaquette. Le prototype est donc capable de répondre aux vibrations dans n'importe quelle direction parallèle au plan du substrat.

Chapitre 6. Etiquette RFID semi-passif assisté par un e-REC

Dans ce chapitre, une étiquette RFID semi-passiveest proposée. Le module de communication du tag est boosté par des e-RECs silicium basses fréquences proposées dans les chapitres précédents.

Conception de l'antenne: paramètres clés et simulation

L'antenne est basée sur un dipôle en spirale avec un circuit d'adaptation en L modifiée. Le dipôle occupe un espace plus petit que les lignes meanderings; tandis que le circuit d'adaptation en L aide l'antenne à atteindre une plus grande bande passante.

Analyse théorique : L'antenne peut être modélisée avec d'éléments localisés comme des résistances, des capacités et des inductances. L'influence de chaque élément discret sur l'adaptation d'impédance est déduite à l'aide d'un modèle à constante localisée.

Paramètres clés pour la conception : Plusieurs paramètres de conception clés extraits de l'analyse théorique ci-dessus sont repris pour l'étude paramétrique par la méthode des éléments finis. Les paramètres comprennent la longueur totale de chaque spirale, la longueur de l'inductance connectée en série avec le dipôle et l'épaisseur du matériau retiré du substrat pendant la fabrication. Le paramètre cardinal affectant la fréquence de résonance de l'antenne est l'épaisseur du matériau retiré plutôt que la longueur des spirales.

Expériences et discussions

Caractérisation de câble de connection : D'abord nous caractérisons le câble utilisé pour la caractérisation de l'antenne, afin d'obtenir sa constante de phase et sa constante d'atténuation. Ensuite, la permittivité relative est calculée en fonction de la constante de phase.

Mesure d'impédance avec un balun : Pour mesurer l'impédance de l'antenne, nous avons fait un premier essai en implémentant une interface balun entre le câble coaxial et l'antenne. Le balun est un fil de 1/4 de longueur d'onde connecté au câble coaxial à la position 1/4 de la longueur d'onde du plan de l'antenne. Ainsi, il peut être considéré comme une charge en circuit ouvert de l'antenne. Le problème de la mesure du balun est sa bande passante étroite, ce qui amène une erreur importante lorsque la fréquence est éloignée de la fréquence centrale.

Mesure d'impédance avec une sonde différentielle : Pour pallier l'inconvénient du balun, on est passé à la technique de la sonde différentielle. Tout d'abord, les deux câbles de la sonde différentielle sont caractérisés respectivement par la mesure de leur coefficient de réflexion avec une charge équivalente et avec un court-circuit. Ensuite, la matrice S de chaque câble est extraite en fonction des coefficients de réflexion (S_1 et S_2). La matrice S de la sonde différentielle chargée avec l'antenne dipolaire en spirale (S_{sys}) est extraite. L'impédance de l'antenne est déduite des matrices S S_1, S_2 et S_{sys}.

Mesure de la plage de lecture : La plage de lecture de l'étiquette RFID est mesurée avec un lecteur de Tagformance avec des polarisations parallèles et perpendiculaires. La distance de lecture maximale atteinte à la fréquence cible (868 MHz) est de 15 m.

Consommation d'énergie avec des sources capacitives : La courbe transitoire de variation de tension d'un condensateur préchargé alimentant le module de communication est enregistrée de manière à avoir une idée de la performance de l'étiquette RFID. La consommation d'énergie de l'étiquette sous une tension de polarisation différente est calculée en conséquence. Le nombre total de communications pouvant être supportées par des condensateurs préchargés de valeurs différentes est compté par un lecteur Impinj. Avec un condensateur de 2,2 μF préchargé à 3,3 V, l'étiquette peut être lue par le lecteur distant 6 fois de suite.

Tag RFID alimentée par un REC MEMS : Une étiquette RFID semi-passive comprenant un REC est testée dans son ensemble. Les RECs testés pour le système comprennent le prototype proposé au chapitre 2 et le modèle R proposé au chapitre 4. L'énergie issue du REC est stockée dans un condensateur réservoir à travers un redresseur AC/DC, et libérée au module de communication par l'intermédiaire d'un commutateur mécanique. Avec 11 Hz et 3 g_{peak}, 3 lectures d'étiquettes toutes les 16 s sont obtenues.

Conclusion

Dans cette thèse, nous avons proposé plusieurs techniques pour améliorer l'adaptabilité des récupérateurs d'énergie cinétique électrostatiques à basses fréquences pour qu'elles puissent être utilisées dans des nœuds de capteurs sans fil et dans l'électronique portable. Nous avons aussi proposé une étiquette RFID semi-passive longue portée qui met en œuvre un récupérateurs d'énergie cinétique à basse fréquence comme source d'alimentation.

Contents

Chapter 1

Introduction to low-frequency miniature kinetic energy harvesters (KEHs) - state of the art

1.1 Background

Nowadays wireless networks have widespread applications, thanks to their higher flexibility than wired systems, easier implementation, better accessibility, more convenient installation, and lower cost. Thanks to the wireless feature, the devices can be installed or retrofitted to previously inaccessible positions, resulting in a much wider variability of network construction. There is a rapid growth of the number of terminals in wireless networks, which is further accelerated by the introduction of "Internet of Things"(or IoT) brought by Ashton in 1998 [5]. In such networks, the information of objects are obtained by sensors, communicated between terminals, collected and utilized by processing terminals, so that smart networks is achievable. Numerous wireless sensors are embedded in objects and distributed throughout the network so that the massive data regarding the conditions of each object can be acquired. The powering issue for each and every sensor node is one of the cardinal problems awaiting to be solved. Initially, the most common solution for power supply of wireless communication sensor nodes is to use batteries, as reported in [6] [7] and [8]. The inconvenience of batteries soon exposes when the networks grows larger: besides their large volume and high cost, the maintenance (replacement or recharging) is a lot of work when the networks are massive. According to [9], the batteries are not practical for networks containing thousands of, or even more nodes. Thus, alternative power sources that could resolve all these problems are desirable, and a variety of efforts are made [10].

Trials to solve the problems include increasing the energy and power density and elongating the sustaining period of power supply elements (to minimize maintenance requirements) [11], reducing the size and cost of the power supply modules, and taking advantage of localized power sources (to avoid recharging). To achieve higher energy and power density than traditional batteries, different energy storage elements are applied to wireless systems, including lithium ion batteries [12], [13], fuel cells [14], [15] and supercapacitors [16], [17], [18], but the demand of recharging is not eliminated. Ambient energy harvesting (also known as energy scavenging) attracts a lot of attention in recent years, because it is the major solution in utilizing local power sources. The energy harvesters can continuously deliver energy whenever the power source is present, so the recharging like for batteries is unnecessary. The recent development of wireless communication reducing the power requirement is another major reason why energy harvesting attracts so much attention. The energy consumption of a typical RFID tag reading communication node is in the order of a few μJ [19]. Ambient energy exists abundantly in many forms, including solar energy, radio-frequency (RF) electromagnetic radiations, thermal energy and mechanical energy (ambient fluid flows, motions and deformations) [20], [21]. Accordingly, energy harvesters are divided into photovoltaic harvesters [22], RF harvesters [23], thermoelectric harvesters [24], turbines [25], and vibration energy harvesters [26], transforming all these forms of energy into electric energy. They are usually optimized according to the features of local available power source, in a variety of specific scenarios of application, such as buildings [27], bridges [28], [29], or human bodies [29], [30].

Kinetic energy, abundantly existing in the environment, is one form of ubiquitous ambient energy, and is thus a localized source of energy for wireless communication nodes for sensor networks or for wearable electronics. The ambient vibration and human motion are usually random signals featured by low frequency, large bandwidth. Typical transduction principles used in kinetic energy harvesters (KEHs) include piezoelectric, electromagnetic, electrostatic, magnetoelectric and other forms of transduction. The first miniature KEH was a piezoelectric prototype invented by Cady in 1968 [31]. Ten years later, the first electrostatic prototype was realized by Jefimenko and Walker [32]. Electromagnetic power generators are dated back to 1866, but miniature electromagnetic KEHs have not been reported until 1996 [33]. Alternative transduction principles are reported during recent years with the emergence of new types of materials [34]. Early KEHs usually target at stable vibrations with sinusoidal or narrow-banded accelerations, they generally work at predefined and rarely changed frequencies. Some narrow-banded KEHs are commercially available [35] [36] [37] [38], but there is still a gap between the power supply capacity of current KEHs and the power requirement of some wireless communication applications (like Bluetooth).

Later it was proposed by Micheson et al. that the power available in inertial KEHs when the work with sinusoidal vibrations has a theoretical ceiling, regardless of the transduction principle [1]. The maximum available power is stated to be dependent on the amplitude and frequency of the acceleration, the mass and the maximum displacement of the proof mass. All these factors lead to a conclusion that the output power of a KEH is limited by its minor size and by the low frequency of motion. Thus, the improvement of energy conversion efficiency is the only way to push the KEH's output power closer to the ceiling. The KEHs reported during recent years mostly emphasize on the improved effectiveness of energy conversion and the miniaturization of the prototypes [39] [40] [41]. Also, a variety of kinetic energy harvesters are reported targeting at wideband random vibrations especially in low frequency range [42] [43] [44], so that the devices can adapt better to the ambient vibrations. The efficiency can be improved by the optimization of the energy transduction coupling, the method of which is dependent to the transduction principles

[45]. In addition, pervasive technique such as mechanical frequency up conversion mechanism [46] and the application of rotational structures [47] are introduced to the systems to make them more adapted to low frequency applications, while maintaining acceptable output powers and minuscule sizes. The output of the KEHs are usually AC signals, which is not applicable for direct power supply. Energy management interface circuits converting the AC signal to DC output are always indispensable[48] [49] and introduces additional power consumption to the system. Recent development of the interface circuits also emphasize on lowering their power consumption and reducing the mismatch of interface condition, which are both very important for the application of KEH power supply modules.

1.2 General principles of kinetic energy harvesters

A kinetic energy harvester is a typical electromechanical system, comprising one part fixed to the carrier and one movable part, while connecting the two parts are an elastic structure (or a spring) and a damper (including the effect of a transducing component and other damping factors), as shown in Figure 1.1. External excitation is typically applied to the movable part either through a direct force or through inertia mechanism, to generate a relative motion, and the kinetic energy is converted to electric energy through the transduction component. Typical external excitations can either be direct forces or vibrating accelerations, while the relative motion can be related to a deformation or an inertia-based displacement. The transduction component can be based on various physical mechanisms such as piezoelectric effect, electromagnetic induction, and electrostatic induction. Like many other electromechanical systems, kinetic energy harvesters can by modeled from either mechanical or electrical points of view. The basis of the KEH modelling is the equation of motions of the moving part of the device, which links the transduction mechanism to the part motion through force.

1.2.1 Lumped-parameter mechanical model

A typical KEH can be easily modeled by a lumped-parameter mechanical model, where the movable part is represented by a mass m, and the elastic structure and the damper are considered massless. The equation of motion regarding the mass is described as follow (taking the carrier as the reference system):

$$m\ddot{x} = F_{\text{excite}} + F_{\text{elastic}} + F_{\text{damper}} \tag{1.1}$$

where x is the net displacement of the mass m relative to the carrier, which is a time dependent variable, while $\dot{x}$ and $\ddot{x}$ are its first and second derivatives with time (mass velocity and acceleration) respectively. F_{excite} (varying with time) the external force or the equivalent force representing the influence of inertia, F_{elastic} is the force from the elastic structure (dependent on the mass displacement), and F_{damper} the force from the damper (dependent on both the mass velocity and displacement). In different types of KEHs, the expressions of the three forces are in different forms.

The excitation force can be a direct force, which can be written directly according to the excitation signal, as shown in Figure 1.1(a). For inertial KEHs, the excitation is a Coriolis inertial force (with the carrier taken as the reference system):

$$F_{\text{excite}} = -ma_{\text{ex}} \tag{1.2}$$

where a_{ex} is the exciting acceleration provided by the carrier of the KEH, a function of time t.

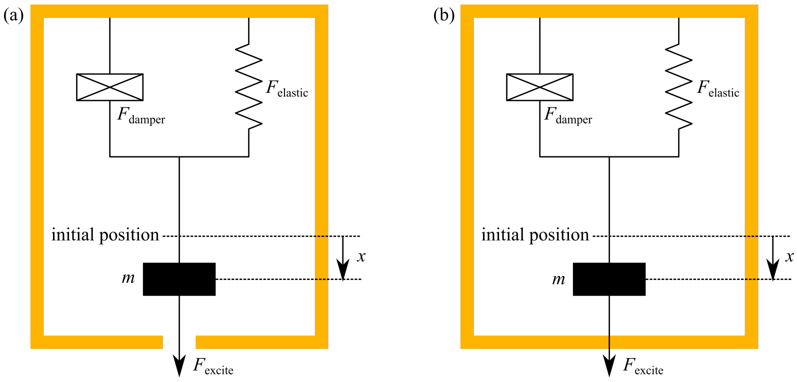

Figure 1.1: Model of a KEH (a) excited by direct force (b) excited through inertia.

1.2.2 Simplest model: linear resonant generators

The simplest model for the KEH is linear resonant generators, which can be applied when the mass displacement is small. The forces in the kinematic equation can be simplified as the following linear functions. The elastic structure is modeled as a linear spring, where the force is proportional to the displacement:

$$F_{\text{elastic}} = -kx \tag{1.3}$$

in which k is the stiffness coefficient of the linear spring.

The damping model is simplified as a linear damper, the force provided which is related only to the mass velocity:

$$F_{\text{damper}} = -c\dot{x} = -\left(c_{\text{e}} + c_{\text{p}}\right)\dot{x} \tag{1.4}$$

where c is the total damping coefficient, c_{e} represents the damping due to the electrical phase coupled to mechanical phase through transduction, while c_{p} the linear parasitic damping effects (not related to the electrical phase). All the damping coefficients are not influenced by x.

The kinematic equation of the inertial KEH with the a sinusoidal excitation $a_{\text{ex}}(t) = A\text{sin}\omega t$ is then transformed into the following form:

$$m\ddot{x} + c\dot{x} + kx = -mA\text{sin}\omega t \tag{1.5}$$

One standard steady-state solution of the equation is:

$$x = \frac{m\omega^2 A}{\sqrt{\left(k - m\omega^2\right)^2 + \left(c\omega\right)^2}} \sin\left(\omega t + \arctan\frac{c\omega}{k - m\omega^2}\right) \tag{1.6}$$

The average mechanical energy of the resonant structure during each structure is:

$$E = \frac{1}{4}\frac{m^2\omega^4 A^2\left(k + m\omega^2\right)}{\left(k - m\omega^2\right)^2 + (c\omega)^2} \tag{1.7}$$

The average electrical power transduced from the mass oscillation is:

$$\bar{P}_{\mathrm{e}} = \frac{1}{T}\int_0^T c_{\mathrm{e}} x^2 \mathrm{d}t = \frac{c_{\mathrm{e}}}{c}\frac{m\zeta A^2\omega_{\mathrm{c}}^3\omega^3}{\left(1 - \omega_{\mathrm{c}}^2\right)^2 + \left(2\zeta\omega_{\mathrm{c}}\right)^2} \tag{1.8}$$

where excitation period $T = \frac{2\pi}{\omega}$; $\omega_{\mathrm{c}} = \frac{\omega}{\omega_0}$ is the normalized excitation frequency. ω_0 is the resonant frequency leading to the maximum amplitude of mass displacement:

$$\omega_0 = \sqrt{\frac{k}{m}} \tag{1.9}$$

ζ is the total damping ratio:

$$\zeta = \frac{c}{2m\omega_0} \tag{1.10}$$

When the device works at the resonant frequency ($\omega_{\mathrm{c}} = 1$), the average output power is given by

$$\bar{P}_{\mathrm{e}} = \frac{m\omega_0^3\zeta_{\mathrm{e}}A^2}{4\left(\zeta_{\mathrm{p}} + \zeta_{\mathrm{e}}\right)^2} \tag{1.11}$$

where ζ_{e} and ζ_{p} are the damping ratios of the electrical damping and parasitic damping respectively:

$$\begin{cases} \zeta_{\mathrm{e}} = \dfrac{c_{\mathrm{e}}}{2m\omega_0} \\ \zeta_{\mathrm{p}} = \dfrac{c_{\mathrm{p}}}{2m\omega_0} \end{cases} \tag{1.12}$$

Given that the parasitic damping ratio is fixed, the maximum electric power extracted from the device is achieved when $\zeta_{\mathrm{e}} = \zeta_{\mathrm{p}}$:

$$\left(\bar{P}_{\mathrm{e}}\right)_{\max} = \frac{m\omega_0^3 A^2}{16\zeta_{\mathrm{p}}} \tag{1.13}$$

The efficiency of energy conversion at the resonant frequency is consequently given by:

$$\eta_{\mathrm{e}} = \frac{4}{2 + \frac{\zeta_{\mathrm{e}}}{\zeta_{\mathrm{p}}} + \frac{\zeta_{\mathrm{p}}}{\zeta_{\mathrm{e}}}} \tag{1.14}$$

1.2.3 Transduction damping coefficients

For different types of KEHs with varied transduction principles each has a particular force component corresponding to the mecha-electronic transduction, so that the resistive load can be regarded as a damper for the mechanical structure. For an electromagnetic harvester, the electronic damper is estimated by the following equation:

$$c_e = \frac{\left(Nl\Delta B\right)^2}{R_{\mathrm{l}} + R_{\mathrm{c}} + j\omega L_{\mathrm{c}}} \tag{1.15}$$

where N is the number of turns of the generator coil, l the effective length of each turn of the coil, ΔB the variation of flux density of the coil during each cycle of motion, R_l the load resistor, R_c and L_c the resistance and inductance of the coil respectively.

For electrostatic KEHs, the electrostatic force is a nonlinear function:

$$F_{\mathrm{e}}(x) = \frac{1}{2}\left(\frac{q}{C}\right)^2 \frac{\mathrm{d}C}{\mathrm{d}x} \tag{1.16}$$

where C is the capacitance of the harvester (defined by the variable capacitors geometry), which is dependent on x, while q is the amount of inducted charge on the electrodes, which is related to the velocity x. While according to Kirchhoff's voltage law, the electronic damping effect of the resistive load is coupled to the force through the charge on electrodes q through its first derivative:

$$\dot{q} = \frac{1}{R_{\mathrm{l}}}\left(-\frac{q}{C} + V_{\mathrm{bias}}\right) \tag{1.17}$$

where V_{bias} represents the bias voltage accross C, and R_{l} the load resistance.

The capacitance C in equation 1.16 consists of the device capacitance and a parasitic capacitance C_{p} introduced by the packaging and the external electronics.

$$C = C_{\mathrm{p}} + C_{\mathrm{d}} \tag{1.18}$$

where C_{d} is the capacitance of the prototype. The capacitance are calculated with regard to the gap between electrodes (or to x), based on either analytic calculation or finite element method (FEM).

1.2.4 KEHs with nonlinear resonators

For a more sophisticated model considers nonlinearity either introduced by a larger mass displacement or nonlinear structures. The nonlinearity of elastic structures are introduced by bistable springs or other forms of nonlinear springs. For nonlinear KEHs with small displacements, the elastic force can usually be described in a general form as following:

$$F_{\mathrm{elastic}}(x) = -\sum_{i=1}^{N} k_i x^i \tag{1.19}$$

where the k_i are constant coefficients, among which k_1 represents the linear factor, while the others describe the nonlinear factors. A less complex model to describe the nonlinear elastic force is expressed in the following form:

$$F_{\mathrm{elastic}}(x) = -kx - k_3x^3 \tag{1.20}$$

The nonlinear damping force is the summary of the transduction damping and parasitic damping effects (such as air damping, material damping, etc.), which is dependent on both the mass displacement and its velocity. A simplified model describes the damping effect as a nonlinear damper:

$$F_{\mathrm{damper}}(x, \dot{x}) = -c(x)\,\dot{x} \tag{1.21}$$

where the damping coefficient c is a function of x.

Another type of nonlinear resonant KEH embodies stoppers (positioned at $\pm X_{\mathrm{s}}$ respectively) confining the displacement of the movable mass, the steady-state solution given by equation (9) is valid only when the acceleration is no larger than the following threshold (excited at resonant frequency $\omega_{\mathrm{c}} = 1$):

$$A_{\mathrm{t}} = 2\zeta X_{\mathrm{s}} \tag{1.22}$$

The maximum average energy extracted from resonant vibration is then:

$$\bar{P}_{\mathrm{e}}\big|_{A=A_{\mathrm{t}}} = \frac{1}{2} c_{\mathrm{e}} \omega_0^2 X_{\mathrm{s}}^2 \tag{1.23}$$

If the acceleration is above the threshold, the elastic force becomes nonlinear, a typical form is a piecewise function. A simplified model regards the stoppers as an additional linear elastic structure:

$$F_{\mathrm{elastic}}\left(x\right) = -kx - k_{\mathrm{s}}\left[x - X_{\mathrm{s}}\mathrm{sgn}\left(x\right)\right] H\left(|x| - X_{\mathrm{s}}\right) \tag{1.24}$$

where k_s is the stiffness coefficient of the stopper, $\mathrm{sgn}\left(\cdot\right)$ is the sign function, while $H\left(\cdot\right)$ is the Heaviside step function.

Usually the stoppers also bring additional parasitic damping c_s to the mass:

$$F_{\mathrm{damper}}\left(x, \dot{x}\right) = -c\dot{x} - c_{\mathrm{s}}\dot{x} H\left(|x| - X_{\mathrm{s}}\right) \tag{1.25}$$

The equation of motion for the mass is the following:

$$m\ddot{x} + \left[c + c_{\mathrm{s}} H\left(|x| - X_{\mathrm{s}}\right)\right]\dot{x} + kx + k_{\mathrm{s}}\left[x - X_{\mathrm{s}}\mathrm{sgn}\left(x\right)\right] H\left(|x| - X_{\mathrm{s}}\right) = -mA\mathrm{sin}\omega t \tag{1.26}$$

Instead of using analytical method, the solution of these nonlinear equations are more complicated. To solve this type of problems, in fact, numerical models are needed, and the solution should be based on finite element method.

1.3 State of the art: mechanical components for low frequency applications

Typically, a vibration energy harvester contains of a spring-mass resonator, where the vibration energy extracted by the spring-mass system is maximized at its resonance frequency. At MEMS scale, the device is limited in size, the KEHs are faced with two problems. On the one hand, the proof masses are low and stiffness coefficients of springs are high, which both lead to high resonance frequencies. It is hard to reduce the volume of the structure with low resonance frequency. The stiffness of the spring can be reduced to reduce the resonance frequency, either by using soft materials for springs [50], or by introducing meandered springs [51] [42] [52] or spiral springs [53] [54], but the bandwidth remains limited while the reliability of the structure deteriorates. On the other hand, the mechanical power of the device is limited by the movable mass and its maximum displacement, both of which are confined by the scale of a MEMS device, restricting the amount of energy extracted in each period of vibration. Thus, the bottleneck for improving the power performance of MEMS KEHs is that their size constrains both the movable mass and its displacement; another limitation is related to expanding the bandwidth without losing too much power at the optimal working frequency [55]. If a resonant system is developed that offers large mechanical amplification, there is a dilemma lying intrinsically in the system: when we try to improve its power at the resonance frequency, the frequency bandwidth becomes very narrow [56][57]. If we use non-resonant systems without any springs, the bandwidth can be very large [58] [59] [44], but these structures could hardly provide satisfying gain in the mechanical response and then, their output powers remain highly limited.

1.3.1 Mechanical frequency up conversion

A major way to improve the power of a KEH is to introduce mechanical frequency up conversion to the system, where several cycles of electro-mechanical transduction take place within a single cycle of low-frequency vibration. The mechanical frequency up conversion is majorly realized through introducing nonlinearity to the system, or through producing a spatial repetitive structures. The nonlinearity can come from nonlinear springs, bistable structures or impact-coupled or bounce-coupled structures; while the spatial repetitive structures are usually arrays of transduction elements.

Nonlinear devices usually perform well for noisy wideband random vibrations [60], but they are less efficient for narrow-band signals, especially single-frequency excitations, due to the hysteresis in the frequency response brought by nonlinearity.

Impact-coupled or bounce-coupled structures

The nonlinear structure is an efficient tool to introduce frequency up conversion into a low frequency system. Among them, the most common structure is impact-coupled or pluckling-coupled structures. The key idea is to trigger the oscillation of a high-frequency resonator with a low-frequency structure through impact [46] or pluckling [61] [62], as shown in Figure 1.2. These devices are usually featured by a piece-wise or other forms of highly nonlinear forces (impacts, pluckling or magnetic forces), so the modeling of this type of prototypes is usually dependent on finite element method. In these types of KEHs, the oscillation of the high-frequency resonator is triggered through a pluckling motion or an impact from the low-frequency structure.

The low frequency structure can be either a resonator as in [63] [64] [65] [66] [62] or a springless structure as in [46] [67] [43]. In the impact-coupled KEHs, the displacement of the moving mass is usually limited by stoppers, so that the device occupies only a limited space [64] [58] [39] [43]. The devices with springless structures are usually efficient within a large bandwidth, but the amplitude of the excitation acceleration must be above certain threshold to enable the motion of the springless mass.

Bistable structures

Another typical structures to realize frequency up conversion are bistable structures. In this type of structures, the switching events of the movable component follows the low frequency mechanical excitation, which trigger the oscillation of the high-frequency resonator. A typical kind of bistable structures is the one in the Frequency Increased Generators (FIGs) proposed by Galchev as shown

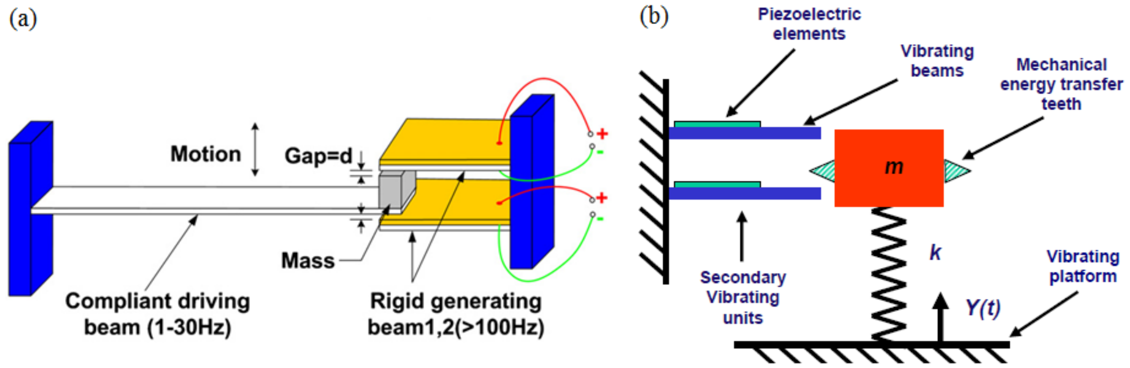

Figure 1.2: Schematic of typical low frequency KEHs based on mechanical frequency up conversion with impact/pluckling structures. (a) an impact-coupled structure [64] (b) a pluckling-coupled structure [61]

in Figure 1.3(a) [68] [69] [70], which consists of a movable mass attracted by two stoppers on the two ends of mass displacement. The stable position of the movable mass is located at the two maximum displacements, thanks to the attraction forces. When the movable mass switches from one stable position to the other, the high-frequency oscillation of the stoppers are triggered. Bistable structures based on attraction forces can also be found in [71] [72] [73] [2] [74].

Bistable structures can also be realized through repulsive forces preventing elastic structures from staying undeformed. The KEH reported in [75] as shown in Figure 1.3(b) is a representative prototype for this category. The repulsive force between the magnets raises the energy at the position of zero displacement, resulting in two wells of energy. Thus, the movable structure is able to switch between the two balance positions when the excitation is above certain threshold. Bistable components based on repulsive forces can be found also in the designs in [76] [77] [78] [79] [80] [81].

Like the repulsive force based bistable structures, a cantilever beam preloaded by a buckling force as shown in Figure 1.3(c) is another way to realize bistability. The energy of zero displacement is increased by the buckling force, resulting in two stable positions. The preloaded beam structures can be found in [82] [83] [84] [85] [86] [87] [88] [89].

1.3.2 Spatial repetitive structures

In low frequency KEHs, the size of the device is usually much larger than that of the high frequency vibrating structures. One technique to improve the efficiency of KEH in regard to the volume is to arrange arrays of high frequency components for energy transduction, so that the electrical energy can be collected in parallel through multiple channels. Shown in Figure 1.4 are several representative designs of spatial repetitive structures applied in low frequency KEHs. In piezoelectric devices, the piezoelectric transduction modules are usually designed as cantilever beams excited directly by vibration as reported in [90] or through pluckling as shown in [61]. As for electromagnetic KEHs as shown in Figure 1.4 [91], the magnets are arranged in an array where the N/S poles are alternately orriented, while the coils can also be arranged in arrays. Arrays of coils and magnets can also be found in [92] [67] [93] [94]. In electrostatic KEHs, the typical array structure of energy transduction are found in the in-plane overlap plate (IPOP) structure, where

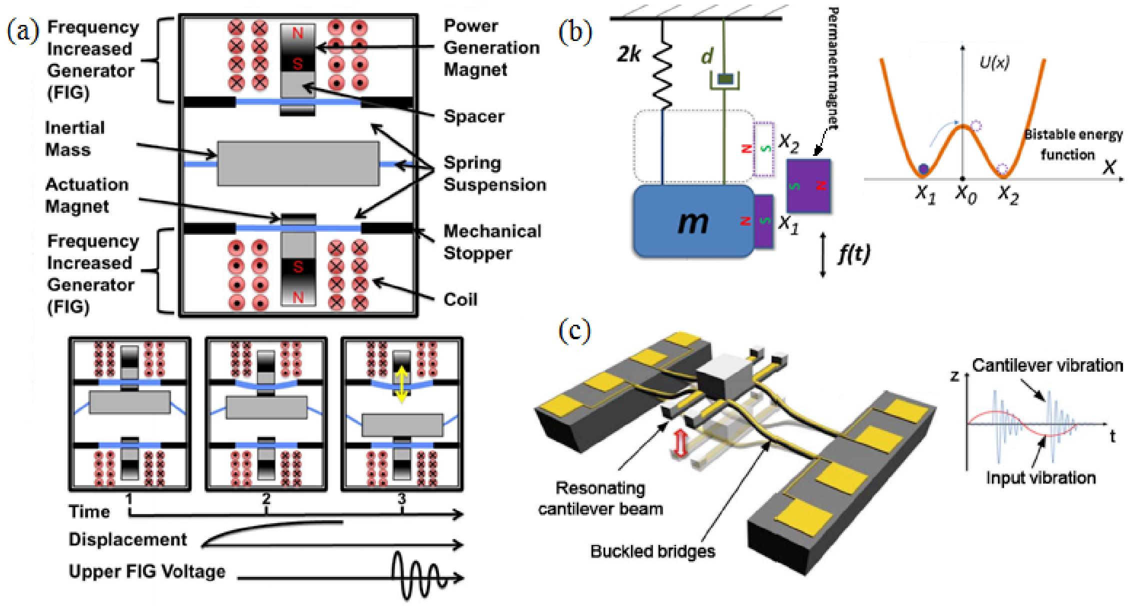

Figure 1.3: Schematic of low frequency KEHs based on mechanical frequency up conversion with bistable structures. (a) Frequency Increased Generator [69] (b) KEH based on repulsive force [75] (c) KEH based on buckled beam [82].

the capacitance of the prototype varies for several times during each stroke of mass displacement [3]. Similar structures can also be found in [95] [96] [97] [98].

1.3.3 Rotational structures

Rotational structures such as rolling structures, or coaxial structures are non resonant structures widely implemented in low frequency KEHs. The rotational structures such as balls [47] as illustrated in Figure 1.5(a) or rolling cylinders[99] as in Figure 1.5(b) usually serve as springless non-resonant structure, so that the friction for transitional movement is small. The displacement of the springless rolling structures are commonly limited by impacts on stoppers, triggering mechanical frequency up conversion mechanisms [47] [100] [101] [43] [41] [102]. The rolling structures are also usually combined with spatial repetitive structures, where a group of energy transduction modules are triggered in a row by the passing of the roller [44] [103] [99]. As for coaxial structures, the transduction module either deals with rotational motions directly as shown in Figure 1.5(c) [104], or transforms transitional vibrations to rotations, such as eccentric wheels as shown in Figure 1.5(d) [105] [106].

1.4 State of the art: transduction principles of KEHs

The energy transduction module in KEHs can be sorted into the following four major principles: piezoelectric transduction [61], electromagnetic transduction [107], and electrostatic transduction [108] [44], and magnetostrictive tranduction [109]. Hybrid KEHs are also reported in a large number, which implements more than one principle of energy transduction. For the low-frequency applications, the effectiveness of the transduction principle of a KEH is one of the key factors

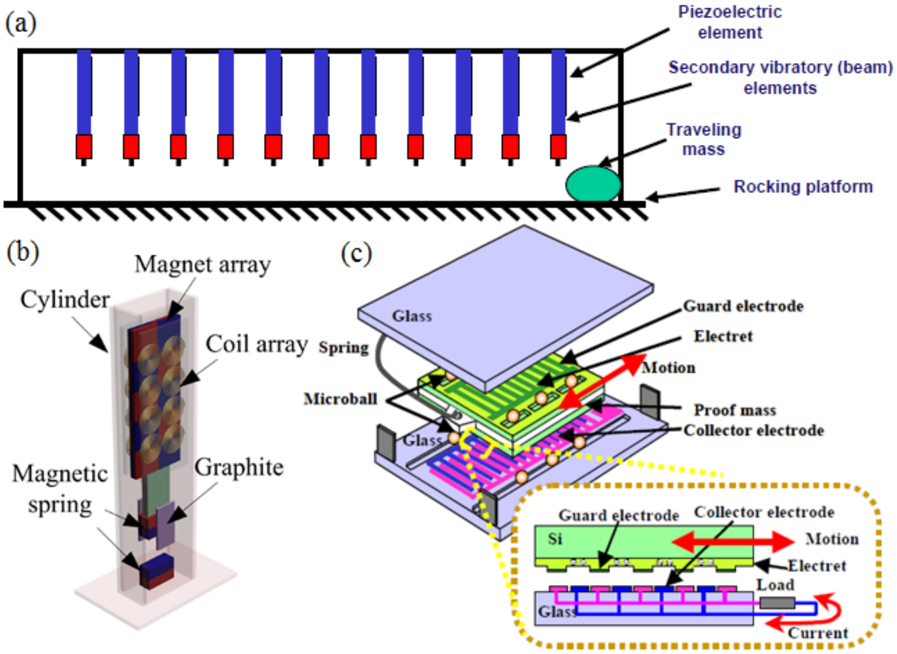

Figure 1.4: Schematic of low frequency KEHs with spatial repetitive structures. (a) Typical structure of piezoelectric module array [61] (b) Magnetic and coil arrays in electromagnetic KEH [91] (c) Electrode array in electrostatic KEHs with IPOP structure [95].

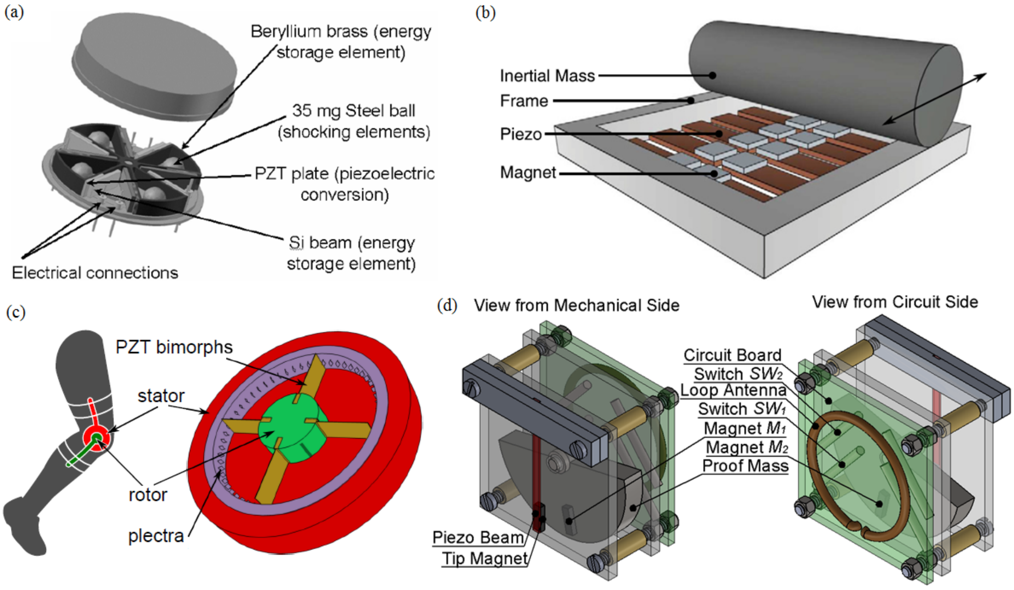

Figure 1.5: Schematic of low frequency KEHs with rotational structures. (a) Non-resonant structure with impact-coupled ball enclosed in cavity [47] (b) Mechanical frequency up conversion structure with rolling cylinders [91] (c) Coaxial structure harvesting rotational motions [104] (d) Eccentric wheel transforming transitional motions to rotations [106].

influencing its output power. In addition, the miniaturized KEHs, the prototypes are confined by the status quo of the micro-machining fabrication techniques, and is thus limited in the material selection and structural designs.

1.4.1 Piezoelectric KEHs (p-KEHs)

Piezoelectric KEHs transduce the mechanical energy into electrical energy through piezoelectric effect. The transduction modules usually consist of layered piezoelectric material covered by thin-film electrodes on top and bottom, and is commonly located on the surface of deformable mechanical structures. PZT is the most commonly used piezoelectric material, because it has a high piezoelectric coefficient, and is can be patterned into various 2-D geometries through lithography and etching processes. Other materials like KEHs driven by direct (bending) force are generally piezoelectric prototypes with layered structure featured by low profile and relatively large area [110] [111] [112]. For inertial p-KEHs, the most common deformable structures are cantilevers [113] [114]. The deformation of the elastic structures will result in the electric field in the piezoelectric film, thus delivers electric energy to the load circuits. In order to lower the resonance frequency of micro-scale p-KEHs, the geometry of the elastic structures are usually adjusted so as to reduce the stiffness, as shown in Figure 1.6(a) [58] [65] [39]. One of the major problems of the p-KEHs is their low effectiveness in contrast with the other two principles, majorly due to the piezoelectric material. In p-KEHs, magnets of mm-scale dimensions are included in a lot of prototypes so as to generate non-contact forces, either working as pluckling components, shown in Figure 1.6(b) [115] [99] [116] [117] [118] [106] or introducing bistability to the resonator, shown in Figure 1.3(b) [75] [77] [78] [79] [119] [80]. Even though the magnets are beneficial for low frequency applications in p-KEHs, they cannot be easily realized through MEMS fabrications, so the miniaturization of these structures is difficult.

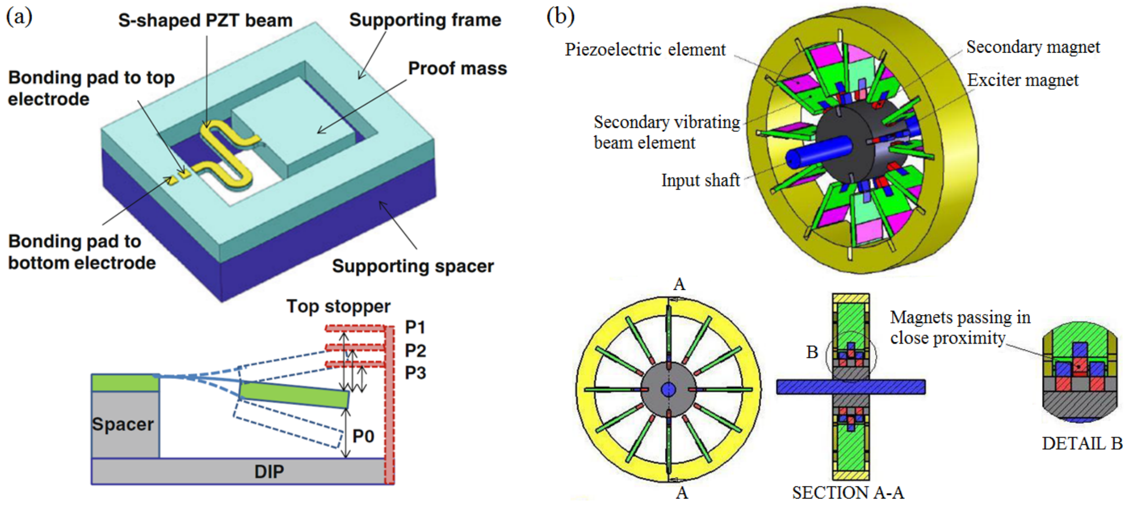

Figure 1.6: Schematic of low frequency p-KEHs. (a) p-KEH with elastic structure of low stiffness [39] (b) p-KEH with magnets working as pluckling components [115].

1.4.2 Electromagnetic KEHs (em-KEHs)

The energy transduction of electromagnetic KEHs are based on Faraday's law of electromagnetic induction, and are composed of magnets and coils that move relative to each other. One of the key parameters influencing the output power of an em-KEH is the variation of magnetic flux across the coils during each cycle of the mass oscillation. A typical geometry of a low frequency em-KEH is an impact-coupled structure based on bulk magnets and bulk coils is shown in Figure 1.7(a), which consists of a shell containing a springless movable magnetic mass, with coils wounding on its outer surface, and with stoppers on the two ends [120] [67] [121] [122] [123] [49] [101] [124]. The efficiency of em-KEHs usually outperforms the KEHs with the other two transduction principles when the dimensions of the devices are within the range of 1∼10 cm. Further miniaturization of em-KEHs usually introduce integration of magnets or coils, because the performance of integrated magnets and coils that have been reported in recent years are still far from satisfactory. The planarized coils as shown in Figure 1.7(b) are most commonly used for integrated structure [125] [126] [66] [127] [40] [128] [91], which deteriorates the power output of the devices. Their performance is much worse than the bulky solenoids [121] [122] [129] [123] [49] [130] [43]. For integrated magnets as shown in Figure 1.7(c), both the fabrication of the magnetic material and its magnetization are problematic in the previously reported prototypes (the output power far from practical requirements) [131] [128] [132]. The problems partly comes from the fact that the electromagnetic field decays drastically with the scaling down of the magnets.

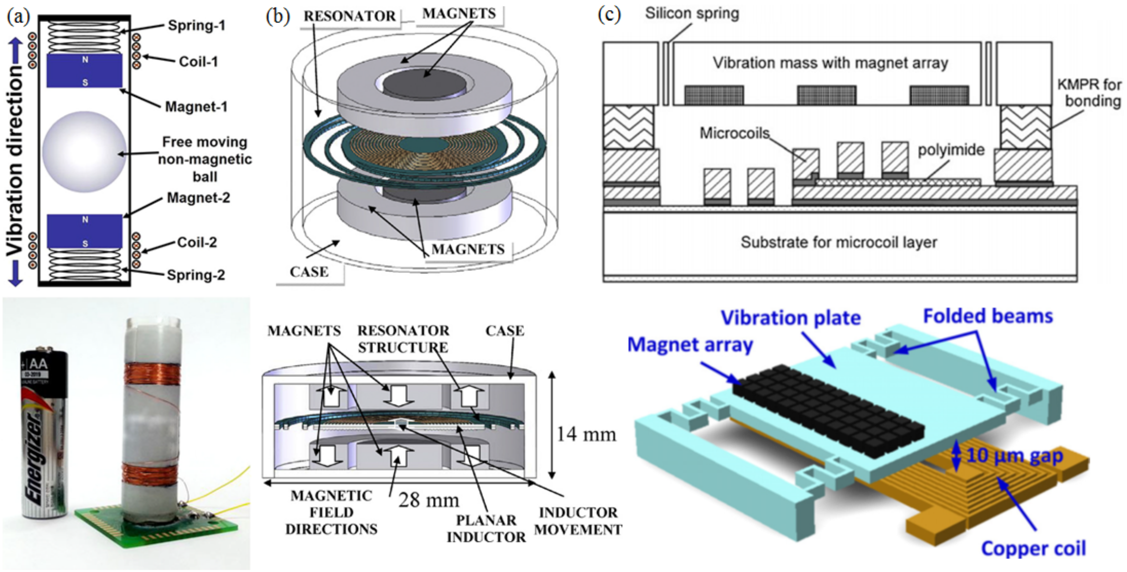

Figure 1.7: Schematic of low frequency em-KEHs. (a) em-KEH with impact-coupled structure consisting of bulk magnets and bulk coils [43] (b) em-KEHs with intagerated coils [66] (c) em-KEHs with fully integrated coils and magnets [131] [132].

1.4.3 Electrostatic KEHs (e-KEHs)

An electrostatic KEH can be intrinsically modeled as an internally DC-biased variable capacitor, transducing energy when the mass movement opposes to the electrostatic force inside the capacitor.

Its efficiency is determined by the evolution of the charge stored in the transducer and the voltage across it (i.e. the QV cycle) during the capacitance variation [133] [134]. There are two ways to improve the efficiency: to create more QV cycles in each period of mechanical excitation (i.e. frequency-up conversion) [69] [64] and to convert more energy in each QV cycle by increasing the ratio of capacitance variation $\eta = \frac{C_{\max}}{C_{\min}}$, by providing a higher bias voltage, or achieving a preferable geometry of the QV cycle [135]. Here $C_{\max}$ and $C_{\min}$ are the maximum and minimum capacitance of the transducer.

The source of the DC-bias voltage of e-KEHs can be either electret or triboelectricity. The electrets are made from materials with the ability to keep charge. The charges are injected into the material for once during the fabrication, mostly through corona charging [108] [44] [136] [137] [138], alternative processes include soft X-ray charging [139] and UV irradiation [140]. The most importance performances of the electret is the lifetime and the density of charge storage. Triboelectricity is generated during the operation of the e-KEH through repetitive friction or contact between different components [141] [142] [59], so the storage time does not have to be long.

As for the geometry of the variable capacitance, the e-KEHs can be categorized into four kinds as shown in Figure 1.8: out-of-plane gap-closing [143] [144] [137] [74], out-of-plane overlapping structure [145], in-plane gap-closing structure [146] [89] [41] [2] [147], in-plane overlapping structure, either with the electrodes in different layers [108] [44] [3] [96] [136] [98] [148], or with electrodes in the same layer [149] [150].

The limitations of e-KEHs come from the following two aspects. On the one hand, the capacitance variation of the overlapping structure is limited by the resolution of the etching process; while that of the gap-closing structure is limited by air damping effect. On the other hand, with a higher bias voltage which gives a higher output power, the risk of pull-in event that interrupts the vibration of the movable mass is also increased. This means that the bias voltage should be kept within a certain threshold if given a certain range of capacitance variation.

1.4.4 Magnetostrictive KEHs (ms-KEH)

In the literature [109] [152] [153] [154], there are also merging KEHs based on magnetostrictive material [155], which generates a deformation under a changing magnetic field, or vice versa. Compared to piezoelectric material, the ms-KEH is announced to have a higher energy conversion efficiency, longer life cycle, lack of depolarization, and higher flexibility to endure large vibration amplitudes [109]. The cardinal component of the ms-KEH in [109] is the deformable MsM film and a coil, as shown in Figure 1.9(a). The deformation of MsM film results in a varied magnetic field, and thus an electric signal in the pick-up coil. In [152] [153] [154], the key components are MPM composite modules, each of which contains two magnetostrictive films clamping a piezoelectric film, as shown in Figure 1.9(b). In these prototypes, the change of magnetic field in the MsM films will lead to the deformation, and consequently a stress in the piezoelectric film, thus generating the electric energy. The draw back of this type of KEHs is that the structures are usually complicated, which is not convenient for miniaturization and integration.

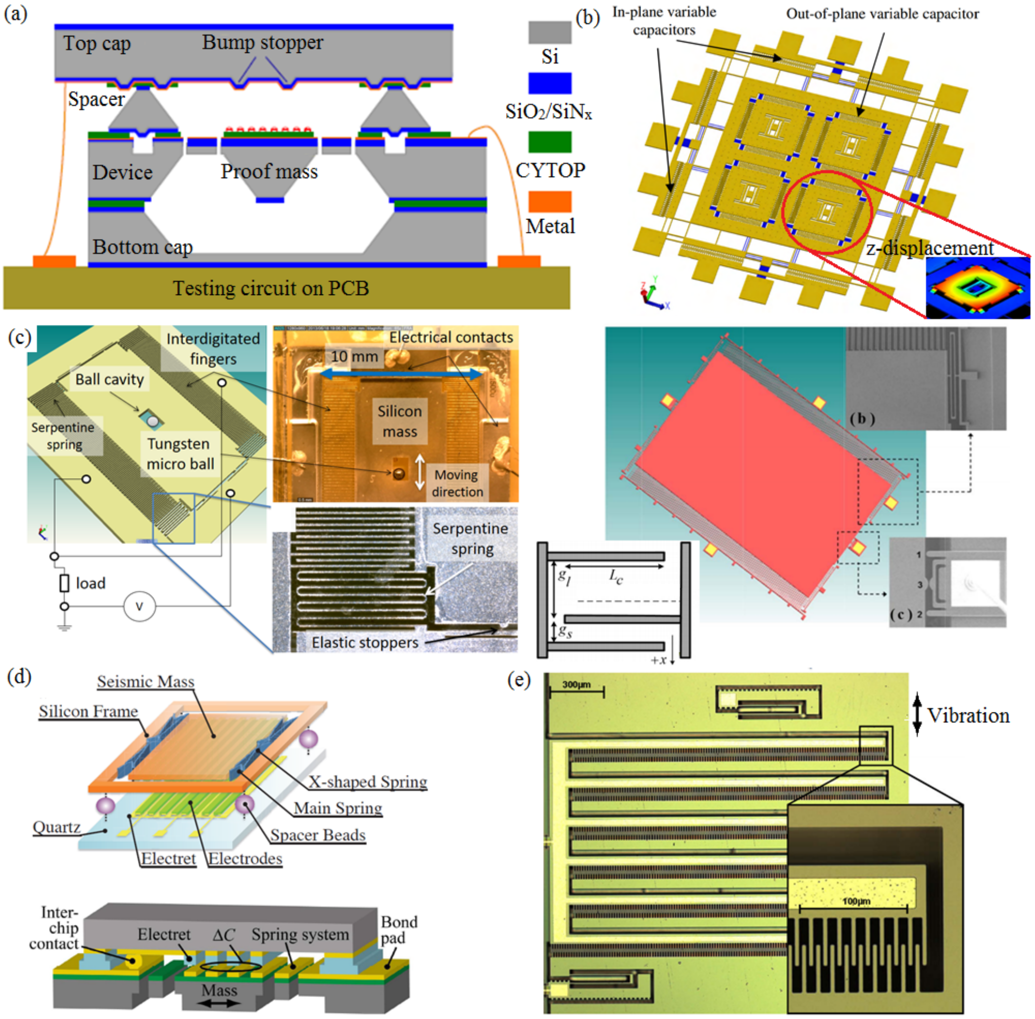

Figure 1.8: Schematic of low frequency e-KEHs. (a) e-KEH with out-of-plane gap-closing structure [144] (b) e-KEH with out-of-plane overlapping structure [145] (c) e-KEH with in-plane gap-closing structure [41] [147] (d) e-KEH with in-plane overlapping structure with electrodes in different layers [108] [136] (e) e-KEH with in-plane overlapping structure with electrodes in the same layer [151].

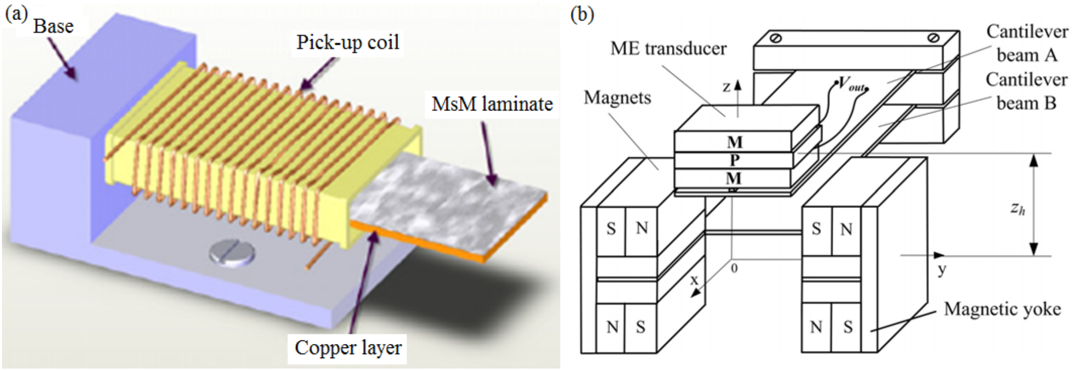

Figure 1.9: Schematic of low frequency ms-KEHs. (a) ms-KEH with deformable MsM film with coil [109] (b) ms-KEH with MPM composite modules [152].

1.4.5 Hybrid KEHs

There are loads of hybrid KEHs available in literature combining several transduction principles into a single prototype [156] [157] [158] [159] [160] [161] [162] [163] [164]. The combination of different transduction modules in most cases is the simple assembly of several modules that hardly couples with each other. In these so-called hybrid designs, there is great disparity between the output power of different transduction modules, and no value is added to improve the energy transduction performance of the prototypes. In more meaningful studies such as [157] [160] [164], the energy transduction modules are strongly coupled and optimized as a single system, where the power dilivery of different modules are comparable. In these systems, the different transduction modules play as parallel dampers in connection with the movable mass, the overall efficiency of the energy transduction is higher than each transduction module. The most common design is the combination of modules of electromagnetic and piezoelectric transduction. The difficulty in such system is to confluence the energy transduced from different channels, while keeping a high efficiency of energy conversion.

1.5 Previous works of the group

The e-KEHs are advantageous for micro-scale designs regarding the scaling laws of electric field, and their fabrication is typically simple thanks to the simple structures. The capacitance of a micro-scale e-KEH is typically realized in the form of comb-shaped electrodes. In 2006, an e-KEH with an In-Plane Overlap-Plate (IPOP) structure was proposed, where the overlapping area between comb electrodes changes with the in-plane motion of the movable electrode [165]. The energy transduction was 1.4 nJ per mechanical cycle at 0.25 g_{rms} 250 Hz. η for this prototype was limited by the invariable gap between electrodes ($\eta = 2$) and the low pull-in voltage (12 V). A 2nd generation of e-KEH based on mono-layer silicon structure with gap-closing interdigital comb electrodes was reported [2]. The converted energy was 15 nJ/cycle at 1 g_{rms} 150 Hz and a maximum bias voltage of 30 V.

The simplified structure of the prototype is shown in Figure 1.10. A silicon-based movable proof mass is connected to fixed ends through linear serpentine springs. Along the two sides of the proof mass in parallel with the direction of vibration, there are arrays of gap-closing interdigited-combs working as a variable capacitance. Opposing to the other two ends of the movable mass, there are clamped-clamped beams working as elastic stoppers, confining the maximum displacement of the proof mass. With enlarged acceleration of vibration, the stoppers will be collided by semi-cylindrical protrusions on the movable mass, the impact force between the stopper and the elastic beam will cause nonlinear deformation of the beams, allowing relatively low frequency and already large wideband response. The elastic beams allow quasi-elastic bouncing and reduce the loss of kinetic energy, introducing non-linearity and expanding the frequency bandwidth. In addition, a cavity located in the center of the proof mass houses a miniature tungsten ball. When the device vibrates at low frequency, the ball impacts with the movable silicon mass and triggers its vibrations at higher frequency. Compared to [2], this generation of KEH is polarized internally by a thin film of electret covers the mobile electrode.

When the device is driven by low frequency vibrations, the movement of the ball interacts

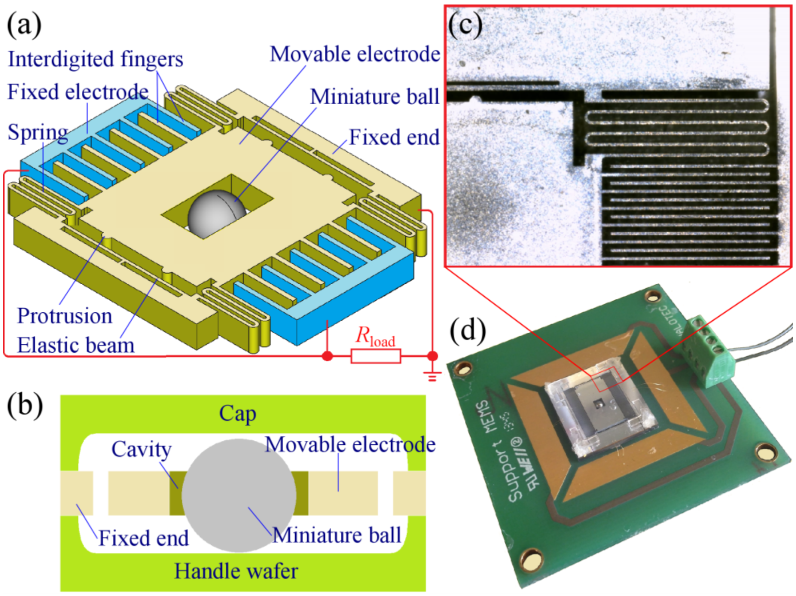

Figure 1.10: Illustration of the electrostatic vibration harvester: schematic of the core structure (a) and the cross section of the full device (b); microscopic photograph of silicon structures (c) and optical photograph of the full device (d).

with the proof mass through impacts, so that the resonant oscillation of the proof mass could be activated. The additional mass coming from the ball also increases the elastic beam displacement and so the total amount of harvested power. The electromechanical transducer is a variable capacitance composed of gap closing interdigited combs that varies inversely with the displacement of the silicon mass. A description of a similar transducer can be found in [2], but here, in addition, an electret covers the mobile electrode. Finally a miniature ball is placed into the cavity, and a glass cap is glued on the top.

The device was fabricated through a simple silicon-glass batch process inspired from [2]. All the movable parts are made in a single 380 μm-thick silicon wafer. The fabrication process of the device is shown in Figure 2.2. A thin layer of aluminum is deposited on the silicon and serves as a mask for Deep-Reactive-Ion-Etching patterning. A pre-etched handle wafer of glass (etched with HF gas) is attached to the silicon wafer through anodic bonding, with shallow grooves just below the movable part of the silicon structures. A series of key parameters of the transducer design is listed in Table 1.1.

1.6 Contents of the thesis

This thesis focuses on the low frequency miniature e-KEH, proposes different designs each suit for specific low frequency applications, and studies the modeling of the prototypes. An energy-autonomous batteryless RFID communication sensor node is proposed, which is powered by low-frequency miniature e-KEH. It consists of six chapters summarized as following:

In the first chapter, a review of the state-of-the-art of low frequency miniature kinetic energy harvesters is made, their current problems are proposed. An externally biased e-KEH proposed previously is presented as the basis of this work, followed by a brief introduction of the contents

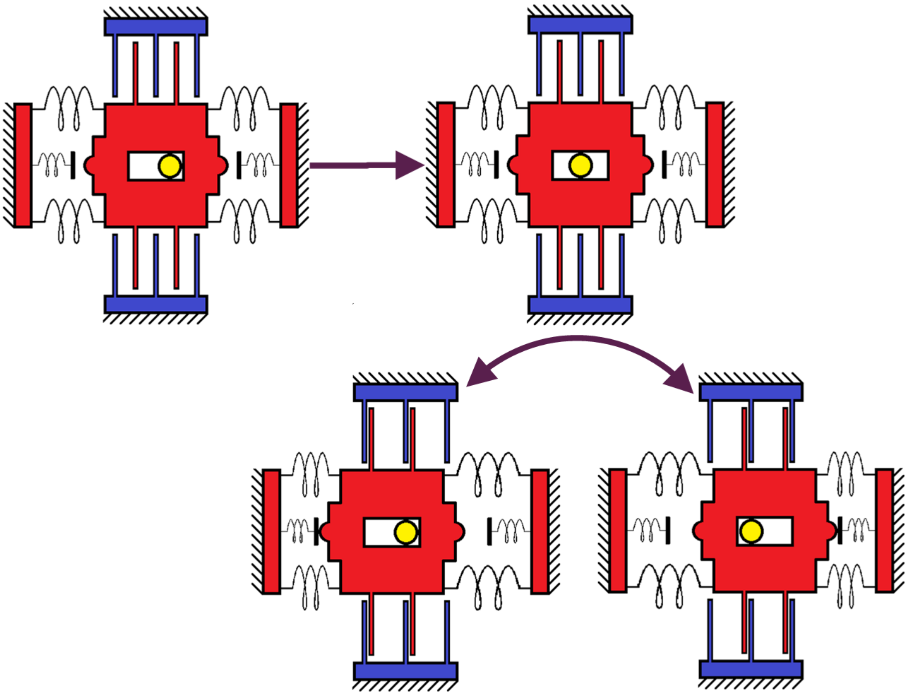

Figure 1.11: Frequency-up conversion mechanism excited by ball-mass impact.

Table 1.1: Key parameters of the transducer

Parameter	Value
Active area (movable mass + springs)	12×10 mm^2
Thickness of the silicon layer	0.38 mm
Width of fingers	30 μm
Overlapping length of comb fingers L	1.97×10^{-3} m
Initial gap between fingers	70 μm
Number of fingers on the fixed electrode	102
Number of fingers on the proof mass	100
Size of the cavity housing the ball	1.8×2.3 mm^2
Silicon proof mass	$\sim 60 \times 10^{-6}$ kg
Diameter of the miniature ball	1.6 mm
Mass of the miniature ball	32×10^{-6} kg

All the dimensions related to the patterning of the silicon layer are at the mask level. Since there is over-etching below the mask during the DRIE process, the real dimensions of the silicon structure are slightly different from the listed values.

in each chapter.

The second chapter presents a simple numeric model is proposed to facilitate the optimization of the impact-coupled in-plane gap-closing e-KEHs. A vertical layer of electret is added to the e-KEH so that the prototype can work without external source. The prototype is then fully characterized, the device performance achieved by the measurement are then compared with the simulation results. The shortcomings of the model is that it has a set of parameters that must be set to different values for different excitations and conditions, which is problematic for predictive studies.

The third chapter proposes a more sophisticated and predictive model of the impact-coupled e-KEHs, which takes into account a strongly nonlinear air damping effect. The new model is better than the previous model because it makes it possible to share the same setting of parameters according to the experimental results with varied excitations and conditions. It is shown that the air damping in the gap-closing model is an important factor that limits the output power of the in-plane gap-closing prototypes.

In the fourth chapter, we present a group of e-KEHs based on an improved comb geometry reducing the air damping force. The benefits of frequency up conversion performance is exaggerated thanks to the reduced air damping force in the new design. The capacitance variation of the prototypes and their output power with resistive load are characterized in comparison with the classic gap-closing device, and the prototypes giving the best performance in air and in vacuum are figured out. In addition, the AC/DC energy conversion performance of the optimal prototype is also measured, and the best operational condition is determined according to the AC/DC energy conversion within each cycle of external excitation.

The fifth chapter discusses about several approaches of e-KEHs to achieve alternative improved features. The first trial is a fully flexible prototype based on electrospun-fibrous electret. The electrospun nanofiber based electret film is fabricated and its charge storage performance characterized. The full prototype is experimentally characterized, and the optimal configuration is figured out. The second proposal is an e-KEH which is sensible to vibrations along 2 orthogonal directions. The design is proposed with a modal simulation, showing the prototype can work with vibrations along any direction parallel to the device plane. Preliminary experimental results of the device characterization is presented.

The sixth chapter shows a full RFID tag wireless communication system powered by a low-frequency e-KEH. We designed the antenna for a commercial RFID chip through finite element method analysis to reach impedance matching with the chip, and characterized through experiment the electromagnetic properties of the antenna fabricated through digital milling process, and the key fabrication parameter influencing the antenna performance is found out. The chip performance is characterized in combination with capacitive as power source, and the minimum value for the reservoir capacitor is determined. Finally, the performance of the full RFID tag system is evaluated through data-transmission experiments.

Chapter 2

First modeling approach and characterization of impact-coupled e-KEHs

In this chapter, we improve the low-frequency electrostatic kinetic energy harvester (e-KEH) proposed in Chapter 1 with a corona-charged electret layer on the vertical surfaces of one electrode, so that the device can be internally biased. The electret also plays as an insulating layer which keeps the two electrodes from touching each other, thus solves the short-circuit problem in the device with bare silicon structure.

Based on a complete experimental characterization, we introduce a model of the prototype impact-coupled frequency up-conversion mechanism, which serves as a tool for parametric studies in the future designs. The frequency up conversion of this FIG-like device is analyzed through the investigation of the output performance with and without the springless mass. In addition, we also study the performance of the device at ultra-low frequencies shaken by hand. Finally, a 47-μF capacitor is charged by the device to 3.5 V, and used to power a batteryless wireless temperature sensor node.

2.1 Preparation of vertical electret layer

Based on the prototype demonstrated in Chapter 1, a layer of conformal Parylene C is deposited on the entire surface of the full device, and the electret on the movable electrode is charged negatively by point-grid-plane corona with temperature control. The design and the photograph of the corona charging setup is shown in Figure 2.1. In order to ensure that only the electret on the movable part is charged, the counter electrode is biased at the same voltage as the grid during the charging. The sample is heated to 100°C during the first 30 min, and cooled to room temperature in the following 30 min, keeping the high voltages on all the electrodes.

Once the built-in voltage on the electret becomes stable, it is measured to be 33 V according to the method described in [166]. Three weeks after the electret charging, the built-in bias voltage provided by the electret was stabilized and measured at 21 V by using a half-wave voltage doubler,

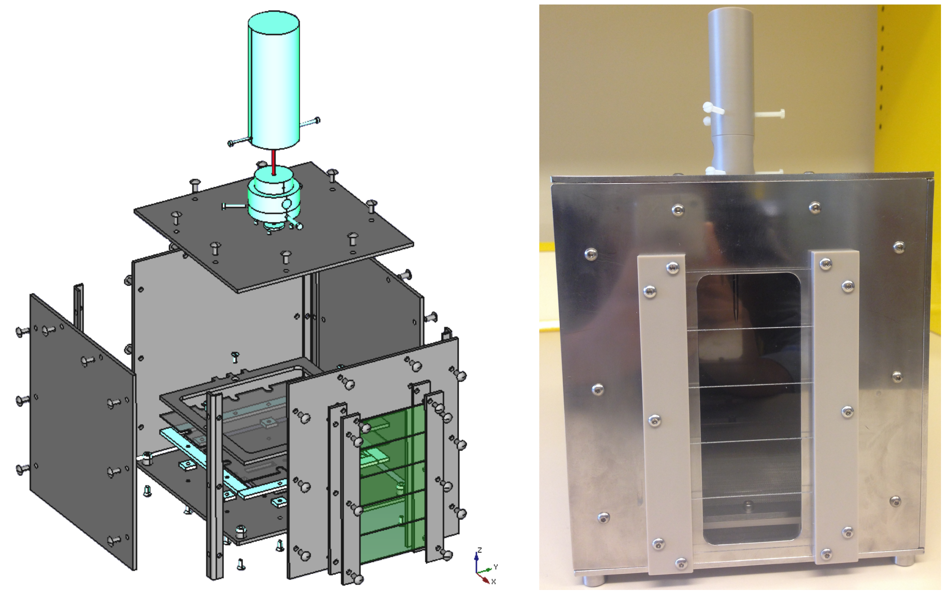

(a) The schematic of corona charging setup assembling (b) The final assembly for corona charging setup

Figure 2.1: The design and the photograph of the corona charging setup.

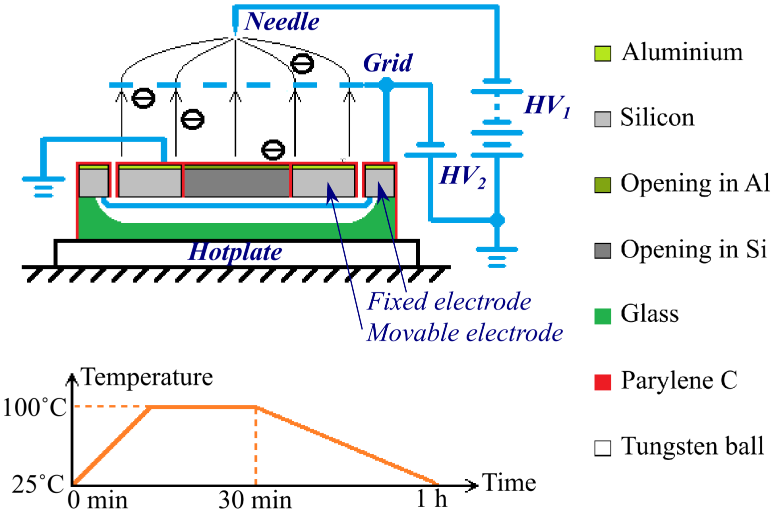

Figure 2.2: Corona charging of the prototype.

which is connected to the e-KEH while submitted to vibrations [167]. However, the transducer could withstand much higher bias voltages and the capability of the prototype is actually fully demonstrated by applying a DC bias of 25 V in addition to the internal bias of the electret. It is thus also possible to investigate the impact of the bias voltage between electrodes on the performance of the device. Finally the miniature ball is placed manually in the central cavity, and a glass cap is fixed on top of the device with double-sided tape.

2.2 Modeling of the impact-coupled KEH with linear air damping

2.2.1 Kinematic equations

A simple electrostatic harvester consists of a second order resonator, a variable capacitor (transducer) C, and a resistive load. The model majorly deals with a time-dependent excitation signal and relates it to the states of the KEH. A simplified schematic of the prototype is shown in Figure 2.3. It successively calculates the instantaneous status of the movable electrode and the mini-ball (the positions and the velocities) in chronological order, based on the excitation and arbitrary initial conditions. The device is modeled as a variable capacitor biased by a DC voltage, the capacitance of which is dependent on the position of its movable electrode. In the model, e-KEH is excited by both a mechanical input (an external acceleration a_{ex}) and an electrical input (an electret bias or an external DC bias voltage). The forces acting on the movable electrode include the forces from the linear springs (F_{spr}) and the stoppers (F_{st}), the electrostatic force (F_{e}), and the air damping force (F_{air}). For a sinusoidal excitation, the mobile mass displacement (x) in the mechanical domain, the kinematic equation of the movable electrode is given by the Newtonian equation:

$$m\ddot{x} = F_{\mathrm{spr}} + F_{\mathrm{st}} + F_{\mathrm{e}} + F_{\mathrm{air}} - m a_{\mathrm{ex}} \tag{2.1}$$

where m is the mass of the movable electrode; x, $\dot{x}$ and $\ddot{x}$ are its position, velocity and acceleration respectively.

The spring force is linear with displacement:

$$F_{\mathrm{spr}} = -kx \tag{2.2}$$

where k is the total stiffness coefficient of the four springs.

The force of the elastic stoppers is a strong nonlinear force due to its piecewise nature. It can be described as:

$$F_{\mathrm{st}} = \begin{cases} 0 & |x| < g_{\mathrm{st}} \\ -k_{\mathrm{st}}\left(|x| - g_{\mathrm{st}}\right) \operatorname{Sgn}(x) & |x| \geq g_{\mathrm{st}} \end{cases} \tag{2.3}$$

where g_{st} is the initial size of the gap between the movable mass and the undeformed stopper beams. k_{st} is the total stiffness of the elastic stopper beams, while $\operatorname{Sgn}(\cdot)$ is the sign function. Nonlinear stoppers along with the electrostatic force are used to enlarge the operating bandwidth and increase power yield. The system of nonlinear ordinary differential Equations 1.16-2.3 is the primary model of this device. However due to the substantial nonlinear behavior it is helpful to

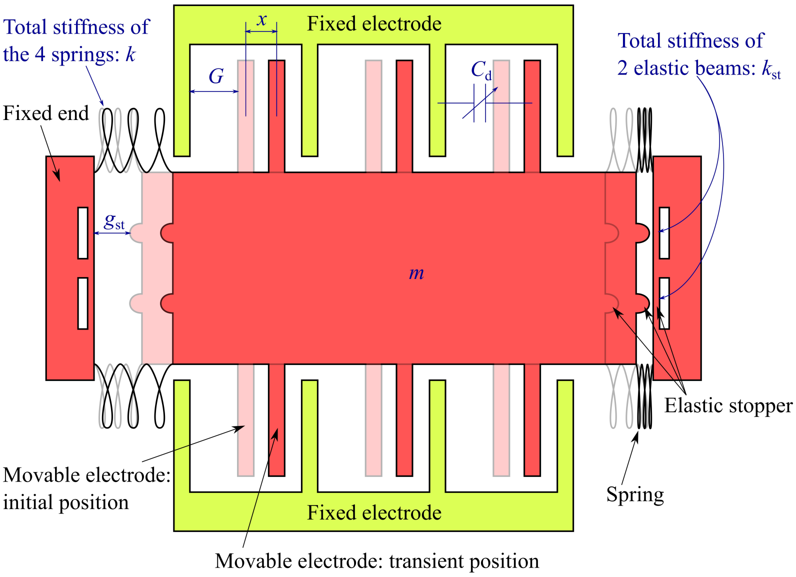

Figure 2.3: A simplified schematic of the prototype (top view) with the parameters and variables used in the model.

employ semi-analytical methods, such as perturbation techniques, to obtain greater understanding of the device dynamics.

The electrostatic force F_e describes the electrical transduction of energy from the mechanical domain, see equation 1.16. The electrostatic force is a nonlinear force which plays a fundamental role in the description and optimization of e-KEHs. The importance of the electrostatic force can be seen if, for example, an external driving frequency near resonance is applied to the device. Increasing the bias voltage V_{bias} will ultimately cause the harvested energy to decrease This effect is due to a shift in the resonance frequency caused by the electromechanical coupling [135]. Such a decrease in power would not occur if a fixed C function was used (as is the case of purely electrical analysis when ignoring F_e). The Kirchhoff's voltage law 1.17 is also taken into account. We note the dependence of the equation on the resonator displacement x, highlighting the electromechanical coupling in the system 1.17.

The air damping force is simplified as a linear damper:

$$F_{\text{air}} = -b\dot{x} \tag{2.4}$$

where b is the damping factor.

A sinusoidal signal $a_{\text{ex}} = A\sin(2\pi ft)$ is applied to the KEH in the experiments, where A and f are the amplitude and the frequency of acceleration.

2.2.2 Time-series recursion

To solve the kinematic equations in section III.A, we apply a simple time-series recursion method. The time is discretized into an arithmetic sequence $\{t_1, t_2, \cdots, t_i, \cdots\}$ with a constant time step of Δt, which is about two orders of magnitude smaller than the period of the excitation vibration. At a given time t_i, the status of the device (the ith status) is described as a vector $(x_i, \dot{x}_i, q_i, x_{\text{b},i}, \dot{x}_{\text{b},i})$.

The kinematic equations of the two masses during the next time step is predicted, according to the range of x_i and $x_{\mathrm{b},i}$. A prediction of the $(i+1)$th status of the device at the time t_{i+1} is achieved according to the following Euler predictors (based on first order Taylor expansions) as well as the ones in section III.A.

$$u_{\mathrm{pr}} = u_i + \dot{u}_i \cdot \Delta t \tag{2.5}$$

herein u stands for any element of the vector $(x, \dot{x}, q, x_{\mathrm{b}}, \dot{x}_{\mathrm{b}})$. If the kinematic equations corresponding to the predicted status at t_{i+1} are the same as the ones of the time t_i, there is no impact or separation within the time slot Δt. The next status is obtained according to the kinematic equations and the trapezoidal correctors shown below:

$$u_{i+1} = u_i + (\dot{u}_i + \dot{u}_{i+1,\mathrm{pr}}) \cdot \frac{\Delta t}{2} \tag{2.6}$$

2.2.3 Impact and separation detection

In other cases, there are impacts and separations between different parts of the device. The impacts and separations are inspected according to the current displacement x_i and the predicted displacement x_{pr}. The judging criteria are the following.

Impact with / separation from the stoppers

The movable electrode impacts with the stopper between t_i and t_{i+1} when

$$|x_i| < g_{\mathrm{st}}, |x_{\mathrm{pr}}| > g_{\mathrm{st}} \tag{2.7}$$

While separation from the stoppers occurs when

$$|x_i| > g_{\mathrm{st}}, |x_{\mathrm{pr}}| < g_{\mathrm{st}} \tag{2.8}$$

The time slots before and after the impact/separation can be estimated by the following equation:

$$t_{\mathrm{imp/sep}} = t_i + \frac{x_i - g_{\mathrm{st}} \cdot \mathrm{Sgn}(x_i)}{x_i - x_{\mathrm{pr}}} \cdot \Delta t \tag{2.9}$$

Impact with the fixed electrode

When the movable electrode is already in contact with the stopper at t_i, and the prediction for t_{i+1} exceeds the maximum possible displacement:

$$|x_i| > g_{\mathrm{st}}, |x_{\mathrm{pr}}| > G \tag{2.10}$$

where G is the initial gap between movable and fixed electrodes, there will be direct impact between electrodes. The time slots before or after the impact are estimated as follows:

$$t_{\mathrm{imp/sep}} = t_i + \frac{x_i - G \cdot \mathrm{Sgn}(x_i)}{x_i - x_{\mathrm{pr}}} \cdot \Delta t \tag{2.11}$$

2.3 Design parameters for modeling

We use the model presented above with the numeric parameters for the prototype in Chapter 2 in order to show the system's dynamic behavior and to determine a configuration (e.g., the load resistance and the bias voltage) maximizing the energy conversion. The solutions resulting from the model are discussed from the perspective of the experimental results given in Section 2.4.5. The parameters used for this modeling are given in Table 2.1. Some parameters are estimated from the geometry of the device with a high degree of confidence (e.g., the mass, the initial gap, the stiffness of the springs), and others are estimated indirectly. According to [168] [169], the damping effect of air thin film is greatly affected by the thickness of air film, and a linear damping model is only a rough approximation of real physical phenomena. The quality factor used in the model represents globally the losses experienced by the resonator during the vibrations. It is estimated to be 6.5, see Table 2.1. We consider that the use of a simplified damping model is the main source of discrepancy between the experimental results and the modeling (see discussion on the comparison with the experiment in Section 2.4.4). The used initial gap value corresponds to the approximated model of the transducer, which is justified in Section 2.4.1. The total parasitic capacitance of the measurement set-up (28 pF) is another parameter not accounted for in the MSM model.

Table 2.1: Parameters of the model used in Figures 2.7 and 2.9

Parameter	Value
Spring Constant k	$27.8\mathrm{N}\cdot\mathrm{m}^{-1}$
Stopper Spring Constant k_{st}	$8.64\times10^{3}\mathrm{N}\cdot\mathrm{m}^{-1}$
Position of the undeformed stopper's beam d_{stop} (estimated)	51 μm
Quality Factor $Q=\frac{\sqrt{m/k}}{b}$ (estimated)	6.5
Parasitic Capacitance of the measurement set-up C_{p} (measured)	28 pF

2.4 Experiments and validation of the model (without ball)

2.4.1 Capacitance variation measurement

Theoretically, the capacitance of the prototype $C_{\mathrm{d}}(x)$ in relation with the mass displacement x is given by:

$$C_{\mathrm{d}}(x)=\epsilon_0\frac{2SG}{G^2-x^2} \tag{2.12}$$

where S is the overlapping area of the electrodes, G is the initial gap between electrodes, ϵ_0 is the permittivity of the vacuum. Hence, if the displacement is sinusoidal with amplitude X_0, the extreme values of the capacitances during the device deformation are given by:

$$C_{\min}=\epsilon_0\frac{2SG}{G^2},C_{\max}=\epsilon_0\frac{2SG}{G^2-X_0^2} \tag{2.13}$$

It can be seen that the minimum capacitance is only defined by the device geometry, whereas the maximum value is a function of the amplitude X_0. In practice, the maximum/minimum capacitance is affected by several factors: fabrication tolerances (actual value of the initial gap, non-verticality of the transducer wall due to the under-etching [2]), the presence of the Parylene

C layer on the electrodes and the importance of the electrostatic force. Moreover, it is difficult to know the real amplitude X_0. Hence, the characterization of the capacitance variation is an important step described in this section.

The schematic of the capacitance measurement is shown in Figure 2.4(a), where an AC signal V_{ac} is applied to the device in series with a resistor R_{load}. By detecting the phase difference of the signals on the two nodes of the device (i.e. signals CH1 and CH2 in Figure 2.4(a)), its capacitance can be measured dynamically [3]. In order to minimize the error of the measurement, the value of the load should be the optimal value given by:

$$R_{\mathrm{opt}} = (\omega C)^{-1} \tag{2.14}$$

where ω stands for the angular frequency of the carrier signal V_{ac}, and C is the average value of the device's capacitance. To choose the optimal load, we firstly employ the capacitance variation range given by simulation, and use the estimated optimal load for a rough measurement. The result of this test is then used for recalculating the optimal load, and the capacitance is re-measured using the new optimal load. In the experiment we apply a sinusoidal carrier (V_{ac}) with the frequency of 50 kHz and the peak-peak amplitude of 2 V, while the load resistance is 53 kΩ. The operational amplifier used is OPA445AP from Texas Instruments (same below). The capacitance variations at 0.5 and 2.0 g_{rms} are shown in Figure 2.4(b).

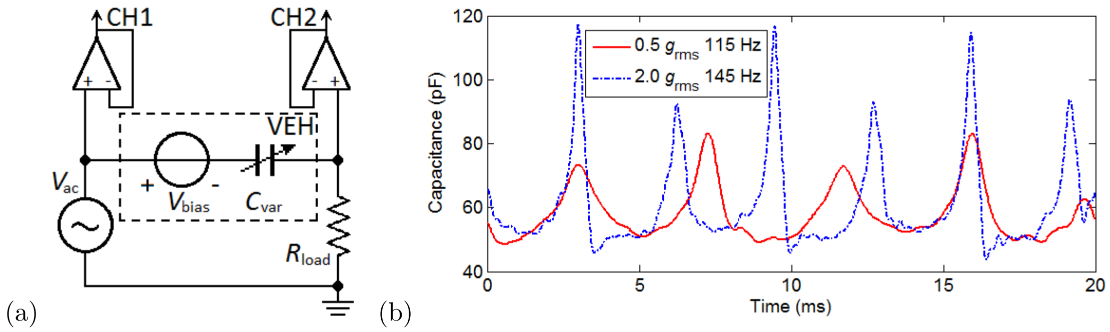

Figure 2.4: (a). Schematic for the measurement of capacitance, (b) capacitance variation at acceleration of 0.5 and 2.0 g_{rms}, including a 28 pF parasitic capacitance.

It is observed that in each period of mechanical vibration, there are 2 peaks in the capacitance evolution, corresponding to the maximum displacement of the movable electrode in 2 directions. This is explained by the fact that the function $C_{\mathrm{var}}(x)$ is even (due to the symmetric geometry of gap-closing combs), see Equation 2.12. There is an obvious difference between the values of the 2 peaks, indicating an asymmetric oscillation of the movable electrode. The increase of acceleration introduces an enlarged range of capacitance variation, where the peak values increase and the minimum remains almost the same: for the acceleration of 0.5 g_{rms} the range of capacitance is 50∼80 pF and the average peak value is 78 pF, while for 2.0 g_{rms} the capacitance varies from 48 pF to 115 pF with the average peak value of 105 pF. These values include a parasitic capacitance of 28 pF induced by the measurement setup.

2.4.2 Built-in voltage measurement

After the corona-charging, when the charge in the electret becomes stable (after 3 weeks), the built-in voltage of the device (V_{bias}) provided by the electret was measured using the circuit shown in Figure 2.6. The output current of the device was connected to a storage capacitor C_{store} through a half-wave diode bridge rectifier. This circuit corresponds to a rectangular QV cycle during the cycle of capacitance variation [134] [135], in which the converted energy in each cycle is given by the equation:

$$\Delta W = (V_2 - V_1)(Q_2 - Q_1) \tag{2.15}$$

where V_1 and V_2 stand for the extreme voltages on the capacitor C_{var}, while Q_1 and Q_2 are the extreme values of transducer charge Q_{var}. Note that the quantity Q_{var} represents the charge on the capacitor in the equivalent model of the transducer in Figures 1.10(a) and 2.4(a), and not the distribution of the physical charges on the capacitor planes. However, the derivative of Q_{var} represents the physical current through the device. These extreme values are given by the following equations,

$$\begin{cases} V_1 = V_{\text{bias}} - V_{\text{store}}; & V_2 = V_{\text{bias}} \\ Q_1 = V_1 C_{\max}; & Q_2 = V_2 C_{\min} \end{cases} \tag{2.16}$$

where V_{store} is the voltage on the storage capacitor, while $C_{\min}$ and $C_{\max}$ are the minimum and the maximum values of the device's variable capacitance respectively. The QV cycles achievable with different values of V_{store} are represented in Figure 2.5.

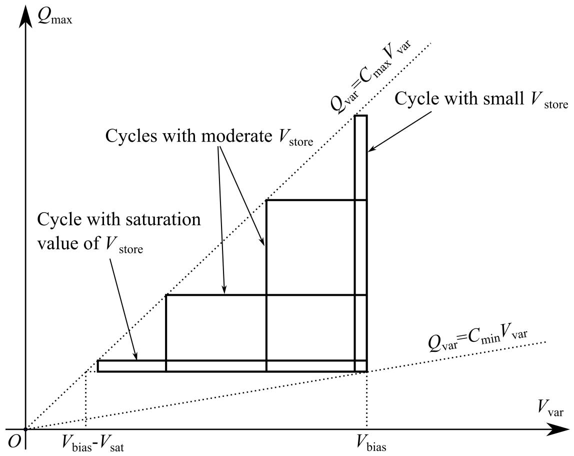

Figure 2.5: QV cycles of the half wave rectifier used with a variable capacitor biased by an electret.

Because of the capacitance variation, the voltage across C_{store} increases and finishes by being saturated. Simple calculation highlights a relation between the measured saturation voltage V_{sat} and the built-in voltage V_{bias}. By merging Equations 2.15 and 2.16, we can derive that:

$$\Delta W = V_{\text{bias}} V_{\text{store}} C_{\max} \left(1 - \frac{V_{\text{store}}}{V_{\text{bias}}} - \frac{C_{\min}}{C_{\max}}\right) \tag{2.17}$$

To ensure non-negative energy conversion, the following relation must be held:

$$\frac{V_{\text{store}}}{V_{\text{bias}}} \leq 1 - \frac{C_{\min}}{C_{\max}} \tag{2.18}$$

so that the maximum allowed V_{store} is the saturation voltage V_{sat}, which is given by:

$$V_{\mathrm{sat}} = V_{\mathrm{bias}}\left(1 - \frac{C_{\mathrm{min}}}{C_{\mathrm{max}}}\right) \tag{2.19}$$

Thus the bias voltage of the device is indicated by the saturation voltage if the ratio of maximum and minimum capacitance is known:

$$V_{\mathrm{bias}} = \frac{V_{\mathrm{sat}}}{1 - C_{\mathrm{min}}/C_{\mathrm{max}}} \tag{2.20}$$

Note that the polarity of the connection of the electret bias matters: for an inverse polarity of V_{bias} in Figure 2.6(a), the expression for the saturation voltage and the aspect of the QV cycles are different [4].

In the experiment, the device was submitted to vibrations with acceleration of 2 g_{rms} and 145 Hz, and the measured saturation voltage is 11.5 V, as shown in Figure 2.6(b). Considering that the capacitance C_{var} is comprised between 48 pF and the peak value of 115 pF, we can infer that the bias voltage of the electret is V_{bias} = 20 V. Since the device can withstand higher bias voltages, we have also applied an external bias in addition to the internal one in some of the following experiments. However, the device could stand for much higher bias voltage. The limit for the bias voltage is the summary of the internal voltage and an additional DC bias of 25 V, and above this value we observe dynamic pull-in between electrodes during the experiment. In order to fully demonstrate the capability of the prototype, we also performed experiments under the maximum durable bias voltage. (According to a previous rough measurement, the saturation voltage is 11 V, C_{var} varies from 50 pF to 105 pF, indicating that the electret voltage is V_{bias} = 21 V, and the total voltage including external bias is up to 46 V. This group of bias voltages are included in some legends of the graphics in this chapter as illustrator of different curves.) In another built-in voltage measurement after another charging on the same device reported in [167], the internal bias voltage is measured as 33 V.

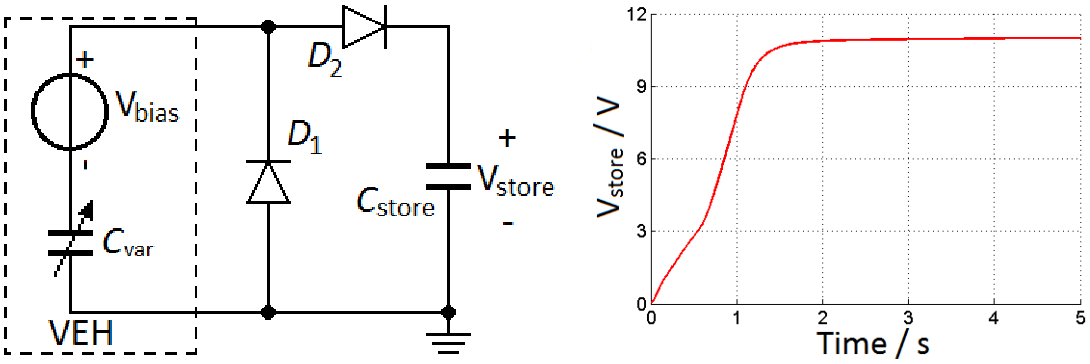

Figure 2.6: (a). Circuit for built-in voltage measurement of the electret layer, where C_{store}=1.1 nF; (b). Evolution of V_{store} at 2.0 g_{rms}, 145 Hz.

2.4.3 Arbitrary parameters in the model

The behavior observed by the experiment in Figure 2.9 is well reproduced by the analytical model presented in Section 2.2, when the system of nonlinear Equation 1.16-2.3 is solved by a numerical method, see Figure 2.9, plain lines. In particular, frequency-up conversion behavior and the bimodality are well predicted. However, because of approximation in the model of the air damping (discussed in Section 2.2), some model parameters need to be tuned for each value of external acceleration, for the numerical values predicted by the model coincide with the experimental results. The adjustment is done on two parameters Q (quality factor) and g_{st} (position of the undeformed stopper's beam) as shown in Table 2.2.

Table 2.2: Parameters of the analytical model of Section 2.2 adjusted for matching with the experimental results given in Figures 2.7 and 2.9.

Parameter	Value
Position of the undeformed stopper's beam g_{st}	52 μm (0.5 g_{rms}) 52.8 μm (1.0 g_{rms} & 2.0 g_{rms})
Quality Factor Q	6.5 (0.5 g_{rms}) 5.4 (1.0 g_{rms}) 4.3 (2.0 g_{rms})

2.4.4 Energy per cycle vs. load resistance

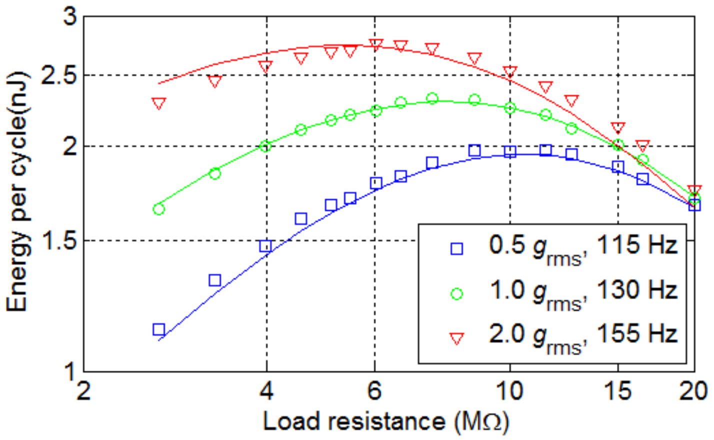

Figure 2.7: Influence of the load resistance on the converted energy in each cycle of mechanical vibration with various amplitudes of acceleration. The device is biased only by the electret at 20 V and is shaken at the frequency that offers maximum capacitance variation. The symbols are experimental results, and the plain lines are the results given by the model of Section 2.2 solved numerically.

The output power of the device was tested with a varying load resistance (see Figure 1.10 for the circuit), so that the optimal matching load could be found for each amplitude of acceleration. The chosen frequency of vibration for each amplitude was the one that provided the maximum variation of capacitance. In these measurements, the device was biased only by the internal voltage of the electret (20 V). Shown in Figure 2.7 are the energy consumptions of the sweeping load resistance at different accelerations. As stated in [2], the load resistance affects the QV cycle in two major aspects: with a large resistance the charge variation is limited, while with a small load the voltage is nearly constant, resulting in limited power in both cases. So we can obtain a medium optimal load resistance corresponding to an optimal energy conversion cycle.

We observe a decreased optimal load (R_{opt}) with increased acceleration, which is similar to the observation in [170]: R_{opt} for 2.0 g_{rms} is 6 MΩ, and is 10 MΩ for 0.5 g_{rms}. This can be explained as a result of the nonlinearity in the system. We also notice that with the increase of the load resistance, the increase of energy conversion in each QV cycle, due to the increase of the acceleration, is less evident. This can be explained as follows. The increase of the load resistance results in an enlargement of the variation of the voltage. Consequently, when the amplitude of the mass motion is large, so that the gap becomes very small at extreme positions of the mobile electrode, the electrostatic force increases significantly (inversely proportional to the square of the gap). This creates a mechanism further reducing the gap, and in turn enlarging the capacitance variation range and the voltage variation. Thanks to this positive feedback mechanism, the increase of maximum displacement with increased acceleration at large R_{load} is less prominent, so is the increase of power.

2.4.5 Power / energy per cycle vs. frequency

In the power measurement, the device without the ball is subjected to frequency sweeps with a load of 6.65 MΩ directly connected across the transducer's terminals. Figure 2.8 shows the measured average power against the frequency at 0.1, 0.5 and 2 g_{rms}. At 0.1 g_{rms}, there is no impact between the protrusions on the proof mass and the elastic beams, and the natural frequency f_0 is measured at 104 Hz without external bias. At higher accelerations, the protrusions on the proof mass knock the elastic beams, which introduces a temporary extra stiffness to the springs. It leads to mechanical nonlinearity and results in hysteresis in the frequency response. An overall frequency shift could also be observed, where the central frequency of the band decreases when the bias voltage varies from 21 V to 46 V. This shift is explained by the spring softening effect caused by the electrostatic negative stiffness [2]. Despite the hysteresis, large bandwidths are observed in both up and down frequency sweeps. For instance, at 2.0 g_{rms} with 46 V of bias (electret @ 21 V + DC bias @ 25 V), the maximum average harvested is 6.6 μW at 432 Hz and the associated -3 dB bandwidth corresponds to 64% of the central frequency of 328 Hz, but only for frequency-up sweeping. If we do not include the hysteresis, the maximum average power is 2.4 μW at 166 Hz and the -3 dB bandwidth is 78 Hz, i.e. 61% of the central frequency of 129 Hz.

Shown in Figure 2.9 are the converted energy in each cycle of the external mechanical vibration at higher accelerations (0.5 and 2.0 g_{rms}), which is obtained by dividing the output power with the mechanical vibration frequency. We observe a hysteresis due to spring-hardening effect of the nonlinear stoppers, which reinforces the bi-modal behavior predicted by the numerical model (see Section 2.2). The frequency range of this spring-hardening hysteresis is greatly increased under large accelerations, bringing great improvement to the bandwidth. At 2.0 g_{rms} with 45 V bias, the maximum -3 dB band is 223∼432 Hz including hysteresis and 88∼166 Hz when excluding it.

Unlike with the amplitude of external vibrations, increasing the bias voltage almost does not

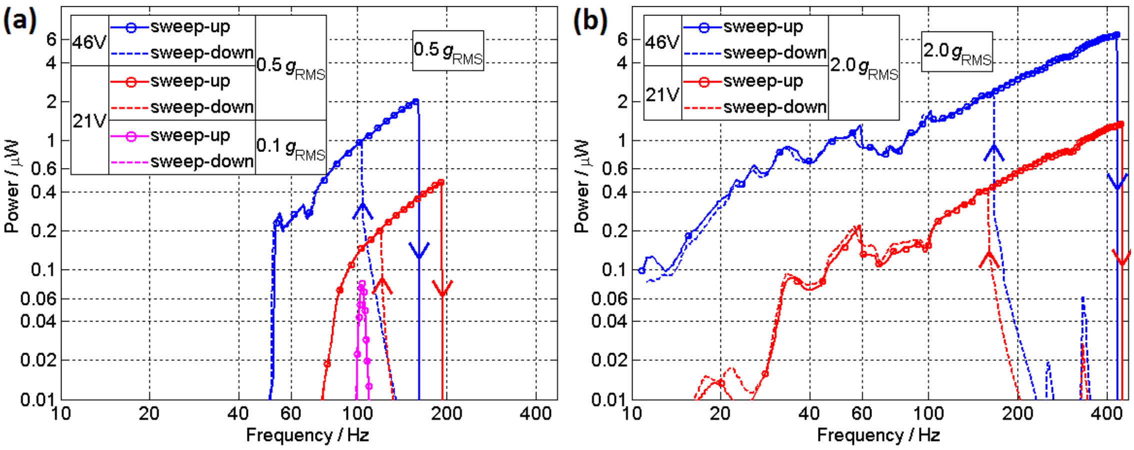

Figure 2.8: Average power versus frequency for the device without ball for bias voltages of 21 V and 46 V at (a) 0.5 g_{rms} and (b) 2.0 g_{rms}.

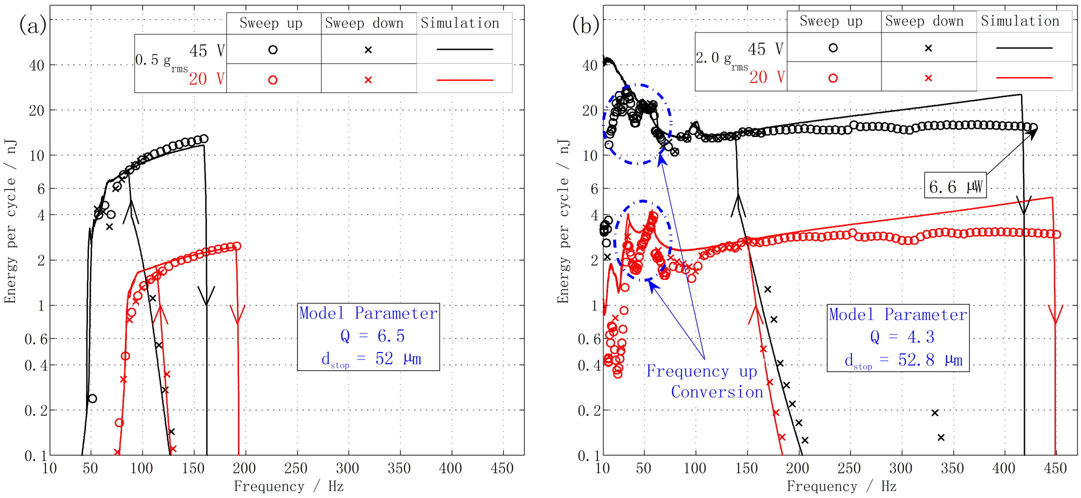

Figure 2.9: Energy converted in each cycle of mechanical vibration vs. its frequency for bias voltages of 20 V (electret alone) and 45 V (electret @ 20 V + DC external bias @ 25 V) at 0.5 g_{rms} (a) and 2.0 g_{rms} (b), $R_{\mathrm{load}} = 6.65$ MΩ. The circles and crosses correspond to the measurement with frequency sweeps, while the plain lines depict the prediction given by the model of Section 2.2 solved numerically.

affect the bandwidth (only a 5% increase of bandwidth with the bias increased from 20 V to 45 V). However, the increased bias increases the electrostatic force between interdigited combs, resulting in a reduced stiffness of the spring system (spring softening effect). The consequence is a shift towards low frequency in the frequency response of the device.

The maximum power that can be achieved at 2.0 g_{rms} is 6.6 μW. It is well established that the converted energy with a given capacitance variation cycle is proportional to the bias voltage squared, and increases with the enlargement of capacitance range [133]. As expected, we observe an approximately linear relationship between the output power and the square of the bias voltage, which suggests that with these parameters of external vibrations the range of capacitance variation is not sensitive with regard to the voltage. As mentioned in section 3.1, it means that the amplitude X_0 is less dependent on the bias voltage than on the mechanical factors.

However, there is an obvious increase of converted energy in each mechanical cycle at the acceleration of 2.0 g_{rms} within the frequency range of 30~60 Hz, instead of keeping a constant value as for higher frequencies. Within this range, there are 2 peaks at 52 Hz and 34 Hz, corresponding to 1/2 and 1/3 of f_0 respectively. This increase of energy is representative of a frequency-up conversion mechanism [70] induced by the elastic stoppers where there are several bounces of the movable mass in each period of external vibration. So that, there are several peaks of capacitance in each cycle of the carrier's vibration.

After this adjustment, the analytical model provides a frequency response very close to what was observed experimentally. One can conclude that the proposed model describes well the main features of the system dynamics, but is still unable to predict the exact numerical values of the dynamic parameters (amplitude, power) without a post-experiment model tuning. This is a serious shortcoming of the analytical and modeling techniques of e-KEH, which is mainly due to the absence of reliable and handful predictive models of the air damping at large motion amplitude.

2.4.6 Performance with wideband Gaussian noise

The device was excited under a wideband colored Gaussian noise (with the autocorrelation time of 1 ms). Figure 2.10 shows the Power-Spectrum Density (PSD) of the input and output signals. The input signals are distributed within the frequency range of 2~450 Hz, and the power density of acceleration throughout the bandwidth is in the order of 10-2 g^2/Hz. These inputs are featured with Gaussian distributions with zero means and standard deviations of 1.7 g_{rms} and 3.6 g_{rms} respectively. The PSD functions are acquired according to the FFT spectrum of transient signals.

We can clearly see 2 major components in the PSD of the output signal. With 20 V bias and 1.7 g_{rms} input, the major components of output are 104 Hz and 208 Hz, which are the device's natural frequency and the second harmonic of the resonance respectively. The second harmonic is caused by the capacitance variation frequency doubling induced by the gap-closing interdigitated comb geometry [2]. The peak at the resonance frequency is related to an asymmetric vibration of the movable mass. With the bias of 45 V, these 2 peaks are shifted to lower frequencies of 85 Hz and 170 Hz, which is caused by the spring-softening effect of the electrostatic force. The peaks are more “rounded” with higher acceleration and higher bias voltage. A flattening of the output power PSD at high bias voltage and at high input vibration amplitude may be explained by frequent collisions on the stoppers. The force field near maximum displacement is complex: it is a superposition of the forces generated by the linear springs, the elastic beams, the air damping and the deep electrostatic potential well near the transducer electrodes. In such a configuration, it is likely that collisions on the stoppers, at high kinetic energy, may lead to chaotic behavior. Chaos produces a dithering effect: the energy of the narrow frequency bands is distributed over a large band.

With an increased rms of the Gaussian acceleration, the output power PSD is increased over the entire spectrum, while the peaks of the output voltage PSD stay approximately at the same position, only a few hertz lower. The peaks of the PSD are not as prominent as with the lower acceleration. Taking the bias of 20 V for example, the level of the "valley" in the PSD observed between the 2 peaks is 22% of the peak values with the acceleration of 3.6 g_{rms}, while the value for 1.7 g_{rms} is only 10%. This indicates a growth of bandwidth with increased acceleration, which can be explained by the effect of the nonlinearity in the system.

By comparing the output PSD under the same excitations with different bias, we also note an obvious enhancement of power with high bias voltages, especially at low frequencies, which is consistent with the frequency sweep measurements (Figure 2.9). An impressive enhancement of the PSD at low frequency for high bias voltage and high amplitude of external vibrations is observed, see the 45 V curve in Figure 2.10(d). This can be explained by the dithering effect mentioned above. Despite of a reduced PSD of the input vibrations at low frequencies, see Figure 2.10(c), the observed output PSD is close to flat over a broad frequency range, approximately from 1 to 200 Hz.

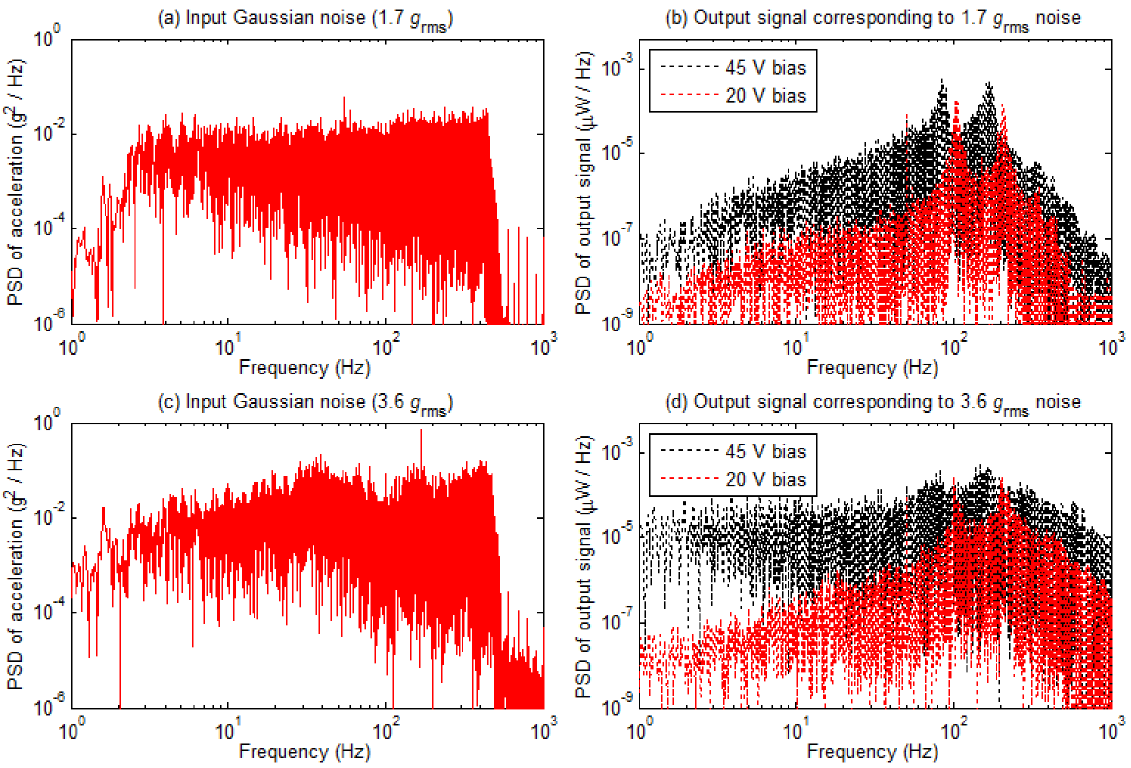

Figure 2.10: The PSD of the device output (b) and (d) to Gaussian noises with the acceleration of amplitudes 1.7 g_{rms} (a) and 3.6 g_{rms} (c) respectively, with varied bias voltage.

2.5 Performance of the complete device (with the ball)

To have an idea of the performance of the complete device, we carried out additional experiments to test it, where the device is inserted with a tungsten miniature ball with the diameter of 1.6 mm and capped by a glass top. To achieve a predictive model for the full KEH with the ball, the current model should be developed and improved: new features should be added to the model, including the squeeze-film air damping effect and the impacts on the ball.

2.5.1 Power vs. frequency

Figure 2.11 shows the $P-f$ measurement of the complete device, where the acceleration vary from 0.5 to 2.0 g_{rms} and varied external bias voltage. The presence of the ball almost eliminates the hysteresis. Also, an important enhancement of the output power is observed, while the effective useful bandwidths are expanded, mostly toward the lower frequency. Shown in Figure 2.11 are the power of the device and the theoretical maximum available power with the acceleration of 0.5 g_{rms} and 2.0 g_{rms} respectively. It can be observed that with a 46 V bias and the acceleration of 2.0 g_{rms}, the average power reaches 0.6 μW at 11 Hz, and it is above 2 μW between 67 and 165 Hz with a maximum of 4.5 μW at 160 Hz. It is interesting to note that the maximal frequency for mechanical energy harvesting with ball corresponds to the start-up frequency of the device without ball in frequency down sweeping, even when the accelerations and bias voltages vary. The theoretical maximum value of average power given in [1] is also plotted in the graphs as reference. It is seen that there is still very large room for the improvement of power through optimization of the device.

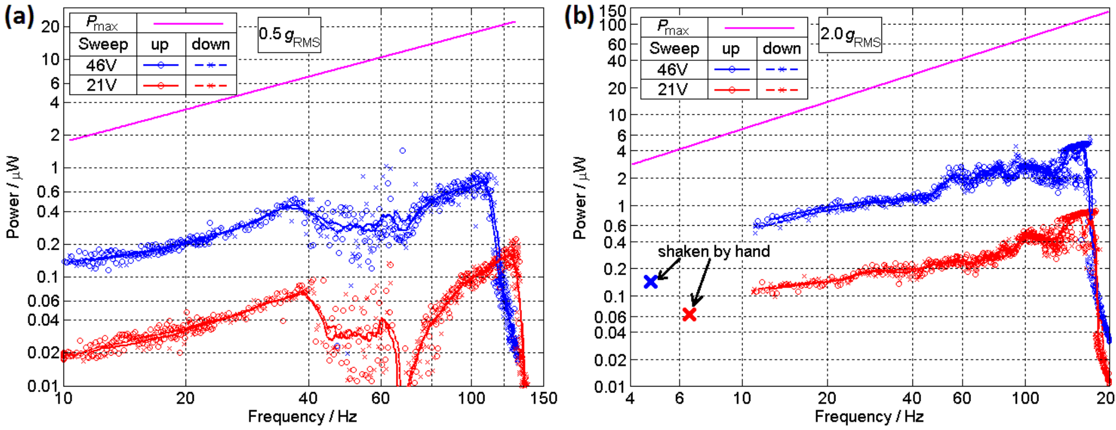

Figure 2.11: Average power versus frequency for the device with the ball for bias voltages of 21 V and 46 V at (a) 0.5 g_{rms} and (b) 2.0 g_{rms}. Theoretical maximum average power P_{max} is plotted as reference for the calculation of the effectiveness, given by $P_{\mathrm{max}} = \frac{2}{\pi} m \omega x_{\mathrm{max}} A_0$ [1], where ω stands for the angular frequency of vibration, m is the total mass of the ball and the silicon mass, x_{max} is the maximum displacement of the silicon mass, and A_0 is the peak amplitude of acceleration of external vibrations.

For an acceleration of 0.5 g_{rms}, peaks of average power arise around 40 Hz. They are due to the phase synchronization between the impact rate of the ball and that of the external excitation. In addition, a chaotic behavior shows up between 40 and 80 Hz, where we observe a frequent alternation between the interrupt and reinforcement of the vibration of the proof mass. This indicates a coupling between the motions of the proof mass and the ball by impacts. The chaos is caused by the difference between the oscillation periods of the ball and the silicon mass. A similar chaos is observed at 2.0 g_{rms} between 120 and 170 Hz. Within the frequency range of the chaos, the average power decreases significantly. With the increase of acceleration, the chaos moves towards higher frequencies. The major cause for this frequency shift is that less time is needed by the ball to travel across the cavity at increased accelerations, coinciding with higher frequency. At 0.5 g_{rms}, extra peaks can easily be identified on both sides of the chaos span. However, they merge at the acceleration of 2.0 g_{rms}.

Within the low frequency range, the correlation between the working frequency and the output power is approximately linear in a log-log coordinate. This gives an empirical formula linking the two physicals:

$$\ln P = k_a \ln f + b_a \Longleftrightarrow P = e^{b_a} f^{k_a} = P_0 f^{k_a} \tag{2.21}$$

where P and f stand for the output power and the working frequency respectively; while the coefficients k_a and b_a are coefficients in regard to the slope and the intercept of the $P - f$ curve respectively.

We notice that at low frequency where the mechanical oscillation of the proof mass is entirely triggered by the ball, the slope coefficient k_a is about 1 for moderate acceleration and bias voltage, such as 0.5 g_{rms} and 21 V. This means the correlation between the power and the frequency is nearly linear, which suggests that the amount of energy converted per cycle of external oscillation is almost constant. In other words, the vibration of the proof mass completely stops before the following knock of the ball. In contrast, with increased bias voltage or acceleration, the slope k_a is lower than 1, indicating that with the drop of frequency there is an increases of energy extracted in each period of external vibration, i.e., the vibration of the proof mass does not stop between knocks of the ball.

It is noticed that the slope coefficient k_a is about 1 in the low frequency range for moderate acceleration and bias voltage like at 0.5 g_{rms} with 21 V bias. This means that the output power grows linearly with frequency and that the energy converted per cycle stays almost constant. In contrast, when the bias voltage grows and the acceleration increase, the slopes of the curves are lower than 1, which indicates that the energy extracted within each period of vibration grows with the drop of frequency. That is to say, with both low acceleration and bias voltage, the vibration of the proof mass completely stops before the following knock by the ball. But for either higher acceleration or higher bias, the proof mass will keep vibrating from one knock to another.

Despite the fact that the device is based on micro-machined silicon structures, it is actually quite robust and durable working with accelerations up to 2 g_{rms}. The performance of the device remains the same even after hours of 2.0 g_{rms} vibrations. This high reliability is introduced by the soft impact of the elastic stoppers together with that between the ball and the silicon mass.

2.5.2 Transient output at ultra-low frequency

In order to investigate the performance of the device at ultra-low frequency below 10 Hz and to evaluate the harvested energy at each impact between the ball and the silicon mass, we test the transient output with both large amplitude and low frequency by hand shaking. The results are shown in Figure 2.12. In each period of hand shaking, the intrinsic vibration of the device is triggered for twice, corresponding to the two impacts between the ball and the mass. In the following oscillations, high and low peak values show up in turn. This means the motions of the mass and the ball are slightly asymmetric.

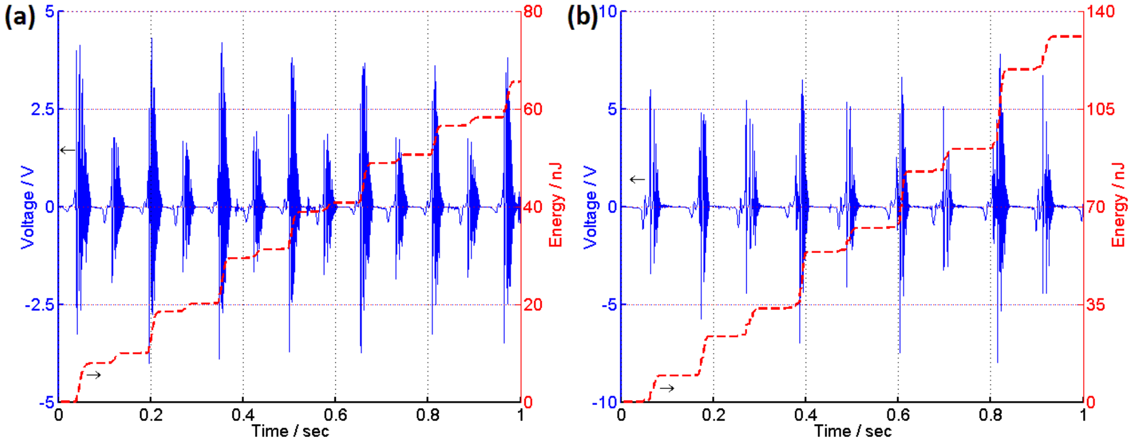

Figure 2.12: Transient output voltage and extracted energy. (a). V_{bias}=21 V, a=2.0 g_{rms}, f=6.5 Hz; (b). V_{bias}=46 V, a=2.0 g_{rms}, f=4.7 Hz.

The voltage oscillation after each knock cannot last for long (only last for 40 ms in average) due to the squeeze film damping of air between electrodes. As a result, the energy harvested after each activation is limited. Thus, when the frequency of shaking drops below $1/(2\times40\text{ ms}) = 12.5$ Hz at 2 g_{rms}, the harvested energy after each knock cannot grow any more with further drop of frequency. This explains why an obvious drop of the average power is observed below 10 Hz even though the slope coefficient k_a above 12 Hz is lower than 1. However, the oscillation can be drastically prolonged with a vacuum packaging, so that the power would be improved at frequencies below 10 Hz. Moreover, the synchronization of the external excitation with the ball impact rate depends on the cavity length. Therefore, the size of the cavity could also be optimized based on the target frequency of the input vibration.

With an increased bias between electrodes, the transient output shares the same features as mentioned above, but the harvested power is improved with the increase of bias. With the bias of 21 V (electret alone), an average power of 62.8 nW is achieved at 2.0 g_{rms} and 6.5 Hz, while with 46 V bias the power reaches 143.9 nW at 2.0 g_{rms} and 4.7 Hz. The average energy in each cycle of shaking is 9.7 nJ with 21 V bias, and 30.6 nJ per cycle with 46 V bias. The capability of the device to harvest energy at such low frequencies gives the opportunity to power biomedical devices by human movement.

2.6 Data transmission experiment (without / with the ball)

The following experiments validate a data-transmission application with the proposed energy harvester. This part of experiments is carried out in collaboration with CEA Leti. The proposed wireless temperature sensor node is powered with the e-KEH described above, the experimental setup is shown in Figure 2.13(a). An energy-autonomous Wireless Sensor Node (WSN) is made by connecting a MEMS harvester to a low-power transmitter through a conditioning circuit. The KEH is excited at a fixed frequency with a sinusoidal signal. In order to generate a DC load supply, the load resistance in Figure 1.10 was replaced by a full-wave diode bridge rectifier, which was connected to a 47-muF reservoir capacitor C_s. The output power of the device without any additional DC bias (electret alone - V_bias = 21 V) is rectified with a diode bridge, and stored in the reservoir capacitor. The capacitor is connected to a low-consumption Schmitt trigger (switch module) controlling the release of energy to a data transmission modules, i.e. a wireless temperature sensor node (including a microcontroller MSP430 from TI and a RF chip CC430 working at 868 MHz). The operation of the switch is automatically controlled by its input voltage: it reads the voltage across C_s. The switch module turns on the transmitter as soon as the voltage on the capacitor C_s reaches 3.5 V, and switches off when C_s drops below 2.5 V so as to avoid uselessly discharge C_s=47 μF, the energy released could support two data transmissions of a temperature sensor node. The current consumption of the switch module is lower than 40 nA at 3 V (only 10% of the consumption of a 10 MΩ oscilloscope probe). When the transmitter was working, the temperature sensor node was read by the microcontroller MSP430, and its data was transferred together with the chip ID within 0.16 s at RF frequency of 868 MHz to a remote receiver at a distance up to 15 m. With the proposed configuration, 102 μJ are required for a full data transmission, which corresponds to a voltage drop on C_s from 3.5 V to 2.5 V. A photograph of the experimental setup is also shown in Figure 2.13(b).

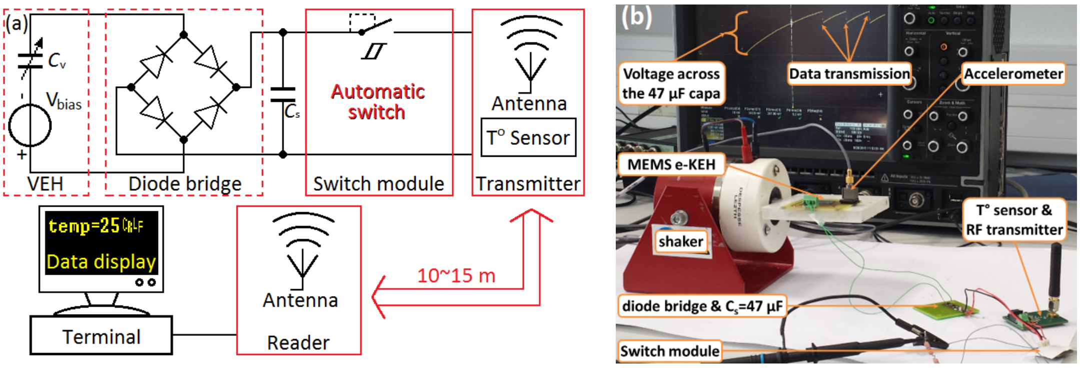

Figure 2.13: (a). Schematic and (b). photograph of the experiment of data transmission.

Figure 2.14 shows the evolution of the voltage V_s on a reservoir capacitor C_s during a charging process. Figure 2.14(a) shows the voltage evolution during a series of data transmission experiment with the KEH excited at 300 Hz with an acceleration of 2.0 g_rms. Thus, unnecessary discharge of the storage capacitor can be prevented, and the voltage on the capacitor will be kept within the range of 2.5~3.5 V after the 1st charging. The storage capacitor C_s is charged with the e-KEH prototype working . The initial voltage across C_s rises from 0 V to 3.5 V in 7.2 min. This corresponds to a stored energy of 334 μJ; then, the average harvested power stored in C_s is 0.77 μW. V_s = 3.5 V is detected by the Schmitt trigger which closes the switch (PMOS transistor) to supply the wireless sensor node. The wireless sensor wakes up, performs its temperature measurement and sends the information wirelessly. This operation occurs twice each time the sensor node is turned on. The voltage drop for a measurement and a transmission up to 10 m is 0.7 V, which corresponds to an energy consumption of 102 μJ (155 μJ for two successive measurements and RF emissions). Finally, it takes about 2 min to recharge C_s from 2.5 V to 3.5 V, which corresponds to an average harvested power of 1.27 μW. Then, a new measurement cycle (2 measures and 2 data emissions) restarts... and so on. The charging of the capacitor takes 13.8 min, where the voltage rises from 0 to 3.5 V corresponding to the initial charging of the capacitor. While the rise of voltage from 2.5 V to 3.5 V takes 4.3 min, corresponding to the following charging processes to start a new set of data transmission.

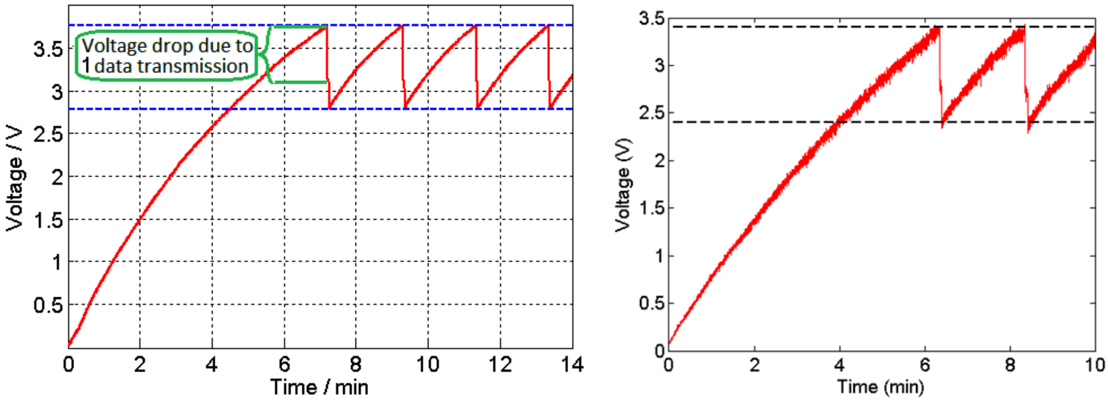

(a) Voltage evolution on C_s with the device working without the ball with an acceleration of 2.0 g_{rms} at 300 Hz.

(b) Charging and discharge curve of C_s loaded with the electronics shown in Figure 2.13(a). KEH working with the acceleration of 3 g_{rms} at 100 Hz.

Figure 2.14: Voltage evolutions of V_s on $C_s = 47$ μF when charged by the KEH without/with the ball.

2.7 Conclusion

In this chapter, we have improved the impact-coupled low frequency e-KEH previously developed by Francesco Cottone during his postdoc at ESYCOM with a corona-charged vertical electret layer. The prototype is fully characterized through experiments. We included an analytical and a numerical model of the presented prototype, which implements the impact-based frequency up conversion behavior. With the numerical model, we can predict the frequency-up conversion behavior at low frequency, but the model needs to be improved at very low frequency. Moreover, both models predict the hysteresis at high frequency range. The main difficulty in the analytical study of the device is an uncertainty of the physical models, in particular, the air damping effects and the shape of the vertical walls in the structure.

The characterization of the device consists of the determination of the optimal load resistor with varied acceleration, capacitance measurement, the measurement of built-in voltage, the investigation of power performance against the frequency sweep with various bias voltages on the electrodes, colored wideband Gaussian noise activation, and the hand shaking of the device.

- For characterizing the prototype, its capacitance variation is measured through a dynamic technique, where we found the ratio η of 4.4 (2.4 when including the parasitic capacitance from the measurement set-up). This means the device is able to work with the Bennet's doubler conditioning circuit [171]. We also observe a difference between the 2 peak values of capacitance corresponding to each single cycle of mechanical vibration, which indicates the asymmetric displacement of the proof mass.

- The internal bias of the electret is characterized by a half-wave diode bridge charging a storage capacitor. The remaining voltage of the electret after 3 weeks is 20 V, which can still be improved to 45 V (the maximum allowed voltage of the device without dynamic pull-in) by optimizing the charging process and the materials (thermal treatments, coatings, ...). The power can be further improved by increasing the surface voltage of the Parylene C electret [56].
- In the power measurement with/without the ball with frequency sweeps, we observe a wide-band behavior from a few Hz up to about 150 Hz. With the ball, a large bandwidth is observed in the tests with frequency sweeps, which is majorly due to an over-all spring-hardening hysteresis introduced by the nonlinear forces. The -3 dB bandwidth with and without hysteresis are 210 Hz and 80 Hz respectively. An increase of power is observed at high acceleration around 50 Hz, which is caused by frequency up-conversion behavior due to multiple bouncing of the mobile mass on the elastic stoppers for a single mechanical oscillation. The maximal output power provided by the device working without ball is 2.3 μW at 165 Hz before hysteresis with acceleration of 2.0 g_{peak} and the bias voltage of 46 V.
- The output power is improved at low frequency by the ball, while the bandwidth is also enlarged. The measured power of energy conversion is 6.6 μW at 2.0 g_{rms} @ 428 Hz and 1 μW at 2.0 g_{rms} @ 50 Hz. The insertion of the ball results in the improvement of maximum output power, and the broaden of the device's bandwidth, especially in the low-frequency range.
- The device has been tested below 10 Hz with hand shaking where the output voltage oscillation vanishes quickly after each impact partly due to the air damping. Therefore there is still a large margin of improvement to increase the output power of the energy harvester by reducing the air damping effect.

The device is also tested with an energy management circuit to power a UHF wireless sensor node. In order to meet the power requirements of a wireless sensor node, the energy harvested by the KEH is stored into a capacitor through a diode bridge rectifier. Then, a Schmitt trigger controls the energy stored in C_{s} and releases the energy as soon as $V_{\text{s}} = 3.5$ V to supply a low-power wireless temperature sensor node. The communication node is able to send data every 4.3 min when the KEH is placed on a 2 g_{rms} @ 130 Hz vibrating source. The 868 MHz communication node could send data beyond 10 m. A series of temperature measurements and data transmissions can be performed every 2 min, validating the whole energy harvesting chain. The average power in each recharging process is 1.27 μW, with the device shaken at 2.0 g_{rms} 300 Hz. These results show that the system has the potential of efficiently harvest kinetic energy from human-like vibrations. Hence, it is suitable for powering wireless sensors for health monitoring applications. The current model should be improved to achieve more accurate predictions: new features should be included, such as squeeze-film air damping effect and the impacts of the ball. In the following chapter, we are will introduce a more sophisticated model including these features.

Chapter 3

A predictive model of an e-KEH comprising a spring-mass resonator coupled with a free mass and considering nonlinear air damping

This chapter describes a complete model of an impact-coupled electrostatic kinetic energy harvester (e-KEH). The oscillation of the movable mass of the device is coupled by the impacts on a miniature ball and on elastic beams. The model takes all these impacts into account. In addition, it models the squeeze-film air damping effect in the gap-closing comb structure, so that the variation of damping coefficient due to different thickness of air film is described. The capacitances of the prototype in relationship with the mass displacement given by an analytic model and by finite-element method analysis are compared. The predictions given a numeric model including all the above features is compared with experimental results, showing a good consistency. The key design parameters of the KEH are analyzed with the proposed model, which can help with the design optimization.

3.1 Introduction

In the last chapter, we proposed a low-frequency KEH based on impact-coupled mechanical frequency up conversion technique, which reaches a large range of capacitance variation through an in-plane gap-closing interdigited comb structure [138]. The prototype consists of a spring-mass structure with elastic stoppers and an impact-coupled miniature ball. Two impact mechanisms are implemented: the movable mass impacting with the ball and with the stoppers. The variable capacitance of the KEH is realized by an in-plane gap-closing interdigited comb structure. The prototype is well adapted to low frequency operations thanks to the impact mechanisms, and the mass displacement reaches the upper limit (determined by the stoppers) even at low frequencies.

The air damping effect is a key factor that influence the maximum capacitance of the prototype [167], and thus very important in the prototype modeling. In the work [172], we model the air damping effect as a constant damping coefficient, which is accurate only for small displacement, and thus suitable only for low acceleration. The squeeze-film air damping force in a gap-closing comb structure increases dramatically with the size reduction of the air gap between electrodes. Thus the influence of the position of the movable electrode must be considered to achieve a more accurate model. The nonlinear air damping in MEMS KEHs is also reported to be modeled through fitting [147]. However, the models of this type are not predictive: they must rely on the post-fabrication measurements.

This paper presents a predictive and more accurate model than the previous work [167], which calculates the squeeze-film air damping force according to the size of air gap. It also takes into account the impacts within the prototype, so that the power output capacity of the prototype with a given excitation can be estimated through simulations of transient output signal. The device's capacitance variation under sinusoidal excitation is simulated against frequency sweeps, and its output power is obtained accordingly. The results given by the simulation is compared with experimental results. Parametric study is proceeded to several design parameters for performance optimization of the KEH.

3.2 KEH modeling considering nonlinear air damping

The object of the model is a gap-closing e-KEH sharing the design described in Chapter 2, and fabricated with a bulk etching technique based on an SOI wafer. The schematic and the microscopic photograph of the prototype are shown in Figure 3.1. The prototype is developed from the previous generation, inheriting the basic structure of a spring-mass system with elastic stoppers and a mini ball. In-plane gap-closing interdigited comb structure is used for the capacitive module. Unlike for standard silicon wafer, the etching of SOI wafer must be done from both sides, because the insulating layer is a stop layer for DRIE etching. The movable electrode is biased to a DC voltage through either an external voltage or a pre-charged electret. A simplified schematic of the prototype (top view) with the design parameters and variables used in the model is shown in Figure 3.2. The resonant frequency of the mass-spring system in the design is around 100 Hz. With an excitation of low frequency (below 100 Hz), the ball easily moves relative to the device case due to inertia, impacting on the movable electrode. Thus the oscillation of the movable electrode at resonant frequency (higher than the excitation frequency) is triggered, resulting in a capacitance variation of the prototype. The device is then able to generate an AC signal between its two electrodes.

The improved model is proposed to achieve better accuracy of the air damping effect, so as to facilitate the performance investigation of the device under various conditions with varied design parameters. The model is based on finite difference time domain method is developed, which takes into account the forces including the impacts and the nonlinear air damping. The calculation technique is the same as in the previous model. The device output signal is calculated according to the capacitance variation and the load in connection to the KEH (either resistive load or AC/DC rectifying module). The performance of the device can then be predicted with a

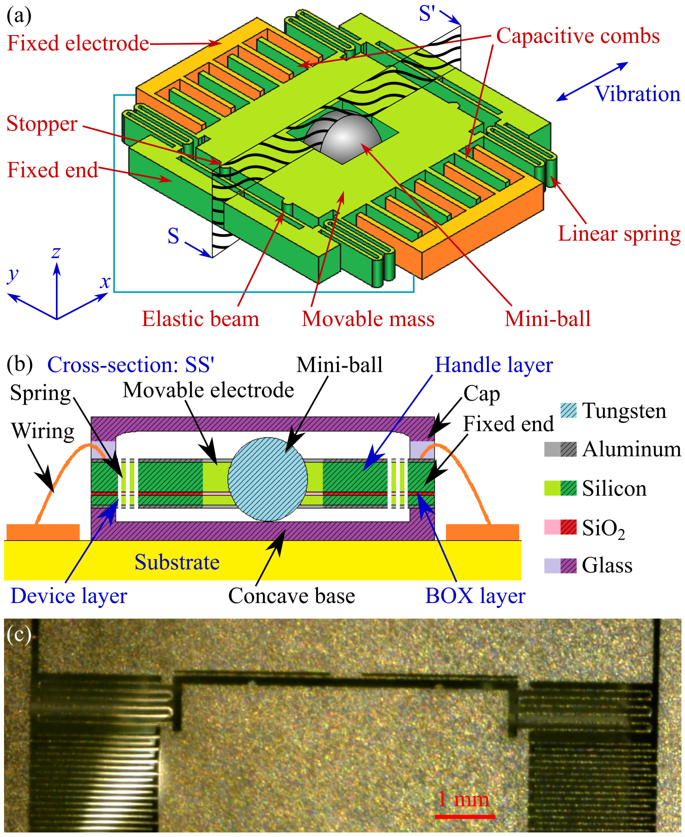

Figure 3.1: Demonstration of the impact-coupled low frequency kinetic energy harvester (a) 3D view (b) cross-section view (c) microscopic photograph.

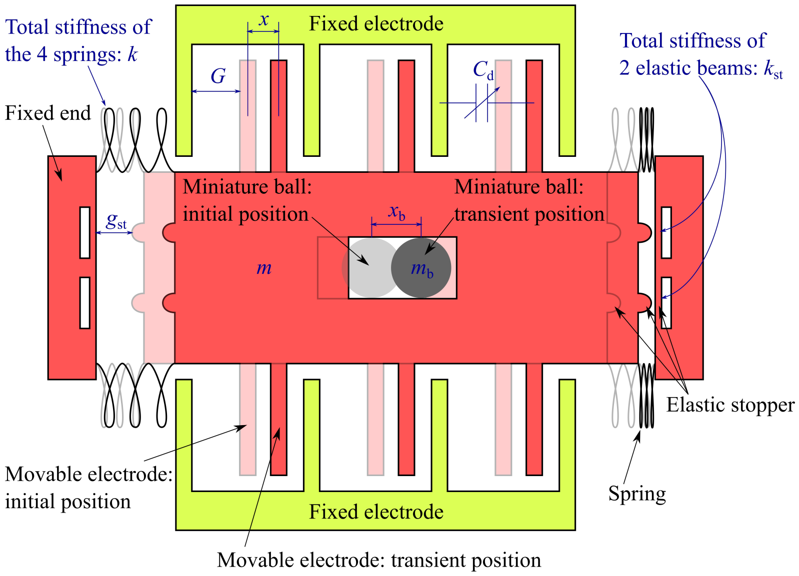

Figure 3.2: A simplified schematic of the prototype (top view) with the parameters and variables used in the model.

well-chosen time step in the transient simulation. In the improved model, the movable electrode shares the basic equations as the previous models except that the nonlinearity of squeeze-film air damping effect is considered, and that the new geometry of the wafer is taken into account.

3.2.1 Squeeze-film air damping

The air damping model is developed from the nonlinear Reynolds equation for compressible air film [169]:

$$\frac{\partial}{\partial x}\left(P\frac{h^3}{\mu}\frac{\partial P}{\partial x}\right)+\frac{\partial}{\partial y}\left(P\frac{h^3}{\mu}\frac{\partial P}{\partial y}\right)+\frac{\partial}{\partial z}\left(P\frac{h^3}{\mu}\frac{\partial P}{\partial z}\right)=12\frac{\partial\left(hP\right)}{\partial t} \tag{3.1}$$

where P is the pressure in the gas film; μ represents the coefficient of viscosity of the fluid; h is the thickness of the film; t is the time. x, y and z are the axes shown in Figure 3.1(a): x is the axis of mass displacement, y is the axis along the comb fingers, z is the thickness of the silicon wafer. Herein the inertia effect of the air and the temperature variation are neglected. For the air film between comb surfaces, the thickness (h) and viscosity coefficient (μ) are uniform everywhere. Neglecting the pressure difference along x (Hypothesis 1), Equation 3.1 is transformed into the following expression:

$$\frac{\partial}{\partial y}\left(P\frac{\partial P}{\partial y}\right)+\frac{\partial}{\partial z}\left(P\frac{\partial P}{\partial z}\right)=\frac{12\mu}{h^3}\frac{\partial\left(hP\right)}{\partial t} \tag{3.2}$$

which is also expressed as:

$$\left(\frac{\partial^2}{\partial y^2}+\frac{\partial^2}{\partial z^2}\right)P^2=\frac{24\mu}{h^3}\frac{\partial\left(hP\right)}{\partial t} \tag{3.3}$$

To simplify the equation, we assume that the pressure proceeds a small variation p around the ambient pressure P_{a} ($p \ll P_{\mathrm{a}}$, Hypothesis 2), while assuming $\frac{12\mu}{h^2P_{\mathrm{a}}}\frac{\partial p}{\partial t} \ll \Delta p$ (Hypothesis 3), equation 3.3 is finally simplified to the form:

$$\left(\frac{\partial^2}{\partial y^2}+\frac{\partial^2}{\partial z^2}\right)p=\frac{12\mu}{h^3}\frac{\partial h}{\partial t} \tag{3.4}$$

Open boundary conditions are applied for solving the differential equation 3.4:

$$\begin{cases} p|_{y=\pm\frac{L}{2}}=0 \\ p|_{z=\pm\frac{T}{2}}=0 \end{cases} \tag{3.5}$$

where L is the overlapping length of combs; T is the thickness of the wafer. Taking the boundary conditions into account, the solution of equation 3.4 has the following approximated form:

$$p=\sum_{\text{odd }k,l}a_{\mathrm{kl}}\cos\frac{k\pi y}{L}\cos\frac{l\pi z}{T} \tag{3.6}$$

where the coefficient $a_m n$ is the given by:

$$a_{\mathrm{mn}}=-\frac{48\mu}{h^3}\frac{\partial h}{\partial t}\frac{\mathrm{Sa}(\frac{m\pi}{2})\mathrm{Sa}\left(\frac{n\pi}{2}\right)}{\left(\frac{m\pi}{L}\right)^2+\left(\frac{n\pi}{T}\right)^2} \tag{3.7}$$

herein $\mathrm{Sa}(\cdot)$ is the sampling function $\mathrm{Sa}(\phi) = \frac{\sin\phi}{\phi}$. The pressure of air on the two sides of each comb is:

$$\begin{cases} p_1 = \dfrac{48\mu\dot{x}}{(G-x)^3} \displaystyle\sum_{\text{odd } k,l} \dfrac{\mathrm{Sa}\left(\frac{k\pi}{2}\right)\mathrm{Sa}\left(\frac{l\pi}{2}\right)\cos\frac{k\pi y}{L}\cos\frac{l\pi z}{T}}{\left(\frac{k\pi}{L}\right)^2 + \left(\frac{l\pi}{T}\right)^2} \\ p_2 = -\dfrac{48\mu\dot{x}}{(G-x)^3} \displaystyle\sum_{\text{odd } k,l} \dfrac{\mathrm{Sa}\left(\frac{k\pi}{2}\right)\mathrm{Sa}\left(\frac{l\pi}{2}\right)\cos\frac{k\pi y}{L}\cos\frac{l\pi z}{T}}{\left(\frac{k\pi}{L}\right)^2 + \left(\frac{l\pi}{T}\right)^2} \end{cases} \tag{3.8}$$

The total air damping force acting on the movable mass is obtained:

$$F_{\text{air}} = N_{\text{f}} \int_{-\frac{T}{2}}^{\frac{T}{2}} \int_{-\frac{L}{2}}^{\frac{L}{2}} (p_2 - p_1)\,\mathrm{d}y\mathrm{d}z = -d(x)\,\dot{x} \tag{3.9}$$

where N_{f} is the number of the comb fingers on the movable electrode, while the expression of the damping coefficient is:

$$d(x) = c\left[\frac{1}{\left(1-\frac{x}{G}\right)^3} + \frac{1}{\left(1+\frac{x}{G}\right)^3}\right] \tag{3.10}$$

herein

$$c = \frac{768}{\pi^6}\frac{\mu T L N_{\text{f}}}{G^3} \sum_{\text{odd } k,l} \frac{1}{k^2 l^2}\left(\frac{k^2}{L^2} + \frac{l^2}{T^2}\right)^{-1} \tag{3.11}$$

The distribution of normalized pressure (p_1 or p_2) on the comb (in regard to the maximum pressure on the surface) is shown in Figure 3.3(a). The maximum pressure is located at the center of the comb surface as expected. The total squeeze-film air damping coefficient of the whole device under standard atmospheric pressure is shown in Figure 3.3(b).

3.2.2 Capacitance variation

Considering the geometry of the sidewall (as shown in Figure 3.4) caused by overetching effect, the capacitance variation cannot be accurately described by the parallel-plate capacitance. The device capacitance is given by analytical calculation.

The capacitance of the SOI-wafer-based device C_{d} is given by:

$$C_{\text{d}} = C_1 + \frac{1}{\frac{1}{C_2} + \frac{1}{C_{\text{A}}} + \frac{1}{C_{\text{B}}}} \tag{3.12}$$

where C_1 and C_2 are the capacitances of the handle layer and the device layer respectively; while C_{A} and C_{B} are the capacitances of the oxide layer on electrodes A and B respectively, as shown in Figure 3.4. The calculation of C_1 and C_2 considers the tilt angle of sidewall (α, also shown in Figure 3.4) caused by the overetch during fabrication.

$$C_i = \frac{N_{\text{f}}\epsilon_0 L}{2\tan\alpha} \ln\frac{g_i^2 - x^2}{G^2 - x^2}, i = 1 \text{ or } 2 \tag{3.13}$$

where N_{f} is the number of fingers on the movable electrode; ϵ_0 is the permittivity of vacuum (air). g_1 and g_2 are the initial gaps between electrodes on the handle layer and device layer caused by

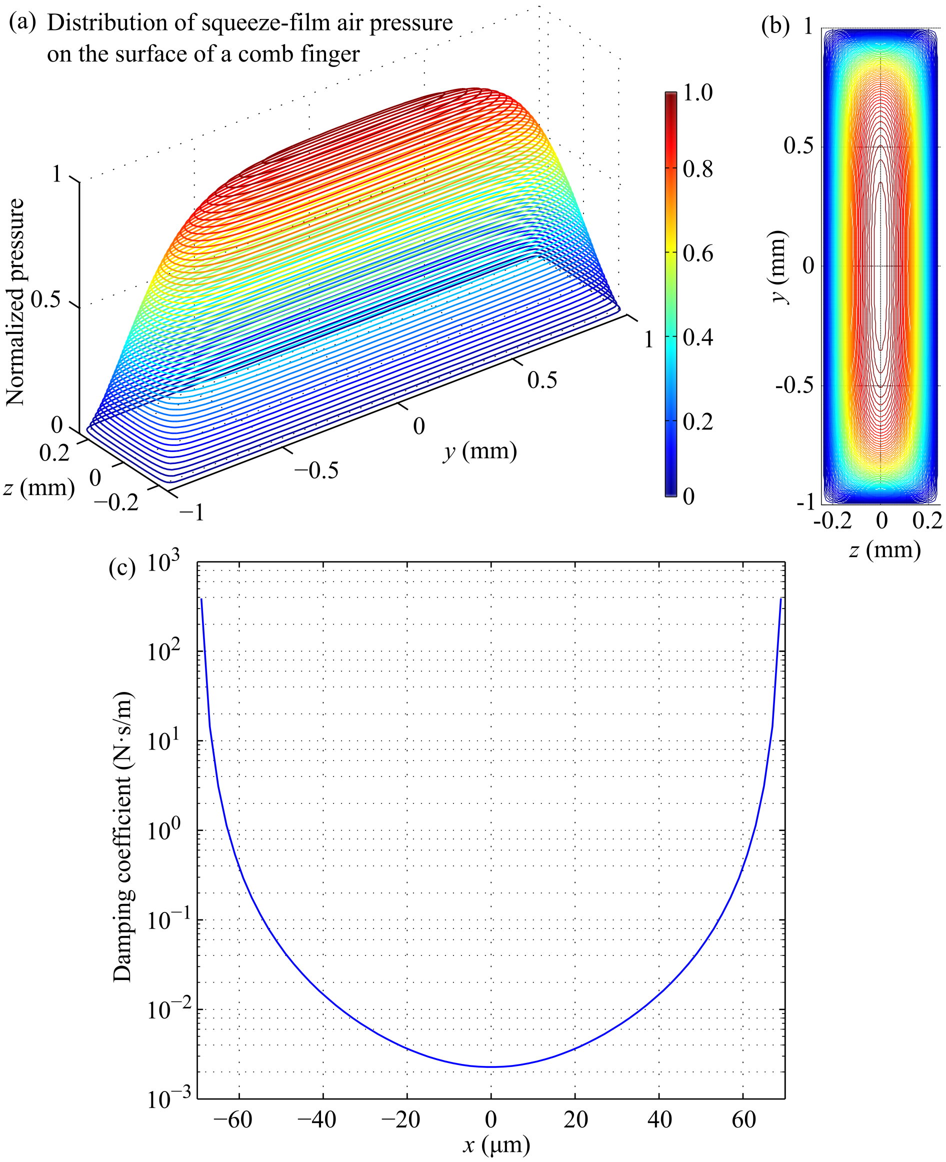

Figure 3.3: (a-b) The pressure distribution (p) on a comb surface, normalized by its maximum value, 3-D view (a) and y-z plane view (b). (c) The overall squeeze-film air damping coefficient $d(x)$ in the prototype in relation with displacement x.

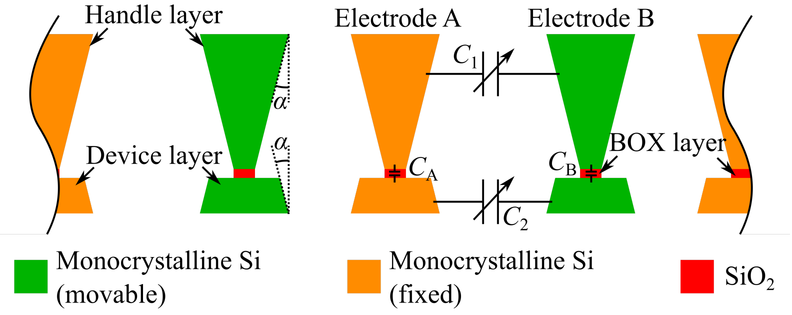

Figure 3.4: Schematic of the capacitances within the SOI-based prototype and the tilt angle of sidewall caused by the DRIE fabrication.

overetch.

$$\begin{cases} C_\mathrm{A} = \dfrac{\epsilon_0\epsilon_\mathrm{r}}{T_\mathrm{ox}S_\mathrm{A}} \\ C_\mathrm{B} = \dfrac{\epsilon_0\epsilon_\mathrm{r}}{T_\mathrm{ox}S_\mathrm{B}} \end{cases} \tag{3.14}$$

where ϵ_r is the relative permittivity of silicon dioxide; T_ox is the thickness of the oxide layer; S_A is the area of the movable electrode; while S_B is the total area of the fixed electrodes.

The result of capacitance calculation is shown in Figure 3.5.

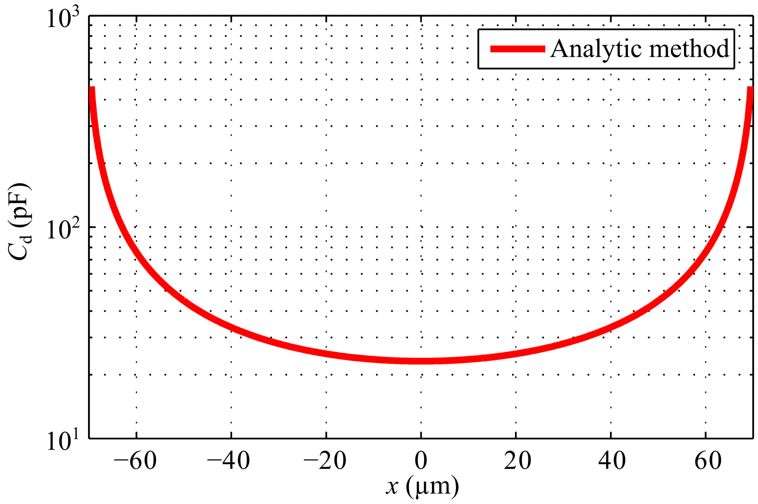

Figure 3.5: The prototype capacitance C with respect to x (analytic method). The sidewall angle $\alpha = 1.055°$ (see Section 3.3 for more details).

3.2.3 Detection of impact with the ball

In addition to the kinematic equation of the movable electrode demonstrated in Chapter 2, the kinematic equation of the miniature ball regarding the external acceleration and the friction is expressed as follows:

$$m_\mathrm{b}\ddot{x}_\mathrm{b} = -m_\mathrm{b}a_\mathrm{ext} - \mu_\mathrm{f}m_\mathrm{b}g \tag{3.15}$$

where m_b and x_b are the mass and position of the ball, μ_f is the coefficient of friction, g is gravity acceleration.

The kinematic equation of the miniature ball is valid when it does not contact with the movable electrode: $|x - x_\mathrm{b}| < \Delta X$. Here ΔX is determined by the cavity length L_cav and the size of the ball (r as radius):

$$\Delta X = \frac{L_\mathrm{cav}}{2} - r \tag{3.16}$$

The impact between the ball and the movable mass occurs between t_i and t_{i+1} if

$$\begin{cases} |x_i - x_{\mathrm{b},i}| < \Delta X \\ |x_\mathrm{pr} - x_\mathrm{b,pr}| \geq \Delta X \end{cases} \tag{3.17}$$

If impact or separation with the stopper or impact with the ball occurs during the time slot

Δt, the kinematic equations are piecewise with time and needs a higher resolution of time step to minimize the error. Similar situations also occur when the displacement of the movable mass is high, when the air damping force is strongly affected even with slight changes of position and velocity. Under these conditions, the model switches to a smaller time step $\mathrm{d}t$ to proceed a more accurate calculation.

3.2.4 Status change with impacts

According to the initial kinematic state of each continuously differentiable interval, the ending state can be deduced on the basis of the kinematic equations. At the inflection points (impacts and separations), the positions of the masses will keep the same, while the velocity changes follow the following rules. During any separations, the velocities stay unchanged:

$$\dot{x}_{\text{after sep}} = \dot{x}_{\text{before sep}} \tag{3.18}$$

where $\dot{x}_{\text{b sep}}$ and $\dot{x}_{\text{a sep}}$ are the velocity of either the movable electrode or the miniature ball before and after any separation mentioned above.

The energy loss of the movable electrode during the impact with the stoppers is modeled as a velocity reduction that occurs right at the time of the impact:

$$\dot{x}_{\text{after imp}} = c_{\text{imp}} \cdot \dot{x}_{\text{before imp}} \tag{3.19}$$

where c_{imp} is the ratio of velocity change due to the energy loss brought by the impact. The motion of the movable electrode when it contacts with the fixed electrodes is considered as an immediate velocity reverse with a certain loss of energy:

$$\dot{x}_{\text{after imp}} = -c_{\text{imp}} \cdot \dot{x}_{\text{before imp}} \tag{3.20}$$

In case that the movable electrode impacts with the fixed electrodes, the displacements corresponding to the beginning of the next time step x_{next} and $x_{\text{b next}}$ are set as:

$$\begin{cases} x_{\text{next}} = G \cdot \operatorname{Sgn}(x_{\text{pr}}) \\ x_{\text{b next}} = x_{\text{b pr}} \end{cases} \tag{3.21}$$

Because the duration of the movable electrode contacting with the fixed electrodes is much shorter than the duration it contacts with the stoppers. While the velocity change of the ball and the movable mass is also considered to occur immediately at the beginning of the contact. The velocity change follows the following rule:

$$(m\dot{x} + m_{\text{b}}\dot{x}_{\text{b}})_{\text{after imp}} = (m\dot{x} + m_{\text{b}}\dot{x}_{\text{b}})_{\text{before imp}} \tag{3.22}$$

A certain amount of energy is assumed to be dissipated when the impact occurs (inelastic collision). The velocity of the movable mass and the mini-ball are given by:

$$\begin{cases} \dot{x}_{\text{after imp}} = \left[\dfrac{C_{\text{ball}} m_{\text{b}} \left(\dot{x}_{\text{b}} - \dot{x}\right) + m\dot{x} + m_{\text{b}}\dot{x}_{\text{b}}}{m + m_{\text{b}}}\right]_{\text{before imp}} \\ \dot{x}_{\text{b,after imp}} = \left[\dfrac{C_{\text{ball}} m \left(\dot{x} - \dot{x}_{\text{b}}\right) + m\dot{x} + m_{\text{b}}\dot{x}_{\text{b}}}{m + m_{\text{b}}}\right]_{\text{before imp}} \end{cases} \tag{3.23}$$

where C_{ball} is the restitution coefficient of the impact. The kinetic energy loss during the impact is given by:

$$\Delta E = \frac{1}{2}\frac{m m_{\text{b}}}{m + m_{\text{b}}}\left(1 - C_b all^2\right)\left[\left(\dot{x} - \dot{x}_{\text{b}}\right)^2\right]_{\text{before imp}} \tag{3.24}$$

In case that the impact with the ball occurs, the displacements corresponding to the beginning of the next time step x_{next} and $x_{\text{b,next}}$ are set as:

$$\begin{cases} x_{\text{next}} = x_{\text{pr}} \\ x_{\text{b next}} = x_{\text{pr}} + \Delta X \cdot \text{Sgn}\left(x_{\text{b pr}} - x_{\text{pr}}\right) \end{cases} \tag{3.25}$$

3.3 Experimental validation of model

In order to validate the solidity of the model, comparisons between the predictions of the model and the experimental measurements with the fabricated prototype is carried out. The performance chosen for comparison is the energy conversion of the prototype during each cycle of excitation in regard to changing frequencies when the device works with an optimal resistive load.

3.3.1 Experimental setup

In the experiments, the prototype is excited by a vibrator that is controlled through a close-loop system. Accelerations with constant amplitudes and varying frequencies (linearly increasing or decreasing with time) is applied to the prototype by the vibrator. The prototype is biased by a DC voltage of 20 V, and connected to the optimal resistive load of 6.6 MΩ. The output signal across the load resistor is recorded, and the output energy during each cycle of excitation is calculated accordingly [138]. The values of acceleration tested for frequency sweeps include 0.5 g_{peak}, 1 g_{peak} and 2 g_{peak}, while the prototype is operated with and without the ball respectively.

3.3.2 Modeling parameters

The parameters in the model described in the previous section are sorted into several categories. Most parameters are physical constants that are known and unchanged, such as the permittivity of materials (ϵ_0, ϵ_{r}) and the viscosity of air (μ). Another category are the design parameters that can be determined directly by the layout or choice of components and is easy to control, such as the initial gap between electrodes (d_{init}) and the radius of the mini-ball (r). There are also parameters related to and confined by the fabrication process or experiments, such as the overetch sidewall angle (α) and the parasitic capacitance brought by the measurement electronics (C_{p}). These parameter can be determined only after a first trial of fabrication. In addition, parameters like the stiffness of elastic structures (k, k_{st}) and the mass of the movable electrode (m) are not only determined by the layout design but also affected by the overetch during fabrication. There are a few parameters (such as c_{imp}) needed to be adjusted according to the measurements proceeded on a first-trial prototype, and can be kept the same for future optimizations.

The sidewall angle can be accurately determined only by destroying the device and observing the dimensions on a cross-section cut. However, this destructive method is not preferable. A more flexible method is to achieve a good guess of the sidewall angle according to the range of capacitance variation of the device. The capacitance of the device measured using a dynamic technique introduced in [3] when the prototype is operated in vacuum with the vibration of 2 g_{peak} at resonant frequency (135 Hz). The maximum capacitance is about 450 pF, as shown in [173]. The sidewall angle α is adjusted so that $C_{\max}$ (the capacitance with maximum allowed x) matches with the experimental result. The dependent parameters are then calculated according to α. A list of key parameters used in the model is shown in Table 3.1.

Table 3.1: Parameters applied in the proposed model

Symbol	Quantity	Value
T	wafer thickness	500 μm
m	mass of movable electrode	77.5 mg
m_{b}	mass of the miniature ball	32 mg
k	total stiffness of linear springs	40.5 N/m
k_{st}	total stiffness of elastic stoppers	1.02×10^{4} N/m
G	initial gap between electrodes (defined in the mask)	70 μm
d_{st}	position of stoppers	68 μm
L	overlapping length of combs	1.97 mm
N_{c}	number of movable combs	100
L_{cav}	cavity length	3 mm
r	radius of the miniature ball	0.8 mm
c_{stop}	restitution coefficient of stoppers	1
c_{ball}	restitution coefficient of ball	0.6
α	overetch sidewall angle	1.055°
C_{p}	parasitic capacitance	28 pF

3.3.3 Predictions of the model

In order to validate the proposed model, the predictions given by the simulation using the parameters stated above is compared with experimental results. The simulation is proceeded both without and with the miniature ball under the excitation of frequency-sweeping accelerations. The time resolution of the simulation is 20 μs / 2 μs, while the size of the time series for simulation has up to 8×10^{6} elements. Series of accelerations with linearly changing frequency are generated with amplitudes 0.5 g_{peak}, 1 g_{peak} and 2 g_{peak} respectively as for the experiments, corresponding to the sweeping rate of about 1 Hz/s. The frequency sweeps from 10 Hz up to 170 Hz. The predictions of the model are compared with the experimental results, as shown in Figure 3.6.

All the parameters adjusted according to the measurements can be kept unchanged once determined, so the model can be considered as a predictive model. It is observed that the energy conversion performance of the device versus frequency sweeps can accurately predict by the model, either without or with the ball. The error of the prediction for the working frequency range is less than 5% of that given by the measurement. Generally speaking, the prototype is wideband either with or without the mini-ball. The mini-ball improves the energy transduction performance majorly at low frequency (<50 Hz).

The resonance frequency of the spring-mass system is about 120 Hz, which is observed from the frequency response of the device without the ball with 0.5 g_{peak} acceleration. With increased accelerations, the range of working frequency is expanded, resulting from the spring softening effect of the electrostatic force and the stiffening effect of the elastic stoppers and the air damping. With the acceleration of 2 g_{peak}, a tiny peak of power is observed at 35 Hz in the frequency response of the prototype without ball, which results from a frequency up-conversion behavior brought by impacts on the elastic stoppers.

The insertion of mini-ball brings an additional working frequency band (below 40 Hz). This makes the device much more efficient for low frequency applications. Between the two working regions, the output power of the prototype is unstable, because within the range of 40-60 Hz, the oscillation of the movable electrode is occasionally interrupted by the ball. The power prediction is less accurate than that of the range of working frequency. With 2 g_{peak} 28 Hz excitation, for example, the energy conversion of the prototype (with ball) is predicted to be 20 nJ/cycle, and is measured as 15 nJ/cycle. This error majorly comes from the underestimation of damping during impacts between the movable electrode and the ball. Despite this, the proposed model is overall very useful for the performance evaluation in parametric studies of gap-closing prototypes suffering from large nonlinear air damping forces.

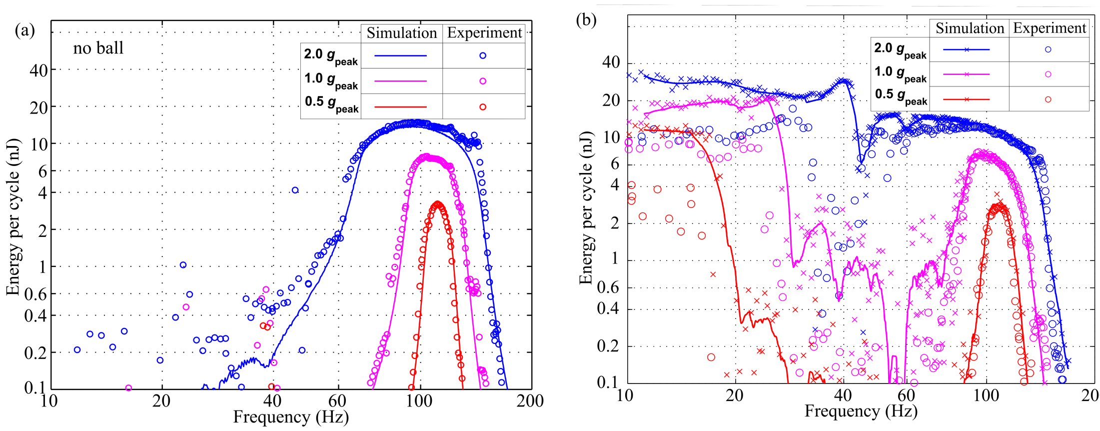

Figure 3.6: Simulated and measured output power of the prototype in air with frequency sweeps: (a) without the mini-ball; (b) with the mini-ball.

3.4 Parametric study

We carry on several parametric studies on some key design parameters.

3.4.1 Cavity length

The influence of cavity length (L_{cav}) on the prototype's frequency response is shown in Figure 3.7(a). With an increased cavity length, the mass of the movable electrode is reduced, leading to an increased resonance frequency. At the same time, the lower band in the frequency response of the prototype is shifted towards even lower frequency. The reason for this is that the time required by the ball to travel between the two ends of the cavity is longer with a longer cavity given a fixed amplitude of excitation. In summary, the two working frequency bands are separated apart by an increased cavity length and the chaotic region is enlarged.

3.4.2 Stopper position

Shown in fig 6b is the influence of the stopper position on the frequency response of the KEH. One of the major functions of the stoppers is to prevent pull-in. Another function is to bounce the movable electrode back when the external oscillation is far lower than the resonance, so that a mechanical frequency up conversion oscillation is reached. We observe that when the stopper move from $d_{\mathrm{st}} = 68\mu\mathrm{m}$ to $d_{\mathrm{st}} = 62\mu\mathrm{m}$, the output power with 1 g_{peak} acceleration between 10 Hz and 25 Hz is reduced by 67%. However, since the air damping effect is significant when the gap is small, the influence of stoppers is negligible when the minimum gap defined by the stopper is below a certain threshold. For example, the power output of the current device will be almost the same even if the stoppers are moved 2 μm apart from the movable electrode.

3.4.3 Stiffness of elastic structures

The KEH behavior with varied stiffness of elastic beams in the stoppers can be observed from Figure 3.7(c) - 3.7(d). The influence of the stiffness of the serpentine springs is obvious: by lowering this stiffness, the frequency response of the prototype is shifts downwards in the frequency domain. This is beneficial for the applications of low frequencies. However, a lower spring force also means that a smaller electrostatic force is allowed so as to avoid pull-in event.

The elastic beams are very important to keep the device from the pull-in status, because it offers an additional force against the electrostatic attraction. The influence of their stiffness to the frequency response of the KEH is negligible, as long as it is high enough to keep the movable electrode from pull-in. The reason for this is that the stoppers that can prevent pull-in are far larger than the linear springs, and the deformation of elastic beams are usually negligible. The energy loss from air damping and that from the impacts are quite huge. Technically, we tend to design elastic stoppers with high stiffness as long as they lead to low impact losses.

3.4.4 Initial gap at rest

Figure 3.7(e) shows the effects brought by a varied initial gap at rest. Provided that the initial gap at rest is smaller, its influences on the power output are generated through two routes. On the one hand, there will be room for more comb fingers which leads to a larger maximum capacitance, with positive influence on the power output. This effect is clearly observed at low frequency (below 25 Hz). On the other hand, the air damping of the KEH with more fingers is larger, confining the capacitance ratio ($\frac{C_{\mathrm{max}}}{C_{\mathrm{min}}}$) and consequently the output power at high frequency (around 100 Hz). With a small initial gap (50 μm), the electrostatic force is large, leading to a strong spring-softening effect, and expanding the resonance peak towards the low frequency (from 100 Hz to 60 Hz). If the initial gap is below 50 μm, the electrodes tend to be trapped in pull-in status due to the large electrostatic attraction.

3.4.5 Bias voltage

The power of the KEH is greatly influenced by the bias voltage between electrodes, as shown in Figure 3.7(f). With an increased bias voltage, the electrostatic force is increased, leading to a stronger spring softening effect. Thus, the resonance frequency and the range of working frequency both move downwards in the frequency domain. Furthermore, both the amount of converted energy and the efficiency are increased dramatically. However, the risks of pull-in events are growing with the increasing bias voltage: the oscillation of the movable mass is more easily stopped by the electrostatic force with low acceleration. There is no pull-in event with 20 V bias, but with 30 V bias, the device is easily interrupted by pull-in with the 1 g_{peak} acceleration. In order to compensate this disadvantage, the stiffness of the spring should be increased so as to avoid the pull-in.

3.5 Discussions

According to the parametric study of the KEH, we observe that there are cases where several design parameters affect the same variable of the device's frequency response; while some of the parameters each can affect the frequency response in several aspects. So, to enable the KEH to achieve its optimal performance, we should usually adjust several design parameters simultaneously. Several issues must be taken into account including the pull-in, the impact losses, and the overlapping parameters.

3.5.1 Pull-in

The output power of the proposed capacitive KEH is determined by the capacitance variation and the bias voltage. Both a high bias voltage and a large range of capacitance variation are preferable for maximizing the output power of the prototype. However, both these factors will give rise to a larger electrostatic force, and if the electrostatic force is overwhelming, the movable structure will be trapped in the status of pull-in. This means that the movable electrode is strongly attracted by the fixed electrodes, and cannot reach high displacement even when excited by a large acceleration. In order to avoid pull-in, the capacitance variation and the bias voltage must be confined under certain limits. With the help of the proposed model, we can easily find out these limits.

3.5.2 Impact losses

In the proposed model, we suppose that a constant percentage of energy is lost from the kinetic energy during the impact between the ball and the movable mass. This is a simple hypothesis that does not seem to be very accurate, according to the power predictions of the model at low frequency (below 25 Hz, when such impacts occur frequently). The present model is capable to predict the frequency up conversion behavior of the KEH and to indicate the change of power with various design parameters, but the level of simulated power below 25 Hz is generally about 3

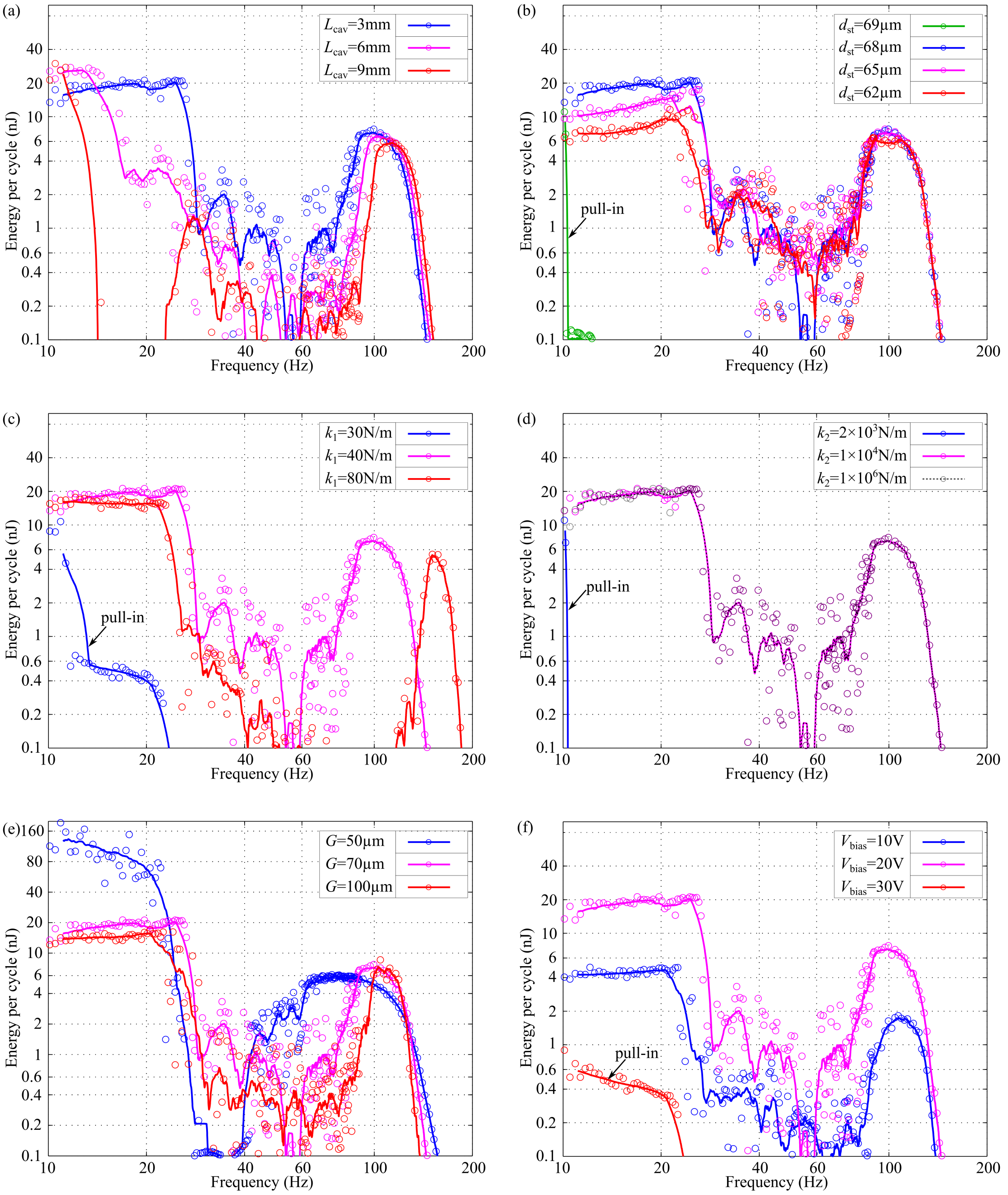

Figure 3.7: Parametric studies: influences of (a) cavity length; (b) stopper position; (c) stiffness of serpentine springs; (d) stiffness of elastic stoppers; (e) initial gap at rest; (f) bias voltage on the frequency-dependent power responses of the KEH with 1 g_{peak} acceleration.

times of the experimental measurements. To achieve a more accurate prediction at low frequency, a more sophisticated model of these impacts is needed.

3.5.3 Overlapping parameters

From Figure 3.7 we observe the influence of several parameters on the KEH's frequency response can overlap with each other. Simultaneously, the effects of changing a single design parameter include changes of the several aspects of the frequency response. For instance, the low frequency power is influenced not only by the bias voltage, but also by the initial gap between electrodes and the stopper position. While an increased cavity length results in not only a higher resonance frequency, but also a lower dropping frequency of the low frequency band. This means that if we want to adjust a single aspect of the frequency curves, we must always co-adjust several design parameters simultaneously.

3.6 Conclusion

In this chapter we propose a model that describes the frequency performance of a gap-closing kinetic energy harvester with impact-coupled mechanical frequency up conversion mechanism. The model is based on a time domain finite difference method, with adaptive time steps. It takes into account all the impacts and the thin-film air damping within the prototype, and is a fully predictive model that can be applied for the simulation of future designs.

1. The predictions of the model are validated through comparing with experimental results, showing a good consistency with the measurements. The output power around resonance frequency (100 Hz) is accurately predicted by the model, but is overestimated by the model at low frequency (below 25 Hz). This overestimation probably results from a rough model of the impact between the ball and the movable electrode. A more sophisticated model for the impact mechanism is needed to improve the accuracy.

2. Parametric study is carried out on the basis of the proposed model. The influences of different design parameters to the device's frequency response are simulated and analyzed, including the cavity length, stopper position, stiffness of the elastic structures, initial gap between electrodes, and the bias voltage. Accordingly, the basic design rules are summarized, and the optimal configuration is determined.

3. According to the parametric studies, we can conclude the following rules:

    - The stiffness of the elastic stoppers should be as high as possible, as long as it ensures low energy loss during impact.

    - A smaller initial gap between two electrodes is beneficial for increasing the low frequency power of the KEH, as long as pull-in does not take place. For the current prototype, the optimal initial gap is 50 μm.

    - A larger bias voltage, a smaller stiffness of the linear springs, and a larger initial at the stoppers are preferable, because they all lead to a larger power. However, their limit is to avoid pull-in. For the current prototype, the optimal stopper position is 68 μm; the optimal bias voltage is 20 V; while the optimal stiffness is 40 N/m.

Chapter 4

E-KEH with hierarchical capacitive structure reducing the air damping effect

In this chapter, a MEMS electrostatic kinetic energy harvester (e-KEH) working at ultralow frequency (1∼20 Hz) of about 1 cm^2 is reported. The proposed e-KEH consists of a capacitor with hierarchical combs, which greatly reduces the air damping effect, thus the capacitance variation remains important regardless of the presence of air. An enclosed miniature ball enables the oscillation of the movable electrode through impact-based frequency up-conversion mechanism. Thanks to the reduced air damping, the proposed design reaches a higher efficiency than the classic gap-closing comb structure, and has a larger bandwidth (1∼180 Hz) in air. The energy per cycle transduced by the proposed KEH is no less than 33 times higher than the classic design within 10∼40 Hz, 2 g_{peak}, while is 85 times higher @ 15 Hz, 2 g_{peak}. A maximum energy conversion of 450 nJ/cycle is obtained with the bias voltage of 45 V and the acceleration of 11 Hz, 3 g_{peak}.

4.1 Introduction

The e-KEH proposed in the last two chapters are gap-closing structures with impact-coupled frequency up conversion mechanisms with elastic stoppers [41] and a mini-ball [138]. The pull-in voltage was higher (46 V) because the impact of the ball counteracts the electrostatic force. A frequency-up conversion behavior was observed in low frequencies (below 50 Hz) [138]. Thus, the efficiency was improved, especially at low frequency: the energy converted in each cycle of excitation was 55 nJ at 2 g_{rms} 11 Hz and 30 nJ at 5 Hz. However, the air damping force in such type of KEHs with gap-closing combs was significant, limiting the frequency-up effect at low frequencies and the capacitance variation at low acceleration, and thus the output power.

We propose e-KEHs with a new hierarchical comb structure that greatly reduces the squeeze film air damping. A new process based on SOI wafers achieves a higher silicon etching aspect-ratio and a higher electrode surface area for a same device area. The converted energy per cycle of excitation with this new comb geometry is more than one order of magnitude higher than that of the previous gap-closing prototypes in air.

4.2 Device description & fabrication

The e-KEHs as shown in Figure 4.1 are developed from the prototype reported in Chapter 2. A simplified schematic of the devices is shown in Figure 4.1(a), and a cross-section view of it is shown in Figure 4.1(b). The kernel structure of the e-KEH is developed from an SOI wafer, consisting of three parts: A, B and C, each of which embodies an electrode. Parts A and C are fixed, and part B is located between A and C, containing a movable mass. The corners of the movable mass are connected to fixed ends through linear springs. The movable mass vibrates along x axis, and its displacement is limited by elastic stoppers on the two fixed ends. In the center of the movable mass, there is a cavity holding a miniature ball. The entire structure is packaged by a concave base and a cap, so that the mini-ball is maintained within the cavity. When the e-KEH is driven at any frequency, the resonant oscillation of the movable mass can be started whenever there is an impact from the ball. Thanks to the frequency-up conversion brought by the ball, the vibration can be triggered even when the excitation frequency is far lower than the natural frequency. The adjacent sides of A/B and B/C are interdigital combs, forming variable capacitors C_{AB} and C_{BC} between the electrodes. A DC bias voltage is applied on the electrode in B. While the electrodes in A and C are electrically connected with each other. Under this configuration, the vibration of the movable mass is transformed to electric energy when the capacitor is electrically charged.

Instead of applying the classic gap-closing structure in the interdigital combs, we introduce hierarchical comb structures, where arrays of hexahedral teeth are distributed equidistantly along the length of combs. The classic gap-closing comb structure is applied in the first prototype to work as a reference. Three new designs with hierarchical structure are proposed for comparison regarding the implementation of the hierarchical structure. Model T is the design where both sides of each comb are modified to hierarchical structures. In the other two configurations, each comb has the teeth array only on one side. In one configuration, the direction of teeth along X axis in capacitor C_{AB} is the same as that in capacitor C_{BC}. The prototype is mirror-symmetric and is named as Model M accordingly. In the other configuration, the directions of teeth on the movable electrode in capacitors C_{AB} and C_{BC} are opposite to each other, and is called Model R due to its rotational symmetry.

The fabrication of the proposed e-KEHs as shown in Figure 4.2 is based on SOI wafers where the thicknesses of the handle layer, the buried oxide (BOX) and the device layer are 380 μm, 2 μm and 100 μm respectively. An aluminum thin film is deposited by sputtering on both sides of the wafer, and patterned to serve as an etching mask layer. The two silicon layers are then fully etched through Deep Reactive Ion Etching. The exposed BOX layer is etched by vapor hydrogen fluoride (HF) to release the movable structure. A glass wafer is processed into a concave structure below the mobile parts through sand blasting, and anodically bonded to the device layer of the SOI wafer. The device is then deposited with a layer of Parylene C through LPCVD process (working as insulator and electret material). The movable electrode is corona charged. A miniature ball is placed in the central cavity of the movable mass, and a glass cap pre-etched by hydrofluoric acid solution is glued on top of the prototype. Eventually, the device is glued to a PCB substrate. The microscopic photographs of the 4 prototypes (before capping) are shown in Figure 4.1(d).

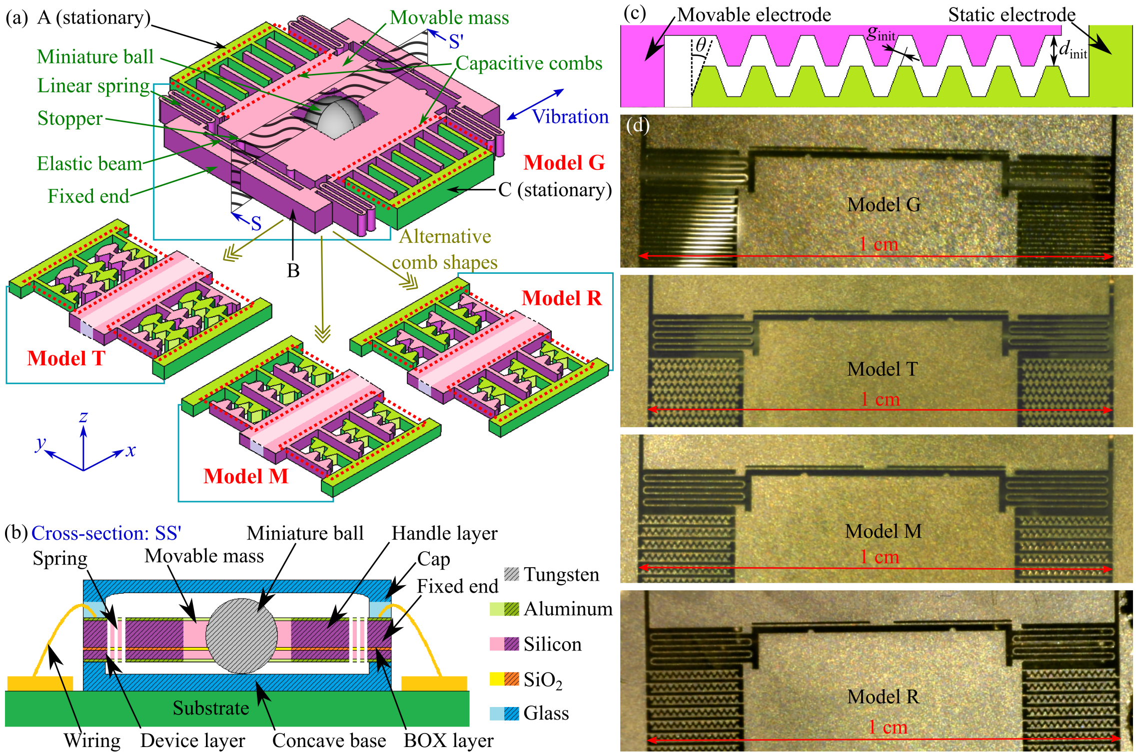

Figure 4.1: (a) Simplified 3D schematic of the kernel structure of the e-KEH; (b) View of the full device from section SS' in (a); (c) The key design parameter of the hierarchical comb structure: side angle θ of the teeth. (d) Microscopic photographs of the KEHs.

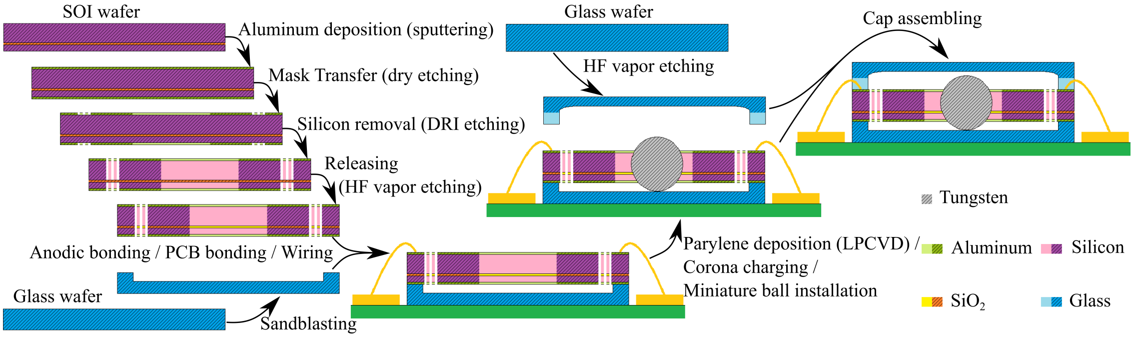

Figure 4.2: Fabrication process of the KEHs.

4.3 Optimization of comb design

A simplified top view of the hierarchical comb structure is shown in Figure 4.1(c). The initial gap between the fixed and movable electrodes along x axis in all the 4 designs are identical (d_{init}) for all the four prototypes, and the length of teeth are identical. In addition, the four prototypes all share the same design for the springs and the elastic stoppers (initial gap on the stoppers are 66 μm), while the size of the capacitive modules are all identical. The capacitances variation of each model are calculated regarding the displacement of the movable electrode x, as shown in Figure 4.3. The ratio of capacitance variation η is affected majorly by the design parameter θ, where C_{max} and C_{min} are maximum and minimum capacitance respectively. The capacitance of the four models are calculated by finite element analysis.

The C_{min} of the 4 models are roughly equivalent to each other ($C_{\text{min}} = 25$ pF). The influences of θ on C_{max} are calculated considering the constrains for layout geometry as stated above. θ is the decisive factor of the capacitance variation ($\theta_{\text{opt}} = 25.5°$). The initial gap between the teeth sides (g_{init}) are constantly 30 μm when $0° < \theta < \theta_{\text{opt}}$ and it increases with the increasing θ when $\theta_{\text{opt}} < \theta < 90°$, while the variation of the gap between teeth sides always increases with the increase of θ. As a result, the minimum gap between teeth sides decreases with an increasing θ from 0° to θ_{opt}, leading to an increasing maximum device capacitance. In addition, the bottom width of each tooth increases with θ, thus the total number of teeth that can be distributed on each comb is reduced, leading to a smaller total capacitance. Considering the large slope of C_{max} against θ when $\theta < \theta_{\text{opt}}$, we apply $\theta = 30°$ in the proposed designs, slightly larger than θ_{opt}.

The major constrains of the fabrication process for the dimensions in the mask are brought by the deep reactive ion etching process on the handle layer. To ensure the reliability of the structure and the successful release of the moving structure, the widths of both remaining structures and the etched part should be no less than 30 μm.

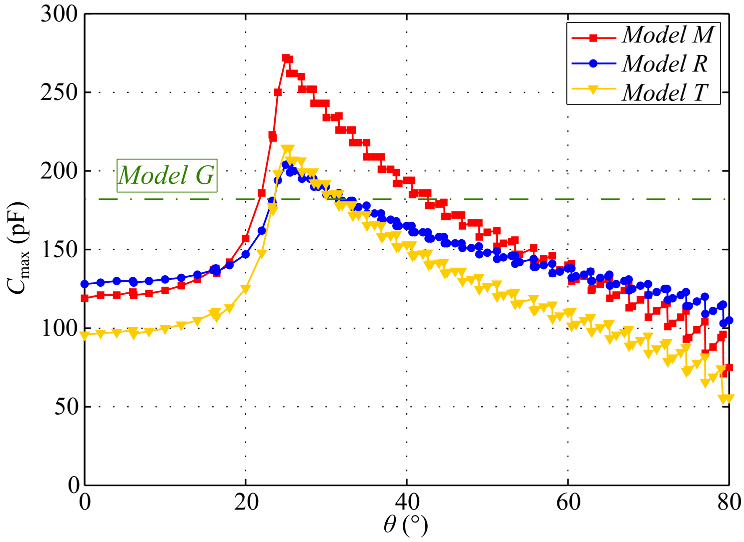

Figure 4.3: The influence of θ on C_{max} (corresponding to the displacement of 66 μm) of the 3 models with hierarchical combs (M, R & T).

4.4 Experimental setups for the KEH characterization

For the electromechanical characterization of the KEH, the schematic of the experimental setup is shown in Figures 4.4. The prototype is installed to a fixture which is connected to the moving platform of a shaker, together with measurement electronics and two accelerometers (Type 4507 B 004 from Brüel & Kjær). The vibrator is model V406 from LDS Test and Measurement, and is controlled by a PC through a feed-back signal provided by one of the accelerometers. For the measurements in air as shown in Figure 4.4(a), the fixture is a horizontal base plate, on which the prototype, the measurement electronics and the accelerometer are fixed. For vacuum measurement (Figure 2b), the KEH and the measurement electronics (including followers) are installed inside a vacuum chamber so as to minimize the parasitic capacitance; while the accelerometers are installed on the exterior of the chamber. The air pressure within the chamber is maintained to 10^{-3} mbar through a vacuum pump (Model D-35614 from pFeiffer Vacuum) during vacuum tests. Different types of pre-defined acceleration series are used to excite the vibrator, including sinusoidal signals with either single frequency or frequency sweeps, or acceleration series recorded from human motions during running or walking.

The measurement electronics are shown in Figures 4.4(c)-(e), including the circuits for capacitance measurement, AC power measurement and AC/DC power conversion respectively. The model of the amplifiers (U1 and U2) is OPA445 from Texas Instruments, while the diodes are low-leakage models PAD5 from Vishay. Up to two channels of electrical signals in the measurement circuits and the output signal of the accelerometer are recorded by a data-acquisition card USB-6366 from National Instruments, and processed by LabVIEW programs.

The capacitance measurement is performed on the four KEH devices both in air and in vacuum before corona charging, using the dynamic measuring method described in reference [3]. The KEHs are excited by single-frequency sinusoidal series of acceleration (with the amplitude of 2 g_{peak}, and the optimal frequency for each model: 135 Hz for Model G, 100 Hz for Model R, 140 Hz for Models M & T). To ensure a periodic capacitance variation, the devices are operated without the mini-ball. Each prototype is loaded with a resistor of 15 kΩ (R_{load}), and excited by a sinusoidal carrier signal of 75 kHz, 0.5 V_{peak}. The signals on the two electrodes of the KEH are recorded, and the dynamic capacitance variation is calculated according to the phase difference between the two signals. Firstly, the capacitances of the device installed on the fixtures in air and in vacuum at stationary state are obtained through dynamic measurement method respectively. The capacitance of the stand-alone stationary device is also measured by a U1732C LCR meter from Agilent. The difference between these two measurements gives the total parasitic capacitance of the fixture and the measurement electronics C_{par}. This parasitic capacitance is removed from the capacitance evolution curves measured with dynamic method before plotting.

For AC power measurement, pre-defined acceleration series with constant amplitudes (0.5 g_{peak}, 1.0 g_{peak} and 2.0 g_{peak}) and sweeping frequencies (either sweeping up or sweeping down within the range between 10 Hz and 600 Hz) are applied on the KEH by the vibrator. The sweeping rate is 1 Hz/s. The models chosen for measurement are the ones offering the maximum capacitance variation ratio either in air or in vacuum (i.e. Models G and R). The prototypes are characterized in both with and without the mini-ball, in air and in vacuum respectively. The prototype is biased by a DC voltage (varying from 20 V up to 45 V), and loaded with an optimal resistor of 6.6 MΩ.

The voltage on the resistive load is read by the data acquisition card, and the average output power corresponding to each frequency is calculated accordingly and recorded by the LabVIEW program.

In AC/DC power conversion experiment, the KEHs are biased with varied DC voltage (from 5 V to 65 V). Single-frequency sinusoidal acceleration with constant amplitude (10 Hz, 2 g_{peak}) is applied to the vibrator. The output signal of the prototype is rectified by half-wave, and the energy is stored with a reservoir capacitor $C_{\text{res}} = 1\ \mu$F. The voltage evolution with time is monitored by the data acquisition card, and recorded by LabVIEW program, and the power is calculated accordingly.

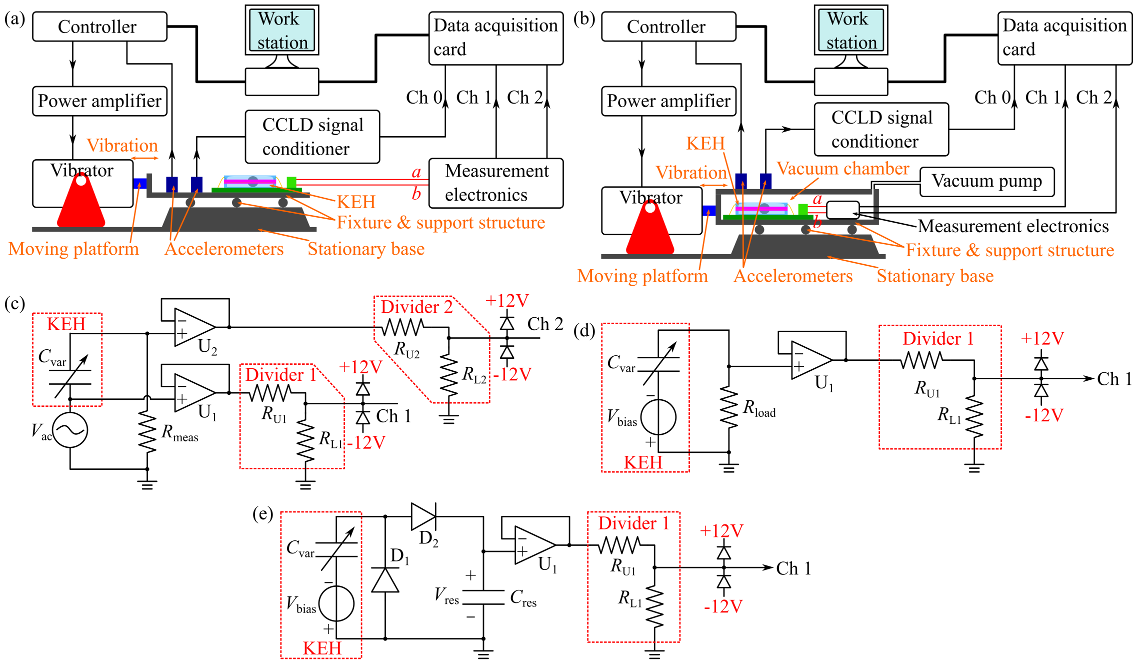

Figure 4.4: Schematic of experimental setups for the KEH characterization in air (a) and in vacuum (b); Schematics of the circuits for experiments including: dynamic capacitance measurement (c), AC power measurement with resistive load (d), AC/DC power measurement with diode bridge rectifier (e).

4.5 Experimental results

4.5.1 Capacitance variation

The capacitance variations of the four models without the ball, in air and in vacuum, under the acceleration of 2 g_{peak} and optimal frequencies, with the best performance in air and in vacuum achieved by Models R and G respectively. The transient curves are shown in Figure 4.5. The parasitic capacitance (28 pF) is removed from the measured values. It is observed that the minimum capacitances of the four models are $C_{\text{min}} = 25$ pF as predicted in the theoretical calculations. In contrast, C_{max} (the average peak capacitances) of the four models varies with the comb shapes and the maximum displacement of the movable mass, which is affected by the air damping effect. In vacuum, the air damping effect can be neglected, so that the capacitance variation ratios η of the four models agree with the theoretical calculations: Model G reaches the highest ratio ($\eta = 17.6$, $C_{\max} = 440$ pF), corresponding to the maximum displacement of 69 μm. In air (with standard pressure), the air damping force hampers the motion of the movable mass, reducing its maximum displacement. Thus, the ratio η for each model in air is lower than that in vacuum.

The influence of air damping in Model G is the most significant among the four models: its peak capacitance in air is 130 pF, less than one third of that in vacuum, corresponding to a displacement of only 64 μm. In addition, the time duration of each pulse of capacitance in air is much larger than that in vacuum, due to the hyperbolic $C(x)$ function in the gap-closing comb structure, which also results from the small mass displacement caused by large damping force of air. The falling edge of the capacitance pulse is less sharper than rising edge, indicating a reduced velocity during the travel from the maximum displacement back to the balance point, which is also an evidence of the air damping effect.

The capacitance variation of Model T in air is very similar to that in vacuum ($\eta = 8$, $C_{\max} = 200$ pF), indicating that the hierarchical comb shape is advantageous in reducing the air damping effect. The approaching motion of the hierarchical combs is a combination between sliding and gap-closing motion, leading to a reduced squeeze film air damping effect, and consequently a reduced damping force. The new comb shape reduces the relative velocity between electrode facets. However, the $C_{\max}$ of Model T is limited because of a limited number of combs for the same area. The design achieving the maximum capacitance ratio in air is Model R ($\eta = 10.8$, $C_{\max} = 270$ pF), thanks to the collective effect of a larger number of combs and a reduced air damping force from the hierarchical combs. The relative difference between its peak capacitances in air and in vacuum is less than 10%.

Although the hierarchical comb structure is applied in Model M as in Models R & T, the air damping force is still significant: its average $C_{\max}$ in air (120 pF) is only 52% of that in vacuum ($C_{\max}$=230 pF). In this prototype, all the planar sides of the combs approach each other simultaneously, leading to a strong air damping force like in Model G but 50% of the time.

Table 4.1: Capacitance variation (in pF) and ratio of the 4 models measured in air / vacuum at 2 g_{peak} at optimal frequency.

	In air			In vacuum		
	$C_{\max}$	$C_{\min}$	η	$C_{\max}$	$C_{\min}$	η
Model G	130	25	5.2	440	25	17.6
Model T	200	25	8	200	25	8
Model R	270	25	10.8	290	25	11.6
Model M	120	25	4.8	230	25	9.2

$C_{\max}$ values are the means of varied peak capacitances. The parasitic capacitance is removed from the measured results.

4.5.2 Energy conversion with frequency sweeps

Figure 4.6 shows the energy converted by the models R & G without the mini-ball through frequency sweeps. The e-KEH are biased at 20 V and submitted to accelerations with varied

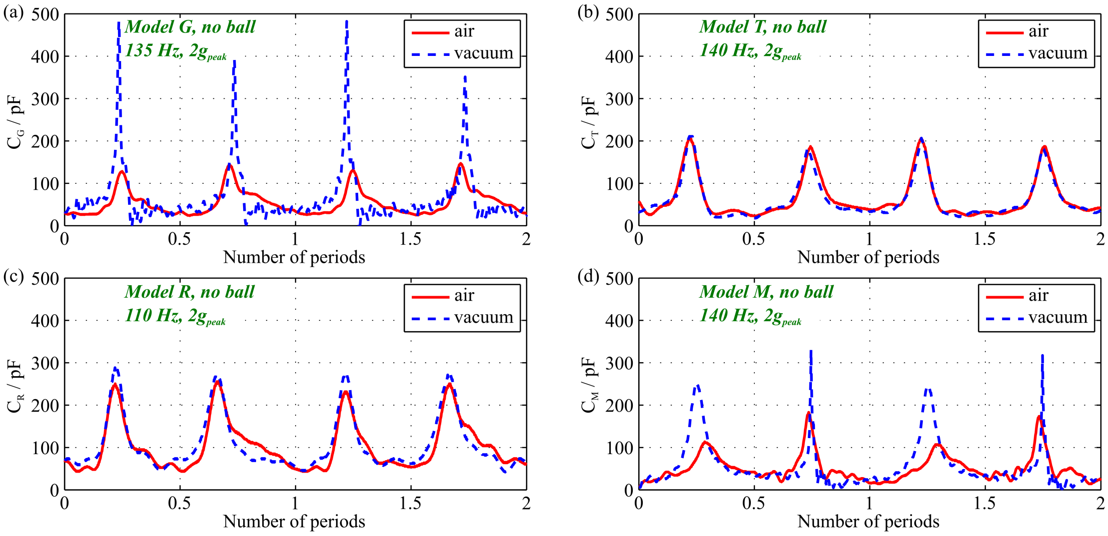

Figure 4.5: 5 Capacitance variation of the Models G, T, R & M (without DC bias voltage) without the mini-ball in air and in vacuum.

amplitudes (0.5 g_{peak}, 1 g_{peak} and 2 g_{peak}), in air and in vacuum respectively. Figure 4.7 shows the measurements when the prototypes work with the ball, sharing all the remaining conditions as for Figure 4.6. The comparison of performances without the ball show the influence of the new comb shape to the air damping effect, while with the mini-ball it demonstrates the collective effect of the new comb design and the impact with the ball. The parasitic capacitance brought by the measurement electronics (C_{par}=28 pF) cannot be excluded simply by calculation as for the dynamic capacitance measurements, so the results are underestimated. The energy per cycle shown in Figures 4.6-4.7 is obtained by dividing the output power by the excitation frequency. The discrete data points (circles and crosses) are the data obtained directly from experiments, and the lines gives the average power of adjacent frequencies.

It is observed from Figure 4.6 that Model G is relatively narrow-banded in air, and the energy conversion drops drastically when the frequency drops below certain thresholds (60 Hz for 2.0 g_{peak}, 85 Hz for 1.0 g_{peak}, 100 Hz for 0.5 g_{peak}). The maximum energy conversion is only 14.7 nJ/cycle at 95 Hz, 2 g_{peak}. In comparison, its effective frequency band is greatly expanded in vacuum and the energy conversion is improved throughout the whole working frequency range. This is particularly true at low frequency (below 60 Hz): At 20 Hz and 2 g_{peak}, the energy conversion in vacuum (20 nJ) is about 50 times of that in air (0.4 nJ). This gives an evidence about the considerable air damping effect in Model G at low frequencies.

In contrast, Model R is wide-band, even in air. An increase of energy conversion with the decrease of frequency (frequency-up conversion behavior) [172] can be easily observed in the entire frequency range at 2 g_{peak}, especially between 10 Hz and 40 Hz, both in air and in vacuum. This behavior takes place only when the air damping is low enough to allow high impacts on the elastic stoppers. The energy conversions with 2 g_{peak} in air and in vacuum are similar, on the contrary that with Model G, indicating again a clear reduced air damping effect. The maximum energy per cycle for Model R in air is ∼66 nJ (@ 12 Hz, 2 g_{peak}), only 14% lower than that in vacuum and about 4.5 times of that for Model G in air.

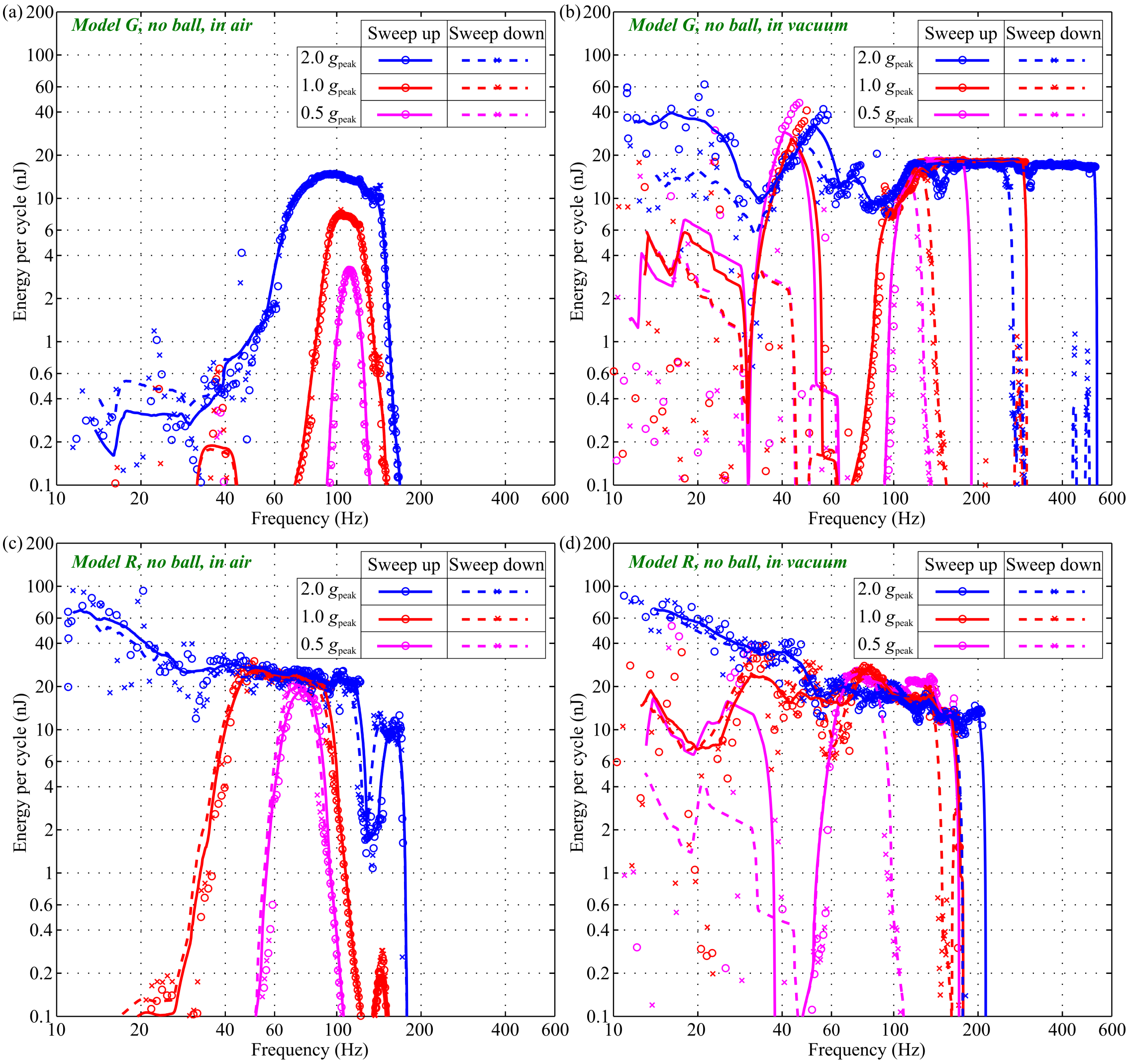

Figure 4.6: Frequency sweeps with resistive load: Energy per cycle of the Models G & R (biased at 20 V) without the mini-ball under varied acceleration: 0.5, 1.0 & 2.0 g_{peak}.

From Figure 4.7 it is observed that the insertion of the mini-ball introduces a significant additional frequency-up conversion behavior at low frequency (below 60 Hz), both in air and in vacuum. The energy conversion of Model G at 20 Hz and 2 g_{peak} is increased by 45 times, from 0.4 nJ/cycle without the ball to 18 nJ/cycle with the ball. In contrast, the power improvement of Model R at low frequency and 2 g_{peak} is less significant, because the model already has a frequency up-conversion behavior due to the impact with the flexible stoppers. However, with the insertion of the ball, the frequency up-conversion occurs at lower accelerations. The energy conversion of Model R in air reaches 12 nJ/cycle at 20 Hz, 1.0 g_{peak} with the ball (about 100 times of the one without the ball).

On the other hand, the improvement of energy conversion due to the ball is negligible in the frequency range above 60 Hz: in air, the optimal energy conversion achieved by Model G (15.2 nJ/cycle) is only 3% higher than without the ball. As for Model R, the maximum power achieved with the ball is even lower than without the ball. This is because of the interruption of vibrations brought by the impacts of the ball. In addition, the frequency hysteresis of Model G in vacuum is mostly eliminated by inserting the ball, see Figure 4.7(b), this hysteresis being negligible in air. Similar phenomenon is observed from the curves of Model R in vacuum, see Figures 4.6(d) and 4.7(d). The cause for this is that the impacts from the ball can easily interrupt the unstable vibrations in the hysteresis region.

To explore maximum energy conversion of the prototype, the bias voltage is increased to the highest (45 V). The vibrations of the combs is interrupted by pull-in when the bias is further increased. The acceleration is also pushed all the way up to maximum (3 g_{peak}). The energy conversion performance of the device under these conditions are shown in Figure 4.8. We observe that the energy conversion rate is increased by more than 4 times compared to the performance with 20 V bias, but the range of working frequency is reduced by 60% (10∼68 Hz). A maximum power of 13.2 μW is achieved at 50 Hz, 3 g_{peak}. Energy drop due to unstable oscillations is observed in the frequency range of 37∼64 Hz with 2 g_{peak} acceleration, and 63∼100 Hz for 3 g_{peak}. The highest effectiveness of 54% is achieved at the frequency of 10 Hz with 2 g_{peak} acceleration (0.33 μJ/cycle), while for the acceleration of 3 g_{peak} is 50% achieved at 12 Hz (0.45 μJ/cycle). The energy conversion with hand shaking motions below 10 Hz are also marked in the figure. 0.36 μJ/cycle is obtained with 5 Hz, 4.2 g_{rms} shaking motion. Besides the drop of acceleration, the cause for the energy decrease below 10 Hz is also related to the interruption of the mass oscillation caused by impacts between the movable electrode and the ball. The current prototype is optimized for oscillations around 10 Hz. To further reduce the optimal working frequency, the cavity length should be enlarged.

4.5.3 AC/DC transduction

Figure 4.9 shows the results of AC/DC transduction experiments where Model R is excited by a sinusoidal acceleration (2 g_{peak}, 10 Hz) in air, working with a half-wave rectifier. The influence of V_{bias} varying from 10 V to 60 V is investigated. The transient evolutions of V_{res} are shown in Figures 4.9(a), while the relation between V_{res} and the average energy conversion during each cycle of excitation is shown in Figures 4.9(b).

It is observed that the optimal energy conversion is reached with V_{bias} of 50 V and V_{res} of 12 V.

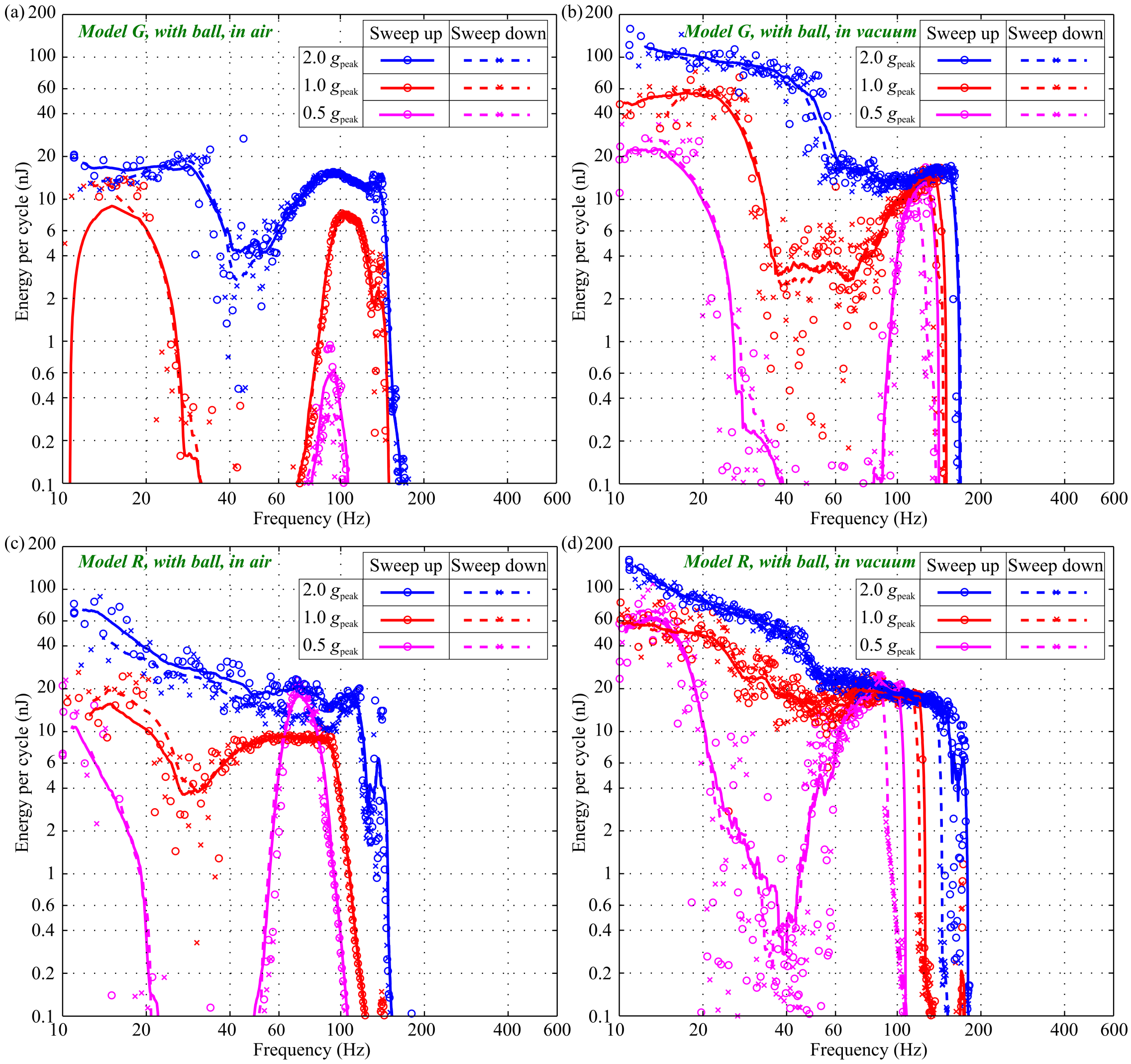

Figure 4.7: Frequency sweeps with resistive load: Energy per cycle of the Models G & R (biased at 20 V) with the mini-ball under varied acceleration: 0.5, 1.0 & 2.0 g_{peak}.

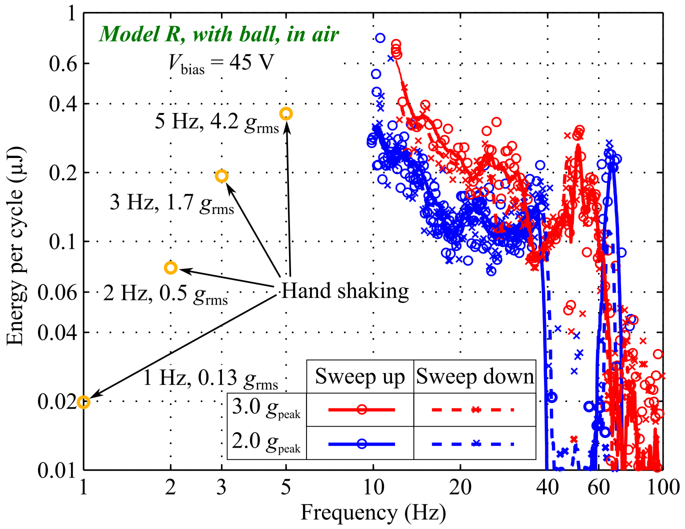

Figure 4.8: Frequency sweeps with resistive load: Energy conversion of Model R in air with frequency sweeps under the accelerations of 2 g_{peak} and 3 g_{peak}, with the maximum allowed bias voltage (45 V).

With these optimal conditions, the converted energy reaches 64.4 nJ/cycle. In each charging curve, the evolution of V_{res} firstly experiences a linear growth with time, before slowing down until a maximum energy conversion is reached. Then the voltage growth gradually approaches saturation, and the energy drops with further increase of V_{res}. This saturation comes from the half-wave diode rectifier, as demonstrated in reference [172]. With the increase of V_{bias}, the initial slope of accumulated energy per cycle vs. voltage increases, but the increment of this slope is unobtrusive when V_{bias} exceeds 30 V, with a value of 8 nJ/V. The saturation voltage and the maximum power increase with increased V_{bias} below 50 V. With a V_{bias} higher than 50 V, the energy conversion is constantly interrupted by the pull-in status of the KEH, so that the average energy conversion is less efficient.

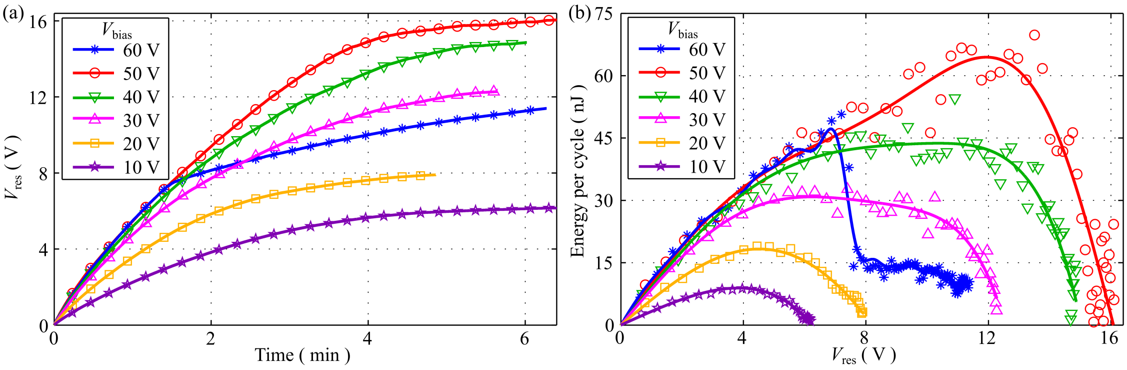

Figure 4.9: (a) Evolution of V_{res} and (b) average energy per cycle vs. V_{res} with Model R biased at varied V_{bias} (10∼60 V) working with half-wave rectifier (2 g_{peak}, 10 Hz).

4.6 Discussion

4.6.1 Dynamic capacitance measurement

In the experiment of capacitance measurement, the accuracy of the results is determined by the accuracy of phase difference between the signals on the two electrodes of the KEH. The calculation is based on the assumption that the capacitance variation is negligible within one period of the input AC signal. The accuracy drops drastically if the capacitance change fast. Moreover, a given resistor R_{meas} corresponds to a "target" capacitance, and the error of measurement grows when C_{var} moves away from the "target". In the experiments, we choose R_{meas} that makes the "target" capacitance to be right equivalent to the average of C_{max} and C_{min}, so as to minimize the error. However, the results for Model G in vacuum shown in Figure 4.5(a) still suffers of inaccuracy: the variation of capacitance is fast when the movable mass is close to the maximum displacement, while the range of capacitance variation is high. The capacitance drops to nearly zero right after each peak, which is not possible according to the device geometry. In order to get a higher accuracy, a higher frequency should be applied to the sampling signal, and the resistor should be adaptive to the capacitance variation.

4.6.2 Frequency-up conversion

In the proposed KEHs, the frequency-up conversion is initiated by impacts of the movable electrodes: either with the elastic stoppers or with the mini-ball. When the air damping is low, the movable electrode can easily reach the elastic beams to trigger the frequency-up conversion. In this case, the oscillation of the movable electrode is more likely to be interrupted than enhanced by the impacts with the mini-ball. So, the combination of the two frequency-up conversion structures does not improve the power further. The frequency-up conversion can be optimized in two aspects: The length of the cavity can be adjusted, so that the time interval between two adjacent impacts with the mini-ball is synchronized with the oscillation of the movable electrode. Moreover, we can adjust the ratio between the mass of the mini-ball and that of the movable electrode (in particular, increase this ratio for this specific design), so that the oscillation of the movable electrode is less likely to be stopped by its impact with the ball. Thus, the power of the KEHs can be boosted by both frequency-up conversion structures simultaneously with less conflict, so that we can expect a better performance from the KEHs, especially at low frequency (below 50 Hz).

4.6.3 Air damping effect

The air damping of the hierarchical comb is drastically reduced in contrast with the classical gap-closing prototype. The reason for this is the relative motion between the surfaces of the two electrodes. In gap-closing interdigital combs, the velocity of the movable electrode is perpendicular to the approaching comb surfaces, so the squeeze film air damping model should be applied [169]. In the prototypes with hierarchical combs, the motion of the teeth facets is the combination of gap-closing and sliding motions. Thus, the squeeze-film air damping model is no longer applicable, and the damping force is much smaller. A complete model of the prototypes including the air damping should be developed to facilitate further optimization.

4.6.4 Conditioning circuit

In the AC/DC transduction experiments, the half-wave diode bridge rectifiers are used because they achieve a higher energy conversion rate than full-wave diode rectifiers. This comes from the fact that at large ratio η, the area of the QV cycle is larger for a half wave rectifier than for a full wave rectifier [4], while in addition, the voltage drop of diodes in a full wave rectifier is larger than half-wave rectifier.

The optimal performance of energy conversion of the KEH biased at V_{bias}=50 V is reached when the voltage across the reservoir capacitor reaches 12 V. In the data transmission experiment, the DC working point of the KEH is far from the optimal condition: V_{res} is directly applied to the following electronics, always no higher than 3.3 V. Therefore the device is less efficient. In order to improve the performance of the KEH in DC power supply applications, the voltage on V_{res} should be adjusted to the optimal working point. Additional electronics for DC/DC voltage conversion is needed as interface

Moreover, an automatic switch [166] is needed to control the release and conservation of energy, to realize the manual operation of the mechanical switch as in the data transmission experiment. However, both the DC/DC voltage conversion interface and the automatic switch will bring additional power consumption. It is challenging to reduce the leakage current of the switch and the power consumption of the DC/DC converter, considering the high optimal reservoir voltage.

4.7 Conclusion

We have introduced three new models of MEMS-based low frequency electrostatic kinetic energy harvesters (models T, R & M), containing a hierarchical comb geometry that drastically reduce the air damping force. The design of the comb shape is optimized regarding the devices' capacitance variation. The prototypes share a unified structure with a movable electrode connected to fixed ends through linear springs, holding a mini-ball in a cavity at the center, and implementing elastic stoppers. The KEHs are based on SOI wafers and a newly developed fabrication process that offers a fabrication resolution higher than that of the previously reported work [166].

The capacitance variation of the three models with the new comb structure is compared to a prototype with classic gap-closing interdigital combs (Model G) both in air and in vacuum and without the mini-ball, so that the prototype achieving the best performance is identified. The minimum capacitance of the four models are approximately equal, so the largest maximum capacitance leads to the highest energy conversion. The performance of Model G is optimal in vacuum as predicted in the theoretical calculation, while Model R is the most efficient prototype in air, thanks to the greatly reduced air damping force. The AC power of Models G and R in air and in vacuum is measured with frequency sweeps, both with and without the mini-ball. Frequency-up conversion behavior is observed, brought by impacts either on elastic stoppers or with the mini-ball. The optimum bias voltage is 45 V, leading to the maximum available energy per cycle of Model R of 0.45 μJ, (3 g_{peak}, 12 Hz), the maximum power is 13.2 μW (3 g_{peak}, 50 Hz) and the maximum effectiveness is 54% (2 g_{peak}, 10 Hz).

The output of Model R with varied bias voltage is converted to DC voltage through a diode bridge rectifier, and the average power is calculated according to the charging curves. The optimal operation point is found to be V_{bias}=50 V, V_{res}=12 V, corresponding to the energy conversion rate of 64.4 nJ/cycle (2 g_{peak}, 10 Hz). The AC/DC converted energy of Model R is used as the power supply of an RFID tag for data transmission. The duration of each charging is 16 s (3 g_{peak}, 11 Hz). With a 3-Hz hand shaking (2 g_{peak}), the charging period is 2.2 min.

Chapter 5

Alternative improvements of low frequency e-KEHs

This chapter reports several approaches of improving various features of e-KEHs.

The first approach is a paper-based flexible e-KEH implementing multilayered electret films based on electrospun nanofibrous material. It is the first time that a fully flexible electret-based e-KEH is reported. The proposed electret, PVDF-PTFE nanofibrous covered by Parylene C, has a faster stabilization of surface potential than a planar thin film of Parylene C, and a higher stability of charge storage. With a maximum force of 0.5 N and a 3-layer electret, the device capacitance increases from 25 pF to 100 pF during a pressing operation. Working with the optimal resistive load of 16 MΩ, the device pressed manually delivers a peak instantaneous power up to 45.6 μW and an average energy of 54 nJ/stroke, corresponding to a peak instantaneous power density of 7.3 $\mu\mathrm{W} \cdot \mathrm{cm}^{-2}$ and an average energy density of 8.6 nJ$\cdot$cm^{-2}/stroke. Within 450 manual strokes, a 10-nF capacitor is charged up to 8.5 V by the prototype through a full-wave diode bridge. On a 1-μF capacitor, the energy delivery of 9.9 nJ/stroke has been obtained with a 10 Hz pressing movement excited by a vibrator with a maximum force of 0.5 N.

The second approach is a silicon-based e-KEH that can respond to the vibration along any direction within the horizontal plane. The basic structure of the prototype is developed from the device described in 1. A round-shaped movable electrode in the center is connected to fixed corners through linear springs, and is surrounded by interdigited comb fingers. Modal simulation of the prototype is proceeded, which shows that the structure is capable to work at multiple modes including transitional and rotational vibrations especially within the wafer plane, thus called a 2D prototype.

5.1 Flexible e-KEH based on electrospun nanofibrous materials

Flexible KEHs are reported in recent years, including piezoelectric [174] [175] and triboelectric KEHs [176] [177], which are applicable for wearable electronics or for installation on complex surfaces. The reported flexible KEHs work mostly in a contact-driven deformation mode. According to the literature, the typical energy conversion density of the piezoelectric KEHs is 0.1∼1 μJ·cm^{-2} per cycle [178] [179], while the triboelectric KEHs offer peak instantaneous power of 10 μW·cm^{-2} under the pressure of 30 mN·cm^{-2} [176]. However, the efficiency of these KEHs is very low considering the large pressure applied during the operation. It is thus desirable to improve their efficiency through systematic optimization.

Electrostatic KEHs can be modelled as a variable capacitor biased by an internal DC voltage, where the energy delivery during each Charge-Voltage (QV) cycle is maximized by high internal bias voltage V_{bias} and high ratio of capacitance variation [133]. Electrets are widely used sources to produce internal bias voltages in capacitive KEHs [180], and the stability of storage charge is a cardinal property of electret for its lifetime. As stated in reference [181], the charge stored in an electret are mostly confined within a superficial region with a minuscule thickness, in other words, charge trapping takes place more easily in the surface than the internal region of a material. Thus it is desirable to introduce a rough surface to the electret in order to improve the charge storage stability. Furthermore, the chemical nature of electrets is also critical to the charge stability. Firstly the material itself must be a good insulator. In addition, certain functional groups such as Benzene rings and halogen elements can help elongate the lifetime of charge storage in the material [182] [183]. The most commonly applied electret materials include fluoropolymers such as CYTOP [184], and Phenyl polymers such as Parylene C [185].

As a mature industrial technique [186], electrospinning is an inexpensive way to fabricate a variety of solvable polymers into fibrous materials with sub-micro or nano-scale dimensions [187], producing high specific surface area films. However, it is difficult to obtain stable charge storage using electrospun nanofibrous materials. Even though solvable polymers such as PET are good electret in bulk volume, the charge storage stability of electrospun nanofibers is poor [4]. Other polymers are not suitable for electrospinning process because of either low solubility (such as Parylene C) or low cure rate (such as CYTOP).

In this section, a first flexible electrostatic KEH is proposed, based on an electret made of electrospun nanofibrous scaffold covered by CVD-deposited Parylene C. The proposed electret has both a large specific area for charge storage and a better storage stability than planar Parylene C films. A high internal bias is provided by a stack of multiple electret films. The structure of the device is described and the working principle is presented. We prepare and characterize the electret material, and the characterization of the device including the capacitance variation and the power measurements is also presented.

5.1.1 Device demonstration

The device has a sandwich structure with two electrodes on top and on bottom, and stacked electret films in between, as shown in Figure 5.1(a). The 2.5 cm × 2.5 cm square-shaped electrodes are made of copper tapes sticking on paper substrates. The two electrodes are connected mechanically with tape along two parallel edges, and are insulated from each other electrically at the junction edges also by tape. A foam-like stacked electret thin film structure, working as a source of internal bias, is inserted between the two electrodes. Each layer of electret is based on electrospun nanofibrous material and is charged negatively separately beforehand. The photograph of the device is shown in Figure 5.1(b).

The device is operated in a press-and-release mode as shown in Figure 5.1(c). The two electrodes of the device form a gap-closing variable capacitor C. By applying a mechanical force on the electrodes, C will vary with the change of gap between electrodes: C_{max} is reached after pressing operation and C_{min} after releasing operation. An air gap of 1∼2 mm between the top and bottom electrode can be achieved each time the structure is released. Meanwhile, the curved shape of both electrodes can be recovered thanks to the electrodes' stiffness and the sticking to the releasing tap-body. The electric field is generated by each layer of electret film located between the electrodes, and is reinforced by stacking several films. The distribution of the electret is random, and results in an asymmetric electric field with a large probability. The electret films as a whole can be modeled as a bias voltage V_{bias} in series with the transducer variable capacitor C. Consequently, certain energy can be delivered within each QV cycle induced by the variation of capacitance C [4].

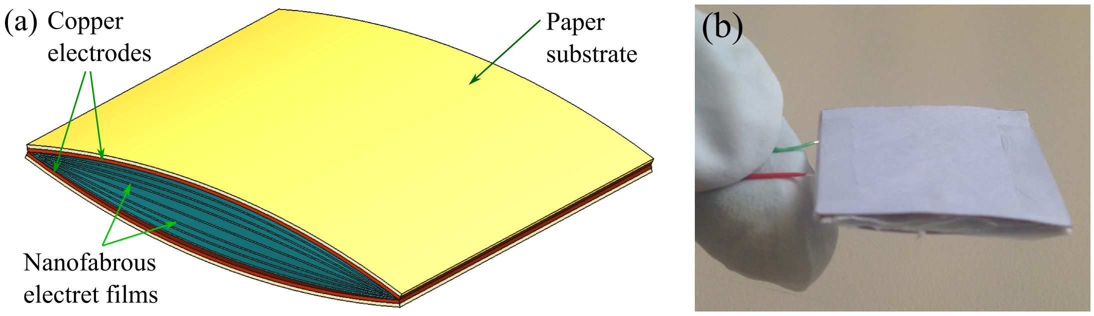

(a) Schematic of the device

(b) Photograph of the device

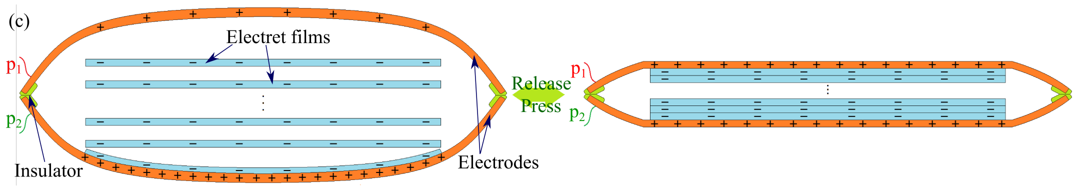

(c) Working principle

Figure 5.1: Proposed paper-based low-frequency e-KEH.

The energy converted by each QV cycle is influenced by the bias voltage and the capacitance, leading to a theoretical optimal KEH configuration. In a rectangular QV cycle as shown in Figure 5.2, the energy converted within one QV cycle is given by the following equation [4]:

$$\Delta E = 2C_{\mathrm{min}}V_{\mathrm{bias}}^{2}\left[(\eta-1)-(\eta+1)\,\eta_{\mathrm{v}}\right]\eta_{\mathrm{v}} \tag{5.1}$$

where C_{min} and C_{max} are the minimum and maximum values of C, $\eta = \frac{C_{\mathrm{max}}}{C_{\mathrm{min}}}$ is the ratio between the maximum and minimum capacitance, $\eta_{\mathrm{v}} = \frac{\Delta V}{V_{\mathrm{bias}}}$ is the ratio of voltage variation $\Delta V = V_{\mathrm{max}} - V_{\mathrm{min}}$ (shown in Figure 5.2) versus the bias voltage. The KEH can be approached as a parallel plate capacitor:

$$C = \frac{\bar{\epsilon}a^{2}}{d} \tag{5.2}$$

where $\bar{\epsilon}$ is the average dielectric constant of the material between the electrodes, a is the dimension of the side of the electrodes, d is the distance between the electrodes. Therefore, C_{max} and C_{min}

can be deduced:

$$\begin{cases} C_{\max} = \dfrac{\epsilon_{\mathrm{e}} a^2}{d_{\min}} \\ C_{\min} = \dfrac{\epsilon_{\mathrm{c}} a^2}{d_{\max}} \end{cases} \tag{5.3}$$

where ϵ_{e} is the dielectric constant of the electret films, ϵ_{c} is the equivalent dielectric constant of the combined structure of air and electret films. $d_{\min}$ and $d_{\max}$ are the minimum and maximum distance between electrodes respectively.

Considering the influence of the number of electret layers on V_{bias} and $d_{\min}$:

$$V_{\mathrm{bias}} = N V_{\mathrm{s}} \tag{5.4}$$

$$d_{\min} = N d_{\mathrm{s}} \tag{5.5}$$

where N is the number of electret layers, V_{s} is the bias voltage offered by a single electret layer, while d_{s} is the thickness of each electret film. Thus, the influence of N on ΔE is shown as follows:

$$\Delta E = \frac{2\epsilon_{\mathrm{c}} \eta_{\mathrm{v}} a^2 V_{\mathrm{s}}^2}{d_{\max}} \left[\frac{\epsilon_{\mathrm{e}} d_{\max}}{\epsilon_{\mathrm{c}} d_{\mathrm{s}}} (1 - \eta_{\mathrm{v}}) - (1 + \eta_{\mathrm{v}}) N \right] N \tag{5.6}$$

Thus we can deduce there should be an optimal number of electret films (N_{opt}) that ensures the KEH to offer the maximum output power.

The asymmetric distribution of electric field under the released status is crucial for the proposed KEH: When the KEH is pressed, the amounts of charge on top and bottom electrodes are equal. Thus, only when the charges induced on the two electrodes differ from each other at released status, can any power be transduced by the KEH. That is to say, besides V_{bias} and C, the positions of the multi-layers of electret also affect the performance of the KEH. The optimal position for the electrets is to always stick to the same electrode. However, this situation cannot be realized on the basis of the current design, because of the repulsive force between electret layers.

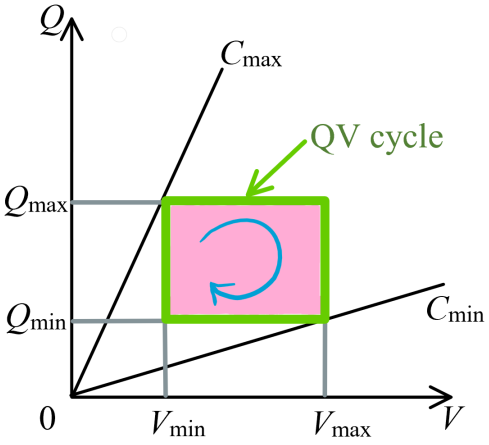

Figure 5.2: A rectangular QV cycle consisting of 2 constant voltage processes and 2 constant charge processes.

5.1.2 Material preparation

Preparation of nanofibrous electret

Firstly a nanofibrous scaffold is prepared through electrospinning method to fabricate a nanostructured basement. The solvent is a mixture of acetone and dimethylformamide (DMF), with the volume ratio of 1:1 (weight ratio of 1:1.32) at room temperature, obtained by a magnetic stirring at 60°C for 30 min. PVDF and PTFE powders are mixed with a weight ratio of 5:1 before being added to the solvent. After a continuous magneto stirring at 60°C for 24 h, a uniform solution is formed with a solute percentage of mass of 18%.

The PVDF/PTFE solution is then contained in a syringe and subjected to an electrospinning process; the schematic of the experimental setup is shown in Figure 5.3. A syringe pump controls the solution pumping rate. The injection port of the syringe is connected to high voltage, while at a distance of 15 cm from the tip of the syringe port there is a grounded planar electrode, perpendicular to the axis of the syringe and working as a receiver of nanofibrous materials. The high voltage applied is 13 kV, while the liquid is pumped with a rate of 0.7 mL/h for 2 h. The thickness of nanofibrous film is about 100 μm. The film is then peeled off from the receiver electrode, and cut to desirable shapes by scissors.

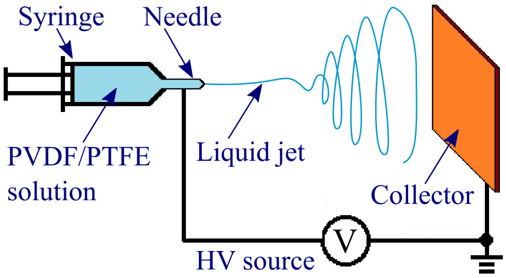

Figure 5.3: Schematic of electrospinning experimental setup.

Then, the nanofibrous films are put under a Chemical Vapor Deposition (CVD) process to coat an additional layer of Parylene C on their surface. 4 g of Parylene C is deposited in the inlet of the furnace, and this amount corresponds to a 2-μm-thick deposition on a planar structure. Figure 5.4 shows the SEM images of the microstructure of the nanofibrous film before and after Parylene C deposition. We can observe that the real thickness of deposited Parylene C on the fibers is closer to 1 μm rather than 2 μm probably due to the increased specific surface area of the nanostructure in the scaffold. It can also be perceived from the graphs that some tiny nanofibers and small cavities are engulfed by the deposited Parylene C. It can be induced that the more material is deposited, the more nanostructure is covered by the deposited material and disappear, so that the specific surface area is smaller.

Precharging

Electret films are prepared from 3 different materials through a tri-electrode corona charging process as described in [172]. The high voltage applied on the needle electrode is -12 kV, while the one applied on the grid electrode is -500 V. The samples are heated at a constant temperature of 90°C during the 30 min of the entire charging procedure. The charged materials include a Parylene

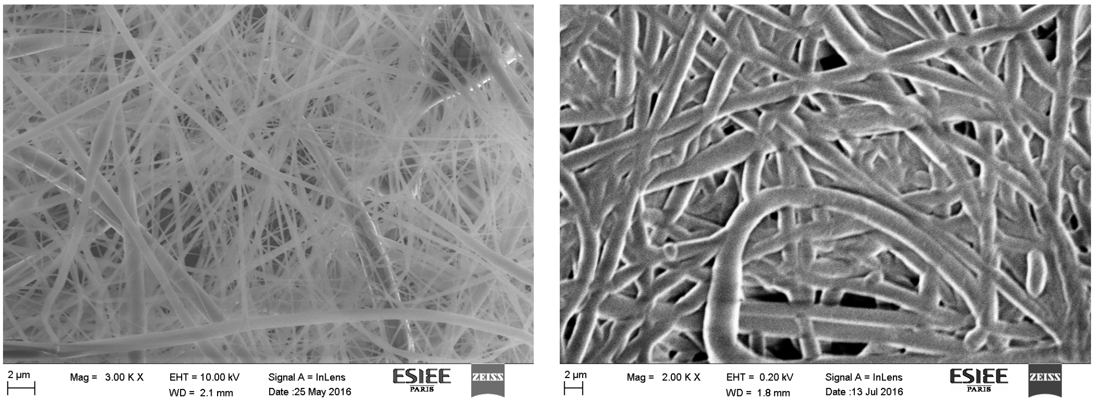

(a) Before CVD deposition of Parylene C

(b) After CVD deposition of Parylene C

Figure 5.4: SEM Photograph of the electrospun nanofiber of PVDF/PTFE.

C film of 2-μm-thick on top of a silicon substrate, a bare electrospun nanofibrous film without Parylene C, and an electrospun mat with the same weight of Parylene C as the planar material. The surface potential evolution with time after corona charging is recorded with a non-contact voltmeter TREK Model 347 and shown in Figure 5.5(a).

It is observed that the bare PVDF/PTFE nanofibers can hardly preserve any charge, thus cannot be directly used as electret. In contrast, the nanofibrous film covered with Parylene C shows a higher stability of charge storage than the planar Parylene C even though its initial surface potential is 45% lower. The surface potential of PVDF/PTFE-Parylene C film stabilizes within only 1 day, faster than the planar Parylene C film (7 days). Moreover, the ratio of the remaining surface potential to initial one of PVDF/PTFE-Parylene C film is 82%, which is higher than that of 2-μm planar Parylene C film (64%). A higher proportion of charge is preserved by the nanofiber-based electret (PVDF/PTFE-Parylene C film), probably due to a larger specific surface area. The interference between the stored charges could be miniaturized, beneficial to the long-term storage of charge. However, both the initial and the remaining surface potential of the PVDF/PTFE-Parylene C film are lower than those of the planar Parylene C film, the probable cause of which is a thickness of deposited Parylene C smaller than 2 μm in the nanofiber-based electret.

The initial surface potential of a stack of electret films with varied number of films is measured, as shown in Figure 5.5(b). Each film is first charged separately and then stacked to get the surface potential. The surface potential is linearly related to the number of stacked electret layers. This can be explained as the total electrostatic field is the summary of the field generated by each layer, considering that the surface potential of each layer are approximately identical. Biased by the stacked electret films, the equivalent internal bias of the devices V_{bias} is thus linearly proportional to the number of electret films. Consequently, we can expect an enhanced output energy per cycle by inserting an additional layer of electret due to increased V_{bias}. However, the insertion of additional electret film also gives rise to a larger minimum gap between electrodes and consequently a smaller C_{max} while keeping an unchanged C_{min} (see Section 5.1.3), leading to a decreased energy per cycle. Therefore, the optimal number of electret layers is determined by a tradeoff between V_{bias} and the capacitance ratio $\eta = \frac{C_{\text{max}}}{C_{\text{min}}}$.

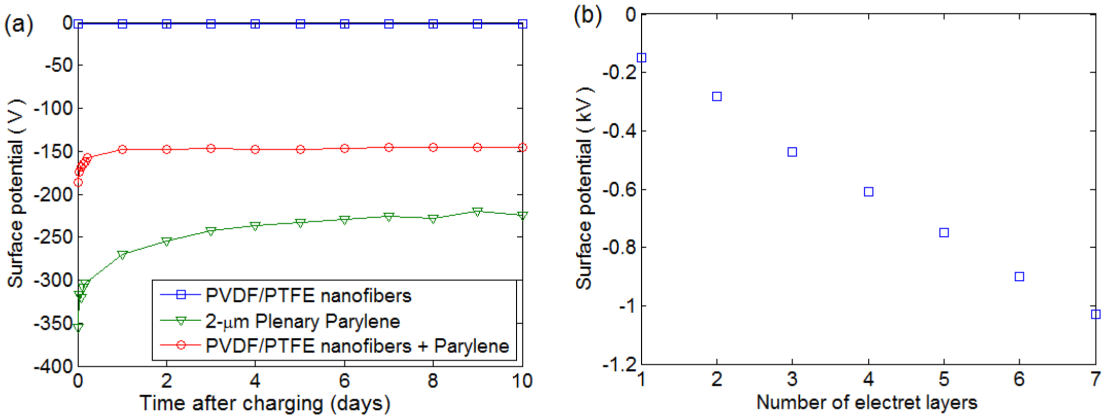

(a) Surface potential evolution of one nanofabrous film after corona charging with and without Parylene C.
(b) Initial surface potential of stacked multi-layered nanofabrous electret.

Figure 5.5: Surface potential of electret films.

5.1.3 Device performance

Capacitance variation

The capacitance variation of the KEH during a vibrator-driven operation is carried out using a dynamic measurement technique introduced in [3], the experimental setup is shown in Figure 5.6. The device is fixed on a movable plate in parallel with and at a distance from a stationary platform. The movable support is carried by a vibrator driven by a sinusoidal signal, and the device is pressed and released repeatedly through the impact and the departure between the movable support and the stationary platform. The circuit of the dynamic capacitance measurement is shown in Figure 5.6(b): a sinusoidal AC signal V_{ac} of high frequency (named as the carrier) is applied on the KEH in series with a resistor R_{ac}. Thus the signal on node b can also be approximated as sinusoid within each period of V_{ac}. The output signals of the two followers Ch1 and Ch2 are recorded by an oscilloscope. And the variable capacitance of the KEH, C_{var}, is calculated afterwards through Matlab programming according to the following equation:

$$C_{\mathrm{var}} = \frac{1}{2\pi f_{\mathrm{c}} \tan\theta R_{\mathrm{ac}}} \tag{5.7}$$

where f_{c} stands for the frequency of the carrier, and θ is the phase difference between the output signals Ch1 and Ch2, which the calculation of each point is based on 100 periods of Vac signal. The optimal load that leads to the lowest error is given by Equation 5.8.

$$(R_{\mathrm{ac}})_{\mathrm{opt}} = \frac{1}{2\pi f_{\mathrm{c}} C_{\mathrm{var,m}}} \tag{5.8}$$

where $C_{\mathrm{var,m}}$ stands for the mean value of the maximum and the minimum of C_{var}.

The excitation frequency of the device is 10 Hz. Note that although this excitation frequency is quite high for wearable electronics, it is chosen considering that the capacitance variation of the device will hardly be affected by a further frequency drop. The excitation frequency is also adapted to the functions of the used oscilloscope (memory, sampling rate, etc.) and the vibrator (displacement limit, drive limit, etc.).

The periodic force applied on the prototype is measured by a force sensor, the amplitude of which is 0.5 N. In order to adapt to the excitation frequency, the carrier frequency has been chosen as 50 kHz, i.e., 5000 sampling points in each period of excitation movement, while the error of measurement is no more than 5 pF. And the minimum and maximum capacitances of the prototype are first measured by an impedance-meter offering an initial reference for choosing the optimal resistance for measurement. The parasitic capacitance of measurement setup (28 pF) is subtracted from the total measured capacitance [172].

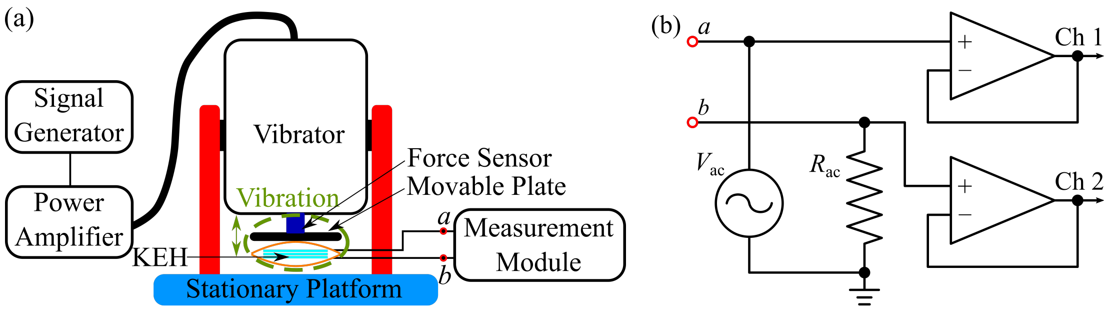

Figure 5.6: Experimental setup for the dynamic capacitance measurement: (a) excitation system for the proposed KEH; (b) circuit of measurement module for dynamic capacitance measurement, where nodes a and b are connected to the KEH.

The transient capacitance variation during one excitation period is shown in Figure 5.7(a), where each curve describes the behavior of one electret configuration. The common behavior of devices is observed: The capacitance of the device when there is no impact stays at the lowest value of ∼25 pF. In addition, there are two separate pulses of capacitance variation in a row during each period of vibration, the amplitude of which (C_{max1}, C_{max2} respectively) are located in the areas circled by the dash lines. The first pulse is induced by the impact between the vibrator and the fixed stopper. Its time span is short (∼5 ms) due to the short duration of the impact on the springless structure. Even though the velocity of the vibrator is inversed by the impact, it will shortly be inversed again by the continuous internal force of the vibrator, resulting in a second impact. Consequently a second pulse of capacitance variation is formed. However, the velocity before the second impact is smaller than the first one, and the peak capacitance of the second pulse C_{max2} is about 10 pF lower than C_{max1}, while the time span of the second pulse is 6 times larger (∼30 ms) than the first pulse.

Shown in Figure 5.7(b) are the two featured peak values of capacitance (C_{max1} and C_{max2}) and the minimum capacitance C_{min} of the prototype in relation with the number of electret layers. C_{min} is calculated by taking the average value of C_{var} in the period without pulses, so that the error introduced by the measurement can be minimized. According to Figure 5.7(c)(b), C_{min} is hardly influenced by the number of the electret layers as expected, due to the non-changing maximum gap between electrodes predefined by the mechanical support structure, i.e., the insulating tape connecting the two electrodes. In contrast, both C_{max1} and C_{max2} decrease with an increased number of electret layers, because they are both related to the total thickness of stacked electret films.

For the configurations with 1∼3 layers of electret, although the amplitude of the second impact force is only ~1/10 of the first one. A time-dependent force variation is given by the force sensor as shown in Figure 5.7(c), in which case the KEH contains 3 electret layers. The peak amplitude of capacitance is only reduced by less than 20%. This phenomenon indicates that the device deformation driven by the pressing force is divided into two regimes. In the first regime, the deformation occurs majorly to the supporting mechanical structures of the device including the paper substrate and the insulating tape. In the second regime, the pressure further deforms the electret layers. The force needed by the first regime is far smaller than the second regime, but the gap decrease between electrodes in the first regime is more significant. Moreover, with the configuration of 4 electret films, the two capacitance pulses have the same amplitude. This indicates that the force of 0.5 N is not sufficient to drive the deformation into the second regime for this configuration.

The bouncing behavior described above only exists in the operations with vibrators, but not shared by the case with finger-tapping. In the finger-tapping operation, the capacitance variation only reaches one peak within one tap, i.e., the finger gets away from the harvester after only one impact on the electrode. This behavior can be affirmed by the transient output voltage shown in Section 5.1.3.

Power delivery with resistive loads

The transient output of the device working with just a resistive load and with different electret configurations (varied number of stacked electret layers) are tested with manual operations. In order to find the best conditions, the values of the resistive loads are varied from 1 MΩ to 100 MΩ, as shown in Figure 5.8. Both the peak voltage and the peak power are plotted in relation to the load resistance, while the power with varied electret configurations is shown as different curves. The inset plotting of Figure 5.8(a) shows the transient voltage signal on the optimal resistive load of 16 MΩ which is featured with narrow peaks having high amplitudes and small timespans. The peak values vary from one pulse to another, which is induced by the inaccuracy of manual operation. The average peak voltage is calculated for each load resistance according to the transient signals so that the error brought by manual operation can be minimized, and the average peak power is calculated accordingly.

As stated in the previous section, the performances of the prototype are affected by the number of electret layers in two senses: increasing a layer of electret in the prototype leads to a growth of V_{bias}, and also results in a larger minimum gap and consequently a smaller $C_{\max}$ and smaller ratio η. Thus, the optimal electret configuration is reached through a trade-off between these two effects, maximizing the output power. According to the measurements, the maximum peak power is achieved with a 3-layer electret, while the optimal resistive load is 16 MΩ. The average width of the pulses in the transient signals is ~30 ms. Under this optimal configuration, the peak output voltage is 27 V; the peak instantaneous output power is 45.6 μW (the average power is 0.29 μW), and the average energy per tap is 53 nJ.

The average peak value of the output pulses (voltage and power) are calculated accordingly, and the variation of these values are plotted with varied load and varied number of electret layers in Figure 5.8. As shown in this inset, sharp pulses with large amplitudes and small timespan are generated repetitively with the same frequency of the excitation force.The increased number of electret layers results in an increased amount of induced charge on the electrodes. At the same time

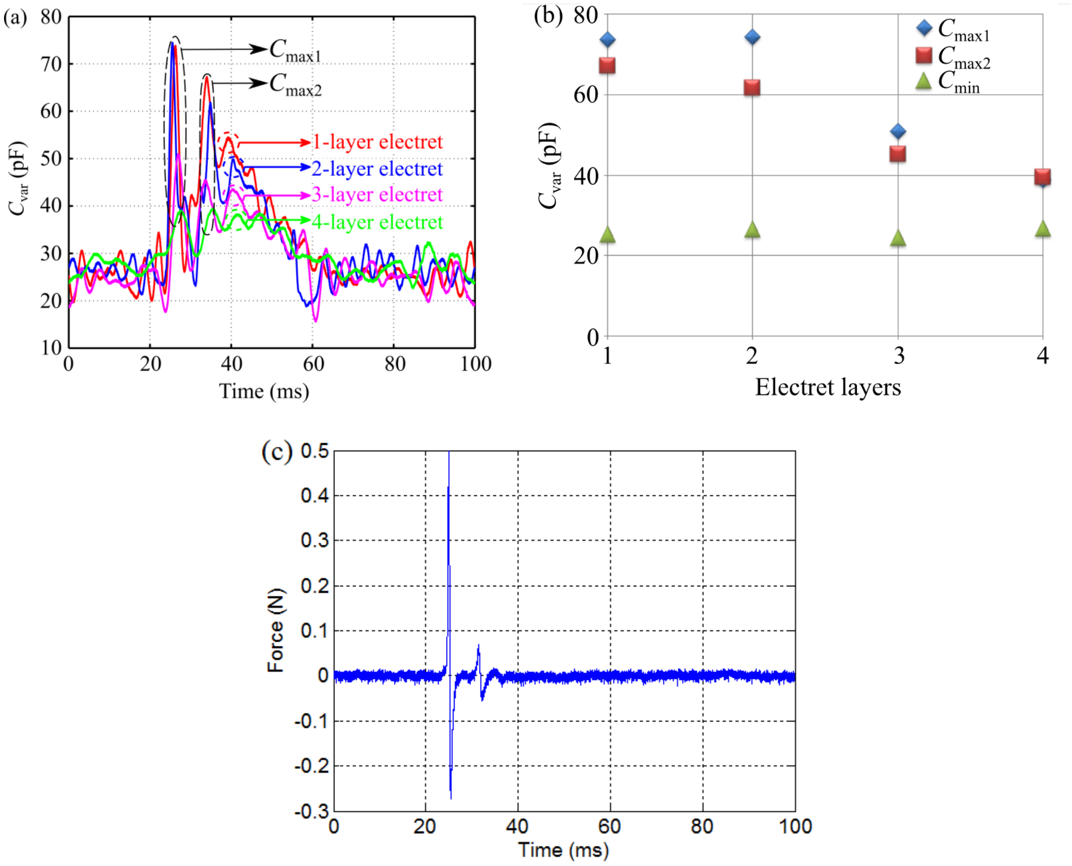

Figure 5.7: Capacitance variation of the proposed e-KEH. (a) Capacitance variation of the prototype with varied number of stacked electret films when excited by 10 Hz pressing-releasing operation (the peak force is ∼0.5 N). (b) C_{max} corresponding to the peak of two capacitance pulses (C_{max1} and C_{max2}) induced by the 10 Hz pressing movement and C_{min} of prototypes with varied number of stacked electret layers. The parasitic capacitance of 28 pF is subtracted from the total measured capacitance. (c) The force variation in one period of mechanical excitation with 3-layer electret configuration.

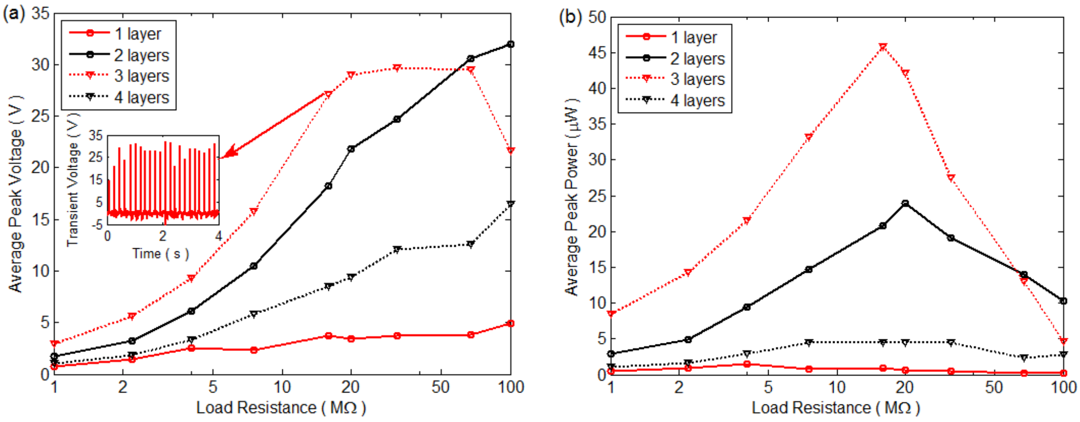

(a) Average peak voltage.

(b) Average peak power.

Figure 5.8: Average peak voltage and power of the proposed device with sweeping load resistance. The inset plot in (a) is the transient output voltage when the device is working with the optimal configuration (3 layers of thin film electret, with the load of 16 MΩ), corresponding to the peak power of 45.6 μW.

the maximum capacitance is reduced due to a larger gap between electrodes while the minimum capacitance is kept approximately the same. Therefore, there is an optimal number of electret layers. By pressing and releasing the device with finger, we get the average peak voltage of 27 V with the load of 16 MΩ and 3 layers of electret material (optimal condition), corresponding to the optimal instantaneous output power of 45.6 μW.

Power delivery with a full-wave diode bridge

In order to evaluate the DC power delivery capability of the best prototype, the device is tested in cooperation with a full-wave diode bridge rectifying circuit. In the first experiment, the KEH is driven manually (under the same excitation conditions as in Section 5.1.3) and works in cooperation with a full-wave rectifier, the results are shown in Figure 5.9. A reservoir capacitor C_{res}=10 nF is charged up to 8.2 V within 210 finger taps on the device with a frequency of ~4 Hz. The evolution of V_{res}, the voltage accross C_{res}, is shown in Figure 5.9(a).

Shown in Figure 5.9(b) is the evolution of the energy conserved in C_{res} per cycle of excitation and the total energy in C_{res}. The energy converted within each charging cycle can be calculated accordingly. The total energy accumulated during the entire charging process is 0.34 μJ (210 taps in total), corresponding to an average energy of 1.6 nJ/tap. While the maximum energy delivery is reached when V_{res} is about 3.5 V and is equal to 1.95 nJ/cycle, corresponding to an optimal power of 11.7 nW (Figure 5.9c) This power is far less than that with the optimal resistive load (the average power 0.29 μW and the peak instantaneous power of 45.6 μW as stated in Section 5.1.3). It results from two effects: the impedance mismatch effect between the rectifying circuit and the optimal resistive load; and the voltage drop of diodes filtering the signals with small amplitude.

In the second experiment, the device is pressed with a repetitive and controllable motion provided by a vibrator, so that the power delivery of the KEH in cooperation with an AC-DC rectifying circuit can be characterized in a stable frequency and uniform force. The schematic of the excitation system for the KEH is shown in Figure 5.6(a). The storage capacitance of the

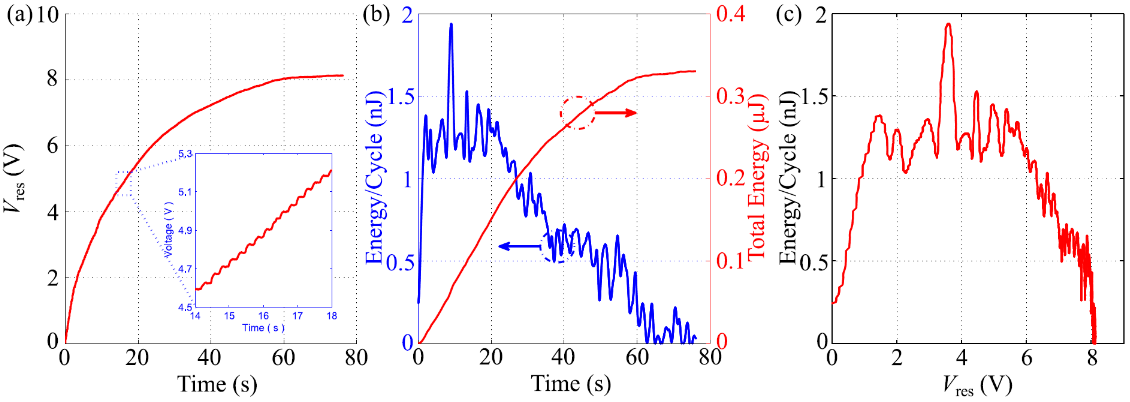

Figure 5.9: Finger-tap (manual operation) charging of a capacitor $C_{\rm res} = 10$ nF through a full-wave rectifier with the tapping frequency of $\sim$4 Hz: (a) evolution of $V_{\rm res}$ with time, (b) the energy per cycle and the total energy vs. the time, (c) the energy per cycle vs. the voltage.

device is 1 μF so that the energy released from the capacitor discharging from 3.3 V down to 1.1 V is able to sustain up to 3 RFID communications, each communication consuming 1.77 μJ of energy [19]. The excitation signal applied on the vibrator is set at 10 Hz, while the maximum force applied is 0.5 N. The rectifying circuit tested is a full-wave diode rectifier. The evolution of $V_{\rm res}$ versus time is shown in Figure 5.10(a). Figure 5.10(b) shows the time-dependent total energy stored in the capacitor, together with the energy transferred to the capacitor during each cycle of charging. It is inferred that the duration of the entire charging process from 0 to 3.3 V is 87 s, and the accumulated energy is 5.5 μJ, corresponding to an average power of 63 nW. Considering the operation frequency of 10 Hz, the average energy accumulated during each cycle is 6.3 nJ. While the recharging process from 1.1 V back to 3.3 V takes 59 s, during which the average power is 82 nW or the energy of 8.2 nJ/cycle.

From Figure 5.10(c) it can be observed that the energy accumulated during each cycle is approximately linear within the range of low storage voltage below 2 V. Within this stage, the charge pumped into the storage capacitor within each tapping operation is almost constant, about 4 nC/cycle. This indicates that the internal bias is capable of pumping a constant amount of charge to the capacitor during each cycle regardless of the increase of the barrier voltage, the sum of the voltage on the storage capacitor $V_{\rm res}$ and the forward voltage drop of the diodes. However, when $V_{\rm res}$ further increase, some of the charges flowing between the two electrodes are blocked from traveling due to a higher barrier voltage, resulting in a smaller amount of delivered charge Q. Since the energy stored to the capacitor is proportional to both $V_{\rm res}$ and Q, the increasing $V_{\rm res}$ accompanied by the decrease of Q, the increase of energy delivered per tap firstly reaches a maximum value and finally drops. Thus there is an optimal $V_{\rm res}$ corresponding to the maximum energy delivery to the storage capacitor per cycle. According to the graph, a maximum power of 99 nW (energy of 9.9 nJ/cycle) is reached when $V_{\rm res}$, is 3 V, while the power is no less than 80 nW (energy of 8 nJ/cycle) when $V_{\rm res}$ is between 2 V and 3.3 V.

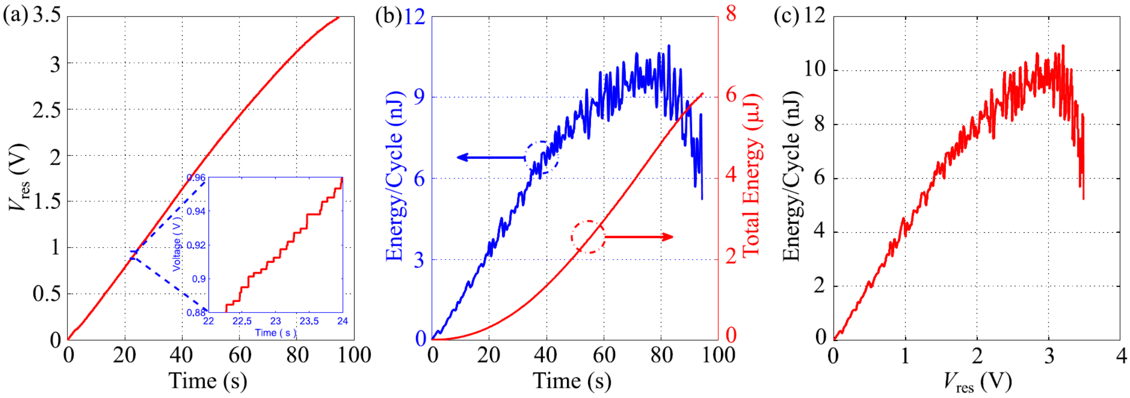

Figure 5.10: Shaker-driven charging of a capacitor $C_{\mathrm{res}} = 1\ \mu$F through a full-wave rectifier with the tapping frequency of 10 Hz with the peak force of 0.5 N: (a) evolution of V_{res} with time, (b) the energy per cycle and the total energy vs. the time, (c) the energy per cycle vs. the voltage.

5.2 2D e-KEH based on rotational structure

In a new design of e-KEH, we introduce a rotational structure suspended by linear springs, as shown in Figure 5.11. The central movable electrode is connected to fixed ends through four serpentine springs. At the center of the movable electrode, there is a cavity that can hold a miniature ball for low frequency actuation. The rotational movable structure is surrounded by gap-closing interdigited combs, which varies with the motion of the movable electrode. Thanks to the design of the electrodes, the structure is capable of responding to all kinds of vibrations within the wafer plane.

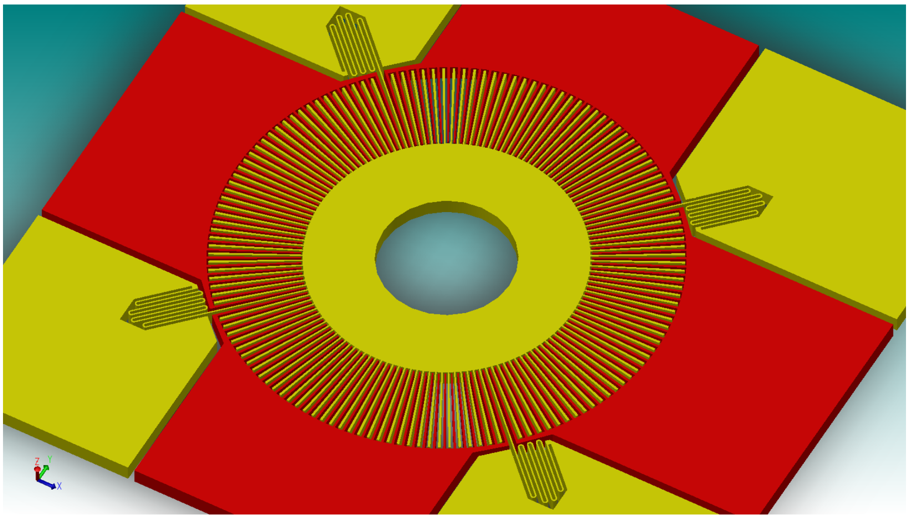

Figure 5.11: 3D view of the e-KEH with rotational structure. The entire structure is developed from SOI wafer. The edges are fixed, while the central part is a movable electrode suspended with linear springs.

Modal simulation of the proposed structure (the structure without miniature ball) is proceeded, giving the resonant frequency of different modes, shown in Figure 5.12. The 1st resonant mode is the rotational motion around the z axis, at the frequency of 445 Hz. The 2nd and 3rd modes are the transitional modes along y and x axes, at 568 Hz and 718 Hz respectively. The simulation indicate that the major resonant modes of the structure are all within the plane of wafer, making the device a fully two-dimensional prototype. This prototype is a demonstrator of the possibility to expand the effective vibration direction of a KEH to multiple dimensions.

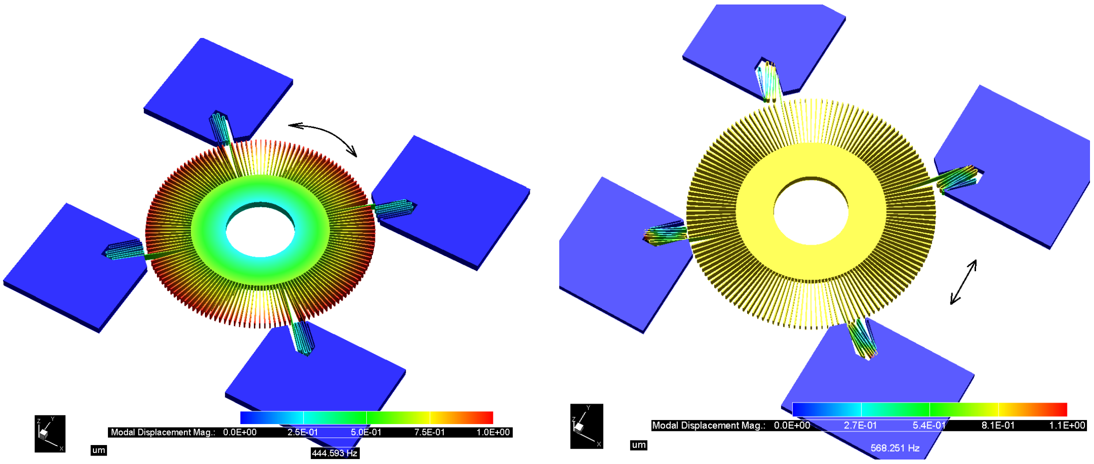

(a) Average peak voltage.

(b) Average peak power.

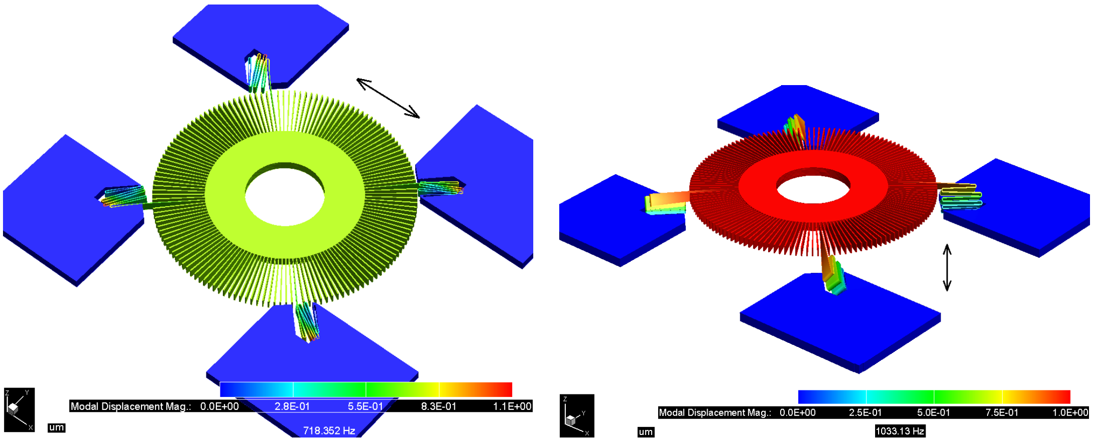

(c) Average peak power.

(d) Average peak power.

Figure 5.12: Average peak voltage and power of the proposed device with sweeping load resistance. The inset plot in (a) 1st mode: rotation around z axis at 445 Hz; (b) 2nd mode: transition along y axis at 568 Hz; (c) 3rd mode: transition along x axis at 718 Hz; (d) 4th mode: transition along z axis at 1003 Hz.

5.3 Conclusion

In this chapter, we firstly introduced the first flexible electret KEH. It is based on a low-cost sandwich-structure implementing stacked nanofiber-based electret films. Thanks to its thin-film components, the design is light-weighted and is less than 1 mm in thickness when it is pressed, thus suitable for wearable electronics. Although as-electrospun nanofibrous material is not suitable for working directly as electret, we propose to cover it with a parylene C layer in order to offer a stable charge storage. However, since the Paryelene C on the electrospun nanofibers has a smaller thickness compared to the planar Parylene C film, its long-term surface potential is lower, and needs to be further improved to take full advantage of its large specific area. The best energy conversion is obtained with a ratio of capacitance variation of 5 with a 3-layer electret. The optimal resistive load of the prototype is 16 MΩ, while the maximum peak power obtained is 45.6 μW, corresponding to 48 nJ/cycle. The typical energy conversion density of piezoelectric KEHs is 0.1$\sim$1 $\mu\mathrm{J}\cdot\mathrm{cm}^{-2}$ per cycle [178] [179], while triboelectric KEHs typically offer peak instantaneous power of $\sim$10 $\mu\mathrm{W}\cdot\mathrm{cm}^{-2}$ [176]. In comparison, the current prototype has an energy density of 8 $\mathrm{nJ}\cdot\mathrm{cm}^{-2}$/cycle. The prototype is able to deliver an optimal energy of 9.9 nJ/cycle with a regular tapping of 0.5 N when working with full-wave conditioning circuit. The optimal energy delivery is relevant to the DC voltage on the storage capacitor and the two key parameters of the prototype, the internal bias voltage and the ratio of capacitance variation. In a finger-tapping experiment, the device charges a capacitor of 10 nF up to 8.5 V within 450 strokes through a full-wave rectifier. The power transmission can be improved through a better impedance matching or a reduced diode voltage drop.

In addition, we propose a two-dimensional e-KEH with rotational structure. The modal simulation of the prototype is proceeded, showing that the device is capable of responding to motions (vibrations and rotations) within the horizontal plane. The device is under fabrication currently.

Chapter 6

A full autonomous RFID communication tag assisted by an e-KEH

In this chapter we report a full Radio Frequency IDentification (RFID) tag system powered by a Microelectromechanical System (MEMS) KEH. We are going to describe the characterization procedure of the system. The tag antenna and its matching interface to the RFID chip are designed with the help of an electromagnetic simulator. The energy provided by the KEH is stored in a reservoir capacitor and released through a mechanical switch to the tag. It is demonstrated that the tag can communicate with a reader at a distance up to 15 m when powered by the KEH working with an acceleration of 2 g_{rms} and 100 Hz. The energy delivered by the KEH within 100 s can sustain up to 6 tag readings using the EPC Gen-2 Class-1 standard.

6.1 Introduction

The RFID technology is widely applicable for identification and positioning of objects or persons. The maximum read/write distances of passive RFID tags working at Ultra High Frequency (UHF) in the 860-960 MHz band reach up to 10 meters [188] depending on the operating conditions. The long-range performance can be further improved by using battery-assisted tags. However, taking into account the environmental issues of batteries and their limited lifetime, there is a demand to replace the batteries powering active and semi-passive RFID tags by energy harvesters, which provide electrical power transduced from the widely existing ambient sources of energy (vibrations, heat, RF or light) [189].

As the amount of power that can be extracted from the environment is limited, it is practical to store the transduced energy into a reservoir capacitor temporarily. This energy is then released intermittently through an electronic control module (such as an automatic switch) [138] to the RFID chip. The minimum energy requirement for a successful tag reading is related to the average time of a full communication cycle between the reader and one tag.

On the other hand, the energy requirement of the RFID chip for each communication is also related to the chip itself and the capacitor. Firstly, the chip must be connected to a minimum bias voltage to sustain a proper working status. The current and the power consumption of the chip depend on its bias voltage and its input impedance. Secondly, a minimum period of time is required to perform a full data transmission, during which there is a voltage drop across the capacitor. Finally, the capacitor value is determined through a trade-off between the amount of ambient power that can be harvested, the available time to power up the tag, the amount of data to be transmitted and the energy required for it.

In this chapter, we describe a procedure to evaluate the performance of a semi-passive UHF RFID tag powered by a capacitive KEH. It is the first time that such a study is proposed with a capacitive KEH assisting intermittent communications of an RFID tag, even though a piezoelectric harvester is reported in [190] supporting a continuous tag communication. Our study gives a better understanding of the limitation of KEH-assisted RFID systems under the conditions where the available environmental vibration power is limited.

The key parameters of the tag antenna are first addressed before the impedance of the optimized antenna and the maximum read range of the tag are measured. Then, the power consumption of the chip biased by a pre-charged reservoir capacitor is evaluated experimentally, together with the minimum energy requirement for a single reading of the tag. In a following communication experiment, the tag is powered by a capacitor which is charged by a KEH through an AC-DC rectifier. Using a sinusoidal signal to excite a vibrator carrying the KEH, the minimum time and energy requirement of the tag to communicate with the reader are fully determined.

6.2 Antenna design: key parameters & simulation

The antenna is based on a spiral-loaded dipole with a modified L-matching circuit interface, the layout of which is shown in Figure 6.1(a), together with the illustration of its design parameters. The dipole is loaded by spirals [191], which occupy a much smaller space than meandering lines providing the same amount of inductance. Hence, although the proposed spiral-loaded dipole shows a larger Q-factor for a given resonant frequency than meandering designs [192], it is preferred because of its small size. The dual matching technique described in [193] is applied to reach the largest possible bandwidth for a given dipole. The equivalent circuit of the full tag is shown in Figure 6.1(b), where the impedance of the dipole antenna (a resistance R_a, an inductance L_a and a capacitance C_a connected in series) is adjusted by a parallel inductance L_h and a series inductance L_e, so as to realize impedance matching between the design and the RFID communication chip.

6.2.1 Theoretical analysis

Typically, the chip impedance is represented as a parallel combination of a capacitance C_chip and a resistance R_chip described as:

$$R_\mathrm{chip} = R_\mathrm{ic}\left[1 + \left(\frac{X_\mathrm{ic}}{R_\mathrm{ic}}\right)^2\right] \tag{6.1}$$

$$C_\mathrm{chip} = -\frac{X_\mathrm{ic}}{R_\mathrm{ic}R_\mathrm{ic}\omega} \tag{6.2}$$

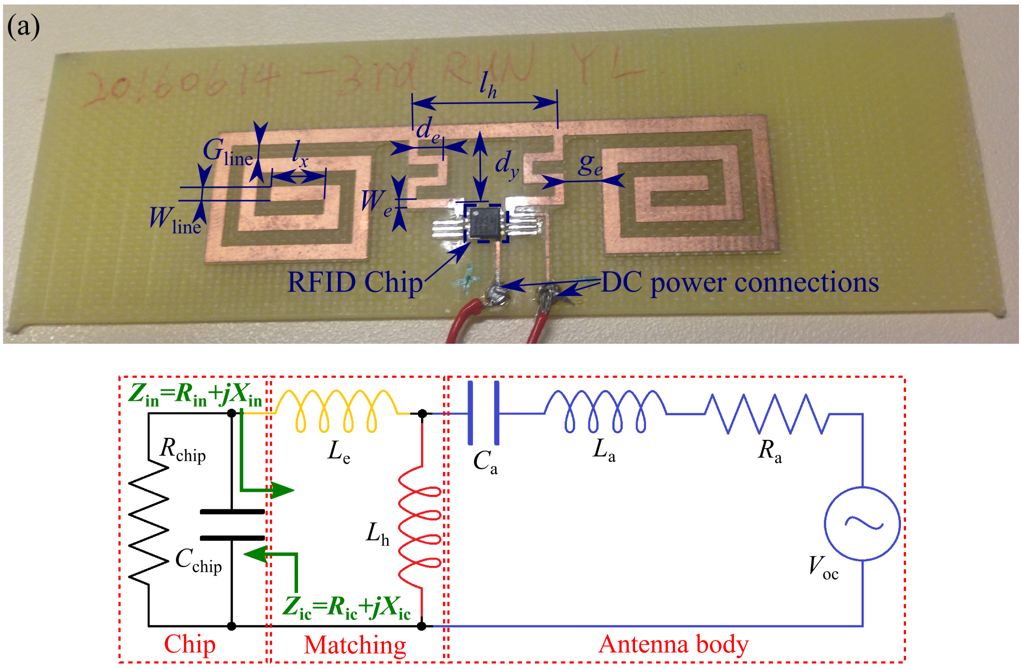

Figure 6.1: (a) Photograph of the L-matched RFID tag antenna, including dimensions. (b) Equivalent circuit of the full RFID tag.

where ω is a certain working angular frequency of the chip, while R_{ic} and X_{ic} are the resistance and reactance of the chip corresponding to the frequency ω. Thus the variation of the chip impedance with frequency is:

$$Z_{\text{ic}} = \frac{R_{\text{chip}}}{1 + R_{\text{chip}}^2 C_{\text{chip}}^2 \omega^2} \left(1 - jR_{\text{chip}} C_{\text{chip}} \omega\right) \tag{6.3}$$

For optimal impedance matching, the input impedance of the antenna design should be the conjugate of the chip impedance (zero reflection):

$$Z_{\text{in,opt}} = Z_{\text{ic}}^* \tag{6.4}$$

According to the equivalent circuit in Figure 6.1(b), the input impedance of the dipole antenna together with the matching circuit is the following:

$$Z_{\text{in}} = j\omega L_{\text{e}} + \left[j\omega L_{\text{h}} \parallel \left(R_{\text{a}} + j\omega L_{\text{a}} - j\frac{1}{\omega C_{\text{a}}} \right) \right] \tag{6.5}$$

which is rewritten into the following form through identical transformations:

$$Z_{\text{in}} = \frac{\omega^2 L_{\text{h}}^2 R_{\text{a}}}{R_{\text{a}}^2 + X_0^2(\omega)} + j\left[\omega \left(L_{\text{e}} + L_{\text{h}} \right) - \frac{\omega^2 L_{\text{h}}^2 X_0(\omega)}{R_{\text{a}}^2 + X_0^2(\omega)} \right] \tag{6.6}$$

where $X_0(\omega) = \omega\left(L_{\text{h}} + L_{\text{a}}\right) - \frac{1}{\omega C_{\text{a}}}$. For easy discussion, we analyze the real and imaginary parts of the input impedance separately. In order to achieve equations of simple form, we also introduce the following auxiliary variables:

$$\omega_{\mathrm{h}} = 1/\sqrt{L_{\mathrm{h}} C_{\mathrm{a}}}, \omega_{\mathrm{ah}} = 1/\sqrt{(L_{\mathrm{a}} + L_{\mathrm{h}}) C_{\mathrm{a}}}, \tau_{\mathrm{a}} = R_{\mathrm{a}} C_{\mathrm{a}} \tag{6.7}$$

Thus the real part is transformed as follows:

$$R_{\mathrm{in}}\left(\omega\right) = \frac{\frac{\omega^4}{\omega_{\mathrm{h}}^4} R_{\mathrm{a}}}{\frac{\omega^4}{\omega_{\mathrm{ah}}^4} + \left(\tau_{\mathrm{a}}^2 - \frac{2}{\omega_{\mathrm{ah}}^2}\right)\omega^2 + 1} \tag{6.8}$$

the first derivative of which is:

$$R_{\mathrm{in}}^{(1)}\left(\omega\right) = \frac{\frac{\omega^4}{\omega_{\mathrm{h}}^4}\left[2\omega^2\left(\tau_{\mathrm{a}}^2 - \frac{2}{\omega_{\mathrm{ah}}^2}\right) + 1\right]}{\left[\omega^4/(\omega_{\mathrm{ah}}^4) + (\tau_{\mathrm{a}}^2 - 2/(\omega_{\mathrm{ah}}^2))\omega^2 + 1\right]^2} \cdot \frac{R_{\mathrm{a}}}{\omega} \tag{6.9}$$

The two equations above depict a function $R_{\mathrm{in}}\left(\omega\right)$ that approaches zero when the frequency approaches zero, and approaches a positive constant when the frequency approaches infinity, both with infinitesimal first derivatives:

$$\begin{cases} R_{\mathrm{in}}\left(\omega\right) \sim \frac{\omega^4}{\omega_{\mathrm{h}}^4} R_{\mathrm{a}} & \text{when } \frac{\omega}{\omega_{\mathrm{h}}} \to 0 \\ \lim\limits_{\omega\to\infty} R_{\mathrm{in}}\left(\omega\right) = \frac{\omega_{\mathrm{ah}}^4}{\omega_{\mathrm{h}}^4} R_{\mathrm{a}}, R_{\mathrm{in}}^{(1)}\left(\omega\right) \sim 2(\tau_{\mathrm{a}}^2\omega_{\mathrm{ah}}^2 - 2)\frac{\omega_{\mathrm{ah}}^6}{\omega_{\mathrm{h}}^4}\frac{R_{\mathrm{a}}}{\omega^3} & \text{when } \frac{\omega}{\omega_{\mathrm{ah}}} \to \infty \end{cases} \tag{6.10}$$

Within the entire frequency domain, provided the prerequisite $2/\left(\omega_{\mathrm{ah}}^2\right) > \tau_{\mathrm{a}}^2$, only one peak is observed in the resistance curve, which is located at the frequency ω_0 satisfying the equation:

$$2\left(\frac{2}{\omega_{\mathrm{ah}}^2} - \tau_{\mathrm{a}}^2\right)\omega_0^2 = 1 \tag{6.11}$$

The peak resistance is

$$R_{\mathrm{in}}\left(\omega_0\right) = \frac{\omega_{\mathrm{ah}}^4}{\omega_{\mathrm{h}}^4}\frac{R_{\mathrm{a}}}{1 + 2(\omega_{\mathrm{ah}}^2\tau_{\mathrm{a}}^2 - 2)^2} \tag{6.12}$$

As for the imaginary part of the input impedance,

$$X_{\mathrm{in}}\left(\omega\right) = \omega\left(L_{\mathrm{e}} + L_{\mathrm{h}}\right) - \frac{\frac{\omega^2}{\omega_{\mathrm{h}}^2}\left(\frac{\omega^2}{\omega_{\mathrm{ah}}^2} - 1\right)}{\frac{\omega^4}{\omega_{\mathrm{ah}}^4} + \frac{\omega^2}{\omega_{\mathrm{ah}}^2}\left(\tau_{\mathrm{a}}^2\omega_{\mathrm{ah}}^2 - 2\right) + 1} \cdot \omega L_{\mathrm{h}} \tag{6.13}$$

Its first derivative is

$$X_{\mathrm{in}}^{(1)}\left(\omega\right) = \left(L_{\mathrm{e}} + L_{\mathrm{h}}\right) - \frac{\omega^2}{\omega_{\mathrm{h}}^2} \cdot \frac{\frac{\omega^6}{\omega_{\mathrm{ah}}^6} + \frac{\omega^4}{\omega_{\mathrm{ah}}^4}(3\tau_{\mathrm{a}}^2\omega_{\mathrm{ah}}^2 - 5) - \frac{\omega^2}{\omega_{\mathrm{ah}}^2}(\tau_{\mathrm{a}}^2\omega_{\mathrm{ah}}^2 - 7) - 3}{\left[\frac{\omega^4}{\omega_{\mathrm{ah}}^4} + \frac{\omega^2}{\omega_{\mathrm{ah}}^2}\left(\tau_{\mathrm{a}}^2\omega_{\mathrm{ah}}^2 - 2\right) + 1\right]^2} \cdot L_{\mathrm{h}} \tag{6.14}$$

The two expressions above gives the idea that the reactance of the design approaches linear functions of the frequency when the frequency approaches both zero and infinity:

$$\begin{cases} X_{\mathrm{in}}\left(\omega\right) \sim \omega\left(L_{\mathrm{e}} + L_{\mathrm{h}}\right) & \text{when } \omega \to 0 \\ X_{\mathrm{in}}\left(\omega\right) \sim \omega\left(L_{\mathrm{e}} + L_{\mathrm{h}} \parallel L_{\mathrm{a}}\right) & \text{when } \omega \to \infty \end{cases} \tag{6.15}$$

According to the expression of the first derivative of input reactance, we also learn that the variation of the reactance near its resonance frequency is majorly influenced by variables ω_{ah} and τ_{a}.

The dipole, the matching circuit and the chip interface are etched out of a low-cost PCB made of FR4 dielect R_{ic} (ϵ_{r}=4.25, $\tan\delta$=0.02, thickness=1.54 mm) with a 35 μm thick copper metallization through a milling process. The RFID chip is then soldered on the chip interface.

The chip used is the EM4324 manufactured by EM Microelectronic communicating with the EPC Gen-2 Class-1 protocol and working with the European standard in the 865-868 MHz band. It can be either battery powered or beam powered by the RF energy transmitted from a reader. According to the datasheet, the input impedance of the chip at 868 MHz is $Z_{\mathrm{ic}} = 11 - j164\Omega$ under battery-assisted mode. It is thus equivalent to the impedance of a resistance R_{cp}=2.456 kΩ in parallel with a capacitor C_{cp}=7.00 pF. The optimal input impedance of the antenna can be calculated accordingly (Equation 6.4). The L-matching interface is applied for the antenna design, the impedance of which is predicted by computer-assisted finite element calculations. The calculations above provides a guideline for the adjustment of the parameters in the antenna design. By investigating all the parameters noted in Figure 6.1(b), we are ended up with several key design parameters, which are discussed in detail in the following section.

6.2.2 Key parameters for the design

The influences of the different key parameters of the antenna predicted by an ANSYS HFSS model are illustrated in Figure 6.2, where the input resistance (R_{in}) and reactance (X_{in}) of the antenna are plotted along with the optimal matching expectations (R_{ic} and $-X_{\mathrm{ic}}$). Here R_{ic} and X_{ic} are the resistance and the reactance of the chip respectively, which dependence on frequency is introduced in [188]. As shown in Figure 6.2(b), the resonance frequency f_0 of the antenna (the frequency where R_{in} reaches maximum) is reduced by elongating the length of the spiral-loaded dipole (increasing l_{x}). l_{x} is thus adjusted so that f_0 is 868 MHz.

Increasing d_{y} mainly increases X_{in} because it increases the length of the series inductance L_{e}. Other parameters that have the similar effect as d_y include the meander length (d_{e}) and the line width (W_{e}), the increment of which brings an increment of L_{e}. In contrast, R_{in} is weakly influenced by these parameters.

By adjusting f_0 and X_{in}, the antenna matching can be reached in the largest achievable bandwidth. All the parameters applied in the final antenna design are listed in Table 6.1. And the reflection coefficient $|\Gamma|$ given by:

$$|\Gamma| = \left|\frac{Z_{\mathrm{in}} - Z_{\mathrm{ic}}^*}{Z_{\mathrm{in}} + Z_{\mathrm{ic}}}\right| = \left|\frac{R_{\mathrm{in}} - R_{\mathrm{ic}} + j\left(X_{\mathrm{in}} + X_{\mathrm{ic}}\right)}{R_{\mathrm{in}} + R_{\mathrm{ic}} + j\left(X_{\mathrm{in}} + X_{\mathrm{ic}}\right)}\right| \tag{6.16}$$

is plotted in Figure 6.3. The -3 dB bandwidth of 97 MHz is obtained between 826 MHz and 923 MHz.

The bottleneck in achieving an accurate numerical model is the consideration of the key factors related to the mechanical micromachining process. Among them is T_{cut}, the thickness of substrate material removed by milling, which influence on the impedance is shown in Figure 6.2(c). It appears that a tiny error during the process (even ±0.1 mm) could bring much larger resonance

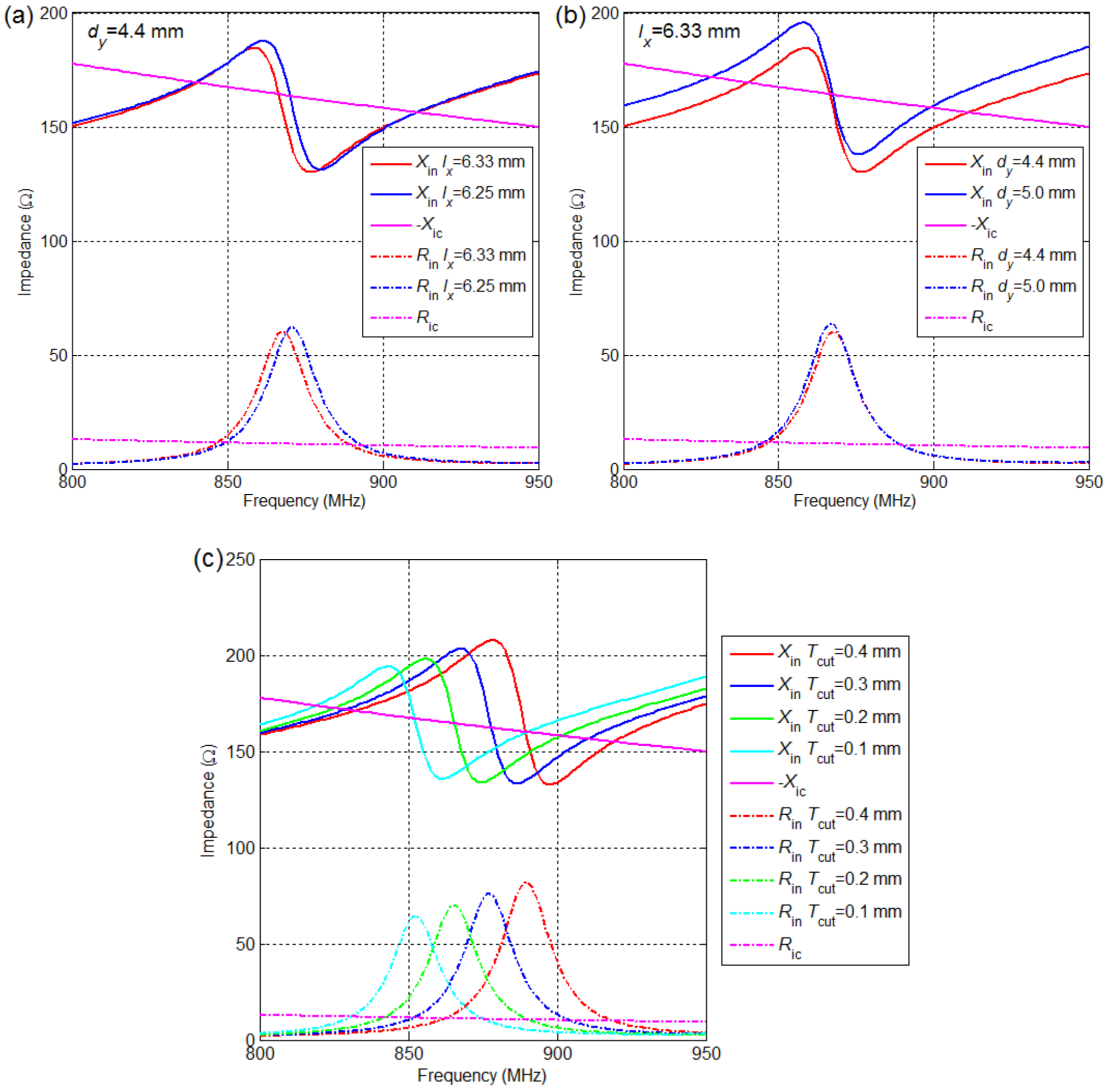

Figure 6.2: Influence of parameters (a) l_x, (b) d_y, and (c) T_{cut} (thickness of the removed substrate material during the milling process) on the design impedance.

Table 6.1: Parameters of the antenna design.

Dimension	Value
Line Width of Dipole and L_{h} (W_{line})	1.5 mm
Gap Between Lines (G_{line})	1.5 mm
Length of the Innermost Segment of the Dipoles (l_x)	6.33 mm
Length of L_{h} (l_{h})	14.2 mm
Meander Length of L_{e} (d_{e})	3 mm
Line Width of L_{e} (W_{e})	0.9 mm
Total Height of L_{e} (d_y)	4.4 mm
Gap Between the Dipole and L_{e} (g_{e})	3.6 mm

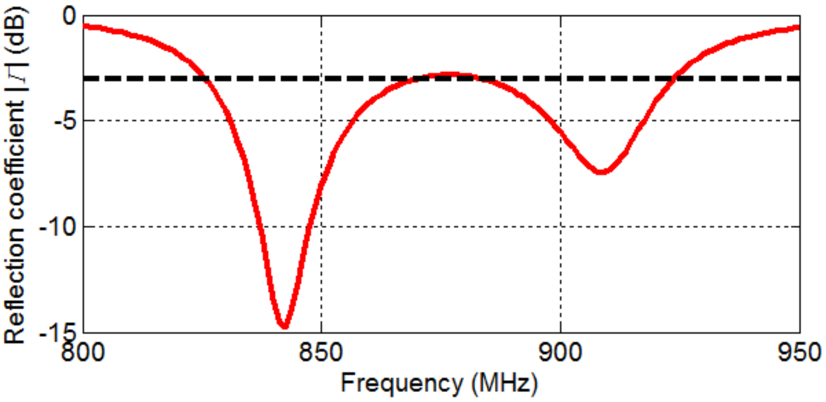

Figure 6.3: Reflection coefficient of the tag with parameters listed in Table 6.1.

shifts than that of the factor l_{x}. The cause for this situation is that removing the substrate material that is close to the metal lines reduces the effective permittivity significantly, thus increasing the relative length of the antenna by a large percentage. The measured thickness of removed substrate material is estimated to 0.15 mm with a digital caliper. However, additional post-fabrication tunable capabilities would help improving the matching performance as recommended in [194] [195] for various types of microwave circuits.

6.3 Experiments and discussions

6.3.1 Cable characterization

Input impedance Z_{in} of a lossy cable with a load Z_{L}:

$$Z_{\mathrm{in}} = Z_0 \frac{Z_{\mathrm{L}} + jZ_0 \frac{e^{\gamma l} - e^{-\gamma l}}{e^{\gamma l} + e^{-\gamma l}}}{Z_0 + jZ_{\mathrm{L}} \frac{e^{\gamma l} - e^{-\gamma l}}{e^{\gamma l} + e^{-\gamma l}}} \tag{6.17}$$

where l stands for the length of the cable, the propagation constant $\gamma = \alpha + j\beta$. Input impedance with short circuit load is:

$$Z_{\mathrm{sc}} = jZ_0 \frac{e^{\gamma l} - e^{-\gamma l}}{e^{\gamma l} + e^{-\gamma l}} \tag{6.18}$$

while that with open circuit load is:

$$Z_{\mathrm{oc}} = -jZ_0 \frac{e^{\gamma l} + e^{-\gamma l}}{e^{\gamma l} - e^{-\gamma l}} \tag{6.19}$$

the ratio of impedances:

$$\frac{Z_{\mathrm{sc}}}{Z_{\mathrm{oc}}} = -\left(\frac{e^{\gamma} l - e^{(} - \gamma l)}{e^{\gamma} l + e^{-\gamma l}} \right)^2 = -\left[\frac{(e^2 \alpha l - 1) + j(e^2 \alpha l + 1) \tan \beta l}{(e^2 \alpha l + 1) + j\,(e^2 \alpha l - 1) \tan \beta l} \right]^2 \tag{6.20}$$

We introduce a variable $t = e^{2\alpha l} - 1$, considering the influence of the attenuation constant ($\alpha \to 0$), the following equivalent infinitesimal relation is reached: $t \sim 2\alpha l$. The ratio of impedances is then expanded according to the Taylor formula as following (accurate to first order infinitesimal):

$$\begin{aligned}\frac{Z_{\text{sc}}}{Z_{\text{oc}}} &= -[\frac{t+j\,(t+2)\tan\beta l}{(t+2)+jt\tan\beta l}]^2 = -\left[t+j\,(t+2)\tan\beta l\right]^2\cdot\frac{1}{4}\left[\Sigma_{n=0}^{\infty}\left(-\frac{1+j\tan\beta l}{2}t\right)^n\right]^2 \\ &\approx \beta l\left(\tan\beta l-\frac{jt}{\cos^2\beta l}\right)\end{aligned} \tag{6.21}$$

If we neglect the loss in the cable ($t \to 0$) in the equation,

$$\lim_{t\to 0}\frac{Z_{\text{sc}}}{Z_{\text{oc}}} = \lim_{t\to 0}\tan^2\beta l \tag{6.22}$$

the relative permittivity can be calculated from the phase constants at different frequencies, and are further related to the open circuit and short circuit impedances:

$$\sqrt{\epsilon_r} = c_0\frac{\Delta\beta}{\Delta\omega} = \frac{c_0}{l}\cdot\frac{\arctan\left(\frac{Z_{\text{sc}}}{Z_{\text{oc}}}\right)^{\frac{1}{2}}|_{\omega=\omega_2} - \arctan\frac{Z_{\text{sc}}}{Z_{\text{oc}}}^{\frac{1}{2}}|_{\omega=\omega_1}}{\omega_2-\omega_1} \tag{6.23}$$

where c_0 is the light speed in vacuum, working frequencies ω_2 and ω_1 should be close enough to meet the following condition:

$$\lfloor\frac{\omega_1 l}{\pi c_0}+\frac{1}{2}\rfloor = \lfloor\frac{\omega_2 l}{\pi c_0}+\frac{1}{2}\rfloor \tag{6.24}$$

where the function $\lfloor\cdot\rfloor$ is the round down operation. In the measurement, we use a cable with a length of 0.253 m, and choose the frequencies 868 MHz and 888 MHz as test point. The input impedances with short circuit and open circuit impedances are as follows:

$$\begin{cases} Z_{\text{oc}}|_{868\text{MHz}} = (2.2-j169.5)\,\Omega & Z_{\text{sc}}|_{868\text{MHz}} = (1.2+j14.72)\,\Omega \\ Z_{\text{oc}}|_{888\text{MHz}} = (0.3-j105.2)\,\Omega & Z_{\text{sc}}|_{888\text{MHz}} = (1.5+j23.00)\,\Omega \end{cases} \tag{6.25}$$

The relative permittivity of the cable is calculated according to equation (1.7): ϵ_{r}=2.0232 Taking the first order infinitesimal in equation (1.5) into account, the attenuation constant can be calculated as follows:

$$\alpha \approx -\frac{\cos^2\beta l\frac{Z_{\text{sc}}}{Z_{\text{oc}}}}{2l\tan\beta l} \tag{6.26}$$

In order to ensure the feasibility of measurement, the cable length l should be long enough ($2\alpha l > 0.1$), otherwise the imaginary component of the impedance ratio $\text{im}\left(\frac{Z_{\text{sc}}}{Z_{\text{oc}}}\right)$ will be submerged in the experimental errors. The length of the cable we use in the measurement is not large enough to obtain the attenuation constant α.

6.3.2 Impedance measurement with a balun

The input impedance of the antenna is measured through a balance-unbalance converter as shown in Figure 6.4(a), where a wire with the length of 1/4 wavelength corresponding to the target frequency f_0 is put in parallel with a coaxial cable, and shorted to the outer conductor the coaxial cable at a distance of 1/4 wavelength from the load plane of the cable. At the frequency f_0, the proposed balun converter acts as a parallelly connected open-circuit load at the input port of the cable.

In the measurement, the load brought by the balun to the antenna plane is a negligible open-circuit load at f_0, but it is narrow-banded. The accuracy of impedance measurement will be high within a bandwidth within which the variation of the phase shift caused by the cable is less than 10% of the wavelength, otherwise the impedance brought by the balun will be far from open-circuit. In the experiment, after calibration at one of the ports of the vector network analyzer (VNA), the balun carrying the antenna is connected to the port for measurement. The relative permittivity of the cable (ϵ_r=2.0232) and its mechanical length (l=0.44 m) are provided to the VNA to indicate the time delay of the cable. The real impedance of the antenna is measured by taking into account the delay of the cable. The accuracy of this measurement is credible within the frequency range between 834 MHz and 900 MHz.

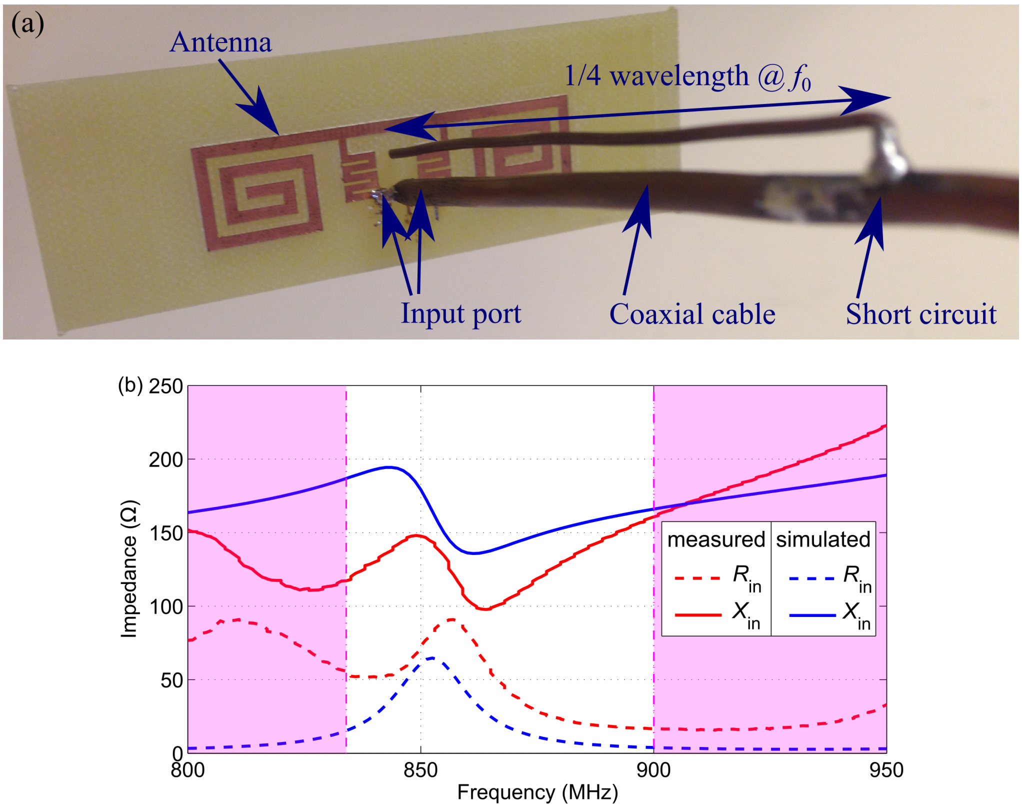

Figure 6.4: (a) The balun used for impedance measurement in connection with the antenna. (b) The input impedance of the antenna given by measurement with balun converter. The frequency range where the measurement is acceptable is between 834 MHz and 900 MHz.

The resonance frequency of the antenna is consistent with the simulation in which the parameter T_{cut} is considered. For now since the control of this parameter is not accurately controlled, we proceed the measurement of T_{cut} after the fabrication. The thickness of removed substrate material is 0.15 mm, which is measured after the fabrication. Since this parameter is very critical in the accuracy control of the frequency response, it is important to improve the accuracy of removed thickness in the milling process for future improvement. We observe that the impedance change within the range of 834∼900 MHz is basically correct in the tendency of variation, while beyond this region the error of measurement is enormous. The cause for this is the narrow bandwidth of the balun: it is open circuit load only to the electromagnetic wave whose wavelength is four times of the length of the balun. While even for the target frequency, the open-circuit is not perfectly realized by the balun.

6.3.3 Impedance measurement with a differential probe

The input impedance of the antenna is measured between 800 and 950 MHz with a differential probe as shown in Figure 6.5(a). The differential probe is made of two 50 Ω semi-rigid coaxial cables 1 and 2 with SMA connectors at one end and small segments (3 mm) of the inner conductors exposed as probes at the other end. The two outer conductors are soldered to get a common reference. For cable 1, the reflection coefficient $\Gamma_{1,\mathrm{match}}$ seen from the SMA connector is measured when a matched load is soldered between the probe and the outer conductor. Similarly, the reflection coefficient $\Gamma_{1,\mathrm{short}}$ seen from the SMA connector is measured when the probe is shorted to the outer conductor. The S-matrix of cable 1 is then extracted:

$$\begin{pmatrix} \Gamma_{1,\mathrm{match}} & \sqrt{|\Gamma_{1,\mathrm{short}}|}\exp\left[i\frac{\arg(\Gamma_{1,\mathrm{short}}-\pi)}{2}\right] \\ \sqrt{|\Gamma_{1,\mathrm{short}}|}\exp\left[i\frac{\arg(\Gamma_{1,\mathrm{short}}-\pi)}{2}\right] & \Gamma_{1,\mathrm{match}} \end{pmatrix} \tag{6.27}$$

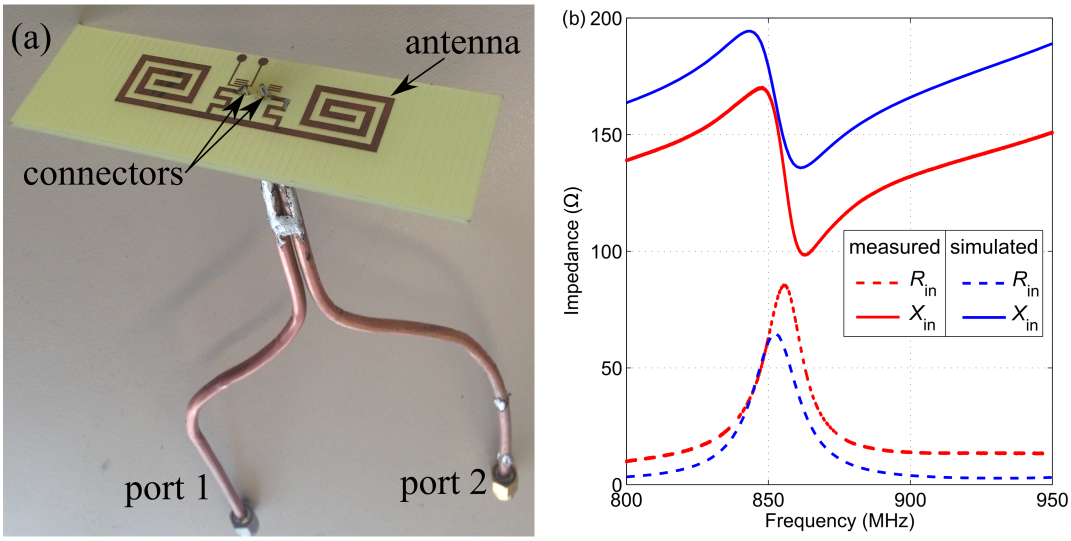

Figure 6.5: (a) Photo of the differential probe used in the impedance measurements. (b) Measured input impedance of the antenna and comparison with simulated results.

Similar expressions can easily be found for cable 2. Next, the spiral-loaded dipole antenna is fed by the differential probe. Let us call S_{sys} the S-matrix measured between port 1 and 2. The ABCD chain matrix of the full system including the probe and the antenna is obtained from S_{sys}. Then, the chain matrix of the antenna is calculated with a pre- and post-multiplication of the chain matrix of the full system with the inverse of the chain matrices of the two semi-rigid cables

$$\begin{pmatrix} A & B \\ C & D \end{pmatrix}_{\mathrm{sys}} = \begin{pmatrix} A & B \\ C & D \end{pmatrix}_1^{-1} \begin{pmatrix} A & B \\ C & D \end{pmatrix}_{\mathrm{sys}} \begin{pmatrix} D & C \\ B & A \end{pmatrix}_2^{-1} \tag{6.28}$$

The differential input impedance of the dipole antennas is finally calculated from its ABCD-parameters [196]. The antenna impedances (measured and simulated) are shown in Figure 6.5(b), the difference between them can be attributed in part to the experimental effect such as the coupling of the dipole near-field with the coaxial cable.

From the measurements we observe that the reactance given by the measurement is about 28% lower than the prediction of the simulations, while the peak resistance is 28% higher than that given by the simulation. The cause for this difference is probably coming from other fabrication factors that are not considered, such as the difference of cutting depth between milling tools of different diameters. Other possible causes for the difference between simulated and measured impedances can be the error brought by the calibration of the cables, during which the impedance matching and the short circuit load are not perfectly realized. After all, the accuracy of impedance measurement through differential probe is higher than that of the balun.

6.3.4 Read range measurement

The maximum read range (RR) of the designed tag was measured between 800 and 950 MHz with the help of Tagformance, the frequency-wobulated RFID reader commercialized by Voyantic. For each frequency, Tagformance evaluates the tag sensitivity by measuring the minimum transmitted power required to wake-up the tag located at a fixed distance of 30 cm. Then, RR is calculated from the Friis formula assuming a maximum allowed transmitted power, i.e. an Effective Radiated Power (ERP) of 2 W according to the European regulations. The RFID tag is powered by a 3.3 V battery during the RR measurement. Shown in Figure 6.6 is the measured RR of the tag, where the main dipole dimension of the tag is either in parallel with or perpendicular to the polarization of the linearly polarized reader antenna. The maximum read range at 868 MHz is 15 m for the parallel polarization. The strong tag response in perpendicular polarization results from the radiation from the orthogonal currents in the spirals.

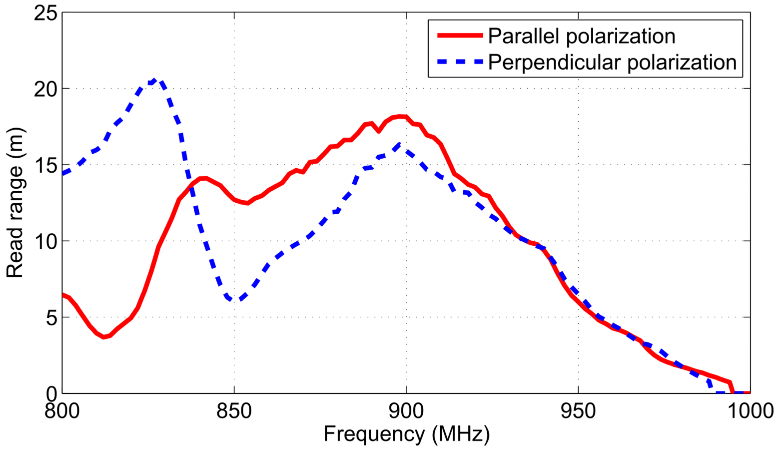

Figure 6.6: Maximum read range of the RFID tag powered by a 3.3 V battery.

6.3.5 Power consumption with capacitive sources

The power consumption of the RFID tag is measured by biasing the RFID chip with a DC voltage provided by a pre-charged reservoir capacitor C_{res}. The circuit is shown in the inset of Figure 6.7(a), where the DC input of the chip (R_{chip}) is connected to C_{res}. The distance between the tag and a commercial reader is set just beyond the maximum read range of the batteryless tag (2.5 m). The capacitor is firstly charged to 3.3 V (maximum supply voltage of the chip). Then the reader is activated and repetitive readings of the tag are proceeded. The evolution of voltage V_{res} across C_{res} with time is measured by a voltage follower, and recorded until there is no more tag reading, i.e., when V_{res} drops below the supply voltage threshold of 1.1 V.

The power consumption of the tag is determined by calculating the time-derivative of the energy stored in C_{res}:

$$P_{\text{chip}} = -\frac{\mathrm{d}}{\mathrm{d}t}\left[\frac{1}{2}C_{\text{res}}V_{\text{res}}^{2}(t)\right] \tag{6.29}$$

The power consumption of the chip (P_{chip}) and its input resistance $\left(R_{\text{chip}} = V_{\text{res}}^{2}/P_{\text{chip}}\right)$ together with the current consumption are calculated. When C_{res} varies from 1 μF to 1 mF, the measured power consumption at given voltages is equivalent, with a relative variation of 10%.

Shown in Figure 6.7 are the power consumption and chip resistance as a function of the biasing voltage (V_{res}) measured with C_{res} = 1 mF. We choose to show this result for C_{res}=1 mF because the largest C_{res} allows the longest discharging time, hence the largest number of sampling points and the highest accuracy. R_{chip} varies between 115 kΩ and 146 kΩ, i.e. 130 kΩ with a maximum relative error of ±12%, while the current consumption increases approximately linearly with voltage.

We also obtain the total number of communications in a row when the RFID tag is powered by different C_{res}. The number of communications grows linearly with the increase of storage capacitor, as shown in Chapter 2. When C_{res}=1 mF, the tag is read 3750 times in a row by the reader during a 2.4-min discharging process from 3.3 V to 1.1 V, corresponding to an average time for a single tag reading of 38 ms. With a capacitor of 2.2 μF, up to 6 tag readings can be proceeded during each discharge starting from 3.3 V. This number of duplicated readings is sufficient to guarantee that at least one successful communication is accomplished in case of any failure. C_{res}=2.2 μF is thus chosen as the power supply for the RFID tag in the experiment of the following section.

6.3.6 RF IDentification powered by a MEMS KEH

According to the power consumption measurement, we can conclude that it is possible to power the RFID tag by a ~1 cm^2 MEMS transducer, i.e. KEH, as proposed in [138]. The e-KEHs are essentially a variable capacitors consisting of gap-closing interdigited combs and biased by a corona-charged electret. It is featured with a wideband resonant structure (spring-mass system) implementing frequency up-conversion mechanisms (miniature ball and elastic stoppers). Working with an optimal resistive load, the KEH demonstrated in Chapter 2 can offer up to 2.5 μW with a 2 g_{rms} 100 Hz vibration, providing energy that is capable of supporting several RFID communications within an acceptable duration.

The communication between the tag and the reader is proceeded. The schematic of the ex-

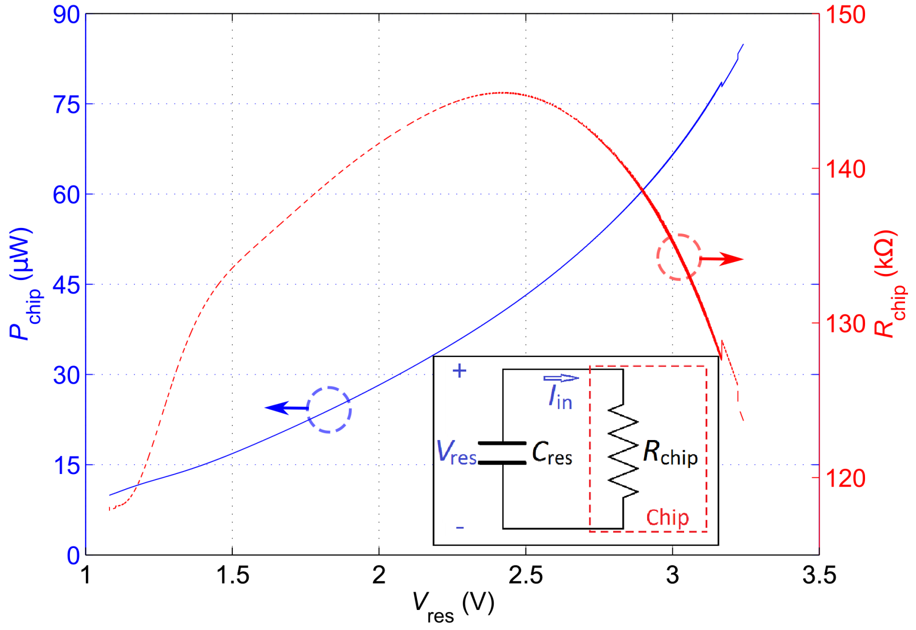

(a) Power consumption $\left(P_{\text{chip}}\right)$ and input resistance of the chip $\left(R_{\text{chip}}\right)$ when powered by a capacitor $C_{\text{res}} = 1$ mF as a function of the bias voltage (V_{res}). The inset shows the experimental schematic.

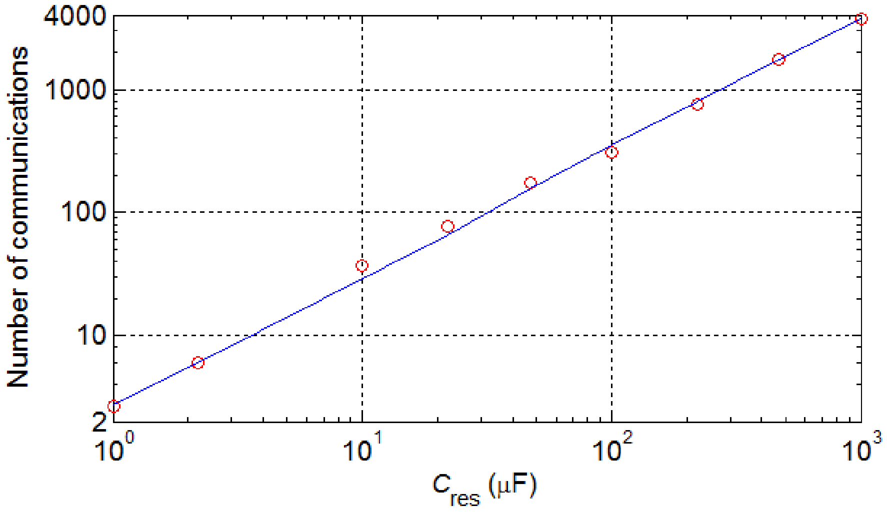

(b) Number of communications in a row as a function of C_{res} during one full discharge process starting from 3.3 V.

Figure 6.7: Power consumption characterization of the RFID tag communication.

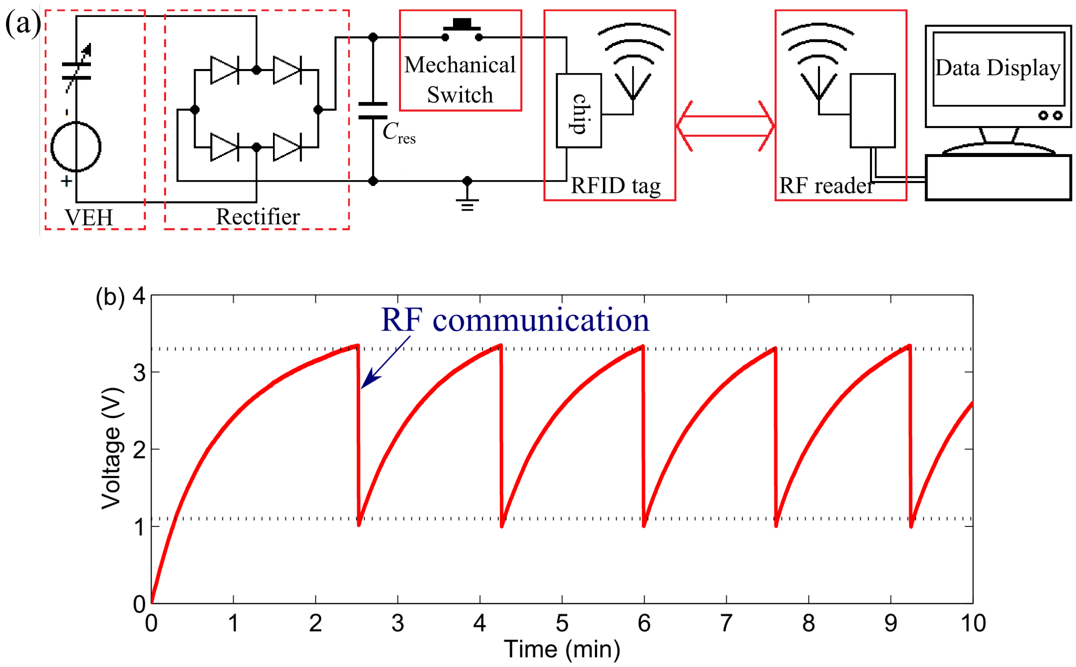

Figure 6.8: (a). Schematic of the RFID communication system where the RF tag is powered by a vibration energy harvester. (b). Measured voltage evolution on the bias capacitor C_{res} during the charging and the communication processes.

periment is shown in Figure 6.8(a), where the reservoir capacitor $C_{\text{res}} = 2.2\ \mu\text{F}$ is charged by the proposed MEMS KEH through a full-wave diode rectifier. The voltage V_{res} across C_{res} is monitored by a data acquisition card through a high-impedance voltage follower. The energy stored in C_{res} is released by manually pressing a tact switch each time after V_{res} reaches 3.3 V.

According to the RC constant of the discharging circuit, V_{res} will drop from the initial voltage to 1.1 V within about 300 ms, after which the current consumption of the chip drops significantly, while there will be no more tag readings. Consequently, the tact switch is released as quickly as possible after pressed. In a future work, the manually controlled mechanical switch for energy release will be replaced by an automatic Schmitt trigger. The KEH is excited with an acceleration of 2 g_{rms} and 100 Hz. The variation of measured V_{res} is shown in Figure 6.8(b). The time required by each charging process from 1.1 V to 3.3 V is 100 s. During the capacitor discharge, an average of 6 tag readings are registered. The average energy consumed by the chip is 1.77 μJ for each tag reading.

Shown in Figure 6.9 is the evolution of V_{res} during the data transmission experiments powered by Model R proposed in Chapter 4, where the prototype is biased at 50 V works as the power supply. Figure 6.9(a) shows the charging / discharge of C_{res} with the KEH excited by a sinusoidal acceleration of 11 Hz, 3 g_{peak}. The initial charging from 0 V to 3.3 V takes 22.4 s, during which 5.4 μJ is accumulated, corresponding to the average energy conversion of 22 nJ/cycle. The energy consumption occurs only when the mechanical switch is turned on (connected), the RFID tag is read by the remote reader three times in a row, after which V_{res} drops from 3.3 V to 1 V (the minimum power supply voltage of the RFID chip), and the RFID tag is unavailable to the reader. During each of the following chargings, V_{res} rises from 1 V to 3.3 V, and the increment of energy stored in C_{res} is 4.9 μJ during 16 s. The average energy of 28 nJ is accumulated during each period of the acceleration. Then the mechanical switch is turned off (disconnected), and the accumulation of energy restarts. Since V_{res} varies between 1 V and 3.3 V, the half-wave rectifier is working far from the optimal condition ($V_{\mathrm{res}} = 12$ V), learnt from Figure 4.9(b), the energy conversion of the KEH is much lower than the value under condition (64.4 nJ/cycle).

Figure 6.9b shows the capacitance charging / discharge with the KEH excited by the acceleration of gentle hand shaking motions at a rate of 180 beats per minute, as shown in the inset. The acceleration is featured with repetitive pulses of random waveforms, the average peak acceleration is about 2 g. The initial charging takes 3 min, corresponding to the average power of 30 nW (10 nJ/cycle). Each following chargings takes 2.2 min, corresponding to the average power of 37 nW (12.4 nJ /cycle). These results give us a view of the KEH performance under a practical situation in wearable electronics.

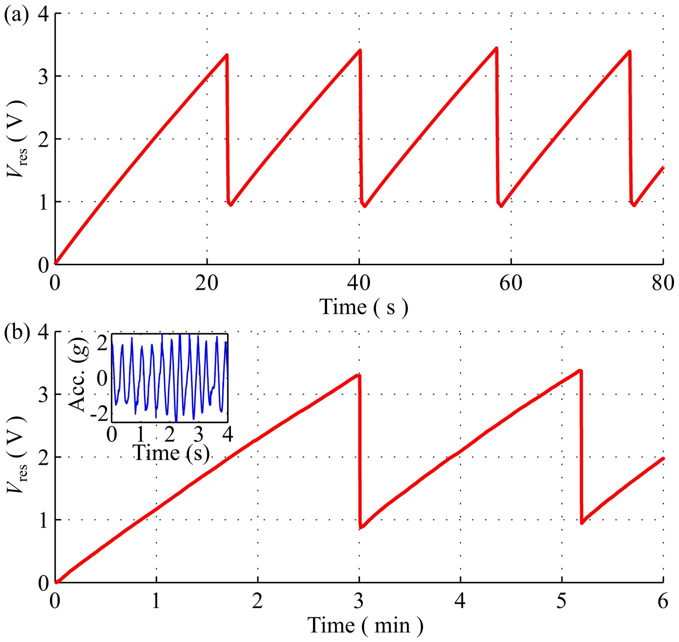

Figure 6.9: Evolution of the voltage across C_{res} (energy conserve / release) during data transmission experiment. Model R biased at 50 V is excited by (a) a sinusoidal acceleration of 11 Hz, 3 g_{peak}, (b) a series of acceleration with shaking motion of hand at ~3 Hz, with the average peak value of 2 g, the inset shows the acceleration recorded from the hand shaking motion.

6.4 Conclusion

In this chapter, a full UHF RFID tag powered by a miniature MEMS KEH was designed. The input impedance of the spiral-loaded dipole was optimized with a commercial electromagnetic simulator. The antenna impedance measured with a differential probe method agreed well with the prediction. The high dependence of the antenna impedance on the fabrication process (milling) was pointed out. The maximum read range of the tag reached 15 m at 868 MHz with a 3.3 V battery.

An experimental methodology to evaluate the performance of the KEH-assisted tag was proposed. The first method is to measure the power consumption of the chip when it is biased by a reservoir capacitor, indicating that the number of tag readings is related to the capacitor value. The second method is to use the full KEH-assisted tag, where the energy delivered by the KEH through an AC-DC rectifier is temporarily stored in a 2.2 μF capacitor. With the KEH working at 2 g_{rms} and 100 Hz, an average of 6 tag readings was observed every 100 s. The average energy consumption of each reading was 1.77 μJ. In real use-cases, the 100-Hz vibration widely exists as a major multiplication of the industrial frequency, while the 2 g_{rms} acceleration is available on electric motors. The design is thus applicable to the industrial environment.

When working with a 1 μF capacitor, the KEH (Model R) proposed in Chapter 4 vibrating at 11 Hz and 3 g_{peak} is able to power 3 tag readings every 16 s. The KEHs applied in the system can also respond to even lower frequencies (less than 10 Hz). Since the power available is proportional to the frequency, the charging duration is inversely proportional to it.

Conclusion and prospect

Conclusion

In this thesis, we have proposed several techniques to improve the adaptability of low frequency electrostatic kinetic energy harvesters to fit for application in wireless sensor nodes and in wearable electronics. And we have proposed a full long read-range battery-less RFID tag which implements a low frequency kinetic energy harvester as power supply.

The first technique proposed for low frequency electrostatic kinetic energy harvester regards the mechanical frequency up conversion (MFuC) mechanism. The prototype for demonstration consists a movable electrode with linear springs and stoppers, and a miniature ball impacting with the movable electrode. It implements the in-plane gap-closing interdigited comb structure for the capacitive component. Corona charging technique is applied to realize the pre-charge of the electret material and internally bias the prototype. The device is then capable to convert mechanical energy into electricity without external bias. The motion of the miniature ball is not limited in frequency domain, and is beneficial for triggering the oscillation of the movable electrode at resonance frequency (around 100 Hz) especially under the excitation of low frequencies (below 50 Hz). The impacts of the movable electrodes on the ball and on the stoppers are both capable of triggering the frequency up conversion behavior. The range of capacitance variation of the prototype is from 22 pF to 87 pF with acceleration of 145 Hz, 2 g_{rms}. Under the optimal configuration (bias voltage of 45 V, excited by the acceleration of 160 Hz 2 g_{rms}, loaded with resistance of 6.6 MΩ), the proposed prototype is able to provide power up to 4.5 μW. It is observed in the transient output signal of the prototype that the huge damping force is a major constrain of the total output power. The source of the huge damping is the thin-film air damping that is inevitable with gap-closing structures with large displacement (i.e. small gap between electrodes).

A fully predictive numeric model of the gap-closing e-KEH is introduced, where the thin-film air damping effect and the geometry of the sidewall resulting from the fabrication processes are taken into account. The model implements several parameters that should be adjusted according to the experimental results. Once these parameters are determined, they can be applied to all the experimental conditions, and is thus predictive and helpful to the simulations for optimization of the design. Adaptive time step is applied in the model to achieve a high accuracy and fast calculation at the same time. The simulation results show a good consistency with the experimental results. From the results of parametric studies using the model, we can clearly see the influence of many key design parameters (the spring stiffness, cavity length, stopper position, etc.) on the performance. With the help of the model, we can easily predict the power performance of the

KEHs at low frequency regardless of the confinement of experimental setup. Taking advantage of the model, we worked out the optimal design parameters of the gap-closing e-KEH that fits the low frequency accelerations (i.e. below 10 Hz).

To minimize the air damping effect in the electrostatic kinetic energy harvesters, we propose in the second demonstrator a hierarchical structure for the capacitive component. Thanks to the new comb geometry, the range of capacitance variation of the prototype is expanded to (25 pF, 400 pF). The power of the hierarchical design is no less than 33 times higher than that of the in-plane gap-closing design at 2 g_{peak} within 10∼40 Hz. Under the optimal configuration in air (Model R with the bias voltage of 45 V and the resistive load of 6.6 MΩ), the prototype with hierarchical comb structure provides the power of 13.2 μW with the vibration of 50 Hz, 3 g_{peak}. The maximum efficiency of AC/DC transduction of 54% is reached through full-wave rectifier (64.4Â nJ/cycle), and its best configuration is the bias voltage of 45 V and the storage voltage of 12 V. The reduction of air damping is a major cause of the power improvement.

A fully flexible e-KEH is demonstrated implementing paper-based electrodes and electret films based on electrospun nanofibrous material, which is applicable to wearable electronics. We propose a new preparation of flexible electret material, where the material for charge storage is deposited on the surface of electrospun nanofibers. The electret prepared in this way provides a better stability of charge storage than planar films. The e-KEH based on this type of electret provides a range of capacitance variation between 28 pF and 75 pF. The peak power of the optimal configuration of flexible e-KEH is 45.6 μW, with the average energy conversion of 54 nJ/stroke, which still needs improvement for real-life applications.

A 2D e-KEH is also proposed so as to make the harvester sensible to vibrations along multiple directions. Some preliminary results based on MEMS+ simulations are presented, which show the prototype's capability to respond to vibrations parallel the wafer plane. The resonant frequency of the spring-mass structure is about 400 Hz, which can be triggered by the impacts from the ball in the center. The device is currently in fabrication, and can soon be ready for characterization.

A long read-range semi-passive RFID tag is proposed, which is powered by e-KEH instead of batteries that needs replacement or recharging. A spiral-loaded dipole antenna with impedance matching circuit is designed for the communication module through HFSS simulations, and the key fabrication parameters determining the accuracy of impedance matching are analyzed. Two methods to measure the impedance of the antenna are compared, showing that the differential probe has a better accuracy. The read range of the tag is 15 m, which can be further maximized by a better impedance matching. The average power consumption of the RFID tag during one tag reading is 1.77 μJ. The current optimal e-KEH prototype is implemented in the system as power supply module, the RFID tag is able to communicate with the remote reader 3 times every 16 s (with the e-KEH excited at 11 Hz 3 g_{peak}).

Prospect

The current designs of the e-KEH are still at a distance from the real-life application, because it is still limited in the power delivery. To further improve their performance, we are now working on implementing other methods and techniques into the system. One method is to introduce different structures on the device and handle layers of the SOI wafer, so as to take advantage of a higher fabrication resolution on the thinner silicon structure. In-plane overlapping structure can be introduced to the mask with higher fabrication resolution, so as to achieve a large capacitance variation even when the excitation acceleration is low. Other improvements include introducing a 3D design that can respond to vibrations along any direction to improve the adaptability of the prototype, implementing stoppers with repulsive electrostatic force to raise the voltage limit brought by pull-in, and integrating silicon-dioxide based electret to improve the charge stability and to enhance the adaptability of the fabrication process. Future works can also emphasize on adjust the design of the entire RFID tag into a fully flexible system, which can be easily integrated into wearable electronics. To reach this goal, we need to redesign the e-KEH to low frequency matching the human motions (between 1 Hz and 10 Hz), and to design a RF communication module on flexible substrate taking into account the influence of human body to the electromagnetic waves. All these are clues for further improving our current results, and are the target of our on-going works.

Achievements

Resume

In 1989, Yingxian LU is born in Zhengzhou, China. In July 2010, she obtained bachelor's degree in electronic and information engineering from Beihang University. She achieved master's degree in integrated circuit engineering from Tsinghua University in July 2014. She worked on an SATT project as a researcher in ESIEE Paris from October 2014 to September 2015, and has been working on the PhD thesis in electronic engineering since October 2015.

Journals

1. Yingxian Lu, Francesco Cottone, Sébastien Boisseau, Frédéric Marty, Dimitri Galayko, and Philippe Basset. A nonlinear mems electrostatic kinetic energy harvester for human-powered biomedical devices. *Applied Physics Letters*, 107(25):253902, 2015

2. Yingxian Lu, Eoghan O'Riordan, Francesco Cottone, Sébastien Boisseau, Dimitri Galayko, Elena Blokhina, Frédéric Marty, and Philippe Basset. A batch-fabricated electret-biased wideband mems vibration energy harvester with frequency-up conversion behavior powering a uhf wireless sensor node. *Journal of Micromechanics and Microengineering*, 26(12):124004, 2016

3. Yingxian Lu, Philippe Basset, and Jean-Marc Laheurte. Performance evaluation of a long-range rfid tag powered by a vibration energy harvester. *IEEE Antennas and Wireless Propagation Letters*, 16:1832–1835, 2017

4. Yingxian Lu, M Capo-Chichi, Yamin Leprince-Wang, and Philippe Basset. A flexible electrostatic kinetic energy harvester based on electret films of electrospun nanofibers. *Smart Materials and Structures*, 27(1):014001, 2017

5. Yingxian Lu, Frédéric Marty, Dimitri Galayko, Jean-Marc Laheurte, and Philippe Basset. A power supply module for autonomous portable electronics: ultralow-frequency mems electrostatic kinetic energy harvester with hierarchical comb structure reducing air damping. *Microsystems and Nanoengineering*, 2018 (Accepted)

6. Yingxian Lu, Juillard Jérôme, Francesco Cottone, Dimitri Galayko, and Philippe Basset. An impact-coupled electrostatic kinetic energy harvester and its predictive model taking

nonlinear air damping effect into account. *Journal of Microelectromechanical Systems*, 2018 (Submitted)

7. Linda Serairi, Long Gu, Yong Qin, Yingxian Lu, Philippe Basset, and Yamin Leprince-Wang. Flexible piezoelectric nanogenerators based on pvdf-trfe nanofibers. *The European Physical Journal Applied Physics*, 80(3):30901, 2017

8. Ali Ghaffarinejad, Yingxian Lu, Ronan Hichet, Dimitri Galayko, Javad Yavand Hasani, Philippe Basset, et al. Bennet's doubler working as a power booster for triboelectric nano generators. *Electronics Letters*, 2017

9. Ronan Hinchet, Ali Ghaffarinejad, Yingxian Lu, Javad Yavand Hasani, Sang-Woo Kim, and Philippe Basset. Understanding and modeling of triboelectric-electret nanogenerator. *Nano Energy*, 2018

Patents

1. Philippe Basset, Yingxian Lu, and Yamin Leprince-Wang. Electrostatic transducer for kinetic energy harvesting or mechanical sensing

2. Philippe Basset and Yingxian Lu. Miniature kinetic energy harvester for generating electrical energy from mechanical vibrations

Conferences

1. Yingxian Lu, Francesco Cottone, Sébastien Boisseau, Dimitri Galayko, Frédéric Marty, and Philippe Basset. Low-frequency mems electrostatic vibration energy harvester with corona-charged vertical electrets and nonlinear stoppers. In *Journal of Physics: Conference Series*, volume 660, page 012003. IOP Publishing, 2015 (PowerMEMS 2015)

2. Yingxian Lu, Francesco Cottone, Sébastien Boisseau, Frédéric Marty, Dimitri Galayko, and Philippe Basset. Low-frequency and ultra-wideband mems electrostatic vibration energy harvester powering an autonomous wireless temperature sensor node. In *Micro Electro Mechanical Systems (MEMS), 2016 IEEE 29th International Conference on*, pages 33–36. IEEE, 2016

3. Yingxian Lu, D Amroun, Yamin Leprince-Wang, and Philippe Basset. A paper-based electrostatic kinetic energy harvester with stacked multiple electret films made of electrospun polymer nanofibers. In *Journal of Physics: Conference Series*, volume 773, page 012032. IOP Publishing, 2016 (PowerMEMS 2016)

4. Yingxian Lu, Frédéric Marty, Dimitri Galayko, and Philippe Basset. New comb geometry of capacitive vibration energy harvesters miniaturizing the air damping effect. In *Micro Electro Mechanical Systems (MEMS), 2017 IEEE 30th International Conference on*, pages 857–860. IEEE, 2017

5. Yingxian Lu, Frédéric Marty, Dimitri Galayko, Jean-Marc Laheurte, and Philippe Basset. A mems eveh-assisted long-range rfid tag system for applications with low-frequency vibrations. In *Multidisciplinary Digital Publishing Institute Proceedings*, volume 1, page 582, 2017 (EuroSensors 2017)

6. MA Ben Ouanes, Yingxian Lu, Hatem Samaali, Philippe Basset, and F Najar. Design and test of a bennet's doubler device with mechanical switches for vibrational energy harvesting. In *Journal of Physics: Conference Series*, volume 773, page 012038. IOP Publishing, 2016 (PowerMEMS 2016)

Honors

1. Yingxian Lu et al, Best oral paper, PowerMEMS 2016

2. Yingxian Lu et al, Outstanding paper finalist, IEEE MEMS 2017

3. Yingxian Lu, 2017 Chinese government award for outstanding self-financed students abroad, China Scholarship Council

Bibliography

[1] Paul D Mitcheson, Eric M Yeatman, G Kondala Rao, Andrew S Holmes, and Tim C Green. Energy harvesting from human and machine motion for wireless electronic devices. *Proceedings of the IEEE*, 96(9):1457–1486, 2008.

[2] Philippe Basset, Dimitri Galayko, Francesco Cottone, Raphaël Guillemet, Elena Blokhina, Frédéric Marty, and Tarik Bourouina. Electrostatic vibration energy harvester with combined effect of electrical nonlinearities and mechanical impact. *Journal of Micromechanics and Microengineering*, 24(3):035001, 2014.

[3] P Basset, D Galayko, A Mahmood Paracha, F Marty, A Dudka, and T Bourouina. A batch-fabricated and electret-free silicon electrostatic vibration energy harvester. *Journal of Micromechanics and Microengineering*, 19(11):115025, 2009.

[4] Philippe Basset, Elena Blokhina, and Dimitri Galayko. *Electrostatic kinetic energy harvesting*. John Wiley & Sons, 2016.

[5] Rolf H Weber and Romana Weber. *Internet of things*, volume 12. Springer, 2010.

[6] Brett Warneke, Matt Last, Brian Liebowitz, and Kristofer SJ Pister. Smart dust: Communicating with a cubic-millimeter computer. *Computer*, 34(1):44–51, 2001.

[7] Alan Mainwaring, David Culler, Joseph Polastre, Robert Szewczyk, and John Anderson. Wireless sensor networks for habitat monitoring. In *Proceedings of the 1st ACM international workshop on Wireless sensor networks and applications*, pages 88–97. Acm, 2002.

[8] Christian C Enz, Amre El-Hoiydi, J-D Decotignie, and Vincent Peiris. Wisenet: an ultralow-power wireless sensor network solution. *Computer*, 37(8):62–70, 2004.

[9] Vijay Raghunathan, Curt Schurgers, Sung Park, and Mani B Srivastava. Energy-aware wireless microsensor networks. *IEEE Signal processing magazine*, 19(2):40–50, 2002.

[10] Shad Roundy, Dan Steingart, Luc Frechette, Paul Wright, and Jan Rabaey. Power sources for wireless sensor networks. In *European workshop on wireless sensor networks*, pages 1–17. Springer, 2004.

[11] Suresh Singh, Mike Woo, and Cauligi S Raghavendra. Power-aware routing in mobile ad hoc networks. In *Proceedings of the 4th annual ACM/IEEE international conference on Mobile computing and networking*, pages 181–190. ACM, 1998.

[12] Kanishka Lahiri, Sujit Dey, Debashis Panigrahi, and Anand Raghunathan. Battery-driven system design: A new frontier in low power design. In *Proceedings of the 2002 Asia and South Pacific Design Automation Conference*, page 261. IEEE Computer Society, 2002.

[13] Fabio Ongaro, Stefano Saggini, and Paolo Mattavelli. Li-ion battery-supercapacitor hybrid storage system for a long lifetime, photovoltaic-based wireless sensor network. *IEEE Transactions on Power Electronics*, 27(9):3944–3952, 2012.

[14] Yohann RJ Thomas, Matthieu Picot, Arnaud Carer, Olivier Berder, Olivier Sentieys, and Frédéric Barrière. A single sediment-microbial fuel cell powering a wireless telecommunication system. *Journal of Power Sources*, 241:703–708, 2013.

[15] Tonia Tommasi, Alessandro Chiolerio, Marco Crepaldi, and Danilo Demarchi. A microbial fuel cell powering an all-digital piezoresistive wireless sensor system. *Microsystem technologies*, 20(4-5):1023–1033, 2014.

[16] Farhan Simjee and Pai H Chou. Everlast: long-life, supercapacitor-operated wireless sensor node. In *Low Power Electronics and Design, 2006. ISLPED'06. Proceedings of the 2006 International Symposium on*, pages 197–202. IEEE, 2006.

[17] Farhan I Simjee and Pai H Chou. Efficient charging of supercapacitors for extended lifetime of wireless sensor nodes. *IEEE Transactions on power electronics*, 23(3):1526–1536, 2008.

[18] Hengzhao Yang and Ying Zhang. Analysis of supercapacitor energy loss for power management in environmentally powered wireless sensor nodes. *IEEE transactions on power electronics*, 28(11):5391–5403, 2013.

[19] Yingxian Lu, Philippe Basset, and Jean-Marc Laheurte. Performance evaluation of a long-range rfid tag powered by a vibration energy harvester. *IEEE Antennas and Wireless Propagation Letters*, 16:1832–1835, 2017.

[20] Winston KG Seah, Zhi Ang Eu, and Hwee-Pink Tan. Wireless sensor networks powered by ambient energy harvesting (wsn-heap)-survey and challenges. In *Wireless Communication, Vehicular Technology, Information Theory and Aerospace & Electronic Systems Technology, 2009. Wireless VITAE 2009. 1st International Conference on*, pages 1–5. IEEE, 2009.

[21] Faruk Yildiz. Potential ambient energy-harvesting sources and techniques. 2009.

[22] Brian O'regan and Michael Grätzel. A low-cost, high-efficiency solar cell based on dye-sensitized colloidal tio2 films. *nature*, 353(6346):737, 1991.

[23] Triet Le, Karti Mayaram, and Terri Fiez. Efficient far-field radio frequency energy harvesting for passively powered sensor networks. *IEEE Journal of solid-state circuits*, 43(5):1287–1302, 2008.

[24] Vladimir Leonov. Thermoelectric energy harvesting of human body heat for wearable sensors. *IEEE Sensors Journal*, 13(6):2284–2291, 2013.

[25] Davide Carli, Davide Brunelli, Davide Bertozzi, and Luca Benini. A high-efficiency wind-flow energy harvester using micro turbine. In *Power electronics electrical drives automation and motion (SPEEDAM), 2010 international symposium on*, pages 778–783. IEEE, 2010.

[26] Steve P Beeby, RN Torah, MJ Tudor, P Glynne-Jones, T O'donnell, CR Saha, and S Roy. A micro electromagnetic generator for vibration energy harvesting. *Journal of Micromechanics and microengineering*, 17(7):1257, 2007.

[27] JW Matiko, NJ Grabham, SP Beeby, and MJ Tudor. Review of the application of energy harvesting in buildings. *Measurement Science and Technology*, 25(1):012002, 2013.

[28] Michael Peigney and Dominique Siegert. Piezoelectric energy harvesting from traffic-induced bridge vibrations. *Smart Materials and Structures*, 22(9):095019, 2013.

[29] Peter L Green, Evangelos Papatheou, and Neil D Sims. Energy harvesting from human motion and bridge vibrations: An evaluation of current nonlinear energy harvesting solutions. *Journal of Intelligent Material Systems and Structures*, 24(12):1494–1505, 2013.

[30] Chung-Yang Sue and Nan-Chyuan Tsai. Human powered mems-based energy harvest devices. *Applied Energy*, 93:390–403, 2012.

[31] Walter G Cady. Piezoelectric vibrators and systems embodying the same for converting the mechanical vibration thereof into electric energy, February 27 1968. US Patent 3,371,234.

[32] Oleg D Jefimenko and David K Walker. Electrostatic current generator having a disk electret as an active element. *IEEE Transactions on Industry Applications*, (6):537–540, 1978.

[33] CB Williams and Rob B Yates. Analysis of a micro-electric generator for microsystems. *sensors and actuators A: Physical*, 52(1-3):8–11, 1996.

[34] Scott D Moss, Joshua E McLeod, Ian G Powlesland, and Steve C Galea. A bi-axial magnetoelectric vibration energy harvester. *Sensors and Actuators A: Physical*, 175:165–168, 2012.

[35] Perpetuum Limited. Pmg17 datasheet. `http://www.perpetuum.co.uk/resource/PMG17-100_dsheet.pdf`.

[36] Ferro Solutions. Veh360 datasheet. `http://www.ferrosi.com/files/VEH360_datasheet.pdf`.

[37] Mide. Peh20w datasheet. `http://www.mide.com/Products/volture/peh20w/peh20w.php`.

[38] Kinetron. Mg204 datasheet. `http://www.kinetron.nl`.

[39] Huicong Liu, Chengkuo Lee, Takeshi Kobayashi, Cho Jui Tay, and Chenggen Quan. A new s-shaped mems pzt cantilever for energy harvesting from low frequency vibrations below 30 hz. *Microsystem technologies*, 18(4):497–506, 2012.

[40] Özge Zorlu, Serol Türkyilmaz, Ali Muhtaroğlu, and Haluk Külah. An electromagnetic energy harvester for low frequency and low-g vibrations with a modified frequency up conversion method. In *Micro Electro Mechanical Systems (MEMS), 2013 IEEE 26th International Conference on*, pages 805–808. IEEE, 2013.

[41] F Cottone, P Basset, F Marty, D Galayko, L Gammaitoni, and T Bourouina. Electrostatic generator with free micro-ball and elastic stoppers for low-frequency vibration harvesting. In *Micro Electro Mechanical Systems (MEMS), 2014 IEEE 27th International Conference on*, pages 385–388. IEEE, 2014.

[42] David F Berdy, Pornsak Srisungsitthisunti, Byunghoo Jung, Xianfan Xu, Jeffrey F Rhoads, and Dimitrios Peroulis. Low-frequency meandering piezoelectric vibration energy harvester. *IEEE transactions on ultrasonics, ferroelectrics, and frequency control*, 59(5):846–858, 2012.

[43] Miah A Halim and Jae Y Park. A non-resonant, frequency up-converted electromagnetic energy harvester from human-body-induced vibration for hand-held smart system applications. *Journal of Applied Physics*, 115(9):094901, 2014.

[44] Y Naruse, N Matsubara, K Mabuchi, M Izumi, and S Suzuki. Electrostatic micro power generation from low-frequency vibration such as human motion. *Journal of Micromechanics and Microengineering*, 19(9):094002, 2009.

[45] SP Beeby, MJ Tudor, and NM White. Energy harvesting vibration sources for microsystems applications. *Measurement science and technology*, 17(12):R175, 2006.

[46] Michael Renaud, Paolo Fiorini, Rob van Schaijk, and Chris Van Hoof. Harvesting energy from the motion of human limbs: the design and analysis of an impact-based piezoelectric generator. *Smart Materials and Structures*, 18(3):035001, 2009.

[47] B Cavallier, P Berthelot, H Nouira, E Foltete, L Hirsinger, S Ballandras, et al. Energy harvesting using vibrating structures excited by shock. In *IEEE Ultrasonics Symposium*, volume 2, pages 943–945, 2005.

[48] Marco Ferrari, Vittorio Ferrari, Michele Guizzetti, and Daniele Marioli. An autonomous battery-less sensor module powered by piezoelectric energy harvesting with rf transmission of multiple measurement signals. *Smart materials and Structures*, 18(8):085023, 2009.

[49] Arian Rahimi, Özge Zorlu, Ali Muhtaroglu, and Haluk Kulah. Fully self-powered electromagnetic energy harvesting system with highly efficient dual rail output. *IEEE Sensors Journal*, 12(6):2287–2298, 2012.

[50] Yoshiaki Minakawa, Rui Chen, and Yuji Suzuki. X-shaped-spring enhanced mems electret generator for energy harvesting. In *Solid-State Sensors, Actuators and Microsystems (TRANSDUCERS & EUROSENSORS XXVII), 2013 Transducers & Eurosensors XXVII: The 17th International Conference on*, pages 2241–2244. IEEE, 2013.

[51] M Amin Karami and Daniel J Inman. Analytical modeling and experimental verification of the vibrations of the zigzag microstructure for energy harvesting. *Journal of Vibration and Acoustics*, 133(1):011002, 2011.

[52] In-Ho Kim, SeungSeop Jin, Seon-Jun Jang, and Hyung-Jo Jung. A performance-enhanced energy harvester for low frequency vibration utilizing a corrugated cantilevered beam. *Smart Materials and Structures*, 23(3):037002, 2014.

[53] Wen Liu, MengDi Han, Bo Meng, XuMing Sun, XianLiang Huang, and HaiXia Zhang. Low frequency wide bandwidth mems energy harvester based on spiral-shaped pvdf cantilever. *Science China Technological Sciences*, 57(6):1068–1072, 2014.

[54] Sachin Nadig, Serhan Ardanuç, and Amit Lal. Monolithic 2-axis in-plane pzt lateral bimorph energy harvester with differential output. In *Micro Electro Mechanical Systems (MEMS), 2015 28th IEEE International Conference on*, pages 1129–1132. IEEE, 2015.

[55] Paul D Mitcheson, Tim C Green, Eric M Yeatman, and Andrew S Holmes. Architectures for vibration-driven micropower generators. *Journal of microelectromechanical systems*, 13(3):429–440, 2004.

[56] Yuji Suzuki, Daigo Miki, Masato Edamoto, and Makoto Honzumi. A mems electret generator with electrostatic levitation for vibration-driven energy-harvesting applications. *Journal of Micromechanics and Microengineering*, 20(10):104002, 2010.

[57] Jiuxuan Zhao, Hong Ding, and Jin Xie. Electrostatic charge sensor based on a micromachined resonator with dual micro-levers. *Applied Physics Letters*, 106(23):233505, 2015.

[58] Huicong Liu, Cho Jui Tay, Chenggen Quan, Takeshi Kobayashi, and Chengkuo Lee. Piezoelectric mems energy harvester for low-frequency vibrations with wideband operation range and steadily increased output power. *Journal of Microelectromechanical systems*, 20(5):1131–1142, 2011.

[59] Yingxian Lu, Xiaohong Wang, Xiaoming Wu, Jin Qin, and Ruochen Lu. A non-resonant, gravity-induced micro triboelectric harvester to collect kinetic energy from low-frequency jiggling movements of human limbs. *Journal of Micromechanics and Microengineering*, 24(6):065010, 2014.

[60] Einar Halvorsen. Energy harvesters driven by broadband random vibrations. *Journal of Microelectromechanical Systems*, 17(5):1061–1071, 2008.

[61] J Rastegar, C Pereira, and H-L Nguyen. Piezoelectric-based power sources for harvesting energy from platforms with low-frequency vibration. In *Smart Structures and Materials 2006: Industrial and Commercial Applications of Smart Structures Technologies*, volume 6171, page 617101. International Society for Optics and Photonics, 2006.

[62] Kai Tao, Lihua Tang, Jin Wu, Sun Woh Lye, Honglong Chang, and Jianmin Miao. Investigation of multimodal electret-based mems energy harvester with impact-induced nonlinearity.

[63] Scott Moss, Alex Barry, Ian Powlesland, Steve Galea, and Gregory P Carman. A low profile vibro-impacting energy harvester with symmetrical stops. *Applied physics letters*, 97(23):234101, 2010.

[64] Lei Gu and Carol Livermore. Impact-driven, frequency up-converting coupled vibration energy harvesting device for low frequency operation. *Smart Materials and Structures*, 20(4):045004, 2011.

[65] S Moss, A Barry, I Powlesland, S Galea, and GP Carman. A broadband vibro-impacting power harvester with symmetrical piezoelectric bimorph-stops. *Smart Materials and Structures*, 20(4):045013, 2011.

[66] Emilio Sardini and Mauro Serpelloni. An efficient electromagnetic power harvesting device for low-frequency applications. *Sensors and Actuators A: Physical*, 172(2):475–482, 2011.

[67] Bin Yang and Chengkuo Lee. Non-resonant electromagnetic wideband energy harvesting mechanism for low frequency vibrations. *Microsystem Technologies*, 16(6):961–966, 2010.

[68] T Galchev, H Kim, and K Najafi. Non-resonant bi-stable frequency-increased power scavenger from low-frequency ambient vibration. In *Solid-State Sensors, Actuators and Microsystems Conference, 2009. TRANSDUCERS 2009. International*, pages 632–635. IEEE, 2009.

[69] Tzeno Galchev, Hanseup Kim, and Khalil Najafi. Micro power generator for harvesting low-frequency and nonperiodic vibrations. *Journal of Microelectromechanical Systems*, 20(4):852–866, 2011.

[70] Tzeno Galchev, Ethem Erkan Aktakka, and Khalil Najafi. A piezoelectric parametric frequency increased generator for harvesting low-frequency vibrations. *Journal of Microelectromechanical Systems*, 21(6):1311–1320, 2012.

[71] SC Chang, FM Yaul, A Dominguez-Garcia, F O'Sullivan, DM Otten, and JH Lang. Harvesting energy from moth vibrations during flight. In *International Workshop on Micro and Nanotechnologies for Power Generation and Energy Conversion Applications*, pages 3–6, 2009.

[72] AM Wickenheiser and E Garcia. Broadband vibration-based energy harvesting improvement through frequency up-conversion by magnetic excitation. *Smart materials and Structures*, 19(6):065020, 2010.

[73] S Möst, M Kluge, J Heinz, and G Krötz. A new high efficiency bidirectional electromagnetic vibration energy harvester for aeronautical applications. In *Proc. PowerMEMS*, pages 115–118, 2010.

[74] Tomokazu Takahashi, Masato Suzuki, Toshio Nishida, Yasuhiro Yoshikawa, and Seiji Aoyagi. Vertical capacitive energy harvester positively using contact between proof mass and electret plate-stiffness matching by spring support of plate and stiction prevention by stopper mechanism. In *Micro Electro Mechanical Systems (MEMS), 2015 28th IEEE International Conference on*, pages 1145–1148. IEEE, 2015.

[75] B Ando, S Baglio, C Trigona, N Dumas, Laurent Latorre, and P Nouet. Nonlinear mechanism in mems devices for energy harvesting applications. *Journal of Micromechanics and Microengineering*, 20(12):125020, 2010.

[76] Francesco Cottone, Helios Vocca, and L Gammaitoni. Nonlinear energy harvesting. *Physical Review Letters*, 102(8):080601, 2009.

[77] M Ferrari, V Ferrari, M Guizzetti, B Andò, S Baglio, and C Trigona. Improved energy harvesting from wideband vibrations by nonlinear piezoelectric converters. *Sensors and Actuators A: Physical*, 162(2):425–431, 2010.

[78] Yu-Yin Chen, Dejan Vasic, François Costa, and WJ Wu. Nonlinear magnetic coupling of a piezoelectric energy harvesting cantilever combined with velocity-controlled synchronized switching technique. *Power MEMS*, 2010.

[79] Helios Vocca, Igor Neri, Flavio Travasso, and Luca Gammaitoni. Kinetic energy harvesting with bistable oscillators. *Applied Energy*, 97:771–776, 2012.

[80] Felice Maiorca, Fabio Giusa, Carlo Trigona, Bruno Andò, Adi R Bulsara, and Salvatore Baglio. Diode-less mechanical h-bridge rectifier for "zero threshold" vibration energy harvesters. *Sensors and Actuators A: Physical*, 201:246–253, 2013.

[81] Takahiro Sato, Kota Watanabe, and Hajime Igarashi. Coupled analysis of electromagnetic vibration energy harvester with nonlinear oscillation. *IEEE Transactions on magnetics*, 50(2):313–316, 2014.

[82] Seok-Min Jung and Kwang-Seok Yun. Energy-harvesting device with mechanical frequency-up conversion mechanism for increased power efficiency and wideband operation. *Applied Physics Letters*, 96(11):111906, 2010.

[83] Ravindra Masana and Mohammed F Daqaq. Exploiting super-harmonic resonances of a bi-stable axially-loaded beam for energy harvesting under low-frequency excitations. In *ASME 2011 International Design Engineering Technical Conferences and Computers and Information in Engineering Conference*, pages 999–1008. American Society of Mechanical Engineers, 2011.

[84] F Cottone, L Gammaitoni, H Vocca, M Ferrari, and V Ferrari. Piezoelectric buckled beams for random vibration energy harvesting. *Smart materials and structures*, 21(3):035021, 2012.

[85] Bruno Ando, Salvatore Baglio, Gaetano L'Episcopo, and Carlo Trigona. Investigation on mechanically bistable mems devices for energy harvesting from vibrations. *Journal of Microelectromechanical Systems*, 21(4):779–790, 2012.

[86] Chundong Xu, Zhu Liang, Bo Ren, Wenning Di, Haosu Luo, Dong Wang, Kailing Wang, and Zhifang Chen. Bi-stable energy harvesting based on a simply supported piezoelectric buckled beam. *Journal of Applied Physics*, 114(11):114507, 2013.

[87] B Andò, S Baglio, AR Bulsara, V Marletta, I Medico, and S Medico. A double piezo-snap through buckling device for energy harvesting. In *Solid-State Sensors, Actuators and Microsystems (TRANSDUCERS & EUROSENSORS XXVII), 2013 Transducers & Eurosensors XXVII: The 17th International Conference on*, pages 43–45. IEEE, 2013.

[88] Wei Qun Liu, Adrien Badel, Fabien Formosa, Yi Peng Wu, and Amen Agbossou. Wideband energy harvesting using a combination of an optimized synchronous electric charge extraction circuit and a bistable harvester. *Smart Materials and Structures*, 22(12):125038, 2013.

[89] Cuong Phu Le and Einar Halvorsen. Wide tuning-range resonant-frequency control by combining electromechanical softening and hardening springs. In *Solid-State Sensors, Actuators and Microsystems (TRANSDUCERS & EUROSENSORS XXVII), 2013 Transducers & Eurosensors XXVII: The 17th International Conference on*, pages 1352–1355. IEEE, 2013.

[90] William B Hobbs and David L Hu. Tree-inspired piezoelectric energy harvesting. *Journal of fluids and Structures*, 28:103–114, 2012.

[91] Qian Zhang, Yufeng Wang, and Eun Sok Kim. Power generation from human body motion through magnet and coil arrays with magnetic spring. *Journal of Applied Physics*, 115(6):064908, 2014.

[92] Shuo Cheng and David P Arnold. A study of a multi-pole magnetic generator for low-frequency vibrational energy harvesting. *Journal of Micromechanics and Microengineering*, 20(2):025015, 2009.

[93] SH Chae, S Ju, Y Choi, S Jun, SM Park, S Lee, HW Lee, and CH Ji. Electromagnetic vibration energy harvester using springless proof mass and ferrofluid as a lubricant. In *Journal of Physics: Conference Series*, volume 476, page 012013. IOP Publishing, 2013.

[94] Soon-Duck Kwon, Jinkyoo Park, and Kincho Law. Electromagnetic energy harvester with repulsively stacked multilayer magnets for low frequency vibrations. *Smart materials and structures*, 22(5):055007, 2013.

[95] Daigo Miki, Makoto Honzumi, Yuji Suzuki, and Nobuhide Kasagi. Large-amplitude mems electret generator with nonlinear spring. In *Micro Electro Mechanical Systems (MEMS), 2010 IEEE 23rd International Conference on*, pages 176–179. IEEE, 2010.

[96] Ling Bu, Xiaoming Wu, and Litian Liu. Collision based capacitive vibration energy harvesting. In *Solid-State and Integrated Circuit Technology (ICSICT), 2010 10th IEEE International Conference on*, pages 1955–1957. IEEE, 2010.

[97] Tatsuakira Masaki, Kenji Sakurai, Toru Yokoyama, Masayo Ikuta, Hiroshi Sameshima, Masashi Doi, Tomonori Seki, and Masatoshi Oba. Power output enhancement of a vibration-driven electret generator for wireless sensor applications. *Journal of Micromechanics and Microengineering*, 21(10):104004, 2011.

[98] SW Liu, JM Miao, and SW Lye. High q and low resonant frequency micro electret energy harvester for harvesting low amplitude harmonic of vibration. In *Micro Electro Mechanical Systems (MEMS), 2013 IEEE 26th International Conference on*, pages 837–840. IEEE, 2013.

[99] P Pillatsch, EM Yeatman, and AS Holmes. A scalable piezoelectric impulse-excited energy harvester for human body excitation. *Smart Materials and Structures*, 21(11):115018, 2012.

[100] Xue Feng He, You Zhu, Yao Qing Cheng, and Jun Gao. Broadband low-frequency vibration energy harvester with a rolling mass. In *Applied Mechanics and Materials*, volume 404, pages 635–639. Trans Tech Publ, 2013.

[101] Y Choi, S Ju, SH Chae, S Jun, SM Park, S Lee, HW Lee, and CH Ji. Low frequency vibration energy harvester using spherical permanent magnet with non-uniform mass distribution. In *Journal of Physics: Conference Series*, volume 476, page 012123. IOP Publishing, 2013.

[102] S Ju and C-H Ji. Indirect impact based piezoelectric energy harvester for low frequency vibration. In *Solid-State Sensors, Actuators and Microsystems (TRANSDUCERS), 2015 Transducers-2015 18th International Conference on*, pages 1913–1916. IEEE, 2015.

[103] N Fondevilla, C Serre, A Peréz-Rodríguez, MC Acero, E Cabruja, H Campanella, and J Esteve. Electromagnetic harvester device for scavenging ambient mechanical energy with slow, variable, and randomness nature. In *Power Engineering, Energy and Electrical Drives (POWERENG), 2011 International Conference on*, pages 1–5. IEEE, 2011.

[104] Michele Pozzi and Meiling Zhu. Plucked piezoelectric bimorphs for knee-joint energy harvesting: modelling and experimental validation. *Smart Materials and Structures*, 20(5):055007, 2011.

[105] E Romero, MR Neuman, and RO Warrington. Kinetic energy harvester for body motion. In *Proc. PowerMEMS*, pages 237–240, 2009.

[106] H Jiang, ME Kiziroglou, DC Yates, and EM Yeatman. A non-harmonic motion-powered piezoelectric fm wireless sensing system. In *Solid-State Sensors, Actuators and Microsystems (TRANSDUCERS), 2015 Transducers-2015 18th International Conference on*, pages 710–713. IEEE, 2015.

[107] Ken Sasaki, Yuji Osaki, Jun Okazaki, Hiroshi Hosaka, and Kiyoshi Itao. Vibration-based automatic power-generation system. *Microsystem technologies*, 11(8-10):965–969, 2005.

[108] Yuji Suzuki, Masato Edamoto, Nobuhide Kasagi, K Kashwagi, and Yoshitomi Morizawa. Micro electret energy harvesting device with analogue impedance conversion circuit. *Proc. PowerMEMS*, 8:7–10, 2008.

[109] Lei Wang and FG Yuan. Vibration energy harvesting by magnetostrictive material. *Smart Materials and Structures*, 17(4):045009, 2008.

[110] Boram Yang and Kwang-Seok Yun. Piezoelectric shell structures as wearable energy harvesters for effective power generation at low-frequency movement. *Sensors and Actuators A: Physical*, 188:427–433, 2012.

[111] Ahmed Almusallam, RN Torah, Dibin Zhu, MJ Tudor, and SP Beeby. Screen-printed piezoelectric shoe-insole energy harvester using an improved flexible pzt-polymer composites. In *Journal of Physics: Conference Series*, volume 476, page 012108. IOP Publishing, 2013.

[112] Takahiro Yamashita, Seiichi Takamatsu, Takeshi Kobayashi, and Toshihiro Itoh. Characterization of an all polymer piezoelectric film using a reel-to-reel continuous fiber process. In *Design, Test, Integration and Packaging of MEMS/MOEMS (DTIP), 2013 Symposium on*, pages 1–4. IEEE, 2013.

[113] Lindsay M Miller, Einar Halvorsen, Tao Dong, and Paul K Wright. Modeling and experimental verification of low-frequency mems energy harvesting from ambient vibrations. *Journal of Micromechanics and Microengineering*, 21(4):045029, 2011.

[114] A Vásquez Quintero, D Briand, P Janphuang, JJ Ruan, R Lockhart, and NF de Rooij. Vibration energy harvesters on plastic foil by lamination of pzt thick sheets. In *Micro Electro Mechanical Systems (MEMS), 2012 IEEE 25th International Conference on*, pages 1289–1292. Ieee, 2012.

[115] J Rastegar and R Murray. Novel two-stage piezoelectric-based electrical energy generators for low and variable speed rotary machinery. In *Active and Passive Smart Structures and Integrated Systems 2009*, volume 7288, page 72880B. International Society for Optics and Photonics, 2009.

[116] Tien-Kan Chung, Chieh-Min Wang, Chia-Yuan Tseng, Tzu-Wei Liu, and Po-Chen Yeh. A micro kinetic energy harvester demonstrating energy harvesting from 3-d mechanical motion and power increasing through magnetic-based frequency rectification. In *ASME 2012 Conference on Smart Materials, Adaptive Structures and Intelligent Systems*, pages 853–858. American Society of Mechanical Engineers, 2012.

[117] P Pillatsch, EM Yeatman, and AS Holmes. Magnetic plucking of piezoelectric beams for frequency up-converting energy harvesters. *Smart Materials and Structures*, 23(2):025009, 2013.

[118] Hao Jiang and Eric M Yeatman. A piezoelectric pulse generator for low frequency non-harmonic vibration. In *Journal of Physics: Conference Series*, volume 476, page 012059. IOP Publishing, 2013.

[119] Wei-Jiun Su and Jean Zu. An innovative tri-directional broadband piezoelectric energy harvester. *Applied Physics Letters*, 103(20):203901, 2013.

[120] Benjamin J Bowers and David P Arnold. Spherical, rolling magnet generators for passive energy harvesting from human motion. *Journal of Micromechanics and Microengineering*, 19(9):094008, 2009.

[121] Christopher Lee, David Stamp, Nitin R Kapania, and José Oscar Mur-Miranda. Harvesting vibration energy using nonlinear oscillations of an electromagnetic inductor. In *Energy Harvesting and Storage: Materials, Devices, and Applications*, volume 7683, page 76830Y. International Society for Optics and Photonics, 2010.

[122] BP Mann and BA Owens. Investigations of a nonlinear energy harvester with a bistable potential well. *Journal of Sound and Vibration*, 329(9):1215–1226, 2010.

[123] Anthony Marin, Patrick Heitzmann, Jens Twiefel, and Shashank Priya. Improved pen harvester for powering a pulse rate sensor. In *Active and Passive Smart Structures and Integrated Systems 2012*, volume 8341, page 83411D. International Society for Optics and Photonics, 2012.

[124] Miah A Halim, Hyunok Cho, and Jae Y Park. Design and experiment of a human-limb driven, frequency up-converted electromagnetic energy harvester. *Energy Conversion and Management*, 106:393–404, 2015.

[125] Serol Turkyilmaz, Haluk Kulah, and Ali Muhtaroglu. Design and prototyping of second generation metu mems electromagnetic micro-power generators. In *Energy Aware Computing (ICEAC), 2010 International Conference on*, pages 1–4. IEEE, 2010.

[126] Farid Khan, Farrokh Sassani, and Boris Stoeber. Copper foil-type vibration-based electromagnetic energy harvester. *Journal of Micromechanics and Microengineering*, 20(12):125006, 2010.

[127] Huicong Liu, Bo Woon Soon, Nan Wang, CJ Tay, Chenggen Quan, and Chengkuo Lee. Feasibility study of a 3d vibration-driven electromagnetic mems energy harvester with multiple vibration modes. *Journal of Micromechanics and Microengineering*, 22(12):125020, 2012.

[128] Mengdi Han, Quan Yuan, Xuming Sun, and Haixia Zhang. Design and fabrication of integrated magnetic mems energy harvester for low frequency applications. *Journal of Microelectromechanical Systems*, 23(1):204–212, 2014.

[129] Özge Zorlu, Emre Tan Topal, and Haluk Kulah. A vibration-based electromagnetic energy harvester using mechanical frequency up-conversion method. *IEEE Sensors Journal*, 11(2):481–488, 2011.

[130] XY Wang, S Palagummi, L Liu, and FG Yuan. A magnetically levitated vibration energy harvester. *Smart Materials and Structures*, 22(5):055016, 2013.

[131] Yonggang Jiang, Shingo Masaoka, Takayuki Fujita, Minoru Uehara, Tomohiko Toyonaga, Kouhei Fujii, Kohei Higuchi, and Kazusuke Maenaka. Fabrication of a vibration-driven electromagnetic energy harvester with integrated ndfeb/ta multilayered micro-magnets. *Journal of Micromechanics and Microengineering*, 21(9):095014, 2011.

[132] Mengdi Han, Zhongliang Li, Xuming Sun, and Haixia Zhang. Analysis of an in-plane electromagnetic energy harvester with integrated magnet array. *Sensors and Actuators A: Physical*, 219:38–46, 2014.

[133] Scott Meninger, Jose Oscar Mur-Miranda, Rajeevan Amirtharajah, Anantha Chandrakasan, and Jeffrey H Lang. Vibration-to-electric energy conversion. *IEEE Transactions on Very Large Scale Integration (VLSI) Systems*, 9(1):64–76, 2001.

[134] Dimitri Galayko, Andrii Dudka, Armine Karami, Eoghan O'Riordan, Elena Blokhina, Orla Feely, and Philippe Basset. Capacitive energy conversion with circuits implementing a rectangular charge-voltage cycle-part 1: Analysis of the electrical domain. *IEEE Transactions on Circuits and Systems I: Regular Papers*, 62(11):2652–2663, 2015.

[135] Vitaly Dorzhiev, Armine Karami, Philippe Basset, Frédéric Marty, Valery Dragunov, and Dimitri Galayko. Electret-free micromachined silicon electrostatic vibration energy harvester with the bennet's doubler as conditioning circuit. *IEEE Electron Device Letters*, 36(2):183–185, 2015.

[136] U Bartsch, J Gaspar, and O Paul. Low-frequency two-dimensional resonators for vibrational micro energy harvesting. *Journal of Micromechanics and Microengineering*, 20(3):035016, 2010.

[137] K Tao, SW Lye, N Wang, X Hu, and JM Miao. A sandwich-structured mems electret power generator for multi-directional vibration energy harvesting. In *Solid-State Sensors, Actuators and Microsystems (TRANSDUCERS), 2015 Transducers-2015 18th International Conference on*, pages 51–54. IEEE, 2015.

[138] Yingxian Lu, Francesco Cottone, Sébastien Boisseau, Frédéric Marty, Dimitri Galayko, and Philippe Basset. A nonlinear mems electrostatic kinetic energy harvester for human-powered biomedical devices. *Applied Physics Letters*, 107(25):253902, 2015.

[139] Makoto Honzumi, Ai Ueno, Kei Hagiwara, Yuji Suzuki, Toshifumi Tajima, and Nobuhide Kasagi. Soft-x-ray-charged vertical electrets and its application to electrostatic transducers. In *Micro Electro Mechanical Systems (MEMS), 2010 IEEE 23rd International Conference on*, pages 635–638. IEEE, 2010.

[140] Makoto Honzumi, Kei Hagiwara, Yoshinori Iguchi, and Yuji Suzuki. High-speed electret charging using vacuum uv photoionization. *Applied Physics Letters*, 98(5):052901, 2011.

[141] Guang Zhu, Zong-Hong Lin, Qingshen Jing, Peng Bai, Caofeng Pan, Ya Yang, Yusheng Zhou, and Zhong Lin Wang. Toward large-scale energy harvesting by a nanoparticle-enhanced triboelectric nanogenerator. *Nano letters*, 13(2):847–853, 2013.

[142] B Meng, W Tang, XS Zhang, MD Han, XM Sun, W Liu, and HX Zhang. A high performance triboelectric generator for harvesting low frequency ambient vibration energy. In *Micro Electro Mechanical Systems (MEMS), 2014 IEEE 27th International Conference on*, pages 346–349. IEEE, 2014.

[143] Jinwen Zhang and Zhiqiu Lv. A fruit jelly mems electret power generator. *Proc. Power-MEMS'08*, pages 285–8, 2008.

[144] Fei Wang and Ole Hansen. Electrostatic energy harvesting device with out-of-the-plane gap closing scheme. *Sensors and Actuators A: Physical*, 211:131–137, 2014.

[145] Anthony G Fowler, SO Reza Moheimani, and Sam Behrens. A 3-dof mems ultrasonic energy harvester. In *Sensors, 2012 IEEE*, pages 1–4. IEEE, 2012.

[146] Cuong P Le, Einar Halvorsen, Oddvar Søråsen, and Eric M Yeatman. Microscale electrostatic energy harvester using internal impacts. *Journal of Intelligent Material Systems and Structures*, 23(13):1409–1421, 2012.

[147] Sukhdeep Kaur, Einar Halvorsen, Oddvar Søråsen, and Eric M Yeatman. Characterization and modeling of nonlinearities in in-plane gap closing electrostatic energy harvester. *Journal of Microelectromechanical Systems*, 24(6):2071–2082, 2015.

[148] Kai Tao, Shuwei Liu, Sun Woh Lye, Jianmin Miao, and Xiao Hu. A three-dimensional electret-based micro power generator for low-level ambient vibrational energy harvesting. *Journal of Micromechanics and Microengineering*, 24(6):065022, 2014.

[149] Bin Yang, Chengkuo Lee, Rama Krishna Kotlanka, Jin Xie, and Siak Piang Lim. A mems rotary comb mechanism for harvesting the kinetic energy of planar vibrations. *Journal of Micromechanics and Microengineering*, 20(6):065017, 2010.

[150] Salar Chamanian, Reza Pakdaman Zangabad, Payam Zarbakhsh, Manouchehr Bahrami, and Mohamad Khodaei. Wideband capacitive energy harvester based on mechanical frequency-up conversion. In *Sensors Applications Symposium (SAS), 2012 IEEE*, pages 1–4. IEEE, 2012.

[151] Hussam Kloub, Daniel Hoffmann, Bernd Folkmer, and Yiannos Manoli. A micro capacitive vibration energy harvester for low power electronics. *Work*, 11(25):1, 2009.

[152] Jin Yang, Yumei Wen, Ping Li, Xianzhi Dai, and Ming Li. A broadband vibration energy harvester using magnetoelectric transducer. In *Sensors, 2010 IEEE*, pages 1905–1909. IEEE, 2010.

[153] S Ju, SH Chae, Y Choi, S Jun, SM Park, S Lee, HW Lee, and C-H Ji. Harvesting energy from low frequency vibration using msma/mfc laminate composite. In *Solid-State Sensors, Actuators and Microsystems (TRANSDUCERS & EUROSENSORS XXVII), 2013 Transducers & Eurosensors XXVII: The 17th International Conference on*, pages 1348–1351. IEEE, 2013.

[154] Ping Li, Yumei Wen, Wenjian Yin, and Hanzhong Wu. An upconversion management circuit for low-frequency vibrating energy harvesting. *IEEE Transactions on Industrial Electronics*, 61(7):3349–3358, 2014.

[155] James Prescott Joule. Xvii. on the effects of magnetism upon the dimensions of iron and steel bars. *Philosophical Magazine Series 3*, 30(199):76–87, 1847.

[156] Hugo Durou, Carole Rossi, Magali Brunet, Claude Vanhecke, Nicolas Bailly, Gustavo Ardila, Lamine Ourak, Adrien Ramond, Patrice Simon, and Pierre-Louis Taberna. Power harvesting and management from vibrations: a multi-source strategy simulation for aircraft structure health monitoring. In *Smart Structures, Devices, and Systems IV*, volume 7268, page 726810. International Society for Optics and Photonics, 2008.

[157] Vinod R Challa, MG Prasad, and Frank T Fisher. A coupled piezoelectric–electromagnetic energy harvesting technique for achieving increased power output through damping matching. *Smart materials and Structures*, 18(9):095029, 2009.

[158] Bin Yang, Chengkuo Lee, Wei Loon Kee, and Siak-Piang Lim. Hybrid energy harvester based on piezoelectric and electromagnetic mechanisms. *Journal of Micro/Nanolithography, MEMS, and MOEMS*, 9(2):023002, 2010.

[159] M Amin Karami and Daniel J Inman. Equivalent damping and frequency change for linear and nonlinear hybrid vibrational energy harvesting systems. *Journal of Sound and Vibration*, 330(23):5583–5597, 2011.

[160] Yingjun Sang, Xueliang Huang, Hexiang Liu, and Ping Jin. A vibration-based hybrid energy harvester for wireless sensor systems. *IEEE transactions on Magnetics*, 48(11):4495–4498, 2012.

[161] Kean C Aw and Siva V Praneeth. Low frequency vibration energy harvesting from human motion using ipmc cantilever with electromagnectic transduction. In *Nano/Micro Engineered and Molecular Systems (NEMS), 2013 8th IEEE International Conference on*, pages 645–648. IEEE, 2013.

[162] Hyung-Jo Jung, In-Ho Kim, Dong Yi Min, Sung-Han Sim, and Jeong-Hoi Koo. A hybrid electromagnetic energy harvesting device for low frequency vibration. In *Active and Passive Smart Structures and Integrated Systems 2013*, volume 8688, page 86881I. International Society for Optics and Photonics, 2013.

[163] Huicong Liu, Kah How Koh, and Chengkuo Lee. Ultra-wide frequency broadening mechanism for micro-scale electromagnetic energy harvester. *Applied Physics Letters*, 104(5):053901, 2014.

[164] S Mahmoudi, N Kacem, and N Bouhaddi. Enhancement of the performance of a hybrid nonlinear vibration energy harvester based on piezoelectric and electromagnetic transductions. *Smart Materials and Structures*, 23(7):075024, 2014.

[165] Ayyaz M Paracha, Philippe Basset, P Lim, Frédéric Marty, and Tarik Bourouina. A bulk silicon-based vibration-to-electric energy converter using an in-plane overlap plate (ipop) mechanism. In *PowerMEMS'2006 Workshop Proceedings*, 2006.

[166] Yingxian Lu, Francesco Cottone, Sébastien Boisseau, Dimitri Galayko, Frédéric Marty, and Philippe Basset. Low-frequency mems electrostatic vibration energy harvester with corona-charged vertical electrets and nonlinear stoppers. In *Journal of Physics: Conference Series*, volume 660, page 012003. IOP Publishing, 2015.

[167] Yingxian Lu, Francesco Cottone, Sébastien Boisseau, Frédéric Marty, Dimitri Galayko, and Philippe Basset. Low-frequency and ultra-wideband mems electrostatic vibration energy harvester powering an autonomous wireless temperature sensor node. In *Micro Electro Mechanical Systems (MEMS), 2016 IEEE 29th International Conference on*, pages 33–36. IEEE, 2016.

[168] Stephen D Senturia. *Microsystem design*. Springer Science & Business Media, 2007.

[169] Minhang Bao and Heng Yang. Squeeze film air damping in mems. *Sensors and Actuators A: Physical*, 136(1):3–27, 2007.

[170] Binh Duc Truong, Cuong Phu Le, and Einar Halvorsen. Experiments on power optimization for displacement-constrained operation of a vibration energy harvester. In *Journal of Physics: Conference Series*, volume 660, page 012012. IOP Publishing, 2015.

[171] Armine Karami, Philippe Basset, and Dimitri Galayko. Electrostatic vibration energy harvester using an electret-charged mems transducer with an unstable auto-synchronous conditioning circuit. In *Journal of Physics: Conference Series*, volume 660, page 012025. IOP Publishing, 2015.

[172] Yingxian Lu, Eoghan O'Riordan, Francesco Cottone, Sébastien Boisseau, Dimitri Galayko, Elena Blokhina, Frédéric Marty, and Philippe Basset. A batch-fabricated electret-biased wideband mems vibration energy harvester with frequency-up conversion behavior powering a uhf wireless sensor node. *Journal of Micromechanics and Microengineering*, 26(12):124004, 2016.

[173] Yingxian Lu, Frédéric Marty, Dimitri Galayko, and Philippe Basset. New comb geometry of capacitive vibration energy harvesters miniaturizing the air damping effect. In *Micro Electro Mechanical Systems (MEMS), 2017 IEEE 30th International Conference on*, pages 857–860. IEEE, 2017.

[174] Geon-Tae Hwang, Myunghwan Byun, Chang Kyu Jeong, and Keon Jae Lee. Flexible piezoelectric thin-film energy harvesters and nanosensors for biomedical applications. *Advanced healthcare materials*, 4(5):646–658, 2015.

[175] Achraf Kachroudi, Skandar Basrour, Libor Rufer, Alain Sylvestre, and Fathi Jomni. Microstructured pdms piezoelectric enhancement through charging conditions. *Smart Materials and Structures*, 25(10):105027, 2016.

[176] Peng Bai, Guang Zhu, Zong-Hong Lin, Qingshen Jing, Jun Chen, Gong Zhang, Jusheng Ma, and Zhong Lin Wang. Integrated multilayered triboelectric nanogenerator for harvesting biomechanical energy from human motions. *ACS nano*, 7(4):3713–3719, 2013.

[177] Bo Meng, Wei Tang, Xiaosheng Zhang, Mengdi Han, Wen Liu, and Haixia Zhang. Self-powered flexible printed circuit board with integrated triboelectric generator. *Nano Energy*, 2(6):1101–1106, 2013.

[178] Ahmed Almusallam, Zhenhua Luo, Abiodun Komolafe, Kai Yang, Andrew Robinson, Russel Torah, and Steve Beeby. Flexible piezoelectric nano-composite films for kinetic energy harvesting from textiles. *Nano Energy*, 33:146–156, 2017.

[179] Aidin Delnavaz and Jérémie Voix. Flexible piezoelectric energy harvesting from jaw movements. *Smart Materials and Structures*, 23(10):105020, 2014.

[180] Yoshihiko Sakane, Yuji Suzuki, and Nobuhide Kasagi. The development of a high-performance perfluorinated polymer electret and its application to micro power generation. *Journal of Micromechanics and Microengineering*, 18(10):104011, 2008.

[181] RE Collins. Distribution of charge in electrets. *Applied Physics Letters*, 26(12):675–677, 1975.

[182] Anu Mishra. Studies of polymer electrets. ii. factors governing the stabilities of homoelectrets obtained from polystyrene and its derivatives. *Journal of Applied Polymer Science*, 27(4):1107–1118, 1982.

[183] W.D. Budinger. Poromeric material having uniformly distributed electrets for maintaining an electrostatic charge, January 24 1995. US Patent 5,384,337.

[184] Kimiaki Kashiwagi, Kuniko Okano, Tatsuya Miyajima, Yoichi Sera, Noriko Tanabe, Yoshitomi Morizawa, and Yuji Suzuki. Nano-cluster-enhanced high-performance perfluoropolymer electrets for energy harvesting. *Journal of Micromechanics and Microengineering*, 21(12):125016, 2011.

[185] Hsi-wen Lo and Yu-Chong Tai. Parylene-based electret power generators. *Journal of Micromechanics and Microengineering*, 18(10):104006, 2008.

[186] Dan Li and Younan Xia. Electrospinning of nanofibers: reinventing the wheel? *Advanced materials*, 16(14):1151–1170, 2004.

[187] Andreas Greiner and Joachim H Wendorff. Electrospinning: a fascinating method for the preparation of ultrathin fibers. *Angewandte Chemie International Edition*, 46(30):5670–5703, 2007.

[188] Jean-Marc Laheurte, Christian Ripoll, Dominique Paret, and Christophe Loussert. *UHF RFID technologies for identification and traceability.* John Wiley & Sons, 2014.

[189] Nicholas S Hudak and Glenn G Amatucci. Small-scale energy harvesting through thermoelectric, vibration, and radiofrequency power conversion. *Journal of Applied Physics*, 103(10):5, 2008.

[190] Abhiman Hande, Raj Bridgelall, and Ben Zoghi. Vibration energy harvesting for disaster asset monitoring using active rfid tags. *Proceedings of the IEEE*, 98(9):1620–1628, 2010.

[191] Satish K Sharma, Anup N Kulkarni, Mukund R Thyagarajan, and Balamurugan Shanmugam. A compact spiral loaded planar dipole antenna with frequency reconfiguration. In *Antennas and Propagation Society International Symposium (APSURSI), 2012 IEEE*, pages 1–2. IEEE, 2012.

[192] Miodrag Bolic, David Simplot-Ryl, and Ivan Stojmenovic. *RFID systems: research trends and challenges.* John Wiley & Sons, 2010.

[193] Daniel D Deavours. Analysis and design of wideband passive uhf rfid tags using a circuit model. In *RFID, 2009 IEEE International Conference on*, pages 283–290. IEEE, 2009.

[194] Kamran Entesari, Alireza Pourghorban Saghati, Vikram Sekar, and Marcelino Armendariz. Tunable siw structures: antennas, vcos, and filters. *IEEE Microwave Magazine*, 16(5):34–54, 2015.

[195] Monageng Kgwadi and Timothy D Drysdale. Parametric study of broadband tunable helix antenna matching. In *Antennas and Propagation Conference (LAPC), 2014 Loughborough*, pages 128–131. IEEE, 2014.

[196] Keith Duncan Palmer and Mel W van Rooyen. Simple broadband measurements of balanced loads using a network analyzer. *IEEE Transactions on Instrumentation and Measurement*, 55(1):266–272, 2006.

[197] Yingxian Lu, M Capo-Chichi, Yamin Leprince-Wang, and Philippe Basset. A flexible electrostatic kinetic energy harvester based on electret films of electrospun nanofibers. *Smart Materials and Structures*, 27(1):014001, 2017.

[198] Yingxian Lu, Frédéric Marty, Dimitri Galayko, Jean-Marc Laheurte, and Philippe Basset. A power supply module for autonomous portable electronics: ultralow-frequency mems electrostatic kinetic energy harvester with hierarchical comb structure reducing air damping. *Microsystems and Nanoengineering*, 2018.

[199] Yingxian Lu, Juillard Jérôme, Francesco Cottone, Dimitri Galayko, and Philippe Basset. An impact-coupled electrostatic kinetic energy harvester and its predictive model taking nonlinear air damping effect into account. *Journal of Microelectromechanical Systems*, 2018.

[200] Linda Serairi, Long Gu, Yong Qin, Yingxian Lu, Philippe Basset, and Yamin Leprince-Wang. Flexible piezoelectric nanogenerators based on pvdf-trfe nanofibers. *The European Physical Journal Applied Physics*, 80(3):30901, 2017.

[201] Ali Ghaffarinejad, Yingxian Lu, Ronan Hichet, Dimitri Galayko, Javad Yavand Hasani, Philippe Basset, et al. Bennet's doubler working as a power booster for triboelectric nano generators. *Electronics Letters*, 2017.

[202] Ronan Hinchet, Ali Ghaffarinejad, Yingxian Lu, Javad Yavand Hasani, Sang-Woo Kim, and Philippe Basset. Understanding and modeling of triboelectric-electret nanogenerator. *Nano Energy*, 2018.

[203] Philippe Basset, Yingxian Lu, and Yamin Leprince-Wang. Electrostatic transducer for kinetic energy harvesting or mechanical sensing.

[204] Philippe Basset and Yingxian Lu. Miniature kinetic energy harvester for generating electrical energy from mechanical vibrations.

[205] Yingxian Lu, D Amroun, Yamin Leprince-Wang, and Philippe Basset. A paper-based electrostatic kinetic energy harvester with stacked multiple electret films made of electrospun polymer nanofibers. In *Journal of Physics: Conference Series*, volume 773, page 012032. IOP Publishing, 2016.

[206] Yingxian Lu, Frédéric Marty, Dimitri Galayko, Jean-Marc Laheurte, and Philippe Basset. A mems eveh-assisted long-range rfid tag system for applications with low-frequency vibrations. In *Multidisciplinary Digital Publishing Institute Proceedings*, volume 1, page 582, 2017.

[207] MA Ben Ouanes, Yingxian Lu, Hatem Samaali, Philippe Basset, and F Najar. Design and test of a bennet's doubler device with mechanical switches for vibrational energy harvesting. In *Journal of Physics: Conference Series*, volume 773, page 012038. IOP Publishing, 2016.

Résumé

Le nombre croissant d'appareils électroniques portables génère une forte demande pour des modules d'alimentation électrique à la fois durables, de faibles dimensions et offrant une puissance de sortie suffisante. Les récupérateurs d'énergie cinétiques (REC), qui transforment les vibrations ou les mouvements ambiants en énergie électrique, sont une alternative prometteuse pour l'alimentation électrique qui est étudiée de manière intensive ces dernières années. Cependant, les performances des RECs miniatures sont fortement limitées par leur taille. De plus, les vibrations ambiantes sont généralement abondantes en basses fréquences, ce qui est également un facteur majeur limitant la puissance de sortie d'un REC miniaturisé.

Dans ce travail de thèse, nous avons proposé d'améliorer la puissance de sortie des RECs électrostatiques basses- fréquences grâce à un mécanisme de déplacement de la conversion d'énergie vers les hautes fréquences obtenu suite à un couplage par impact. Nous avons proposé un modèle numérique prédictif d'un prototype réalisé dans les salles blanches d'ESIEE Paris qui prend en compte l'effet d'amortissement de l'air et les impacts. Un second prototype avec une géométrie améliorée du module capacitif réduisant considérablement la force d'amortissement de l'air a aussi été réalisé. Par ailleurs, des approches alternatives pour des applications variées ont été proposées, comme un REC entièrement flexible et un REC 2-D sensible aux vibrations suivant deux directions orthogonales. Enfin, un module de communication RFID semi-passif, boosté grâce à un REC basse fréquence, est présenté.

Abstract

A growing number of portable and wearable electronics results in an increasing demand of sustainable and localized power supply module of small size and weight, and offering high output power. As a promising choice for the power supply, Kinetic energy harvesters (KEHs), transforming the ambient vibrations or motions into electrical energy, are studied intensively in recent years. The performance of the miniature KEHs available in literature are generally confined by their sized. The ambient vibrations are usually abundant in low frequency, which is also a major factor restricting the output power of the KEH. In order to enhance the power output, we should improve the energy conversion efficiency, which is related to the transduction principle. This work presents the improvement of the output power of low frequency electrostatic KEHs through impact-coupled mechanical frequency up conversion mechanism, and proposes a predictive numerical model of the prototype which considers the squeeze film air damping effect and the impacts in the prototype. A prototype is proposed with improved geometry of capacitive module reducing the air damping force. Alternative approaches to adjust the KEHs to varied applications are proposed, including a fully flexible KEH designed for wearable electronics, and a 2-D low frequency KEH that is sensible to vibrations along two orthogonal directions. In addition, a fully energy-autonomous RFID tag system implementing the low frequency KEH as the power supply module and a semi-passive RFID communication module is presented.